Reconfigurable transmitarray antennas at millimeter-wave frequencies

Luca Di Palma

ANNÉE 2015

UNIVERSITÉ DE RENNES 1

THÈSE / UNIVERSITÉ DE RENNES 1
sous le sceau de l'Université Européenne de Bretagne

pour le grade de

DOCTEUR DE L'UNIVERSITÉ DE RENNES 1
Mention : Traitement du Signal et Télécomumnications

Ecole doctorale MATISSE

présentée par

Luca Di Palma

préparée au CEA-Leti en collaboration avec l'unité de recherche UMR CNRS 6164
Institut d'Electronique et de Télécommunications de Rennes
UFR Informatique - Électronique

Antennes Réseaux Transmetteurs Reconfigurables aux Fréquences Millimétriques

Thèse soutenue à Grenoble
le 16 décembre 2015
devant le jury composé de :

Stefano MACI
Professeur, Université de Sienne, Italie / président du jury

José A. ENCINAR
Professeur, Université de Madrid, Espagne / rapporteur

Claire MIGLIACCIO
Professeur, Université de Nice / rapporteur

Cyril MANGENOT
Chef de division, ESA-ESTEC / examinateur

Laurent PETIT
Ingénieur de recherche, Radiall / examinateur

Philippe POULIGUEN
Ingénieur de recherche, DGA-MI / examinateur

Laurent DUSSOPT
Ingénieur de recherche, CEA-Leti / encadrant

Ronan SAULEAU
Professeur, Université de Rennes / directeur de thèse

To my family

"There are two possible outcomes: if the result confirms the hypothesis, then you've made a measurement. If the result is contrary to the hypothesis, then you've made a discovery."

Enrico Fermi

Contents

Acknowledgements

First, I would like to express my special appreciation and thanks to my supervisors Prof. Ronan Sauleau, Professor at the University of Rennes 1, and Dr. Laurent Dussopt, Senior Research Engineer at CEA-Leti. You have been great mentors during the last years. I would like to thank you for encouraging my research and for allowing me to grow as a research scientist. Your knowledge and your wisdom have been sources of inspiration.

Je suis honoré d'avoir eu l'occasion de travailler avec vous pendant ces trois années.

I would like to express my gratitude to Dr. Patrick Potier and Dr. Philippe Pouliguen, Research Engineers at the *Diretion Générale de l'Armement*, for having accepted to supervise my work. The brilliant comments and suggestions you gave me during our meetings have been precious.

I would like to extend my thanks to Dr. Antonio Clemente, Research Engineer at CEA-Leti. His moral and technical support has been fundamental. I will never forget your help and our friendship. *Antonio, grazie di tutto!*

I would like to give thanks to Prof. Claire Migliaccio, Professor at the University of Nice Sophia-Antipolis, and Prof. José A. Encinar, Professor at the Polytechnic University of Madrid (Spain), for having accepted to evaluate this thesis manuscript and to be part of the jury. Their valuable comments have been very useful.

I extend my thanks to Prof. Stefano Maci, Professor at the University of Siena (Italy), for having accepted to participate to the defence and chairing the jury.

I express my gratitude to Dr. Cyril Mangenot, Head of Electromagnetic and Space Environment Division at the European Space Agency (ESA-ESTEC, Noordwijk, The Netherlands) for the interest he demonstrated in my research activity and for having accepted to take part to the defence. I would also give thanks to Dr. Laurent Petit, Research Engineer at Radiall, for having accepted to be a member of the jury.

I would like to thank Dr. Roland Blanpain, Head of the System and Integration Department, and Dr. Dominique Noguet, Head of the Telecommunication and Security Service,

for welcoming me at the Laboratories of CEA-Leti in Grenoble. I extend my thanks to Dr. Christophe Delaveaud, Head of the Laboratory of Antennas and Propagation, for welcoming me in his team and having supported my work. I want to mention the engineers and all the colleagues of the Laboratory. In particular, I would like to thank Raffaele, Julien, Francesco M., Jean-François, Francesco G., Anna, Lotfi and Laurent. Their interest in my research activity allowed to improve the quality of this work.

I would like to express my gratitude to Francesco S. and Andrea C., supportive friends and colleagues since we were first-year students in Rome. Despite the thousands of kilometres of distance, you played important roles during these years helping me throughout all the difficulties.

Finally, I would like to give special thanks to my brother, Andrea, to my parents, Stella and Marco, and to all my family. Words can not express how grateful I am to you. You have always supported me and encouraged me to follow my dreams.

Grenoble, December 2015

L. di P.

List of Figures

List of Tables

Résumé en français

De nombreuses applications civiles et militaires (faisceaux hertziens, communications par satellite, radars automobiles, systèmes d'imagerie haute résolution) nécessitent des antennes à faisceau reconfigurable (dépointage de faisceau, faisceaux multiples, faisceaux formés).

Les antennes à réseaux transmetteurs apparaissent comme une alternative aux réseaux phasés classiques ou aux réseaux réflecteurs pour ces applications. Le principal objectif de cette thèse est de démontrer la faisabilité de réseaux reconfigurables fabriqués avec des technologies standards en bande Ka (20-30 GHz) qui est envisagée pour de nombreuses applications de communication.

Les antennes à réseau transmetteur sont constituées d'une ou plusieurs sources focales qui illuminent un réseau de cellules élémentaires, comme montré sur le schema de la Fig. 1. Chaque cellule élémentaire se compose d'une antenne en réception, d'un système de déphasage et d'une antenne en transmission. Le contrôle de la phase de l'onde transmise, qui est réalisé électroniquement dans le cas de réseaux reconfigurables, permet de focaliser le faisceau dans une direction donnée et/ou de générer un diagramme avec un gabarit prédéfini. Dans le cas des cellules reconfigurables, la fonction de déphasage est généralement mise en œuvre en utilisant des diodes varactor, des diodes p-i-n, des commutateurs MEMS, ou des matériaux accordables. Un nombre limité d'états de phase (quantification de phase) peut être utilisé afin de réduire d'une part la complexité de la cellule élémentaire et de la logique de commande du réseau, et d'autre part les pertes d'insertion liées aux dispositifs intégrés sur les cellules.

Une cellule élémentaire a été développée et optimisée en utilisant le simulateur commercial Ansys HFSS ; elle est constituée de quatre couches métalliques (élément rayonnant du côté réception, élément rayonnant du côté transmission, plan de masse et lignes de polarisation) réalisées sur deux substrats identiques (Fig. 2). Une antenne patch rectangulaire chargée par une fente en U est réalisée sur la couche supérieure (patch passif). Sur la couche inférieure de la structure, une antenne patch rectangulaire chargée avec une fente en forme de O a été réalisée (patch actif). Deux diodes p-i-n (M/ACOM MA4GP907) sont intégrées sur cette antenne afin de contrôler la phase de l'onde transmise. Les deux patchs sont connectés entre eux par un via métallique traversant. Les deux diodes ont été montées

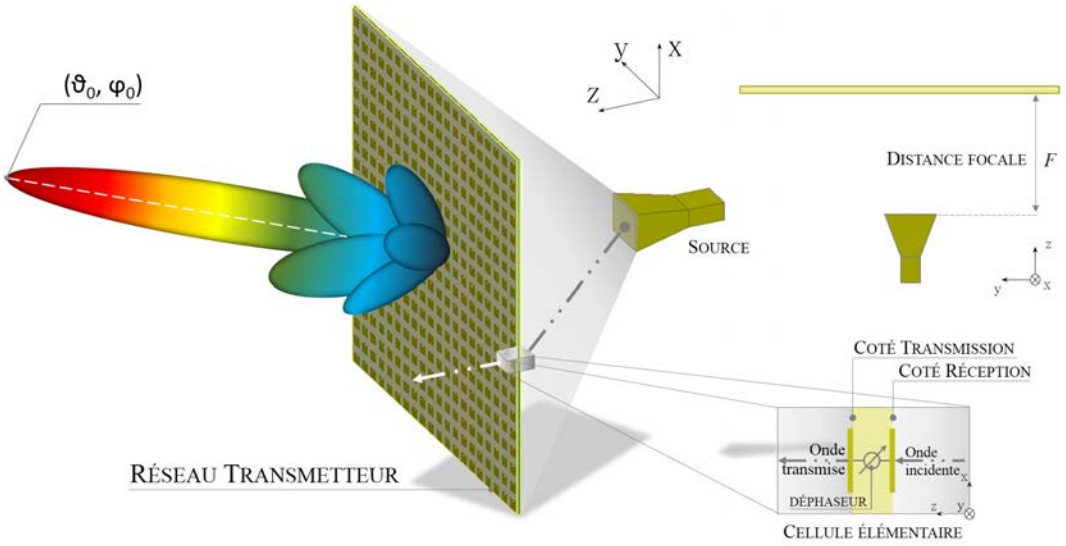

Figure 1: Schéma du principe de fonctionnement des réseaux transmetteurs. Vue 3D, en coupe et section d'une cellule élémentaire.

en antiparallèle afin de les contrôler par une seule ligne de commande avec un courant de polarisation positif ou négatif (±10 mA). Ainsi, une des extrémités de la fente en forme de O est toujours court-circuitée par une des diodes, formant une fente en U similaire à celle du patch passif. Les paramètres S simulés de la cellule élémentaire en considérant le sytème de mesure en guide sont montrés en Fig. 2(a) (lignes pointillées) pour les deux états de phase. Les mesures (symboles) montrent 1,09 dB et 1,29 dB de pertes minimales pour les états 0° et 180°, respectivement. La bande passante à 3 dB s'étend de 27,0 à 30,2 GHz et de 26,7 à 31,0 GHz dans les deux cas. Un bon accord entre mesures et simulation a été trouvé. La différence de phase mesurée en transmission entre les deux états est d'environ 180° sur toute la bande avec une erreur maximale de 13° à 26,8 GHz.

Le réseau transmetteur considéré se compose de 400 cellules élémentaires. Une méthode de simulation hybride, basée sur les résultats de simulations électromagnétiques (source focale, cellules élémentaires) et des formules analytiques, a été développée afin d'analyser ce type de structures avec des temps de simulation considérablement inférieurs à une simulation électromagnétique complète. Le réseau est illuminé par une source focale de type cornet d'un gain de 10 dBi. Une distance focale optimale (compromis entre pertes par débordement et apodisation) de 60 mm ($F/D = 0{,}59$) a été calculée à 29 GHz. Afin de générer une polarisation circulaire à partir d'une polarisation linéaire, la rotation séquentielle des éléments rayonnants a été appliquée côté transmission. En particulier, nous avons utilisé des rotations séquentielles aléatoires de 0°, 90°, 180° et 270° afin de minimiser les niveaux de lobes secondaires. La distribution de phase optimale est calculée en considérant ce type de rotations.

Un prototype, montré en Fig. 3(a), a été realisé et caracterisé en chambre anéchoïque.

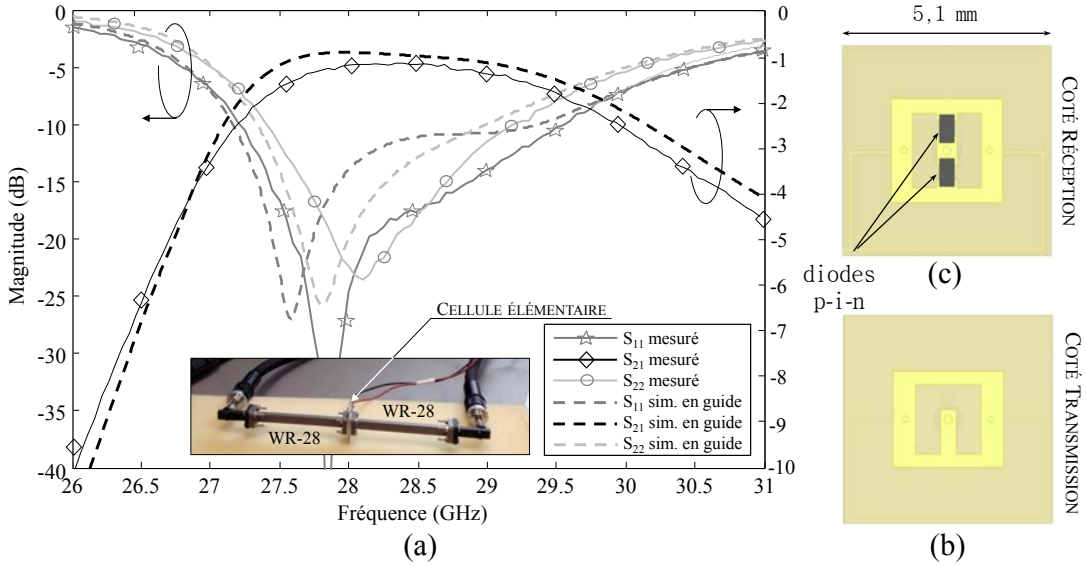

Figure 2: Paramètres S (a) et schéma (b,c) de la cellule élémentaire reconfigurable developpée en polarisation circulaire en bande Ka. (b) Côté réception et (c) côté transmission. Insert: photographie du système utilisé pour la characterisation en guide d'onde.

Le réseau présente 20,8 dBi de gain dans l'axe en polarisation circulaire gauche à 29 GHz avec une discrimination de polarisation de 20 dB. La bande passante à 3 dB est de 14,6% (27.4-30.7 GHz). Sur cette bande de fréquence, le rapport axial est inférieur à 1.8 dB.

En ajoutant un gradient à la loi de phase, le faisceau peut être dépointé électroniquement sur chaque plan. Les diagrammes de rayonnement avec angles de dépointage entre -60° et +60° dans le plan horizontal sont montrés en Fig. 3. Une bonne discrimination de polarisation dans la direction du faisceau principal a été préservée. En modifiant la distribution de phase, ce même réseau peut travailler en polarisation circulaire droite, en inversant les états des cellules 90° et 270°. Cette opération est purement électronique, elle est effectuée en commandant les diodes p-i-n intégrées du côté réception. Les diagrammes de rayonnements montrent des performances similaires aux faisceaux en polarisation circulaire gauche pour chaque angle de dépointage.

Une cellule réconfigurable travaillant en polarisation circulaire a également été conçue pour augmenter l'efficacité de surface du réseau transmetteur. Cela permet d'atteindre un gain maximal plus élevé en perdant la possibilité de commuter entre les deux polarisations circulaires (droite ou gauche). Plusieurs architectures ont été proposées en considérant les tolérances de fabrication. Des performances similaires à la cellule en polarisation linéaire déjá présentée (Fig. 2) ont été démontrées. Un dispositif et une procédure de calibration *ad hoc* ont été developpés pour sa caractérisation expérimentale en guide d'onde.

Enfin, des réseaux transmetteurs avec distance focale réduite et capables de générer plusieurs faisceaux ont été étudiés et caractérisés expérimentalement. La synthèse de fais-

ceaux pour application aux systèmes radars monopulse a été étudiée et validée en bande X. Les faisceaux somme et différence ont été mesurés sur les deux plans cardinaux avec des angles de dépointage entre -40° et +40°. Avec le même réseau, la réduction de la distance focale de l'antenne par un facteur deux a été vérifiée en utilisant quatre cornets comme sources focales. Un très bon accord entre les mesures et les simulations a été obtenu.

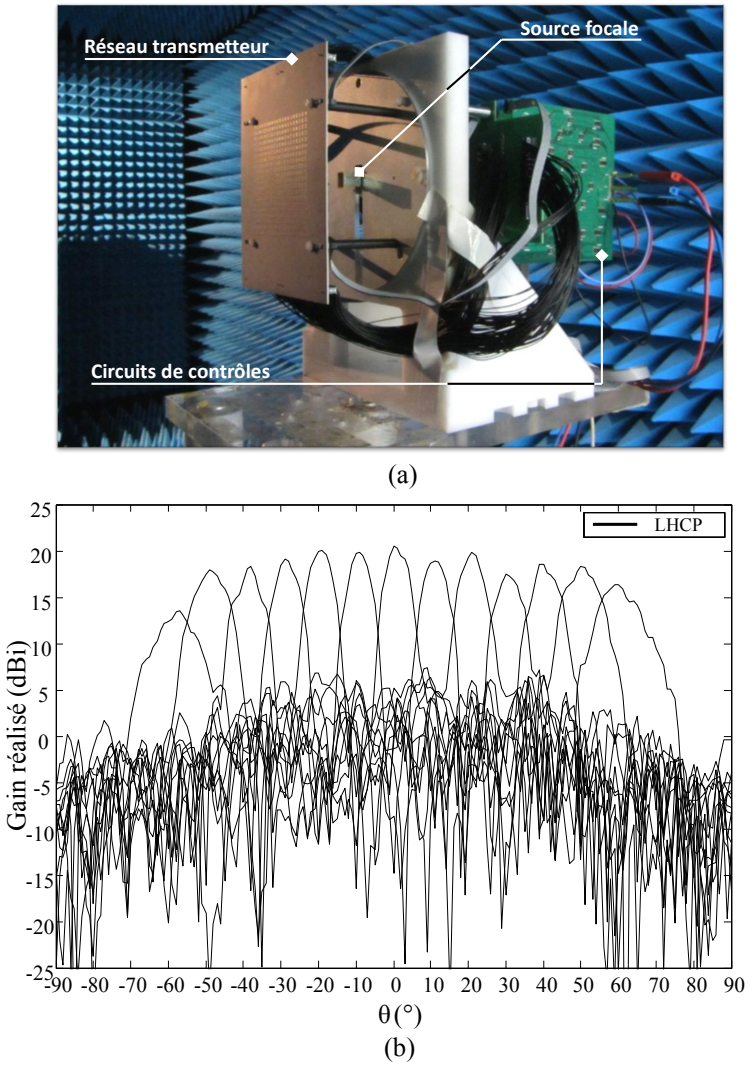

Figure 3: Photographie du prototype réalisé (a) et diagrammes de rayonnement (b) mesurés en chambre anéchoïque à 29 GHz pour angles de dépointages entre -60° et +60° sur le plan horizontal.

General introduction

Transmitarray antennas are gaining more and more interest for millimeter-wave wireless and radar applications where a high radiation gain is needed. They are based on a thin multi-layer array of transmitting unit-cells focusing/collimating the radiation to/from one or several focal sources by locally tuning the phase of the transmitted signals. Each unit-cell includes at least three functions: receiving, phase shifting and transmitting the signal.

The low fabrication cost, the absence of feed blockage, and the possibility to illuminate the surface with multiple sources, leading to more compact systems, are some of the transmitarray advantages.

Some promising applications are in the field of radar systems, satellite communications and next-generation wireless metropolitan area networks. In many cases, electronic reconfiguration capabilities are required, such as beamforming, beamsteering or polarization switching.

The main objective of this work is to propose and demonstrate the design of electronic reconfigurable transmitarray antennas in Ka-band manufactured with standard PCB technologies.

In Chapter 1, the working principle of transmitarray antennas is explained and compared to traditional phased array reflectarray technologies. The state-of-the-art of reconfigurable designs in different technologies is presented.

In Chapter 2, a hybrid simulation tool for these structures is proposed. It is based on numerical simulations and analytical formulations and allowing the analysis and synthesis of transmitarrays with a reduced computational effort. The sequential rotation technique is implemented and several rotation distributions are considered. A passive transmitarray has been prototyped for the experimental validation.

In Chapter 3, a reconfigurable unit-cell design in Ka-band and working in linear polarization is presented. The p-i-n diodes used in the design are characterized and modelled. The bias network design and the integration of several bias lines are developed. A sensitivity analysis and oblique incidence angle impact are studied. Measurements in waveguides are carried out in order to validate the design.

In Chapter 4, the design of a reconfigurable 400-elements transmitarray working in cir-

cular polarization in Ka-band is presented. It is based on the unit-cells of Chapter 3. A random sequential rotation is applied to the transmitting layer in order to generate a circularly-polarized beam. Measurements in anechoic chamber demonstrate the beam-tilting capabilities of the proposed antenna.

In Chapter 5, the design of a reconfigurable unit-cell in circular polarization in Ka-band is presented. Several architectures are investigated and the definition of an ad-hoc characterization setup in waveguide is proposed.

In Chapter 6, the radiation pattern synthesis for monopulse radar application is presented. Two strategies are considered and validated experimentally with anechoic chamber measurements in X band.

General conclusions and perspectives are finally drawn.

Chapter 1

Introduction

In this chapter, the transmitarray working principle and the comparison with other antenna technologies will be presented. The state-of-the-art on passive and reconfigurable transmitarrays is also reported. Finally, some application fields where this technology could be attractive and the main specifications (frequency, polarization, ...) will be illustrated.

1.1 Transmitarray: operating principle

There are many applications, such as in the fields of satellite communications and radars, in which high-gain antennas are needed and advanced beam controls, such as beam-steering and beam-forming, are desired. Most antennas currently used are based on phased arrays and parabolic reflector antennas. Large scanning angles can be obtained with phased arrays but the beam-forming network required is in general very complex and expensive. On the other hand, parabolic reflector antennas require a mechanical beam scanning. From a combination of the two systems, reflectarray antennas were born [1]. An alternative approach developed in the last years consists in the transmitarray antennas or planar discrete lenses.

A general scheme of a transmitarray antenna is shown in Fig. 1.1. It is formed by a feed, labelled focal source, placed at a distance F, labelled focal distance, which illuminates a first array, labelled receiving layer, working in receiving mode. This array is connected or coupled through a matrix of phase shifters to another one, labelled transmitting layer, working in transmitting mode. The focal distance is selected as a trade-off between spillover losses and illumination tapering in order to maximize the gain. Each unit-cell provides the phase shift required to compensate the differential path r_m from the source position and to generate the desired phase distribution (Fig. 1.1).

Most of the transmitarrays proposed during the last years are based on a planar technology reducing the cost of fabrication thanks to the standard PCB (Printed Circuit Board) manufacturing process. The main advantages of transmitarray antennas are the absence of

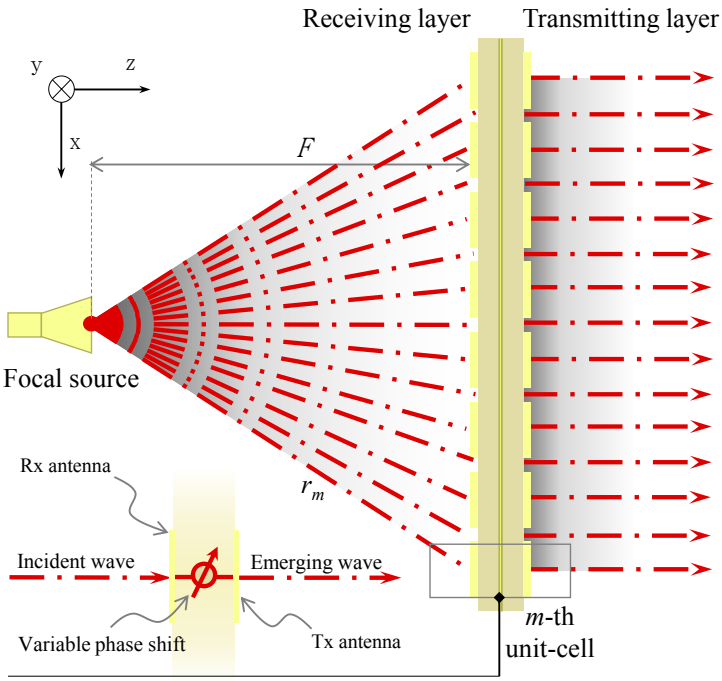

Figure 1.1: Scheme of the working principle of a transmitarray.

feed blockage area and the possibility to reduce the focal distance to obtain compact systems to mount on mobile platforms, such as aircraft, high-speed trains, etc. Controlling the phase shift given by each unit-cell, the main beam direction and shape can be changed dynamically and the transmitarray becomes reconfigurable. This phase shifting functionality can be implemented in different technologies and a summary of the state-of-the-art is presented in this chapter.

The competing technologies of transmitarrays are phased arrays and reflectarrays. Phased array systems are the most common antennas used in high-end radar applications. Excellent beam scanning capabilities are obtained with the control of the excitation phase and amplitude of each antenna element realized with complex networks, as shown in the scheme of Fig. 1.2(a), which can be implemented in different technologies. The main limitations of phased arrays are related to the design of the feed network. In fact, its complexity results in high losses which usually have to be compensated by amplifiers. In addition, this grade of complexity is directly proportional to the array size and it covers a significant share of the total costs. For electronic reconfigurable designs, high power consumption is another drawback. Quasi optical feeding systems, such as Rotman lenses, reflectarray and transmitarray antennas reduce the losses and complexity of the feeding network, especially for reconfigurable designs. However, phased arrays are still preferred where high performance radiation patterns characteristics are needed.

Reflectarrays are composed of an array of reflecting unit-cells illuminated by a focal

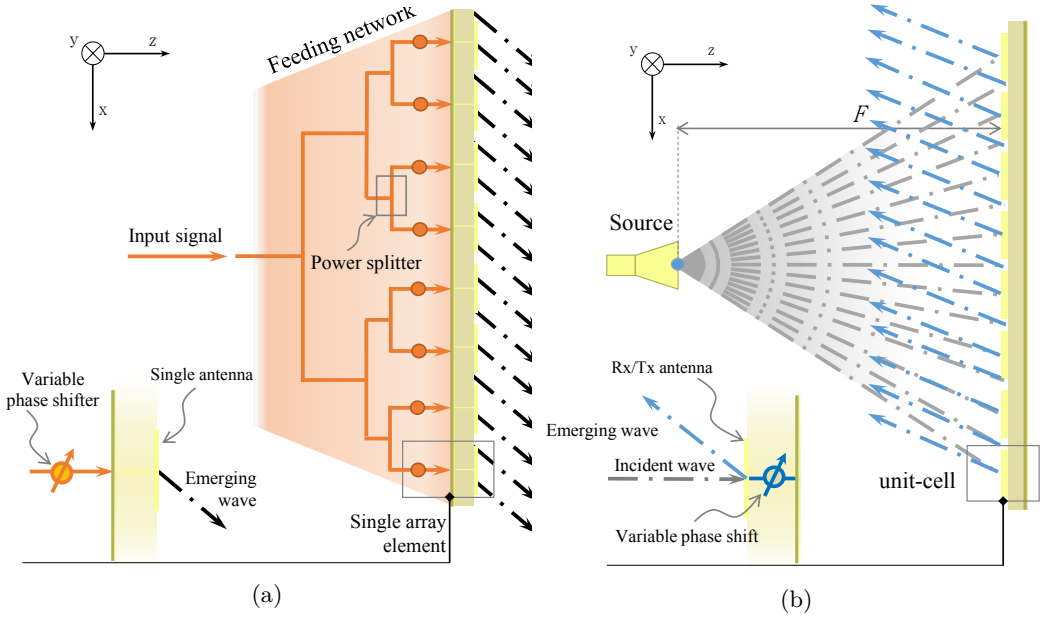

Figure 1.2: Scheme of the working principle of phased array (a) and reflectarray (b) antennas.

source, a horn antenna for example, as shown in the scheme of Fig. 1.2(b) [1]. By controlling the phase of the reflected waves locally with each unit-cell, it is possible to obtain the desired main beam direction and/or beam shape. Many designs based on this architecture were proposed in the last years [2, 3, 4, 5, 6, 7, 8, 9, 10, 11, 12, 13, 14]. However, the feed position introduces a blocking area which may perturb the radiated field in some applications. For this reason, tilted feed positions and sub-reflector systems are developed, similarly for the traditional parabolic reflector antennas, but this source position still limits the possibility of integration. On the other hand, the reflectarray systems facilitate the placement of the control logics for reconfigurable design on the back side of the structure.

In terms of complexity, unit-cells for transmitarray applications require more layers and then higher design complexity. However, this increases the degrees of freedom of the structure making easier the introduction of advanced controls on the transmitted waves, such as the polarization. In addition, in transmitarray antennas, the feed source placed on the opposite side of the radiation surface leads to multi source illumination and reduced focal distance possibilities, paving the way to integrate these antennas on vehicles, such as high-speed trains and aircrafts, leading to smart skin systems.

1.2 Passive transmitarrays: State-of-the-art

In this section, some examples of passive unit-cell and transmitarray designs proposed in the literature are presented. The main specification is usually to obtain a good transmission with different phase shifts by varying one or more dimensions of the structure. In [15], a

first simple design working in L-band is proposed. It is based on a patch loaded by two stubs printed on the transmitting layer. On the receiving layer, a ground plane with a slot is

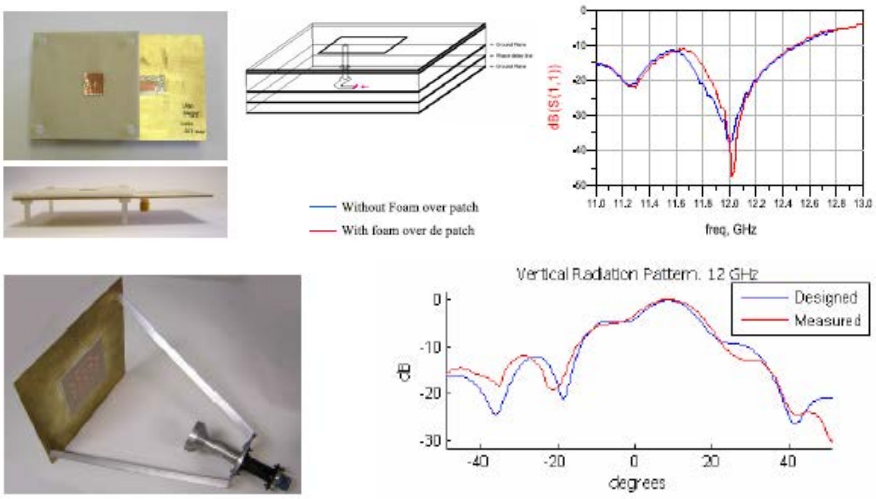

Figure 1.3: Scheme of unit cell with two ground planes and a delay line. 5×5 array designed and measured radiation pattern at 12 GHz [16].

considered to feed the patch. Different phase shifts can be achieved by using multiple stubs or a multilayer structure.

The solution proposed in [16, 17] considers one rectangular patch on both sides with two different ground planes in order to obtain a high level of isolation between the receiving and transmitting layers, as shown in Fig. 1.3. The intermediate layer includes a delay line in stripline technology connected to the two patches with two metallized vias to realize the required phase shifting function. A photograph of the 5×5 array prototype realized at 12 GHz and the measured radiation pattern are shown in Fig. 1.3. Despite the high level of isolation, a double ground plane stacking requires a high number of layers complicating the design. In addition, undesired modes could easily propagate in the intermediate layer between the ground planes (parallel-plate modes).

A simpler stacking was considered in [19, 18]. The transmitarrays proposed in these works at X- and V-band frequencies require only two rectangular patches printed on two substrates separated by one ground plane and connected to each other with a via (Fig. 1.4). The phase shift is obtained by considering different angles of rotation of the transmitting layer patch. In this way, the frequency response of the unit-cell is the same for all the phase states and a high phase resolution can be obtained while generating a circular polarization (Fig. 1.4). This unit-cell has been also studied analytically defining a lumped elements equivalent circuit in order to simplify the design procedure. A 20×20 unit-cell array with four different types of unit cells with phase shifts of 0°, 90°, 180° and 270° (2-bit of phase quantization) is designed and tested in X-band [19]. The structure and the radiation pattern

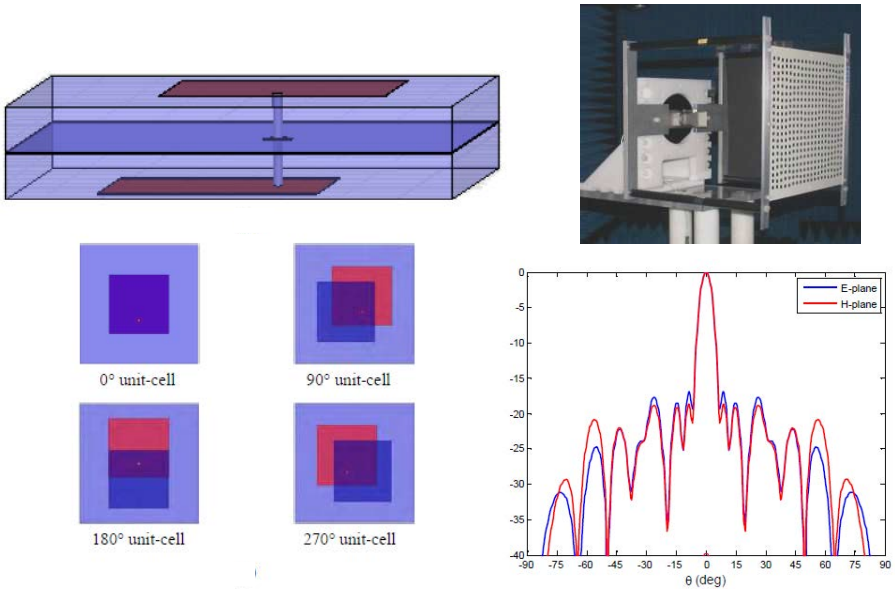

Figure 1.4: 3D sketch and top view of the unit cell proposed with different angles of rotation. Prototype of the transmitarray with 2-bit unit cells and radiation pattern at 10 GHz [18].

on both principal planes are shown in Fig. 1.4.

In the solution proposed in [20, 21] at 30 GHz, the resonant element of the unit-cell is formed by two concentric rings printed on a substrate. By using a double ring structure, the double resonant behaviour leads to a wider operational bandwidth. Varying the gap between the two rings or the width of the outer ring, the phase shift can be varied. The whole structure is formed by four different layers, as shown in Fig. 1.5, in order to increase the phase range. Different unit-cells are studied in this work: fixed gap and different ring dimensions, different gap between the rings, ring printed on different substrates and fixed external ring dimensions. After an optimization study, the last solution presents better performances in terms of phase variation (about 80°) and then it is chosen to realize a prototype of a 21×21 transmitarray. The air gap between the different layers is equal to 0.3 wavelengths (3 mm) in order to maximize the transmission coefficient at the center frequency (30 GHz). The number of layers is chosen as the best trade off between the complexity of the whole structure and the possible phase shifts range. In particular, a range of 270° of phase shift has been found with four layers. The maximum gain is 28.59 dBi at 30 GHz with a bandwidth of 2.25 GHz (7.5%) and a total radiation efficiency of 42% with the F/D ratio equal to 0.9. The measured radiation pattern is shown in the graphs of Fig. 1.5. The Side Lobes Level (SLL) is about -17 dB. The main drawback of this approach is the limited phase range achieved with a single layer that obliges to cascade several panels to extend it. This aspect limits also a possible implementation of the electronic control of the phase.

The structure proposed in [22] is based on dielectric resonators. The unit-cell designed to

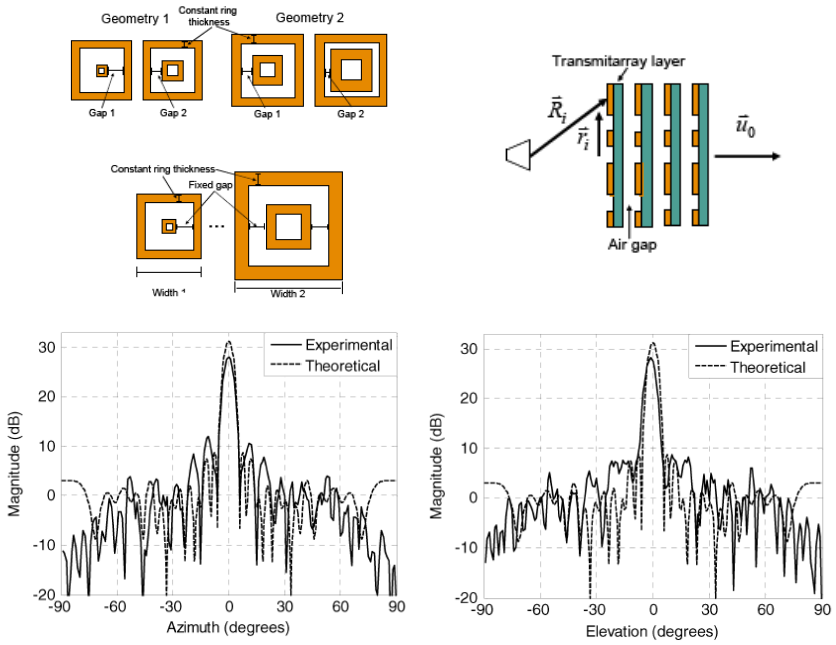

Figure 1.5: Scheme of the transmitarray and different unit-cells studied in [20], [21] based on multi-ring resonators. Simulated and measured radiation patterns at 30 GHz for a four-layer structure based on a concentric double-ring unit cell in E-plane and H-plane.

work in the C band is shown in Fig. 1.6. It is formed by three-layer square elements mounted on different dielectric substrates. As always, the dimensions have been optimized to obtain a low insertion loss and a wide range of the transmitted field phase. A 9×9 transmit-array has been studied with a circular horn as focal source located at 28.9 cm from the array working at 5.8 GHz. The simulated patterns optimized for broadside radiation of Fig. 1.6 show good performance. However, even in this case, multiple layers are required to achieve a wide phase range. Tolerances on the fabrication of the different layers and their alignment limit the scalability to higher frequencies.

The solution proposed in [23] in W-band for automotive applications is based on standard waveguide sections (WR12) loaded with iris and slot realized on a printed circuit board (Fig. 1.7). Four different designs are studied to obtain 2 bits of phase quantization. A 21×10 transmit-array based on these unit-cells has been designed with a 10-dBi pyramidal horn as focal source ($F = 30\,\text{mm}$). The simulated patterns in both planes show a maximum gain of 25.5 dBi (Fig. 1.7). With an offset configuration, i.e. translating the feed horn along the axis of the E-plane, beam steering capabilities have been obtained (Fig. 1.7). This functionality can be implemented electronically by switching between different sources placed in the focal plane. However, it is characterized by limited steering capability and high scanning losses. This is mainly due to the increased spillover losses which are proportional to the angle of tilting. Due to the use of waveguide sections, the proposed solution has a

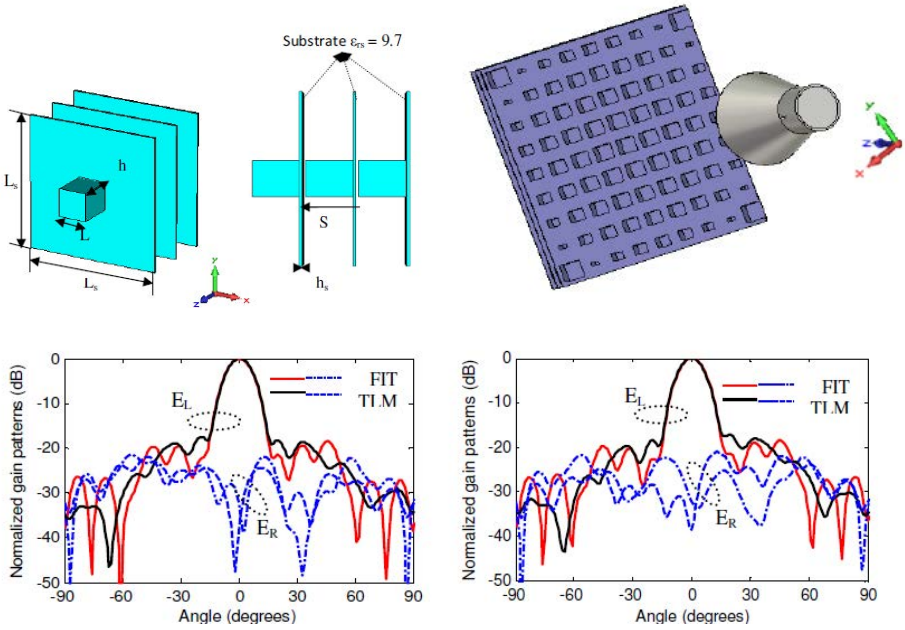

Figure 1.6: Unit-cell based on dielectric resonator. Simulated radiation patterns in the planes $\phi = 0°$ and $\phi = 90°$ at 5.8 GHz of the transmit-array [22].

significant thickness (about $2\,\lambda_0$ at 77 GHz), limiting its application to W-band frequencies.

Passive transmitarrays based on Spatial Elliptic filters (SEFs) have been proposed in [24, 25]. The working principle is similar to the spatial low-pass filters. The gap between the different patch layers is narrowed to increase the capacitive coupling. The architecture proposed and the equivalent lumped-element circuit model are shown in Fig. 1.8. The appropriate combination of the different capacitive layers provides the Nth-order SEF frequency response. A combination of different-order of spatial filters (called 'mixed-order') is implemented to reduce the required number of metal layers and maintaining a good phase variation. Despite this optimization, several layers are required and only a 3.5% 3-dB bandwidth (1 GHz at 28 GHz) bandwidth is achieved with a phase range of 160° (Fig. 1.8).

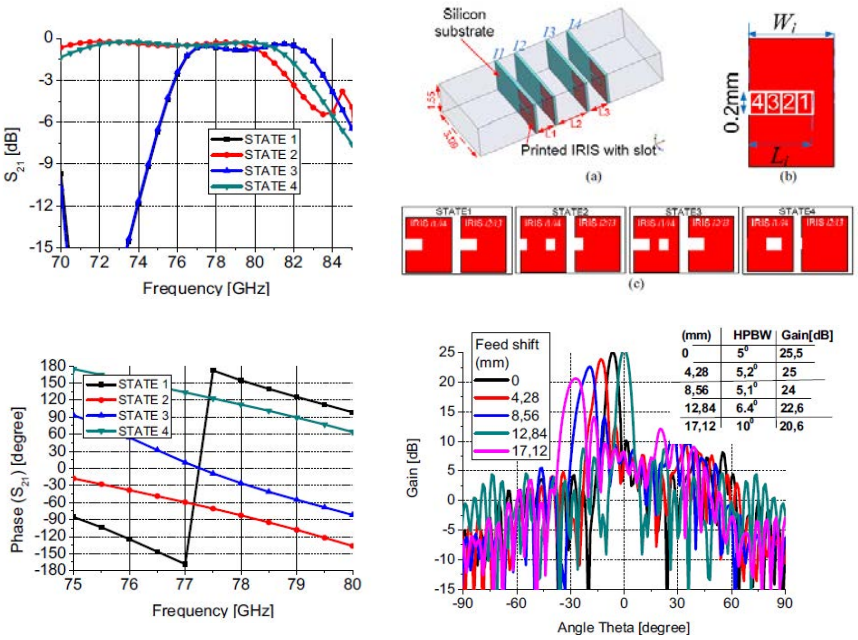

Figure 1.7: Unit-cell based on iris in waveguide. Simulated S-parameters in magnitude and phase for all the four unit-cells proposed. Radiation patterns simulated for different offset horn configurations [23].

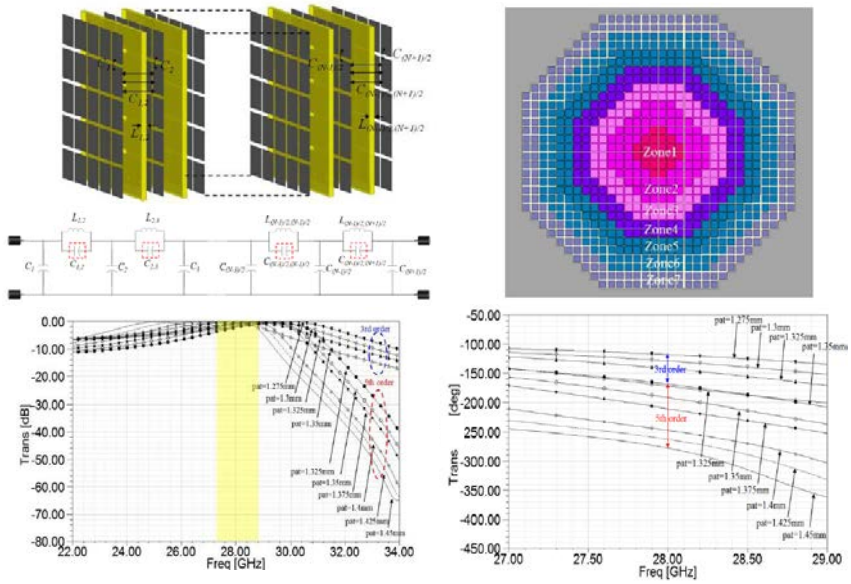

Figure 1.8: 3D topology and equivalent circuit model of the Nth-order SEF only capacitive layers. Simulated magnitude and phase of the transmission coefficient. Sketch of a planar lens based on the Nth-order SEF [24], [25].

1.3 Reconfigurable transmitarrays: State-of-the-art

To obtain an electronically reconfigurable beam, the phase distribution on the array surface, and then the phase of each unit-cell, must be changed dynamically. This functionality can be implemented with different techniques. The most diffused one is based on the electronic control realized by loading the resonant elements designed on the unit-cell with one or more active devices (e.g. varactor diodes, MEMS switches, p-i-n diodes) on one (or more) layer of the unit-cell. Other approaches are based on the use of tunable materials (ferroelectric, liquid crystals) or by using microfluidic tubes.

The reconfiguration obtained by changing the position of the source (i.e. mechanical steering or switching between different sources in the focal plane) which illuminates a passive transmitarray is not considered here. In fact, only limited scanning capability can be achieved with these systems.

1.3.1 Semiconductor varactor diodes

The solution presented in [26] and [27] proposes a multilayer structure with a slot aperture loaded with a varactor diode in the middle layer and a slot-loaded patch with two varactor diodes on the lower and top layers (Fig. 1.9). The structure, working in C band, has been studied by numerical simulations and tested in a waveguide simulator.

The magnitudes and phases of the S parameters with different capacitance loads given by the diodes polarized with different voltage values are shown in the graphs of Fig. 1.9. As the phase of the transmitted wave varies, the transmission bandwidth is shifted in frequency as well due to the variation of the resonant frequencies of the structure. This is typically the behavior which affects this approach and leads to reduced transmission bandwidth for the transmitarray configuration. A 6×6 transmitarray based on this unit cell is proposed in [28]. The measured radiation patterns on E- and H- planes for the realized prototype with different tilting angles are shown in Fig. 1.10. The maximum gain is 13.0 dBi at broadside

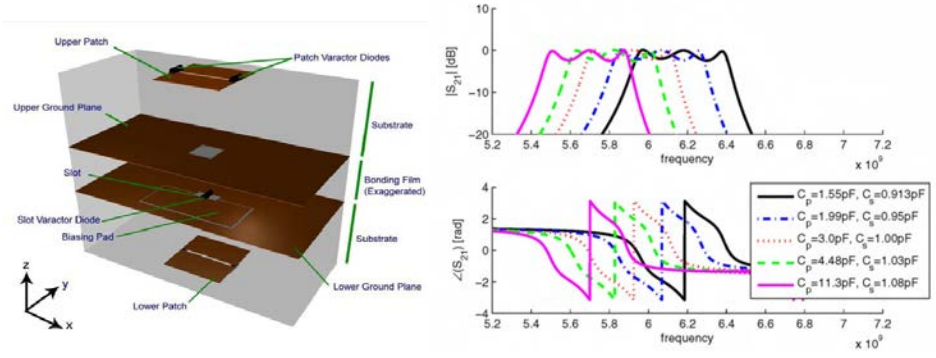

Figure 1.9: Section and top view of the reconfigurable active unit cell designed with varactor diodes [27].

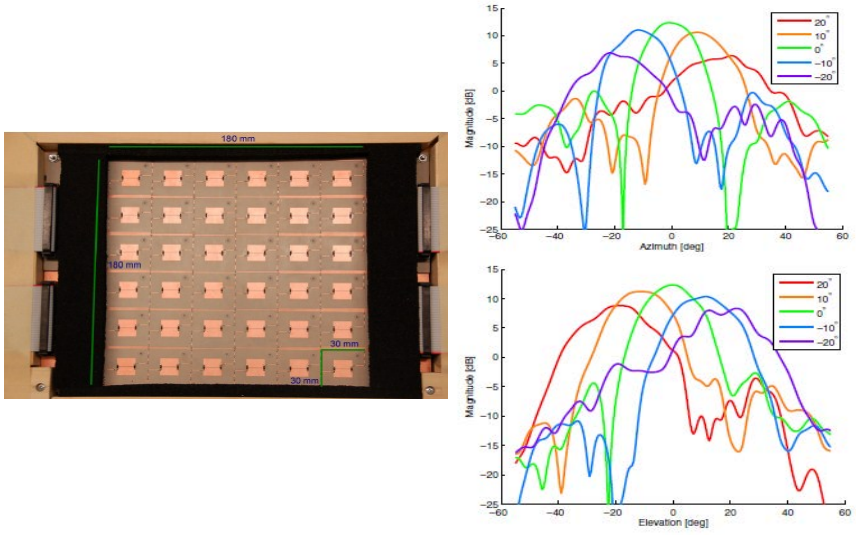

Figure 1.10: Realized 6×6 transmit-array and measured radiation pattern [28].

and a beam tilting of $\pm 20°$ capability has been demonstrated on both planes.

An alternative solution, referred as Antenna-Filter-Antenna, is based on the use of a RF circuit with a microwave phase shifter implemented in an intermediate layer between the receiving and the transmitting one. An example is proposed in [29] in X band (12 GHz). The two radiating layers are formed by stacked rectangular patches separated by 0.7λ. The phase shifters implemented in the intermediate layer, orthogonally placed, are based on reflective circuit (RTPS) with hybrid couplers in microstrip technology tuned with varactor diodes, as shown in the picture of the realized circuit layout in Fig. 1.11. Varying the bias voltage of the diodes between 0 V and 16 V, a phase range of 378° is achieved. This circuit connects the two radiating layers working in the receiving and transmitting modes. The experimental results show limited tilting capabilities (see Fig. 1.11). This is mainly due to the phase shift control applied to sub-arrays of 2×2 unit-cells instead of the single unit-cell.

An extension of the concept of Antenna-Filter-Antenna is proposed in [30]. It consists of multiple antenna layers cascaded to form a spatially band-pass filter. Phase agility is achieved by tuning the resonant frequency of each layer. As for the design already presented, three aspects must be taken into account: phase tuning range, maximum losses of the single unit-cell and the needed operational bandwidth. The proposed scheme is based on varactor-loaded slot antennas, shown in Fig. 1.12. The analysis of the single unit-cell is carried out with a full-wave commercial simulation software with periodic boundary conditions and Floquet port excitations. The active devices are included in the model with their equivalent lumped element circuit. With this approach, it is possible to obtain the scattering parameters. The whole structure can be analyzed with a transmission line equivalent model, considering the air gap between two layers as a transmission line with 377 Ohm as

characteristic impedance. The prototype and the S parameters are shown in Fig. 1.12. The drawbacks of this solution is the large thickness and the reduced bandwidth as well as the complexity required to handle the varactor diodes mounted on the different panels in the final transmitarray configuration.

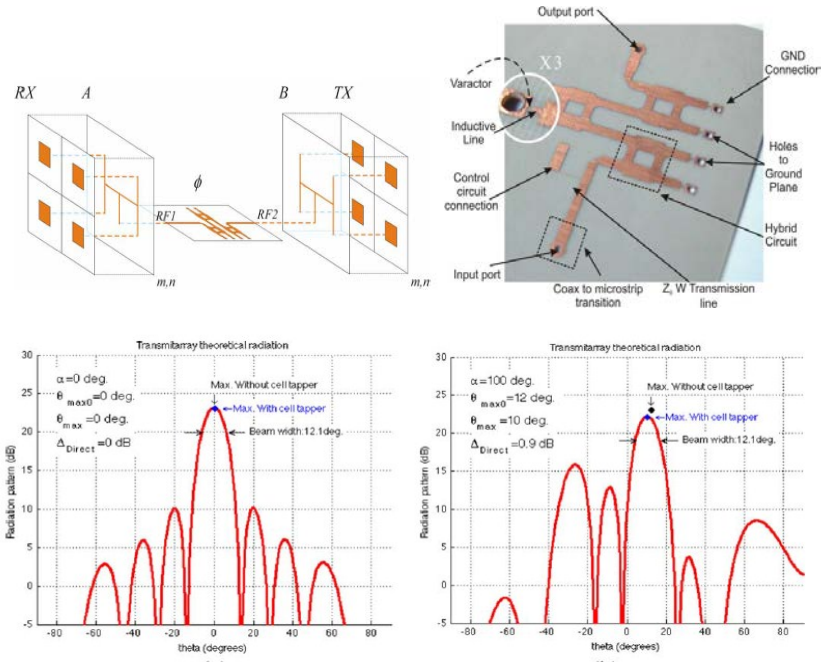

Figure 1.11: Scheme of the array based on microwave phase shifters connecting 2×2 subarrays; radiation pattern for a broadside beam and beam tilted at 10° [29].

Similar approaches are proposed in [31, 32] in C-band. The structure, shown in Fig. 1.13, is formed by several layers: a patch antenna coupled with a differential microstrip transmission line (receiving layer), a ground plane with coupling apertures for the transmission lines, an active microstrip circuit with varactor diodes [31]. Finally, the transmitting layer includes another patch antenna with the same dimensions as the first layer. A filter, whose scheme is shown in Fig. 1.13, based on a bridged T topology operating in differential mode is designed on the intermediate layer in microstrip technology: the capacitance of the integrated varactor diodes provides the required phase shift between the receiving and trasmitting layers. The unit cell is realized and characterized in a standard rectangular waveguide (WR-187). The measured S parameters exhibit a bandwidth of 100 MHz and the insertion losses are 2.1-4.3 dB around 4.87 GHz. This approach allows to maintain the transmission bandwidth almost unchanged while tuning the phase shift with the varactor diodes, because the receiving/transmitting antenna resonant modes are not perturbed. However, these unit-cells require a complex stack with several layers and high insertion losses as well as high realization costs for a narrowband behavior.

In order to extend the bandwidth of the unit-cell, the two planar antennas on the re-

ceiving and transmitting layers can be coupled with two stacked patches [32]; in particular, between the lower and the upper patch, printed on a 1.57 mm thick substrate of Duroid 5880, there is an air gap of 1.6 mm, realized with the appropriate spacers. The prototype realized and measured in WR-187 setup presents an insertion loss variation of 1.7-5.2 dB from 4.6 GHz to 5.2 GHz, as shown in Fig. 1.14, with a phase range of 400°. The greater bandwidth is achieved but higher insertion losses are introduced due to the increased complexity of the architecture.

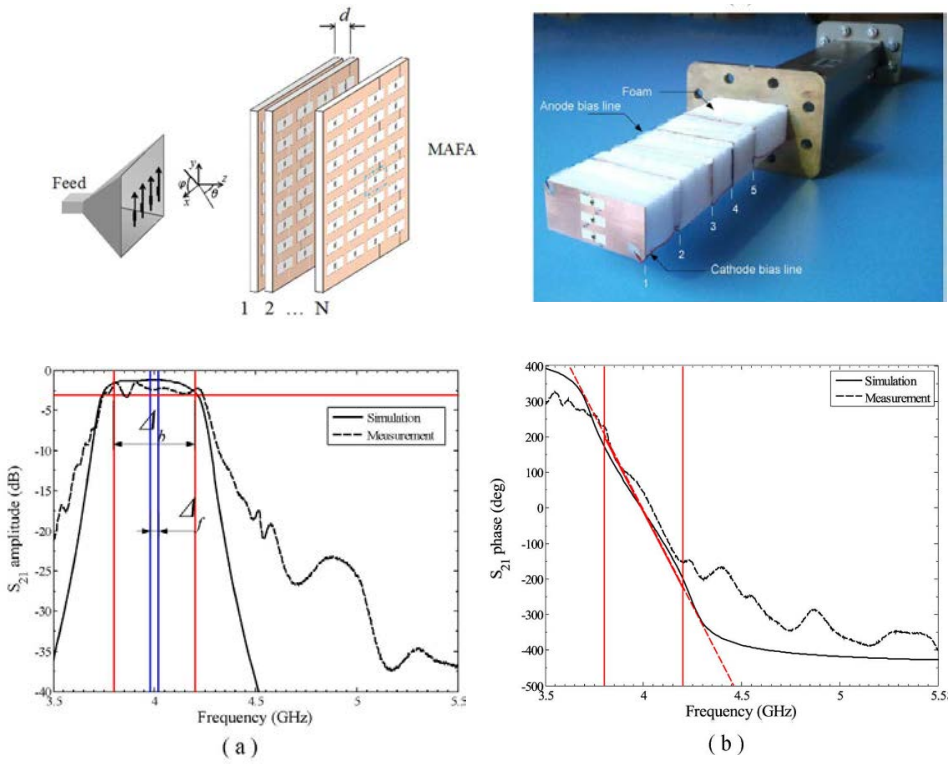

Figure 1.12: Photograph of the M-A-F-A prototype measured in waveguide. Simulated and measured S-parameters in magnitude and phase [30].

A prototype of 6×6 element array with the presented unit-cell has been realized and tested in [32]. The measured radiation patterns for the different configurations are shown in Fig. 1.15. The maximum gain is 16 dBi in the broadside configuration at 4.7 GHz. A beam tilting of $\pm 50°$ on both E- and H-planes has been demonstrated. In addition to the pencil beam configuration, the realized transmit-array has been also tested to generate beams with different shapes, using the projection matrix algorithm. The measured 2D patterns for two-beams, three-beams, rectangular flat-top and donut-shaped configurations are shown in Fig. 1.15.

In order to overcome the losses introduced by varactor diodes, the possibility to integrate an amplifier in the unit-cell design has been investigated in [33] at 5 GHz. The structure is very similar to the one proposed in [31]. The two intermediate layers, which connect the

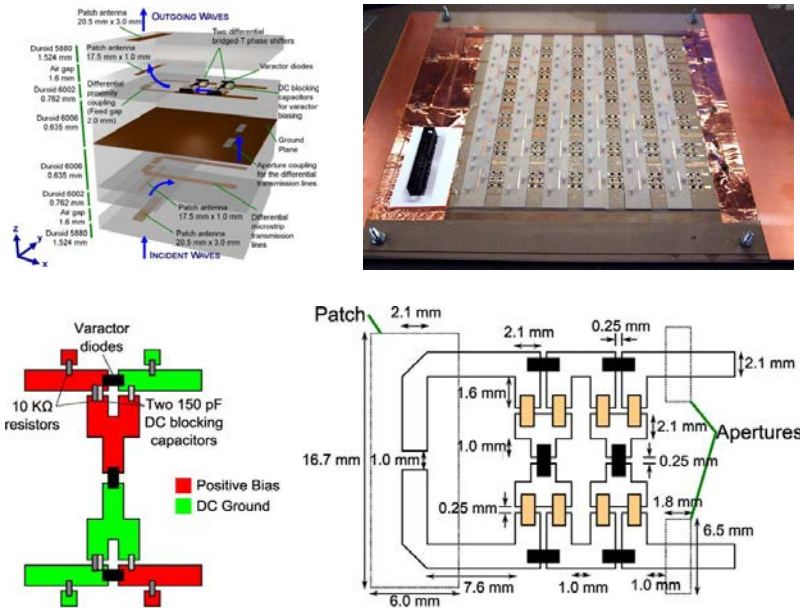

Figure 1.13: Scheme of the single unit cell and picture of the internal layer of the realized array [31], [32].

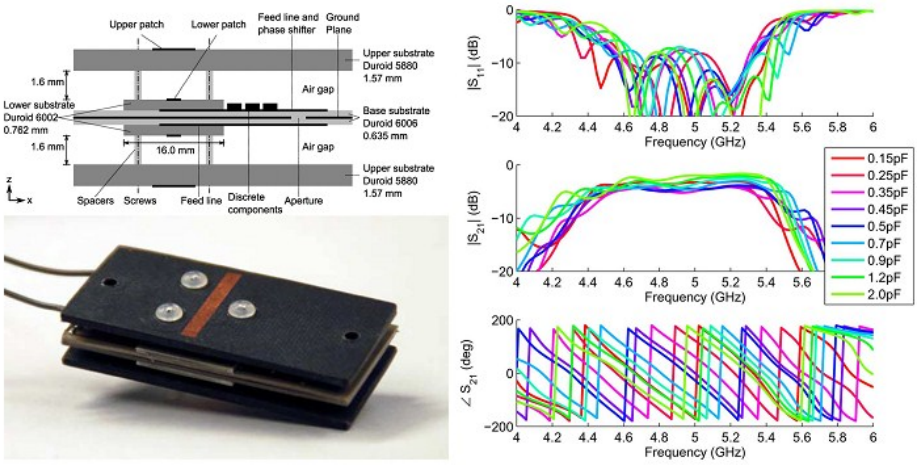

Figure 1.14: Measured S-parameter of the single unit cell prototype with T-bridged phase shifter and stacked patch [31], [32].

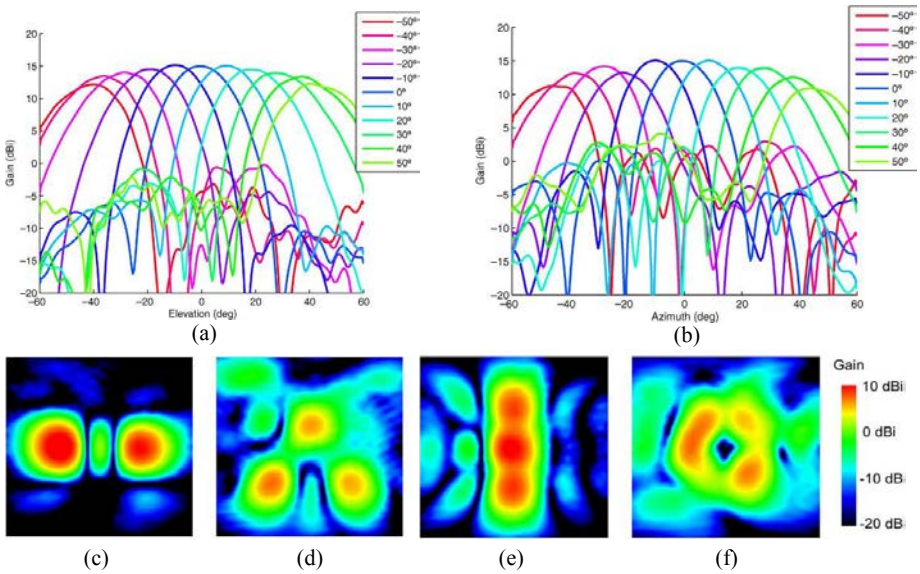

Figure 1.15: Measured radiation patterns on the two cardinal planes (a, b) with tilted beams and 2D maps of synthesized shaped beams: two beams (c), three beams (d), fan (e) and a donut (f).

two patch antennas on the receiving and transmitting layers coupled with parasitic patch, are occupied by a variable phase shifter realized with two hybrid junctions in microstrip technology loaded by a varactor diode. An amplifier is included in one of these layers, as shown in Fig. 1.16. The experimental results demonstrate a phase range of 400° between 4.95 and 5.5 GHz (10.6% of 3-dB fractional bandwidth). A gain of 7.7 dB is obtained thanks to the amplifier. Even if this solution is attractive for the performance in terms of bandwidth and phase range, it has some limitations. First, the proposed design is complex to realize with the standard PCB technology. In fact, the presence of the amplifiers and diodes on an intermediate layer requires truncated substrates for the top and bottom layers which cannot be included in the same fabrication process. This aspect limits the scalability towards higher frequencies. Alignment errors and spurious radiation effects from the hybrid coupler are other drawbacks. Finally, the bias signals required to polarize the diodes and the amplifier increase significantly the power consumption of the structure.

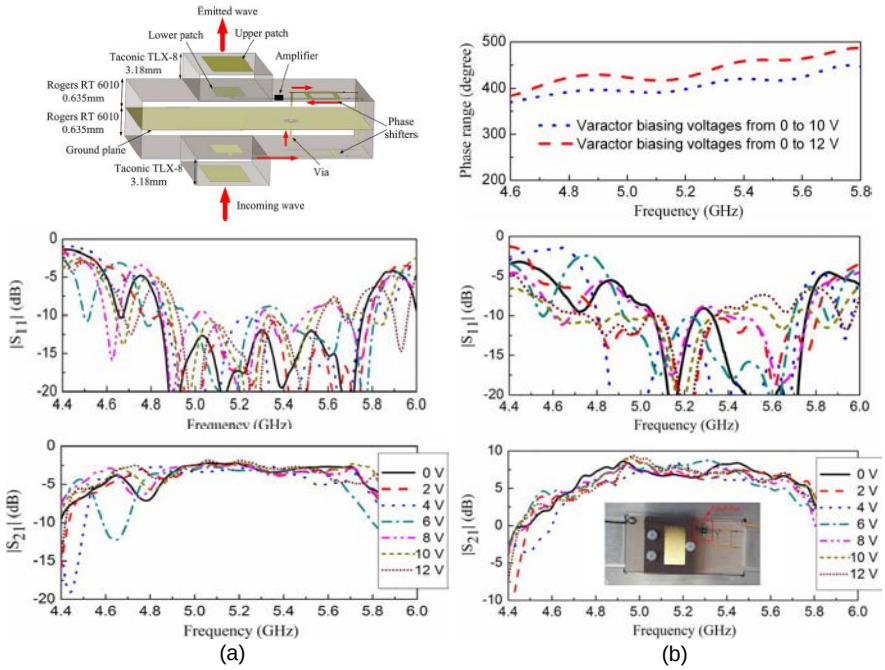

Figure 1.16: Unit-cell based on varactor diodes which include an amplifier. Photograph of the realized prototype and measured scattering parameters with (a) and w/o (b) the amplifier [33].

1.3.2 Ferroelectric varactor diodes

In [34], a tunable frequency selective surface (FSS) is used as a transmitarray in Ku-band. The periodic sub-wavelength unit-cells are composed of capacitive and inductive structures creating a bandpass filter for an incident wave. By patterning the capacitive elements on a screen-printed barium-strontium-titanate (BST) thick-film ceramic, the resonant frequency of the FSS is tuned, controlling locally the phase of the transmitted waves (Fig. 1.17). A permittivity varying between $\epsilon_r^{BST} = 380$ (0 V) and $\epsilon_r^{BST} = 275$ (120 V), which correspond to a tunability of 28%, has been found. A phase shift range of 360° is covered only by cascading several FSS panels. 1600 integrated BST varactors are fabricated on a 40×40 cm area using a patterning and metallization process. A total of 3200 varactors are integrated in the FSS prototype within only one standard patterning process (Fig. 1.17).

The realized FSS panel gives a maximum phase shift of 121° at 12 GHz. The corresponding required voltage is changed between 0 V and 120 V. The beam steering capability is proven by far-field measurements in a scanning range of only ±10°, with a maximum loss of 2.9 dB (Fig. 1.17). For expanding this range, several FSS panels must be cascaded to offer a wider phase shift range. This means that a good tilting capability (±40°), which is the main objective of a reconfigurable design and justifies the insertion losses introduced by the surface, can be obtained only by increasing significantly the complexity of the system.

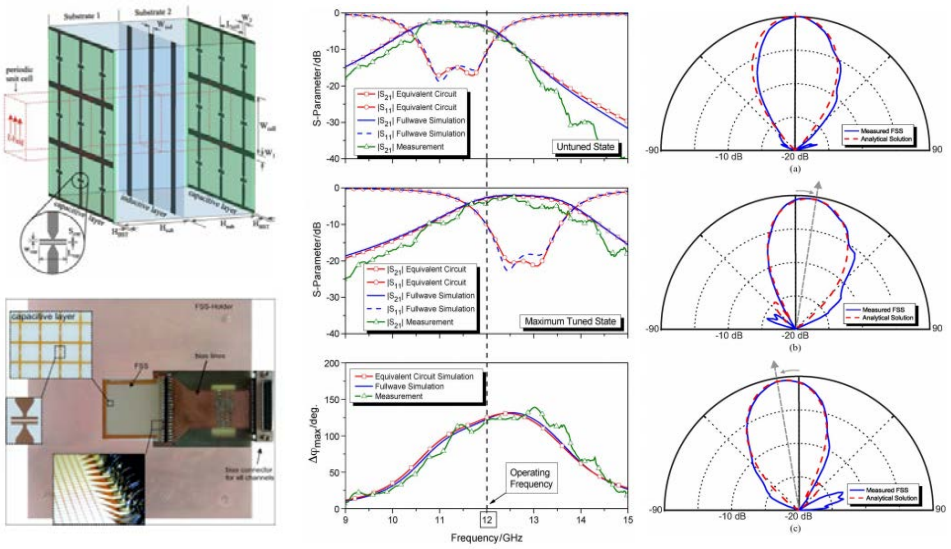

Figure 1.17: Transmitarray based on ferroelectric varactor diodes. Realized prototype, unit-cell frequency response with 0V and 120V of bias voltage and measured radiation patterns [34].

Moreover, the bandwidth achieved is quite narrow.

1.3.3 Microfluidics

In [35], a microfluidics approach to develop a reconfigurable circularly polarized transmitarray unit cell is proposed. The unit-cell is formed by two nested split ring slots formed as microfluidic channels that can be filled by fluids. Split regions in the slots are realized by injecting liquid metal into the channels (Fig. 1.18). Beam steering is obtained by implementing rotational phase shifting when moving the liquid metal in the slots. Due to the circular symmetry of the unit cell, the rotation of the element is achieved with the controlled displacement of the liquid metal resulting in a shift of the transmitting phase equal to twice the angle of rotation. The major advantage of this structure is the 0°-360° continuous phase shifting capability provided by the displacement of the conductive fluid inside the ring channels. Several passive prototypes working at 8.8 GHz are fabricated on a glass substrate carrying a patterned metal film, and the slot channels are formed by Polydimethylsiloxane (PDMS) (Fig. 1.18). The rotation angle considered are between 0° and 90°. The measured scattering parameters in waveguide are shown in Fig. 1.19. The estimated insertion loss is between 2-3 dB with a variation in function of the rotations within 1 dB. However, the characterization setup considered in waveguide shows significantly higher losses, even greater than 10 dB. The authors attributed these losses to the excitation condition in waveguide (incidence angle of 42° in WR-90 at 8.8 GHz), without considering the impact of the waveguide on the circular polarization generated by the unit-cell. An advantage is the zero-power con-

sumption in the static mode. However, the time required to reconfigure the transmitarray could be not negligible and limit their application. In addition, the solution proposed in [35] is characterized by an increased thickness with limited transmission bandwidth and reduced possibility of frequency scaling. Moreover, the transmitarray full configuration design and realization must consider the implementation of a microfluidic network formed by several tubes in order to inject the liquid metal inside each unit-cell. This aspect will lead to higher unit-cell sizes in order to accommodate the different tubes.

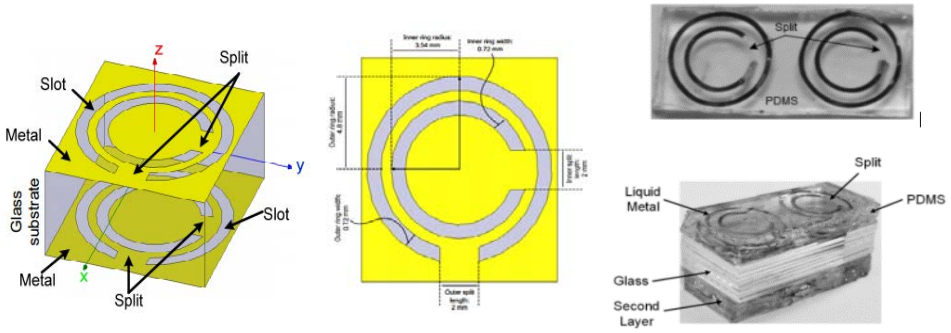

Figure 1.18: Reconfigurable unit-cell based on microfluidic split-ring resonators [35].

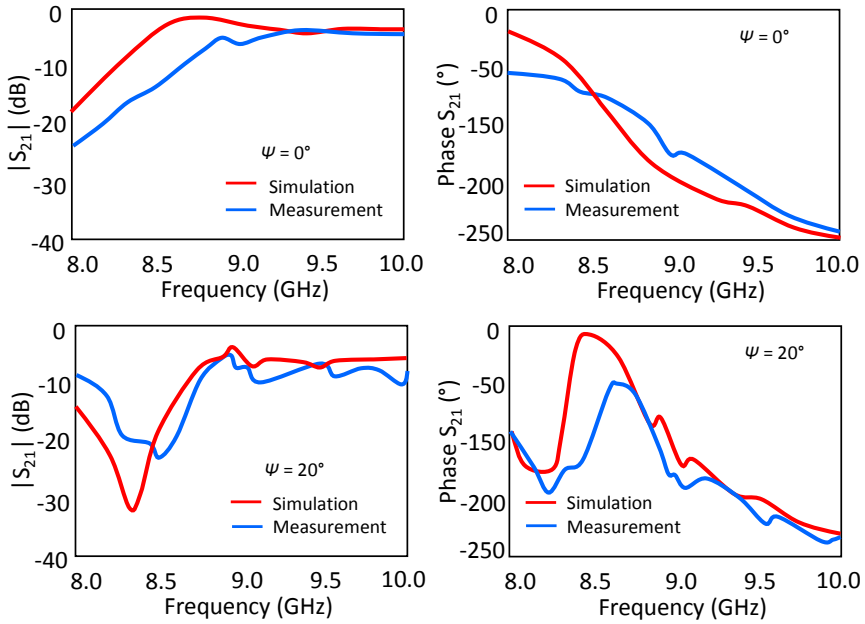

Figure 1.19: Measured scattering parameters of the unit-cell based on microfluidic split-ring resonators in waveguide [35].

1.3.4 MMIC

In [36], an architecture of active dual-band transceiver array in Ku/Ka band based on the transmitarray concept has been proposed. The frequency bands for bi-directional data links are from 19.7 GHz to 21.0 GHz for downlink and 29.5 GHz to 30.8 GHz for uplink, respectively. The schematic cross-section of the array architecture is illustrated in Fig. 1.20. In Ka-band transmit mode (dashed rays), the feed antenna distributes the RF signal by a space-fed arrangement to the dual-band antenna elements where the signal is guided to the multi-functional ICs, which warranties the amplitude and phase adjustments to synthesize the radiation pattern diagram. Subsequently, the modified RF signal is carried to the individual antenna elements on the top side of the array for re-emission of the electromagnetic wave. In the receive mode, the array operates in the same manner as for the transmit case but with orthogonal polarizations for both frequency bands.

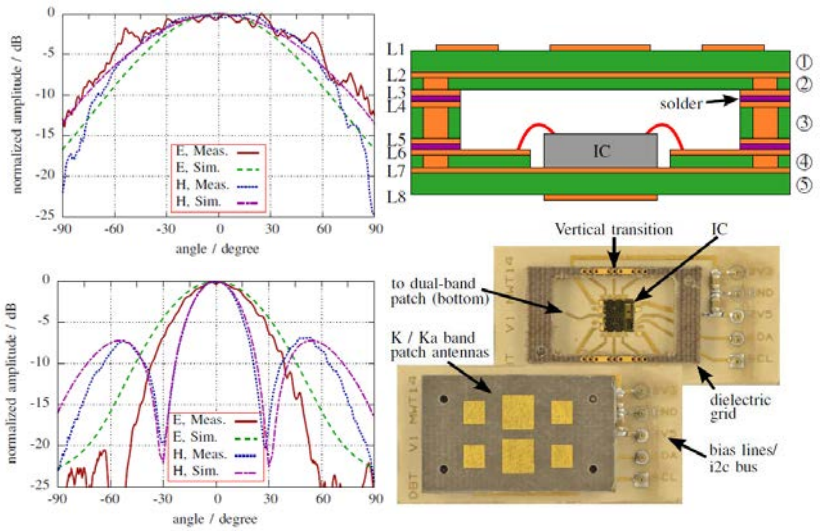

Figure 1.20: Photograph and layer stackup of the active transmitarray submodule. Simulated and measured radiation patterns at 20 GHz and 30 GHz [36].

The IC, with which the phase compensation is achieved, is based on a SiGe BiCMOS chip realized by IHP Microelectronics (IHP SG25 BiCMOS). It includes four transmit and two receive channels with a digital bus interface for serial control of all functions. Each receive channel is formed by a low-noise amplifier (LNA) followed by a vector modulator (VM), and the transmit channel is cascaded with a vector modulator, a driver amplifier (DA) and a power amplifier (PA). The antenna elements on the upper board are connected with the lower one by vertical board-to-board transitions which have been optimized. Each submodule includes two patch antennas for downlink (Ku-band) and four patch antennas for uplink (Ka-band). Even if a dual-band behavior is obtained, the proposed architecture is characterized by several stacked layers increasing the realization cost. Furthermore, the high number of control lines required for the IC would represent a limit for the implementation

of large panels.

1.3.5 MEMS switches

There are different solutions of transmitarray unit-cells in the literature based on MEMS active devices. The structure presented in [37] at 16 GHz and 32 GHz is based on an antenna-filter-antenna (A-F-A) scheme with three layers, as shown in Fig. 1.21. The receiving and transmitting layers of the unit-cell are formed by two slots orthogonally oriented. In the middle layer, several stripline resonators coupled by capacitive gaps and loaded by switches couple the receiving and transmitting slots. The MEMS switches are not included in the preliminary design in which they are modelled ideally with a short circuit in the *on* state and an open circuit in the *off* state. Unlike the design presented in the previous paragraph, only four different phase shifts are possible: 0°,90°,180° and 270°. This corresponds to a 2-bit quantization of the phase law applied to the transmitarray and leads to a reduction of the directivity, called quantization loss. The design proposed exhibits insertion losses between 1.4 and 1.6 dB in the different states. To validate the unit-cell working principle, different arrays of 1021 unit-cells have been considered without the MEMS switches with main beam directions between 0° and 60°. The F/D ratio is equal to 1. The measured patterns for 40° and 60° configurations are shown in the graphs of Fig. 1.21.

The reconfigurable design in Ka-band based on this unit-cell is proposed in [38]. The 2-bit unit-cell has been modified in order to integrate the MEMS switches in the design. The structure is shown in Fig. 1.22. The frequency response of the unit-cell is reported in Fig. 1.22. The insertion losses are 4.3 dB and 4.9 dB for the 0° and 180° states and 8.2 dB and 9.8 dB for the 90° and 270° states. A prototype of 22×22 unit cells at 34.8 GHz has been realized and tested. 3420 MEMS switches are integrated in the antenna to obtain a ±40° tilting capability. The measured radiation patterns are shown in Fig. 1.22. The maximum gain is 9.2 dBi with total losses of 11.2 dB. The high insertion losses, due to the low reliability of the actual MEMS technology, lead to very poor power efficiencies and it is actually the main limiting aspect of this approach.

In [39], a reduction of the phase resolution is proposed in X-band. Only two packaged MEMS ohmic switches are mounted directly on a slot-loaded patch antenna on the transmitting layer realized with standard PCB technology. Each switch is modelled with a resistance or a capacitance for the *on* and *off* state, respectively. A schematic view of the unit-cell working in X-band is shown in Fig. 1.23. One bias line for each switch is included. Even if this approach could be innovative, the experimental results obtained with a WR-90 waveguide setup (Fig. 1.23) show very poor performances, with a minimum insertion loss of 5.0 dB and a 10-dB return loss bandwidth less than 3%. This is mainly due to the modelling and reliability issues of the switches.

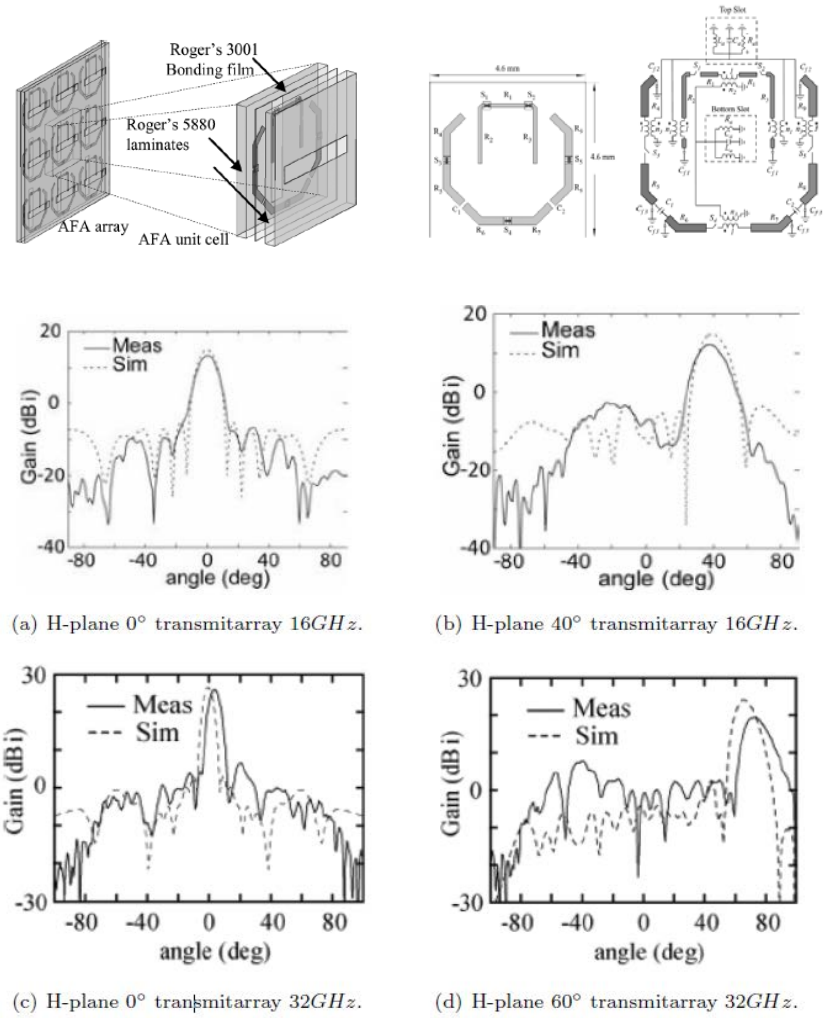

(a) H-plane 0° transmitarray $16GHz$.

(b) H-plane 40° transmitarray $16GHz$.

(c) H-plane 0° transmitarray $32GHz$.

(d) H-plane 60° transmitarray $32GHz$.

Figure 1.21: 3D sketch of the A-F-A array, scheme and model of the coupling resonators presented in [37]. Measured radiated pattern in the H-plane for the two arrays designed at 16 GHz and 32 GHz for several scanning angles.

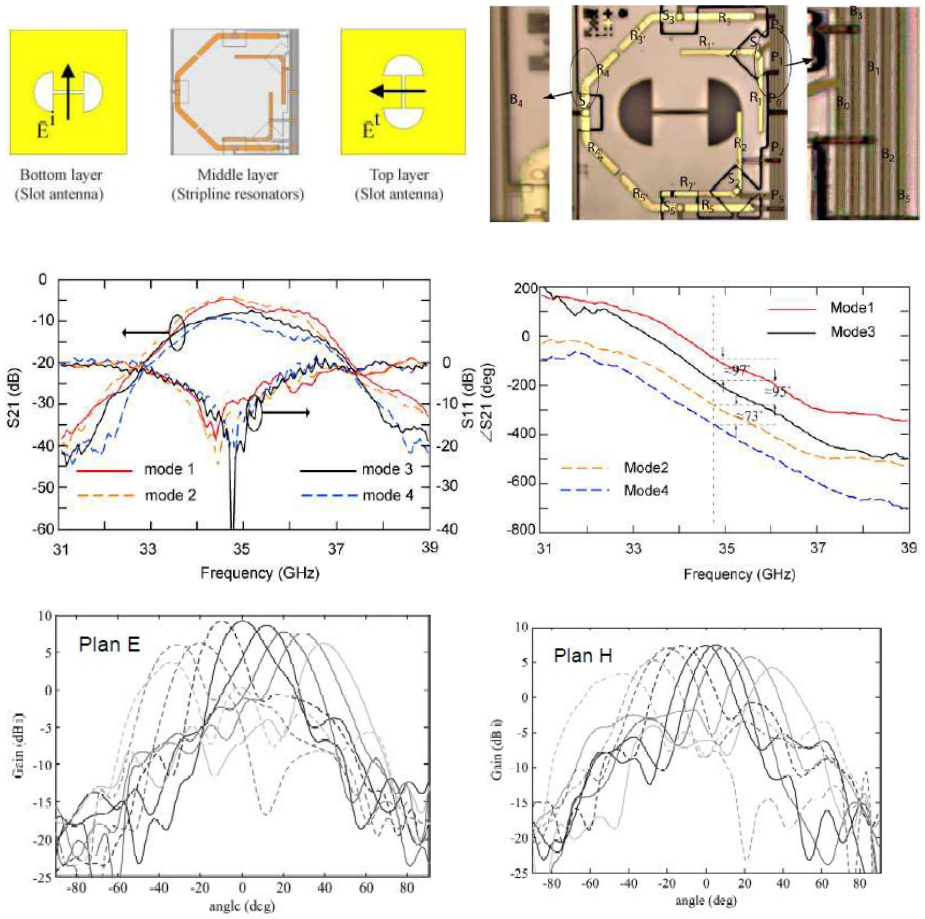

Figure 1.22: Scheme and picture of the unit-cell with stripline resonator and integrated MEMS switches. Measured unit-cell scattering parameters. Measured radiation patterns on E- and H-planes [38].

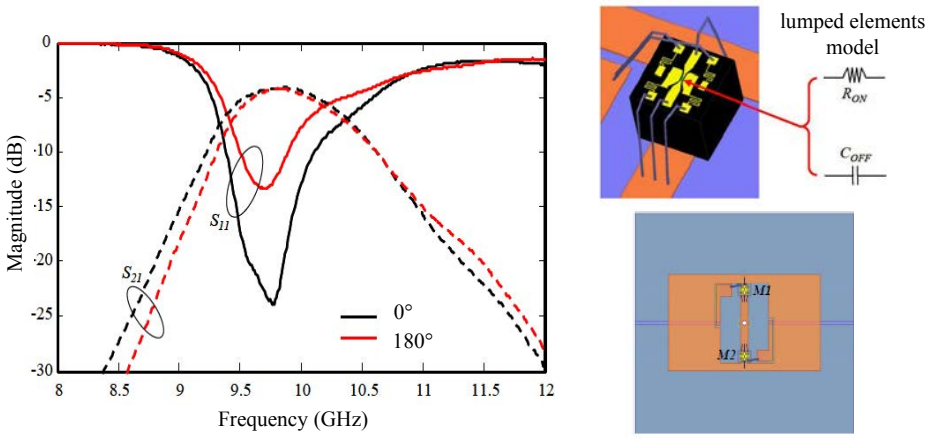

Figure 1.23: 3D sketch of the MEMS devices produced by CEA-LETI and used in the transmitarray unit-cell implementation. Measured scattering parameters in waveguide setup [39].

1.3.6 P-i-n diodes

The authors of [40] proposed the use of two p-i-n diodes mounted directly on the transmitting layer patch antenna. Only two phase states are possible (corresponding to 1 bit of phase quantization): 0° or 180°. The unit-cell architecture is shown in Fig. 1.24. On the receiving layer, there is a passive patch loaded with a "U" slot. On the opposite side (transmitting layer), there is a patch loaded with an O-shaped slot and two p-i-n diodes. A bias line is required to polarize one diode in *on* state and the other one in the *off* state. The two layers are connected with a via through a hole etched in the ground plane. Only four metallized layers and only one bias layer are required resulting in a low complexity.

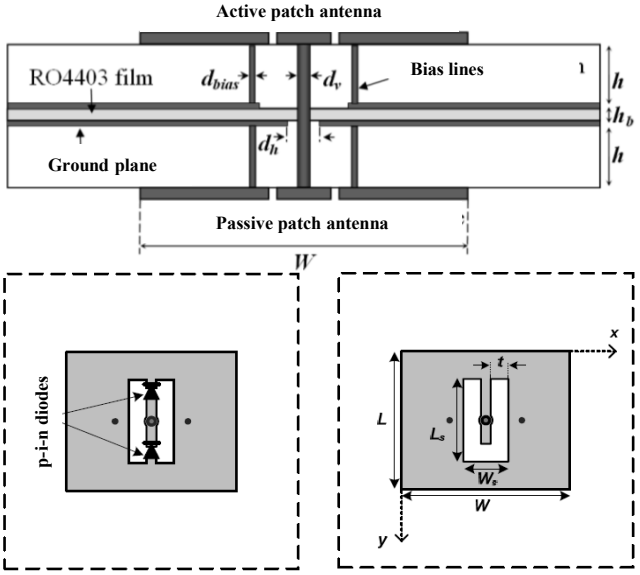

Figure 1.24: Side view, top view and bottom view of the reconfigurable 1-bit unit cell based on p-i-n diodes [40].

The AlGaAs p-i-n diode has been characterized experimentally in order to define an equivalent circuit model with lumped elements and include it in the EM model of the structure: a resistance in series with an inductance for the *on* state and a resistance in parallel with a capacitance for the *off* state. In order to take into account the effect of the GaAs substrate of the p-i-n diode, an additional shunt capacitance of 25 fF has been considered. A general model of the structure is developed to calculate the S parameters of the structure analytically. The measurement setup for the single unit cell is based on a standard waveguide WR90 with two ad-hoc transitions of length $\lambda_0/8$ minimizing the impedance mismatch. The experimental results are shown in Fig. 1.25. A relative 3-dB bandwidth of 14.7% with minimum insertion losses of 1.8 dB are demonstrated. The phase difference between the two states exhibits a maximum error of 14°. The measured 1-dB compression point shows a maximum accepted power of about 15 dBm.

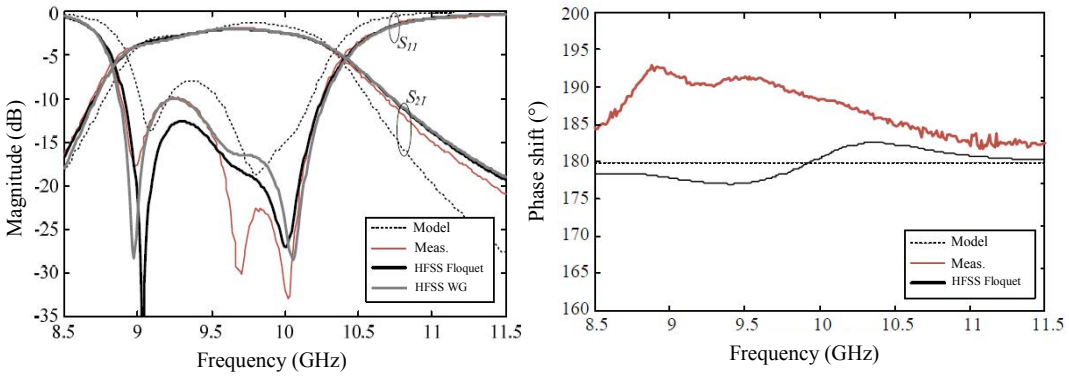

Figure 1.25: Simulated and measured S-parameters (magnitudes) in the two phase states in waveguide WR90. Simulated and measured phase difference [40].

A transmitarray formed by 20×20 unit-cells has been realized (Fig. 1.26) and tested in [40]. The feed is a WR-90 horn with 10 dBi of nominal gain and the focal distance is F/D=0.71. The radiation patterns have been measured with several tilted beams on E- and H-planes. A tilting capability of $\pm 70°$ on H-plane is obtained with a maximum gain of 22.7 dBi at broadside and a power efficiency of 50%.

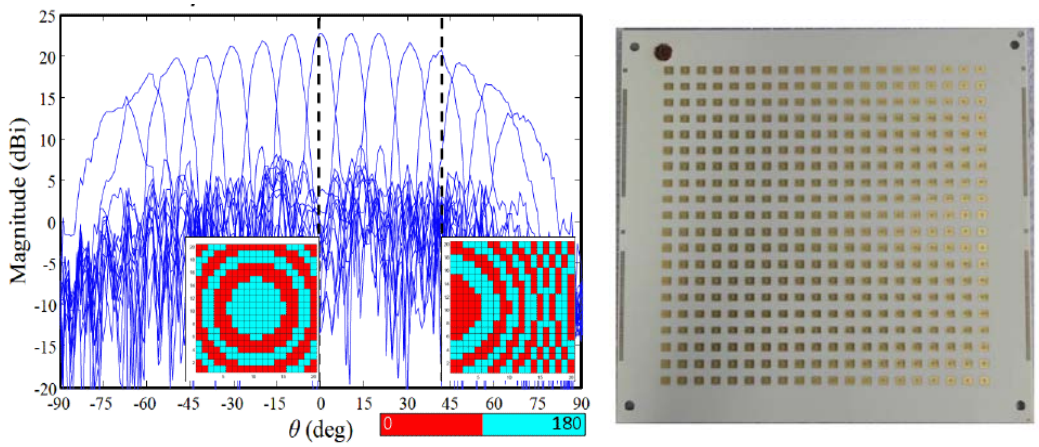

Figure 1.26: Measured gain of the transmit-array for the different phase distribution in H-plane [40].

In [41], a design based on the unit-cell presented in [39] in X-band is proposed. The passive patch is replaced with a slot-loaded patch with two p-i-n diodes and two inderdigital capacitors. The unit-cell architecture is shown in Fig. 1.27. The 1-bit phase quantization is maintained and, in addition, the transmitted wave can be vertically or horizontally polarized. However, poor isolation between the two orthogonal polarizations and limited frequency scaling possibility are the main drawbacks for this architecture.

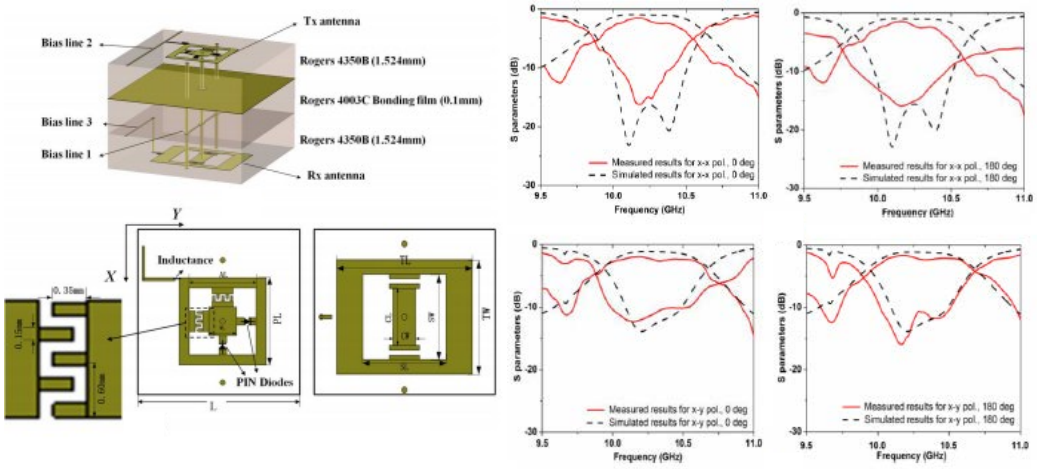

Figure 1.27: Unit-cell based on 4 p-i-n diodes with 1 bit of phase quantization and linear polarization control. Measured scattering parameters in waveguide [41].

1.4 Applications

1.4.1 Satellites communications

Transmitarray antennas are considered as attractive solutions for satellite communications since high gain and advanced beam controls are required. They can be used mainly as mobile earth stations mounted on platforms (ESOMPs), where beam-tilting capabilities are needed. The main requirements for this application are in terms of frequency bands, polarization and radiation pattern masks, and are provided by the international standardization institutions.

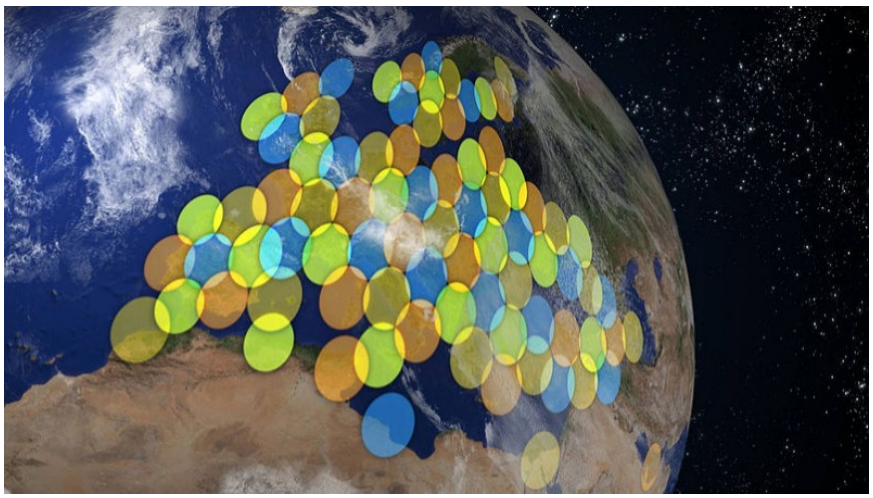

Figure 1.28: Coverage of the Eutelsat satellite KA-SAT in the ITU region 1 [42].

Several bands are assigned to satellites communications in the Ku-band for the downlink channel (from the satellite to earth station) and in Ka-band for the uplink channel (from

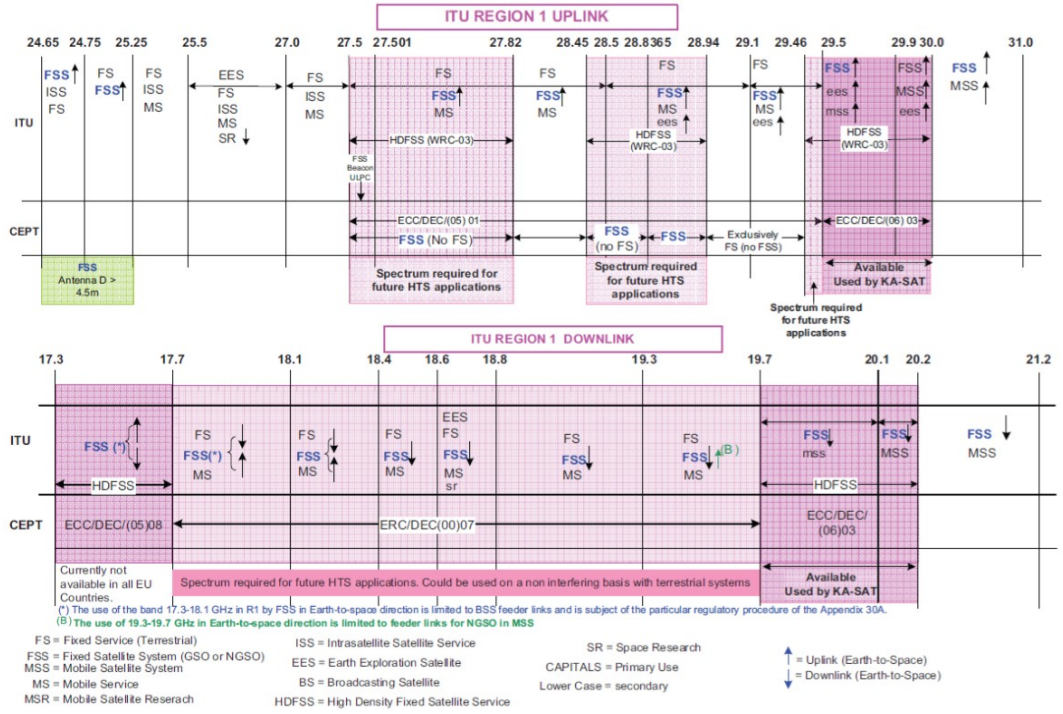

Figure 1.29: Satellite channels in Ku- and Ka-band for the ITU region 1 [43].

earth to the satellite station). The bands assigned to the different services are reported in the scheme of Fig. 1.29 [43]. The Fixed Satellite service (FSS) including the Local Multipoint Distribution Service (LMDS), the High Density Fixed Satellite Service (HDFSS) and the other channels for the communications with the geostationary orbit (GSO) covers the bandwidth from 17.7 to 20.2 GHz in downlink and from 27.5 to 30.0 GHz in uplink [44]. Military communications occupy the reserved bands 20.2-21.2 GHz (downlink) and 30.0-31.0 GHz (uplink) [45].

Due to the Faraday rotation effect introduced by the atmosphere in the link between the earth station and the satellite, circular polarization is required in order to avoid any polarization mismatch in the link power budget.

In order to obtain a high throughput, a multi-beam spot coverage has been defined with an appropriate frequency reuse factor of the sub-channels (500-MHz) [42]. In addition, the use of both circular polarizations (left-handed, right-handed) to serve adjacent regions led to further improvement of the throughput. In Fig. 1.28, the coverage of the Eutelsat Ka-sat satellite launched in 2011 for the coverage of the ITU region 1 (Europe, Middle-East and North Africa) is shown with the different spot beams used. At each color corresponds one polarization (LH, RH) and one sub-channel. Several radiation pattern masks are given by the principal standardization and regulation institutions in order to avoid co-channel interference and warranty the appropriate coverage on the different world regions.

The International Telecommunication Union (ITU), the Federal Communications Com-

mission (FCC) and the European Telecommunications Standard Institute (ETSI) provide the requirements for earth and satellite stations for the different services. In particular, fixed earth stations and earth stations on mobile platforms (ESOMPs) must respect different regulations.

The recommendation ITU S.456-6 [46] gives the requirements for the earth stations in the FSS service. The radiation masks are defined as follows:

$$G(\psi) = 32 - 25\log(\psi)\,,\ \psi_{min} < \psi < 48^\circ \tag{1.1}$$

$$G(\psi) = -10,\ 48^\circ < \psi < 180^\circ \tag{1.2}$$

where ψ_{min} is 1°, 2° or 2.5° if the antenna size D/λ is greater than 50, between 50 and 33.3 or less than 33.3, respectively.

The recommendation ITU S.580-6 defines the requirements for the earth stations operating on the GSO orbit. One region between 1° and 20° in which the gain of the antenna must be below the curve is lower than:

$$G(\psi) = 29 - 25\log(\psi)\,. \tag{1.3}$$

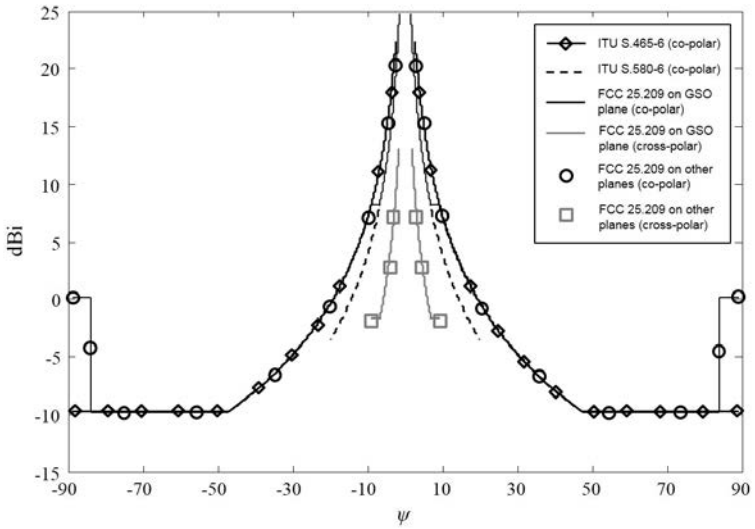

Figure 1.30: Radiation masks provided by ITU S.465-6, S.580-6 [46] and provided by FCC [47] 25.209 for the earth station.

The masks are shown in Fig. 1.30. Similar masks are given by the Federal Communication Commission (FCC) 25.209 [48] for the co- and cross-polar on the geostationary plane, as shown in Fig. 1.30. Different limits are defined in all other planes (Fig. 1.30).

The limits defined in the recommendation ITU S.456-6 for the co-polar component is very similar to the limits of FCC 25.209 outside the GSO plane except for the angles greater than 85°. On the GSO plane, this regulation gives more stringent limits inside the angular

region $|\psi| < 10°$. The recommendation ITU S.456-6 extends this limit up to 20°.

The recommendation FCC 25.138 [48] gives the limits for the earth station on the effective isotropic radiated power (EIRP) spectral density on a channel bandwidth of 40 kHz inside the arc between 3° and -3 ° of the GSO orbit. The masks are defined as follows:

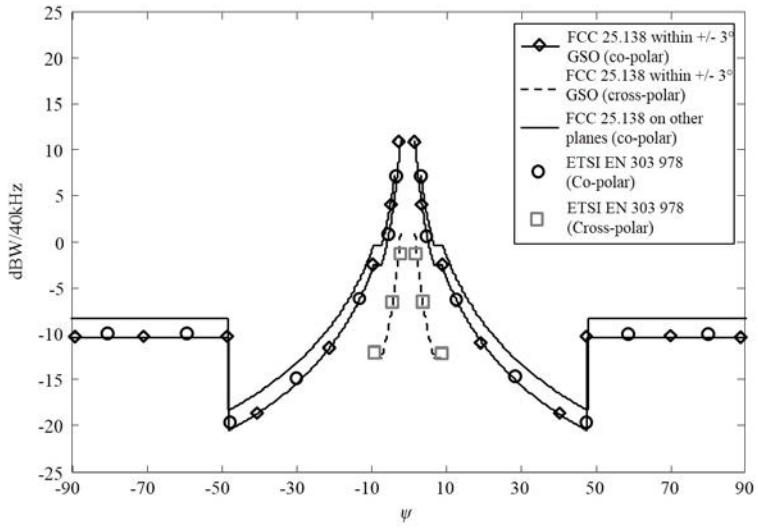

Figure 1.31: Radiation masks provided by FCC 25.138 [48] for the earth station and by ETSI EN 303 978 [47] for the earth stations on mobile platforms (ESOMPs).

$$EIRP(\psi) = 18.5 - 25\log(\psi) - 10\log(N), 2.0° < \psi < 7.0° \tag{1.4}$$

$$EIRP(\psi) = -2.63 - 10\log(N), 7.0° < \psi < 9.23° \tag{1.5}$$

$$EIRP(\psi) = 21.5 - 25\log(\psi) - 10\log(N), 9.23° < \psi < 48.0° \tag{1.6}$$

$$EIRP(\psi) = -10.5 - 10\log(N), 48.0° < \psi < 180.0° \tag{1.7}$$

where N is the maximum number of simultaneous transmitting co-frequency earth stations in the receiving beam of the satellite. For the TDMA multiplexing, N is equal to 1. For the cross-polar components, the masks are defined by:

$$EIRP(\psi) = 8.5 - 25\log(\psi) - 10\log(N), 2° < \psi < 7° \tag{1.8}$$

$$EIRP(\psi) = -12.63 - 10\log(N), 7° < \psi < 9.23° \tag{1.9}$$

In all the other directions, the recommendation FCC 25.138 gives different limits shown in Fig. 1.31.

For ESOMPs, the ETSI recommendation EN 303 978 gives the limits on EIRP for the co- and cross-polar components shown in Fig. 1.31. These limits are the same as the ones defined in the regulation FCC 25.138 within ±3° on the GSO plane. In other planes, the

limits are less stringent.

1.4.2 5G heterogeneous networks

Today, cellular and wireless local area networks (WLAN) operate between 800 MHz and 5.8 GHz, but new 60 GHz WLAN products are emerging. The growing market for broadband wireless services has led to a global bandwidth shortage for carriers [49, 50, 51]. Recent works suggest that mobile cellular communications are possible at carrier frequencies of tens of GHz, an order of magnitude greater than today's cellular spectrum bands, where high-gain miniaturized steerable antennas could be used to exploit the smaller wavelength [49, 50, 51, 52], thus motivating researchers to develop new steerable antenna systems for millimeter wave (mm-wave) frequency bands.

A scheme of the future 5G heterogeneous network architecture is shown in Fig. 1.32. It includes several cells of reduced sizes, called small cells, inside a traditional cell, called macro cell. Inside each small cell, the mm-waves coverage is realized with an access point connected to the macro cell base station with a point-to-point link (backhauling). Transmitarrays can be used to realize the backhauling between each access point and the base station (Fig. 1.32). A tilting capability of some degrees would be needed for self-alignment functions. They also can find application as access point antennas to serve the mobile terminals. In this case, extensive beam-steering capabilities are needed to cope with the mobility of users. In first trials, planar phased arrays have been used but it is expected that reconfigurable transmitarray antennas can realize the same function at lower cost and power consumption.

At mm-wave bands and in particular at 28 GHz and 38 GHz, unlike at 60 GHz or 380 GHz, atmospheric absorption does not significantly contribute to additional path loss, making it suitable for outdoor mobile communications [49]. Even with very heavy rainfall of 25 mm/hour, the rain attenuation over 200 m distance is only 1.4 dB at 28 GHz and 1.6 dB at 38 GHz. Thus, proper link design (with varying gain antennas, for example) could account for rain margin in future mobile mm-wave cellular systems.

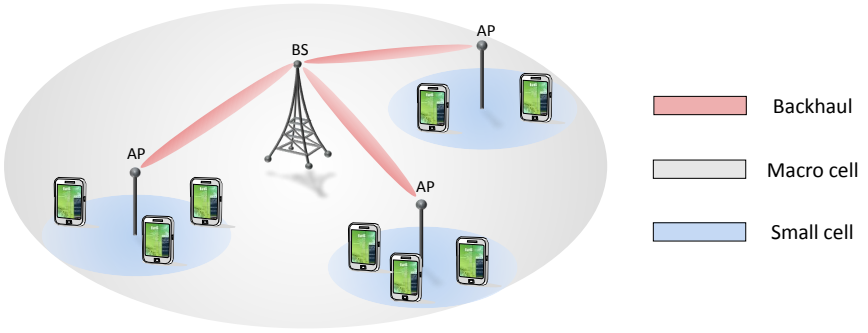

Figure 1.32: Sketch of a heterogeneous wireless network with backhauling channels.

During the last years, preliminary 5G tests throughout the industry have been conducted

in laboratories and indoor environments. Outdoor measurements in Ka-band have been carried out at the New York University [53], the University of Texas at Austin [54], and by Samsung in Korea [54]. The experimental results have shown the feasibility of these radio links in realistic environments by using directive horn antennas.

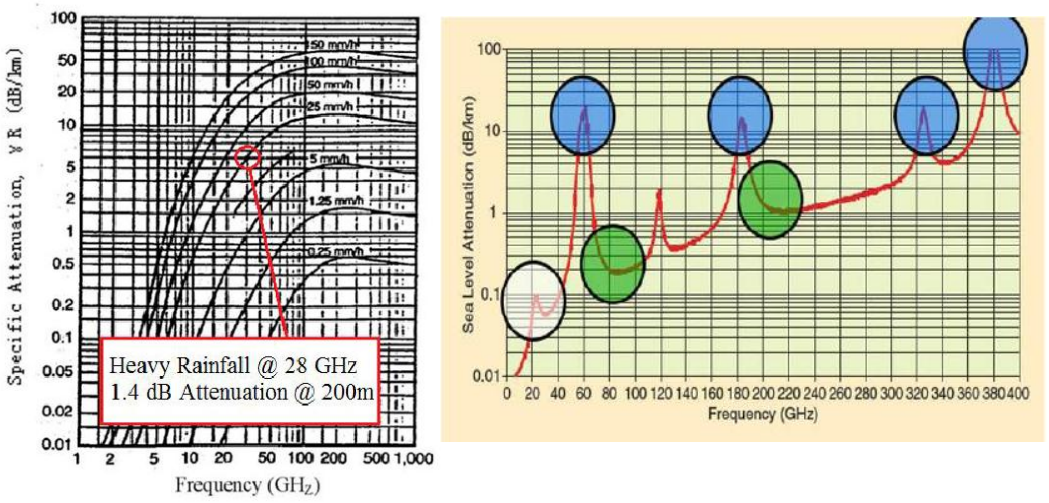

Figure 1.33: Rain attenuation in dB/km across frequency at various rainfall rates. The rain attenuation at 28 GHz has an attenuation of 7 dB/km for a very heavy rainfall of 25 mm/hr. Attenuation caused by atmospheric absorption. It is 0.012 dB over 200 m at 28 GHz and 0.016 dB over 200 m at 38 GHz.

Samsung carried out some tests at 27.925 GHz with planar phased array antennas for both the base station and mobile stations with a half-power beamwidth of 10°. The bandwidth considered was 500 MHz. With a QPSK/16QAM modulation and a low-density parity code for the channel coding, data rates up to 1056 Mbps have been demonstrated with a range of 2 km in line-of-sight conditions.

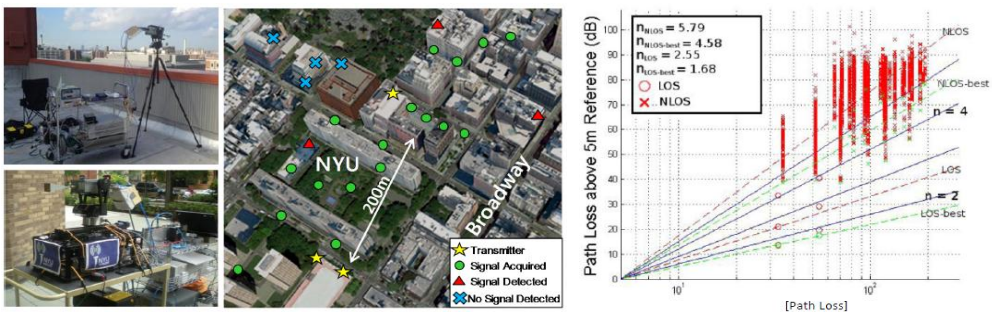

Figure 1.34: Experimental setup and measured path losses at 28 GHz in the experiment carried out at the NYU, US [53].

Further tests have been carried out with a vehicle racing at high speeds on a 4.35 km

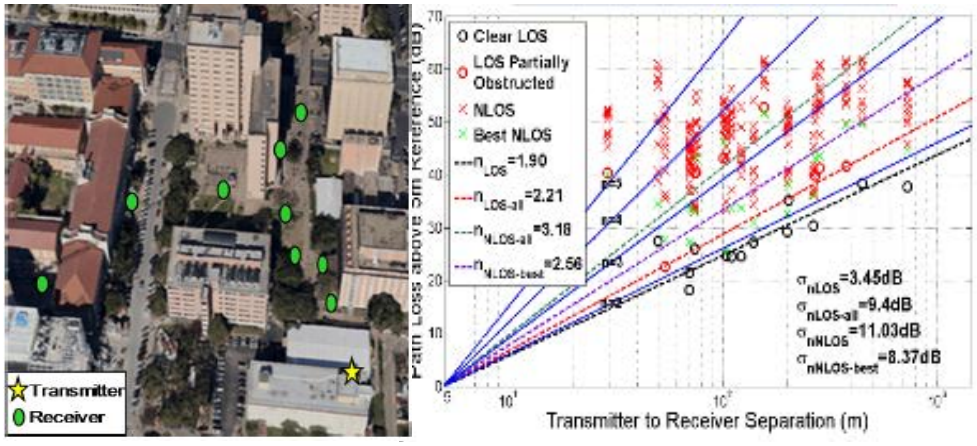

Figure 1.35: Experimental setup and measured path losses at 37.6 GHz in the experiment carried out at the University of Texas, US [53].

professional outdoor race track. Both the stationary and mobile tests were conducted at 28 GHz carrier frequency. While the 5G standard has yet to be defined, 5G networks are expected to offer data transmission rates that are tens, if not hundreds, of times greater than 4G LTE.

1.4.3 Fixed radio links

Transmit-array antennas can be used also in point-to-point fixed radio links, which are frequently used within telecommunications networks, broadcast networks, or local access networks on either a permanent or temporary basis. While these systems essentially use fixed beams, accurate beam-switching functionalities over a narrow angle are desired to perform an automatic beam alignment. Point-to-multipoint (PMP) links are also used within access networks. A point to multipoint network topology provides a communication route (on a single radio channel for each sector) from one central point to a number of terminals where users are located. Each user location may be served directly from the central location or via one or more radio repeaters. Multipoint to multipoint (MPMP) links, sometimes called mesh networks, provide communication pathways between various system nodes where each node has a communication pathway with a few of its near neighbours.

Characteristics and requirements for point-to-point equipments and antennas are given in the ETSI EN 302 217-4-2 regulation. Several radiation masks are provided for the co-polar and cross-polar components in the different frequency ranges and for different antenna classes. Some of these masks for the Ka-band operation (26.0-40.0 GHz) are shown in Figs. 1.36, 1.37.

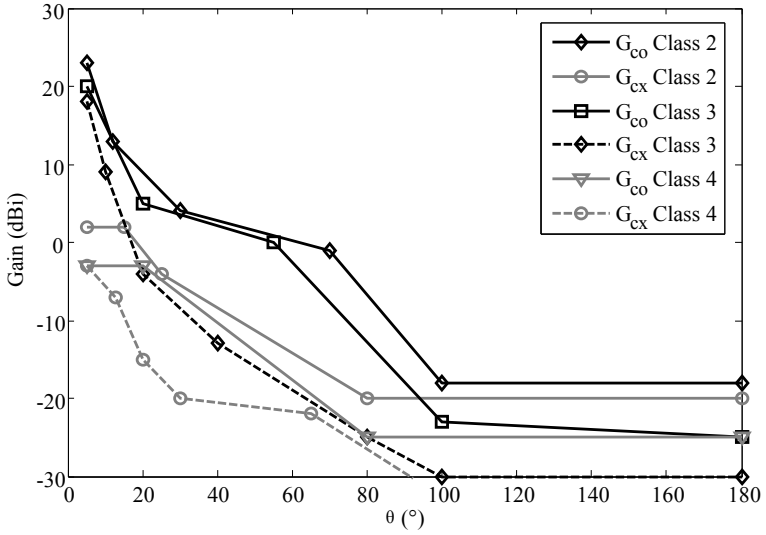

Figure 1.36: Radiation masks provided by ETSI EN 302 217-4-2 [47] for the point-to-point links in the 24-30 GHz band. Antenna classes 2, 3 and 4 are reported.

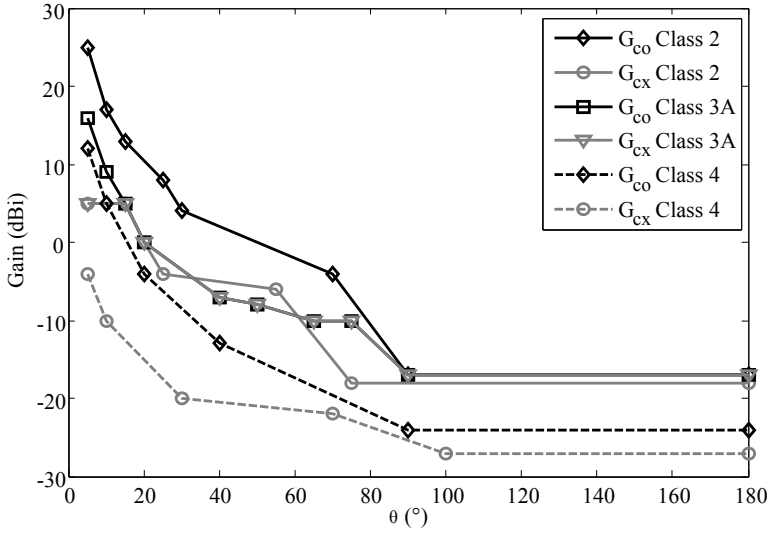

Figure 1.37: Radiation masks provided by ETSI EN 302 217-4-2 [47] for the point-to-point links in the 30-47 GHz band. Antenna classes 2, 3A and 4 are reported.

1.4.4 Radar systems

A first basic type of radar is the Pulse-Wave radar operating by generating pulses of radio frequency energy and transmitting them via a directional antenna. When a pulse impinges on an object in its path, a small part of the energy is reflected back to the radar antenna. The radar receives the reflected pulse if it is strong enough. The object range is given as a function of the round-trip propagation delay between the radar and the target. The direction of the object is the direction of the main beam radiated by the antenna at the time the reflected pulse was received.

These systems require high gain antennas for a good angular resolution, and a narrow pulse width for the best range resolution. Among their applications we find: air traffic control, aeronautical radio navigation, space, environmental monitoring, instrumentations and defence.

Another important radar principle is the Frequency Modulation Continuous-Wave radar (FM-CW). The transmitting signal is a sine wave modulated in frequency. In the receiving mode, the signal is amplified and mixed with the local oscillator to create a beat frequency proportional to the distance from the target. Its range resolution varies with the radar bandwidth. FM-CW radars find applications in through-wall sensing, transit tracking systems and automotive radars.

The specific application of the radar imposes a particular frequency range. In fact, the frequency is a primary parameter for the target recognition (aircrafts, clouds, ...). In Ka-band, the frequency range between 31.8 and 36.0 GHz is used for the radionavigation and radiolocation services. The military services have radars in this band for airborne navigational and mapping radars, airborne terrain following and avoidance radars, aircraft carrier precision approach and landing system radars, cloud measurement radars and vehicle speed detection radars.

Several automotive radar systems operate at millimeter-wave frequencies with different typologies based on the detection range: Short Range Radar (SRR), Medium Range Radar (MRR) and Long Range Radar (LRR). SRR sensors look in all directions around the vehicle at an approximate range of 0-30 meters, with a field of view up to 160° and operate typically at 24 GHz but 77 GHz can be considered in order to improve the angular and speed resolutions and reduce the antenna sizes [55, 56]. Long Range Radar (LRR) sensors require a range up to 200 meters with a narrow (10° to 20°) field of view (FOV). For this reason, they are also known as *forward-looking radars*. They operate in the 76 – 77 GHz band with a bandwidth of 0.5 to 1 GHz in order to achieve a range resolution of around 0.5 m [57]. Medium Range Radars (MRR) have been introduced to cover a range between SRR and LRR fields of detection. They typically operate at narrow-band at 24 GHz or ultra-wide-band at 79 GHz.

1.5 Conclusions

In this chapter, an introduction to transmitarray antennas is presented. After the description of their working principle, a comparison with reflectarrays and traditional phased arrays is proposed. The state-of-the-art of passive and active transmitarrays based on different technologies and at different frequencies is reviewed. In particular, several example of reconfigurable unit-cells based on the main reconfiguration technologies such as varactor and ferroelectric varactor diodes, microfluidic technology, MEMS switches and p-i-n diodes are presented.
The potential applications of transmitarray antennas, include satellite communications, future 5G cellular networks, point-to-point radio links and radar systems. An overview of all these applications has been presented and some requirements for satellites earth stations and point-to-point communications in Ka-band have been discussed. Radiation masks provided by ITU, FCC and ETSI are also provided.

Today, the main challenges in the domain of reconfigurable transmitarrays are to increase their operating frequency and to improve their performance in terms of efficiency and SLL. Furthermore, transmitarrays working in circular and dual-polarization need to be studied to broaden their field of applications. Improving their integration on mobile platforms by considering reduced focal distances and multi-facets or conformal structures is another important research area.

In the following chapters, we will investigate passive and reconfigurable transmitarrays working in circular polarization in Ka-band. First, a hybrid analytical/numerical method with reduced computational cost will be proposed for the analysis and synthesis of these antennas. Then, a passive unit-cell and several transmitarray designs will be presented in order to experimentally validate this method. Several reconfigurable unit-cells based on p-i-n diodes will be proposed in linear and circular polarization. The design, optimization, fabrication and test of a circularly-polarized reconfigurable transmitarray with 400 unit cells will be presented. Applications to monopulse radar systems will be also investigated.

Chapter 2

Circularly-polarized transmitarrays with sequential rotations

In this Chapter, the design, modelling and measurements of transmitarrays in circular polarization based on the sequential rotation technique are presented. A simulation tool based on a hybrid modelling technique is proposed to accurately predict the radiation performance at low computational cost. Several sequential rotation schemes are considered based on the theory developed for traditional phased array antennas.

In order to validate the performance numerically, a simple passive transmitarray working in circular polarization is considered. The mutual coupling between different unit-cells in the irregular lattice of the array is taken into account by proper calculation of the embedded radiation pattern. A prototype has been fabricated and tested in anechoic chamber in order to validate the proposed model.

2.1 Sequential rotations

Several approaches are investigated in the literature in order to generate circularly-polarized (CP) beams with transmitarray antennas. The first one is to consider CP sources and double linearly-polarized (LP) unit-cells [59, 60, 61]. In this case, the obtained polarization purity depends directly on the focal source axial ratio (AR) and the polarization discrimination of the unit-cell. This implies the use of expensive focal sources and adds constraints in the unit-cell design. Good results in terms of AR 3-dB bandwidth (about 20%) have been demonstrated in Ku-band by illuminating a transmitarray of unit-cells based on perforated dielectric with a 4×4 sequentially-rotated phased array as a focal source [60].

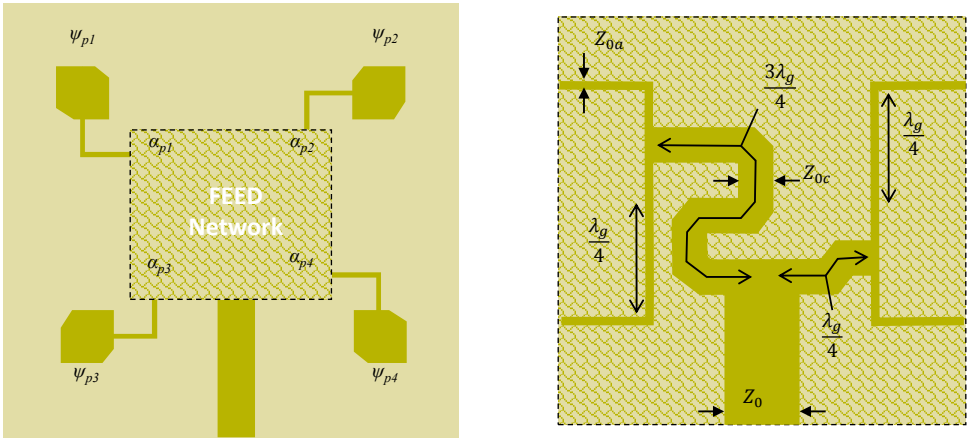

Figure 2.1: Scheme of a phased four-elements sub-array with sequental rotations (T=4, p=2) (a) and example of a feeding network based on quarter-wavelength impedance transformers and delay lines in microstrip technology (b) [58].

A second approach consists in rotating the radiating element of the unit-cells accordingly with the required phase shift [62, 63]. In [62], a 2-dB AR bandwidth of 7% is achieved in X-band by rotating the LP patches both on the receiving and transmitting layers. However, a CP source is required even in this case. In [63], a 2-bit phase quantization is achieved in Ku-band by rotating only the LP patches printed on the transmitting layer and using a simple LP horn as focal source; this configuration leads to a 3-dB AR bandwidth larger than 20%.

In [64], a design based on quarter-wave plates is proposed in E-band. In that work, two identical layers with capacitive and inductive behaviors on the two orthogonal axis are placed on the top and bottom of the unit-cell with a period of $\lambda_0/3.5$. A third resonator is realized on the intermediate layer. Five unit-cells with different dimensions have been optimized to obtain the phase compensation. A 3-dB gain bandwidth of 17% with AR under 2.5 dB has been demonstrated experimentally. However, the reduced unit-cell sizes and the irregularity of the generated lattice lead to a limitation of the local periodicity approximation, increasing the complexity of the analysis and its accuracy.

In this work, the application of the sequential rotations to the transmitarrays is proposed. The sequential rotation technique, originally developed for traditional phased arrays [65, 66, 67, 68], allows naturally the generation of circularly-polarized beams (even with linearly-polarized unit-cells) with a low axial ratio over a wide band. It allows to obtain the cancellation of the cross polarization components of the radiated fields from each antenna reducing the axial ratio, increasing the cross polarization discrimination, in the main beam direction, as demonstrated in [69, 70, 71, 72]. This technique can also be applied to transmitarrays built with circularly-polarized unit-cells in order to further improve the axial ratio bandwidth, otherwise limited to 3-4% in the case of single-layer printed antennas,

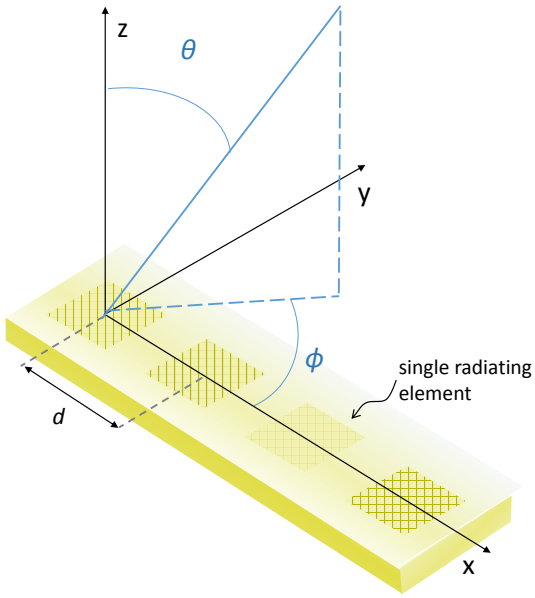

Figure 2.2: Scheme of the setup considered in a first-order analysis for T=4.

and maximize the array gain and aperture efficiency. One challenge in the design of phased arrays based on this technique is the complexity of the beam-forming network generating the correct phase excitation of each antenna element accordingly with its rotation angle [69] (see Fig. 2.1). In contrast, in the case of transmitarrays, the sequential rotations do not introduce any further complexity to the structure design since transmitarray unit-cells are designed to generate multiple phase states. Moreover, the insertion loss and the bandwidth of the single unit-cell are not really affected by the rotation.

In theory, high phase resolution unit-cells are desirable to achieve a high aperture efficiency. Such cells, especially in the case of electronically reconfigurable elements, results in several limitations: higher insertion loss, variation of the frequency response, and complexity. Practically, a relaxed phase resolution may be chosen when the power efficiency and complexity are a primary concern. A 1-bit (180° phase step) approach enables the design of reconfigurable transmitarrays with good power efficiency, reduced bias network complexity, and large bandwidth, as demonstrated in [73]. In this chapter, the feasibility of a circularly-polarized 1-bit transmitarray with sequential rotations in view of the realization of an electronically reconfigurable structure is proposed.

Arrays of sequentially-rotated antennas are usually organized in sub-arrays of T elements where the rotation angle applied to the m-th element of the sub-array can be defined as [70]

$$\psi_{pm} = (m-1)\frac{p\pi}{T}, \tag{2.1}$$

where p is an integer and m is chosen between 1 and T. The corresponding excitation phase

for each element is given by

$$\alpha_{pm} = (m-1)\frac{p\pi}{T}. \tag{2.2}$$

The values of p and T considered are summarized in Table 2.1. Sub-arrays of two, three or four elements with different angles of rotations and arrangements will be investigated. A sub-array of circularly-polarized patch antennas with $T = 4$ and $p = 2$ and a simple example of a feed network in microstrip technology used for generating the phase excitations α_m are shown in Fig. 2.1. This network is an essential part of the design and could limit the bandwidth of the array and its polarization purity. If it is realized on the top layer (as in the example of Fig. 2.1) the feeding network can be responsible of spurious radiation impacting the axial ratio performance. Only complex designs with several layers avoid the perturbation of the array radiation.

A first order analysis, proposed for the traditional phased array in [70], can be used to demonstrate the cross polarization cancellation at boresight. A linear array of T elements spaced by a distance d is considered. A sketch for $T = 4$ of the considered configuration is shown in Fig. 2.2. Considering right-handed circularly polarized unit-cells, the generic electric field radiated by the single radiating element m can be written as

$$\mathbf{E}_m(\theta,\phi) = a(\theta,\phi)\widehat{\theta} + jb(\theta,\phi)\widehat{\phi}, \tag{2.3}$$

where a and b are the field amplitudes components along $\widehat{\theta}$ and $\widehat{\phi}$, respectively. We suppose that all the elements have the same radiation pattern and the feeding amplitude is the same. In addition, they are aligned on one axis for the sake of simplicity (Fig. 2.2). Considering a cosine function model for the electric field with dependency on only θ, the total electric field radiated by a sub-array of T elements in the cut-plane $\phi = 0°$ is given by

$$\mathbf{E}_T(\theta,0) = \sum_{m=1}^{T}\mathbf{E}_m(\theta,0) = \sum_{m=1}^{T}\{E_{m\theta}(\theta,0)\widehat{\theta} + E_{m\phi}(\theta,0)\widehat{\phi}\}e^{j(\psi_{pm}-\chi_{pm})}, \tag{2.4}$$

where the electric field components along $\widehat{\theta}$ and $\widehat{\phi}$ are

$$E_{m\theta}(\theta,0) = a(\theta,0)\cos(n\alpha_{pm}) - jb(\theta,0)\sin(n\alpha_{pm}), \tag{2.5}$$

$$E_{m\phi}(\theta,0) = a(\theta,0)\sin(n\alpha_{pm}) - jb(\theta,0)\cos(n\alpha_{pm}). \tag{2.6}$$

The phase factor χ_{pm} is

$$\chi_{pm} = (m-1)k_0 d\sin(\theta), \tag{2.7}$$

where k_0 is the free-space propagation constant and d is the distance between the radiating

Table 2.1: Angles of rotations assigned to the antenna m for different T and p values.

T	2	3	3	4	4
p	1	1	2	1	2
ψ_m	0, 90°	0, 60°, 120°	0, 120°, 240°	0, 45°, 90°, 135°	0, 90°, 180°, 270°

elements. The equation 2.4 can be written at boresight ($\theta = 0°$) in the following way

$$\mathbf{E}_T(0,0) = \frac{T}{2}(a+b)(\widehat{\theta} + j\widehat{\phi}) + \frac{1}{2}(a-b)(\widehat{\theta} - j\widehat{\phi})\frac{\sin(p\pi)}{\sin\frac{p\pi}{T}}e^{j\frac{(T-1)p\pi}{T}}, \tag{2.8}$$

The second term of the equation 2.8 is

$$X = \frac{1}{2}(a-b)\frac{\sin(p\pi)}{\sin\frac{p\pi}{T}}e^{j\frac{(T-1)p\pi}{T}} \tag{2.9}$$

and corresponds to the left-handed circular polarization radiation. It is equal to 0 when p is within 1 and T-1. In this condition, the cross polarization component radiated from the sub-array of T elements is cancelled in the boresight direction.

This analytical approach gives only a first order estimation of the cross polarization cancellation obtained with this technique. The actual radiation pattern of the single element and the mutual coupling must be taken into account in order to estimate correctly the radiation performance. In fact, mutual coupling plays a key role in the radiation performance evaluation and it will be considered in the embedded pattern calculations.

2.2 Transmitarray model

The electrical dimensions of transmitarray antennas are quite large and a brute-force approach would require a huge amount of computational resources to simulate accurately all the entire structure. An ad-hoc efficient simulation technique has been successfully developed in previous works and its accuracy has been already confirmed in X- [73, 74] and V-bands [63, 75]. This hybrid method is based on full-wave simulations combined with analytical formulations [63] and will be illustrated in this paragraph. Several modifications have been developed in this work:

- Calculation of the optimal phase compensations on the receiving layer;
- Calculation of the transmitarray performances with application of the sequential rotation technique to the transmitting layer;
- Analysis and optimization of several schemes of rotations (Chapters 2 and 4);

- Commutation between the two circular polarizations (LHCP/RHCP) of the main beam (Chapter 4).

2.2.1 Focal source

The focal source has been selected by considering an ideal radiation pattern (gain) $H_{FS}(\theta^m, \phi^m)$, defined as

$$H_{FS}^n(\theta, \phi) = \frac{n+1}{2\pi} \cos^n(\theta). \tag{2.10}$$

With $n = 4$, 10 dBi of maximum gain are obtained, as shown in Fig. 2.3. The corresponding beam-width is 65.5°. Different real focal sources are compared, in particular three standard gain horn antennas manufactured by Flann Microwave [76] and ATM [77]: Flann 22240-10 (WR-28), ATM 28-440-6 (WR-28), ATM 34-440-6 (WR-34). Their geometrical dimensions are listed in Table 2.2. Their radiation patterns at 29 GHz in the two cardinal planes have been compared with the ideal cosine function (Fig. 2.3). The broadside gain is lower for the two horns in WR28 than for the ATM 34-440-6, but higher values of radiation in the angular range between 60° and 90° can be observed. This leads to higher spillover radiation and then lower transmitarray efficiency. For this reason, the ATM 34-440-6 waveguide horn was selected for the design.

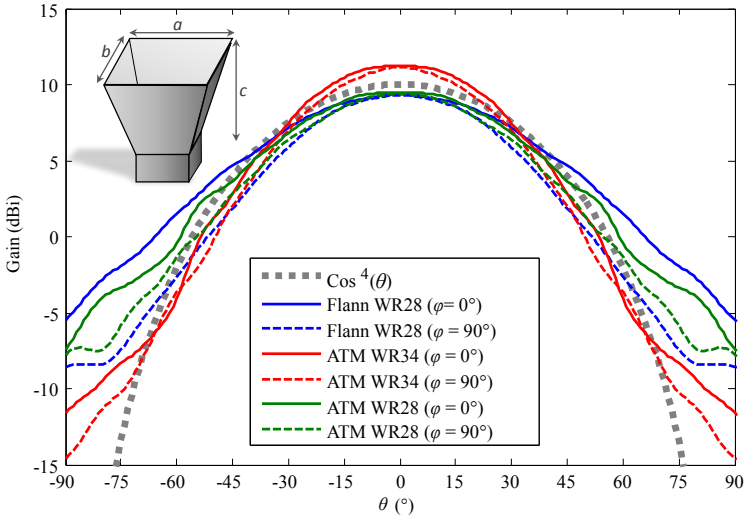

Figure 2.3: Simulated co-polar radiation pattern of the three horn antennas (Flann 22240-10 (WR-28), ATM 28-440-6 (WR-28) and ATM 34-440-6 (WR-34)) compared with the cosine function.

The radiation pattern for the WR34 horn is evaluated with full-wave simulations at each frequency of the band of interest. The gain in the two cardinal planes is shown in Fig. 2.4. The gain and the phase of the radiated fields are exported and used for the transmitarray design. The antenna has been tested in anechoic chamber and the measurement results are reported in Fig. 2.4 and Fig. 2.5. A good agreement with the numerical results is obtained.

Table 2.2: Geometrical dimensions of the horn antennas considered as feed (Fig. 2.3).

horn model	a	b	c
Flann 22240-10 (WR-28)	11.5	7.2	12.0
ATM 28-440-6 (WR-28)	10.6	7.8	12.7
ATM 34-440-6 (WR-34)	13.5	9.9	15.0

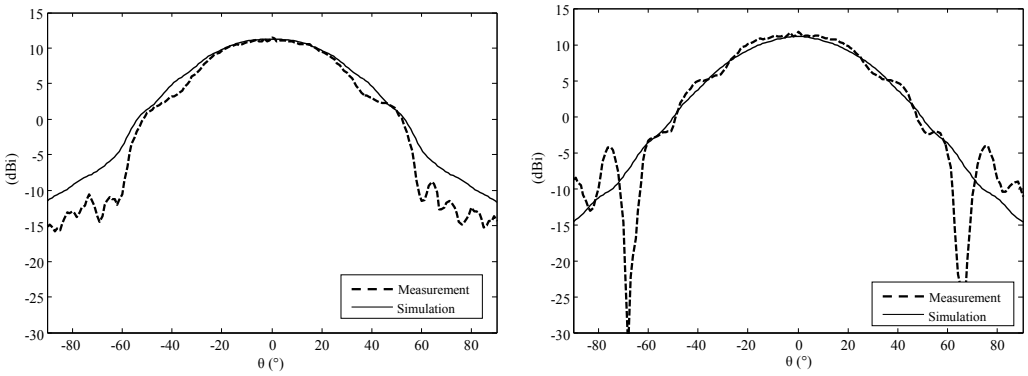

(a) (b)

Figure 2.4: Simulated and measured co-polar radiation pattern of a WR34 standard gain horn with 10 dBi of nominal gain in the horizontal (a) and vertical (b) planes.

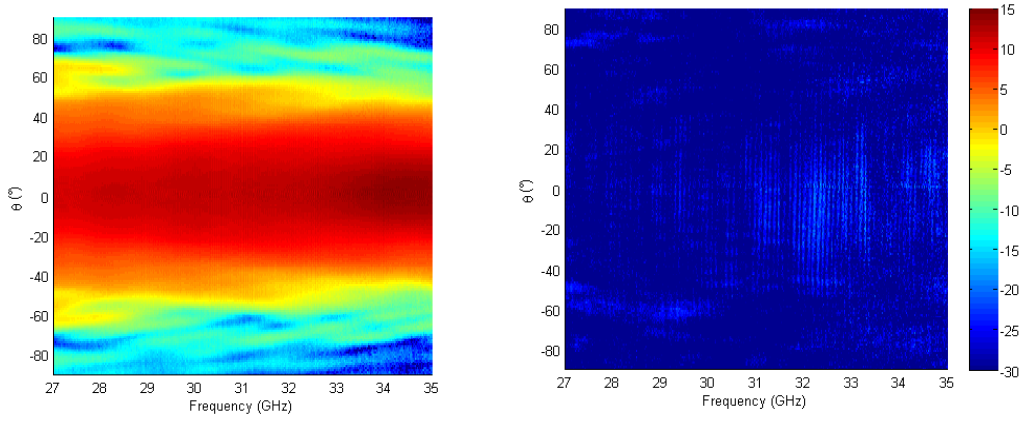

(a) (b)

Figure 2.5: Measured co-polar (a) and cross-polar (b) radiation patterns of a WR34 standard gain horn with 10 dBi of nominal gain in the horizontal plane.

2.2.2 Unit-cell

The unit-cell, whose dimensions are in general chosen as half-wavelength in free space, is formed in the model by a first antenna working in receiving mode connected to another one working in transmitting mode separated by at least a ground plane. The connection can be realized in different ways such as a metallized via or coupling slots. Several unit-cells are designed to realize the different phase shifts. The frequency response is optimized for each one by using numerical simulations and considering the whole structure in a periodic lattice. By considering periodic boundary conditions and Floquet port excitations, the scattering parameters S_m are calculated for each unit-cell. The radiation pattern (directivity) associated to the receiving and transmitting antennas, $H_m^{Rx}(\theta^m, \phi^m)$ and $H_m^{Tx}(\theta^m, \phi^m)$, are calculated by considering another setup. Only half of the unit-cell is excited with a lumped port excitation. Periodic boundary conditions are maintained on the edges of the unit-cell. A scheme of the unit-cell model is shown in Fig. 2.6.

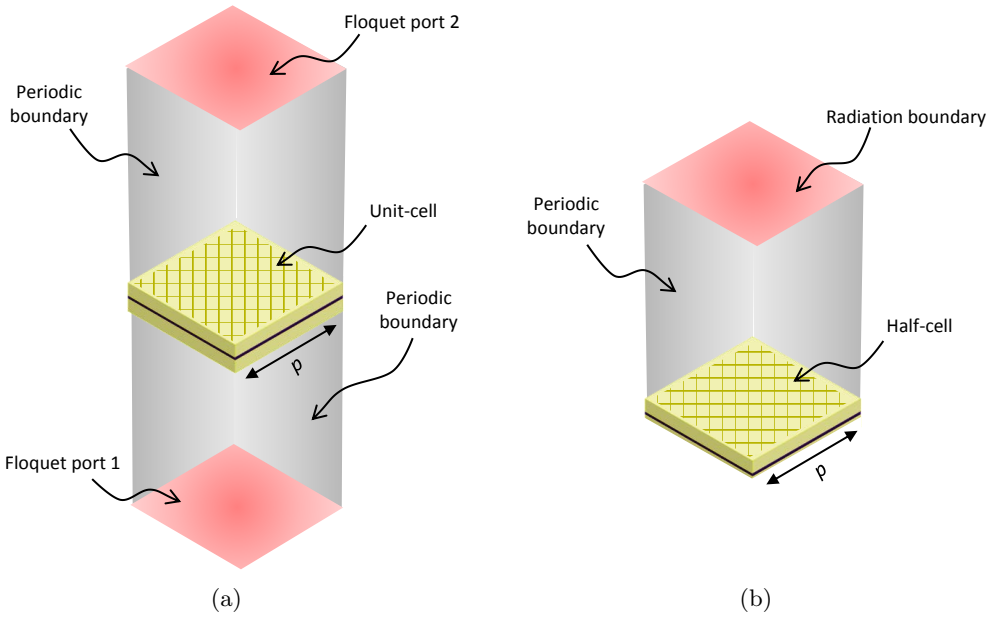

(a) (b)

Figure 2.6: Schematic view of the setup used for the calculation of the unit-cell scattering parameters (a) and (b) radiation patterns.

2.2.3 Model of the full transmitarray

In the proposed model, the focal source radiation pattern, the unit-cells scattering parameters and their radiation patterns are used as input data of an in-house code which allows computing the radiation performance of the entire array using the standard array theory [74, 75]. The incident wave a_1^m associated to the unit-cell m shown in the scheme of Fig. 2.7 is given by

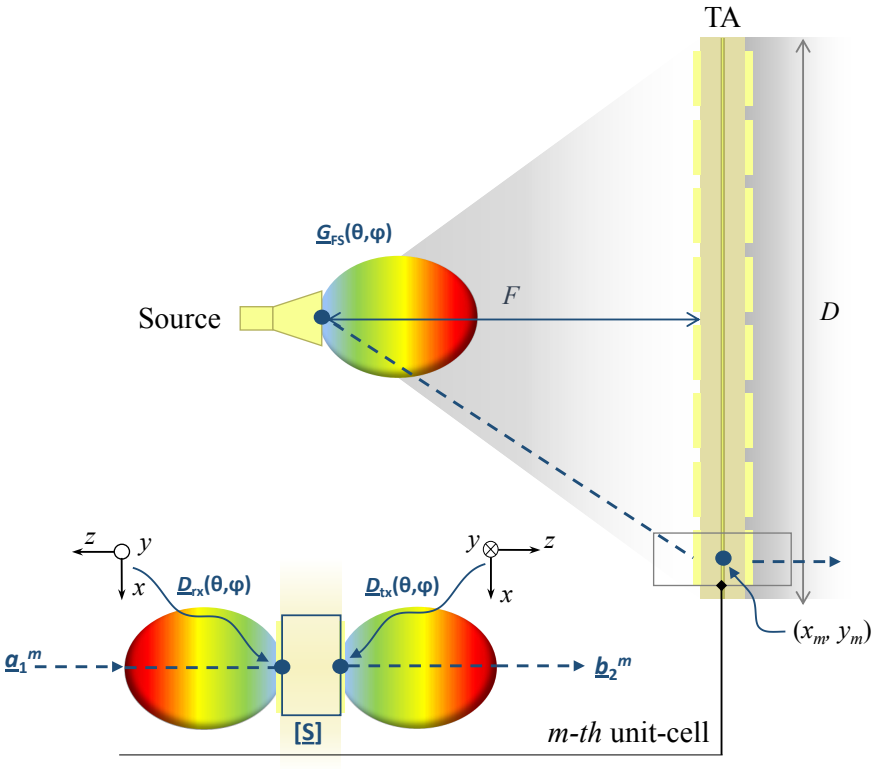

Figure 2.7: Scheme of the model used for the analysis of transmitarray antennas.

$$a_1^m = \sqrt{P_1}\frac{\lambda}{4\pi r_m}e^{-j\frac{2\pi r_m}{\lambda}}H_{FS}(\theta^m,\phi^m)H_m^{Rx}(\theta^m,\phi^m), \tag{2.11}$$

where P_1 is the input power to the focal source, r_m is the distance between the center of the unit-cell m and the focal source center, λ is the free-space wavelength. Here we assumed that the focal source has a radiation efficiency of 100%. The radiation pattern $H_m^{Rx}(\theta^m,\phi^m)$ associated to the unit-cell m is selected following the phase law required for the compensation of the differential paths. The latter is defined in accordance to the rotation angle ψ_m applied to the transmitting layer. A perfect phase compensation is given by

$$\Delta\phi_m = \phi_m - \psi_m, \tag{2.12}$$

where ϕ_m is the phase of the incident wave a_1^m. Applying a phase quantization of 1 bit, i.e. only two phase states are possible for each unit-cell m, the equation 2.12 becomes

$$\Delta\phi_m = \psi_m, \tag{2.13}$$

if $|\phi_m - \psi_m| < \frac{\pi}{2}$, else

$$\Delta\phi_m = \psi_m + \pi. \tag{2.14}$$

In order to calculate the optimal phase distribution, the waves a_1^m associated to the different unit-cells are calculated and the corresponding unit-cell is selected for each position on the array lattice. On the transmitting layer, the waves b_2^m can be written as

$$b_2^m = S_{21}^m a_1^m, \tag{2.15}$$

where S_{21}^m is the transmission coefficient calculated numerically by simulating the unit-cell m in a periodic environment. The power density $S(\theta, \phi)$ radiated from the array surface can be calculated as

$$S(\theta,\phi) = \frac{1}{4\pi r^2}\left|\sum_{m=1}^{M} b_2^m e^{j\frac{2\pi}{\lambda}(x_m \sin\theta cos\phi + y_m \sin\theta sin\phi)} H_m^{Tx}(\theta,\phi)\right|^2, \tag{2.16}$$

where (x_m, y_m) are the coordinates of the m-th unit-cell center, (θ, ϕ) are the spherical coordinates related to the coordinate system centred on the transmit-array surface and M is the total number of unit-cells in the array. The directivity $D(\theta, \phi)$ of the antenna is defined as

$$D(\theta,\phi) = \frac{S(\theta,\phi)}{S_i(\theta,\phi)} = \frac{S(\theta,\phi)}{P/4\pi r^2} = \frac{\left|\sum_{m=1}^{M} b_2^m e^{j\frac{2\pi}{\lambda}(x_m \sin\theta cos\phi + y_m \sin\theta sin\phi)} H_m^{Tx}(\theta,\phi)\right|^2}{\sum_{m=1}^{M} |b_2^m|^2}. \tag{2.17}$$

This formulation takes into account the radiation pattern H_m^{Tx} of the m-th unit-cell transmitting layer, its orientation ψ_m and the excitation in magnitude and phase through the vector b_2^m. Considering the efficiency associated to the focal source η_{FS} and the efficiency associated to the spillover losses η_{SO}, which will be defined in the next paragraph, the realized gain of the transmitarray antenna is

$$G(\theta,\phi) = \eta_{FS}\eta_{SO}\frac{\left|\sum_{m=1}^{M} b_2^m e^{j\frac{2\pi}{\lambda}(x_m \sin\theta cos\phi + y_m \sin\theta sin\phi)} H_m^{Tx}(\theta,\phi)\right|^2}{\sum_{m=1}^{M} |b_2^m|^2}. \tag{2.18}$$

The proposed method allows the evaluation of the radiation characteristics of the transmitarray reducing the calculation complexity to the single unit-cell and the focal source. This powerful and efficient model is very useful in the definition of the gain, side lobe level and bandwidth of a transmitarray antenna. The spillover radiation can be taken into account by full-wave simulation of the whole configuration at the end of the design and optimization process carried out with the proposed model.

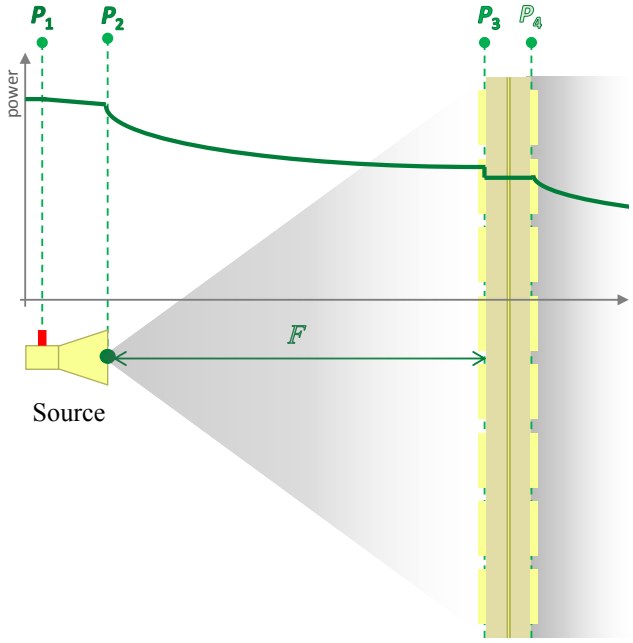

Figure 2.8: Schematic view of the power budget quantities considered in the proposed transmitarray model.

2.2.4 Power budget

Considering the scheme of Fig. 2.8, P_1 is the power given to the focal source of the array and it is fixed to 1 W. The total power radiated from the same antenna (P_2) is calculated by integrating the radiation pattern obtained with full-wave simulations. Then, the efficiency of the feed can be defined as

$$\eta_{FS} = \frac{P_2}{P_1}. \tag{2.19}$$

The power collected from the transmitarray receiving layers P_3 can be calculated as the sum of the incident waves a_1^m:

$$P_3 = \sum_{m=1}^{M} |a_1^m|^2, \tag{2.20}$$

where M is the total number of unit-cells. The radiated power P_2 from the feed is partly received from the array receiving layer. The difference between P_2 and P_3 is the spillover efficiency defined as

$$\eta_{SO} = \frac{P_3}{P_2}. \tag{2.21}$$

The power transmitted to the transmitting layer is given by

$$P_4 = \sum_{m=1}^{M} |b_2^m|^2, \tag{2.22}$$

The difference between P_4 and P_3 represents the dissipation and reflection losses introduced by the unit-cells. The related efficiency is

$$\eta_{IL} = \frac{P_4}{P_3}. \tag{2.23}$$

The total efficiency is

$$\eta_{tot} = \eta_{FS} \cdot \eta_{SO} \cdot \eta_{IL}. \tag{2.24}$$

2.3 Passive unit-cell design

The proposed unit-cell is composed of three metal layers printed on two identical substrates Rogers RT/Duroid 6002 ($h_s = 0.508mm$, $\epsilon_r = 2.94$, $tan\delta = 0.0012$), Fig. 2.9 [78]. The two substrates are bonded using an Arlon CuClad6700 film ($h_f = 0.114$ mm, $\epsilon_r = 2.35$, $tan\delta = 0.0025$) [79]. A linearly-polarized rectangular patch is realized on the receiving (bottom) layer of the structure. A circularly-polarized square patch with two truncated corners is placed on the transmitting (top) layer. The two patches are connected with a metallized via (diameter $d_V = 200$ μm) through a hole (diameter $d_h = 700$ μm) etched in the ground plane. All the unit-cell geometrical parameters are defined in Fig. 2.9 and their numerical values are reported in Table 2.3. The design has been optimized with the commercial software Ansys HFSS v.15 [80]. Periodic boundary conditions and Floquet port excitations have been considered to take into account the mutual couplings with the surrounding unit-cells assuming a periodic arrangement of identical unit-cells. The magnitude of the simulated scattering parameters calculated for $\psi_l = \psi_c = 0°$ under normal incidence are shown in Fig. 2.11. These parameters are referred to the right-handed circular polarization (RHCP) at port 2 and have been obtained with the correct combination of the two TE and TM orthogonal Floquet modes excited in the structure, as reported in Appendix A. The insertion loss equals 0.2 dB at 30 GHz, and the 1-dB transmission bandwidth spans between 28.5 GHz and 31.4 GHz, which corresponds to a 10% fractional bandwidth. The return loss remains below 10 dB between 28.6 and 31.8 GHz for both receiving (port 1) and transmitting (port 2) layers. Similar scattering parameters are obtained for the different angles of rotations ψ_c using the same simulation setup.

The radiation patterns of the unit-cell from the receiving and transmitting sides have been calculated by using a lumped port excitation and proper radiation boundary conditions (Figs. 2.6, 2.10). For the circularly-polarized side, the broadside gain in right-handed circular polarization is 4.7 dBi at 30 GHz and the 3-dB beam-width is 86° on the two principal planes (Fig. 2.12). The cross-polarized component is 27 dB below. The broadside gain is higher than 2.7 dBi between 28.0 and 31 GHz and the cross- polarization discrimination is higher than 15 dB between 29.5 and 30.4 GHz.

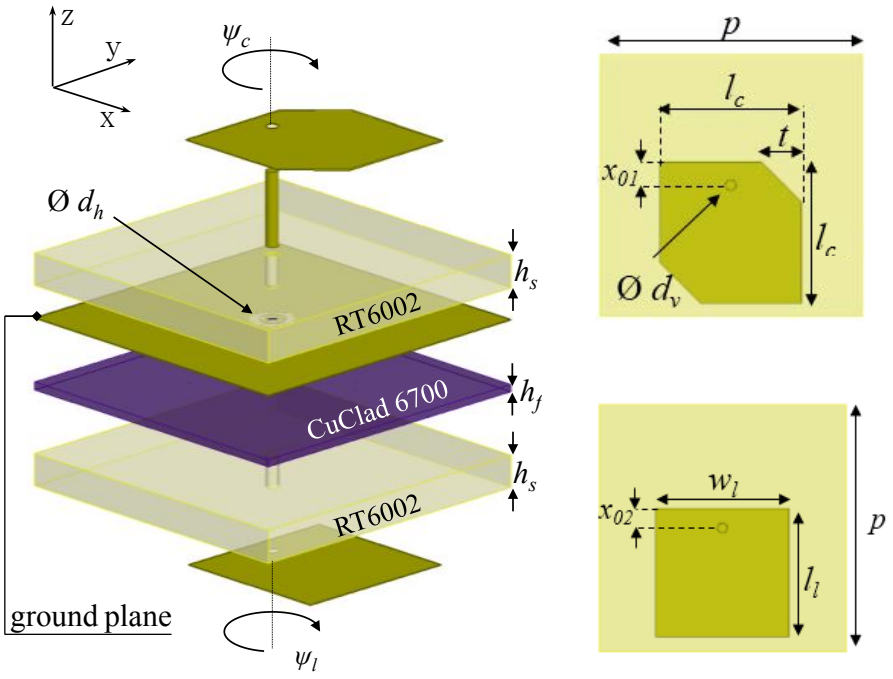

Figure 2.9: Scheme of the circularly-polarized unit-cell. Receiving and transmitting layers. All the dimensions are listed in Table 2.3.

Table 2.3: Unit-cell geometrical dimensions.

	mm		mm
p	5	d_V	0.2
l_l	2.6	d_h	0.7
w_l	2.7	h_s	0.508
l_c	2.7	x_{01}	0.45
t	0.77	x_{02}	0.4

For the linearly-polarized side, the broadside gain is 4.85 dBi at 30 GHz and the 3-dB beam-width is 87°. The cross-polarized component is 25 dB below (Fig. 2.13). The broadside gain is higher than 3.1 dBi between 28.0 and 31 GHz and the cross-polarization discrimination is higher than 25 dB in the same frequency range.

By rotating the rectangular patch on the receiving layer by an angle $\psi_l = 180°$ with respect to the metallic via, a 180° phase difference is obtained. This 1-bit phase resolution has been selected in order to demonstrate the feasibility of a fully-reconfigurable array with good radiation performances as such a phase quantization can be quite easily implemented in a reconfigurable unit-cell with low losses and large bandwidth, as demonstrated in X band [73] and as will be demonstrated in Ka band in Chapter 3, enabling dynamic beam-steering/beam-forming.

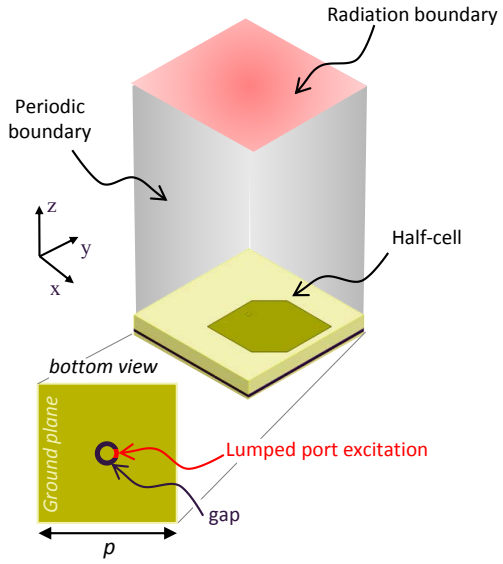

Figure 2.10: Full-wave simulation setup used to calculate the radiation patterns for the transmitting layer ($\psi_c = 0°$). A similar configuration has been considered for the receiving layer side.

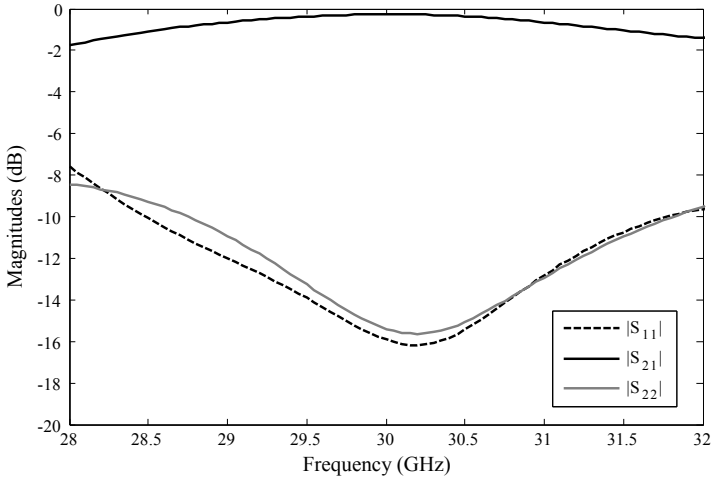

Figure 2.11: Scattering parameters magnitudes of the unit-cell simulated with periodic boundary conditions and Floquet port excitations ($\psi_l = \psi_c = 0°$). A similar behavior is obtained for the different values of ψ_c.

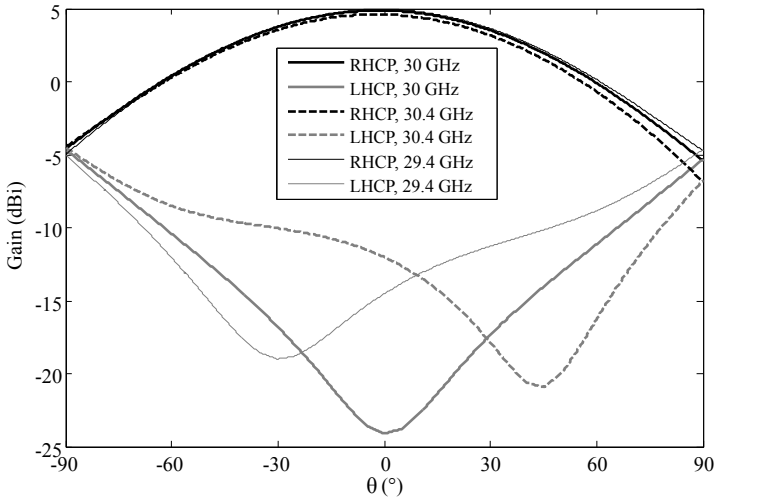

(a)

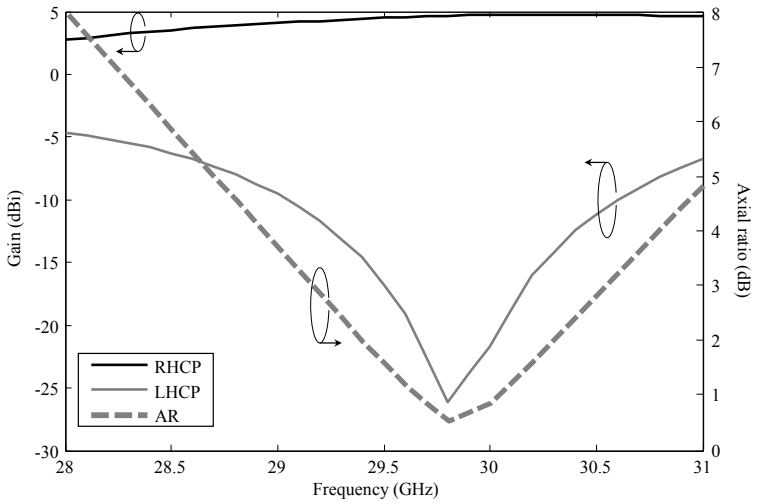

(b)

Figure 2.12: Radiation pattern at 29.4, 30 and 30.4 GHz (a), broadside realized gains and axial ratio (b) of the unit-cell from transmitting circularly-polarized side.

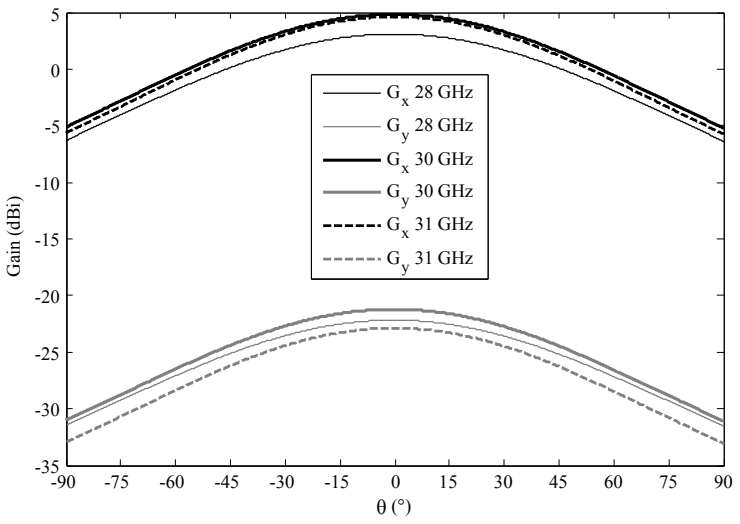

(a)

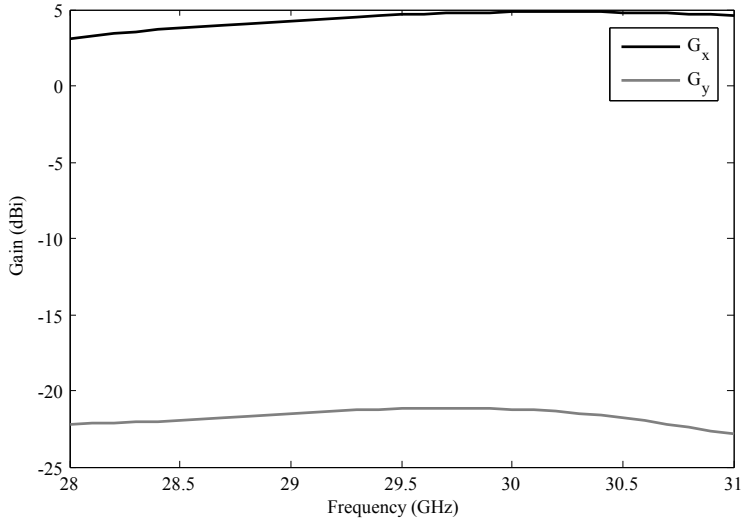

(b)

Figure 2.13: Radiation pattern at 28, 30 and 31 GHz (a) and broadside realized gains (b) of the unit-cell from receiving linearly-polarized side.

2.4 Simulation of transmitarrays with several sequential rotation schemes

In this paragraph, the design of a 400-elements transmitarray without rotations based on the unit-cell proposed in the previous section is considered firstly as reference. Then, several sequential rotation schemes are applied and the simulated radiation characteristics are compared.

The 10-dBi standard gain horn antenna in WR-34 manufactured by ATM (ATM 34-440-6, [77]) is used as focal source. The inter-element spacing is $0.5\lambda_0$ (5 mm) at 30 GHz. A focal distance of 60 mm ($F/D = 0.6$, where $D = 100$ mm is the size of the antenna panel) is obtained by maximizing the broadside gain (Fig. 2.14). This point corresponds to a trade-off between the spillover losses and tapering losses. For the transmitarray without rotations, a maximum gain in the broadside direction of 24.7 dBi is obtained at 30 GHz. The corresponding axial ratio, which is identical to the AR of the single unit-cell, equals 1.65 dB at 30 GHz with a minimum of 0.35 dB at 29.6 GHz and a 3-dB bandwidth of about 1.5 GHz (5%)(Fig. 2.15).

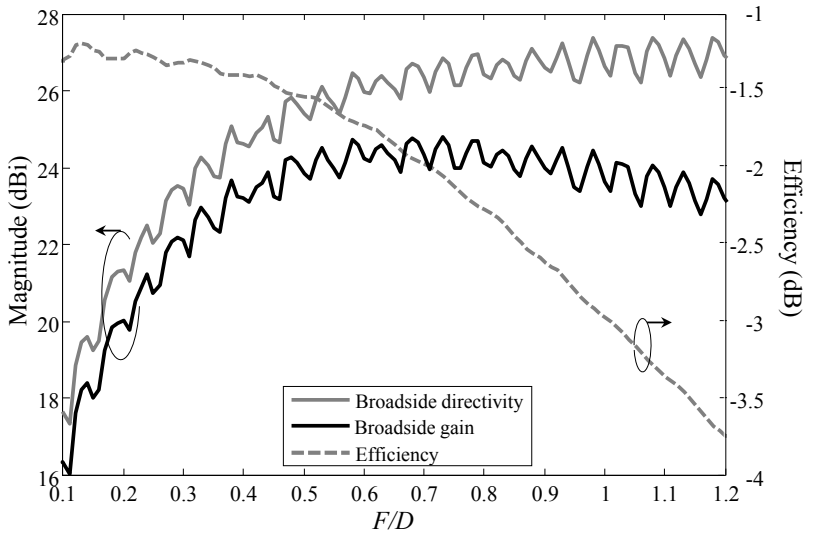

Figure 2.14: Broadside gain and efficiency of the 400-elements transmitarray without rotations at 30.0 GHz as a function of the focal distance F.

As previously discussed, the performances of the array can be improved by using the sequential rotation technique. We have considered several configurations of sequential rotation given by the combination of p and T values. The results are summarized in Tables 2.4 and 2.5. For $T = 2$, $p = 1$, sub-arrays of two patch antennas with 90° of rotation angles on a chessboard scheme are defined on the transmitting layer (Fig. 2.16b).Over a 10% fractional bandwidth around 30 GHz, a reduction of the maximal axial ratio to 1.25 dB are obtained with 0.5-dB lower gain.

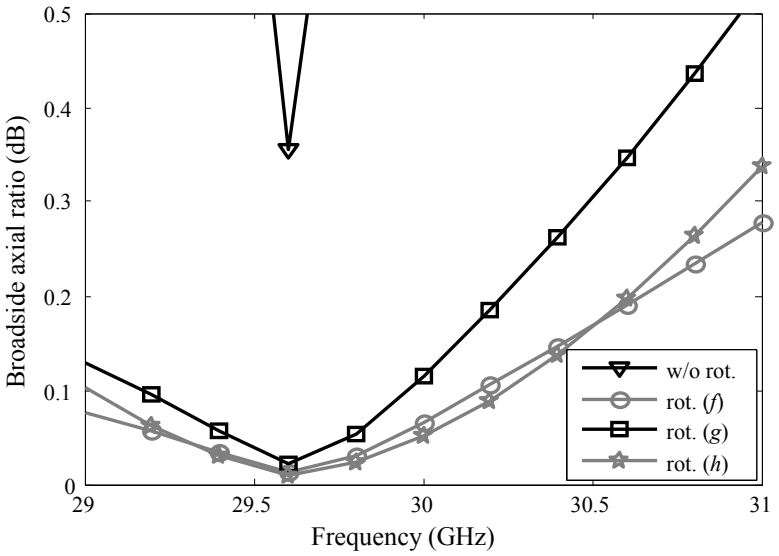

Figure 2.15: Axial ratios in the broadside direction for the transmitarray without and with sequential rotation schemes of Fig. 2.16(f),(g),(h).

For $T = 3$, $p = 1$, sub-arrays of three patch antennas with 0°, 60° and 120° of rotation angles on a triangular scheme are defined on the transmitting layer (Fig. 2.16c). The maximal axial ratio is further reduced to 0.61 dB and a reduction of 0.4 dB in the broadside gain is observed. Similar results are obtained for $T = 3$, $p = 2$ (Fig. 2.16d) and $T = 4$, $p = 1$ (Fig. 2.16e). For $T = 4$, $p = 2$, sub-arrays of four patch antennas with 0°, 90°, 180° and 270° of rotation angles on different schemes are studied: a clockwise distribution and two different distributions with sub-array rotations (Tab. 2.5, Fig. 2.16f, g, h). The phase distribution w/o rotations and with the different rotation schemes are calculated by using the equations 2.13 and 2.14 and they are shown in Fig. 2.17. The unit-cell distribution in the receiving layer can be easily determined by subtracting the rotation angles to the phase distribution masks calculated as illustrated above. The simulated axial ratios (AR) are shown in Fig. 2.15. Their values is under 0.02 dB at 29.6 GHz in all sequential rotations schemes. The best results are obtained with the last rotation configuration (h) for which the Cross Polarization Discrimination (XPD) reaches 65 dB. The radiation pattern (gain) of the arrays without rotation and with rotations in this configuration in the principal and diagonal planes ($\phi = 0$ and $\phi = 45°$) are reported in Fig 2.18. The cross-polarized gain (RHCP) in the broadside direction decreases from 4.2 dBi to -26 dBi thanks to the sequential rotations. The performances in terms of gain, polarization purity and Side-Lobe Level (SLL) for all the designed arrays are reported in Tables 2.4, 2.5.

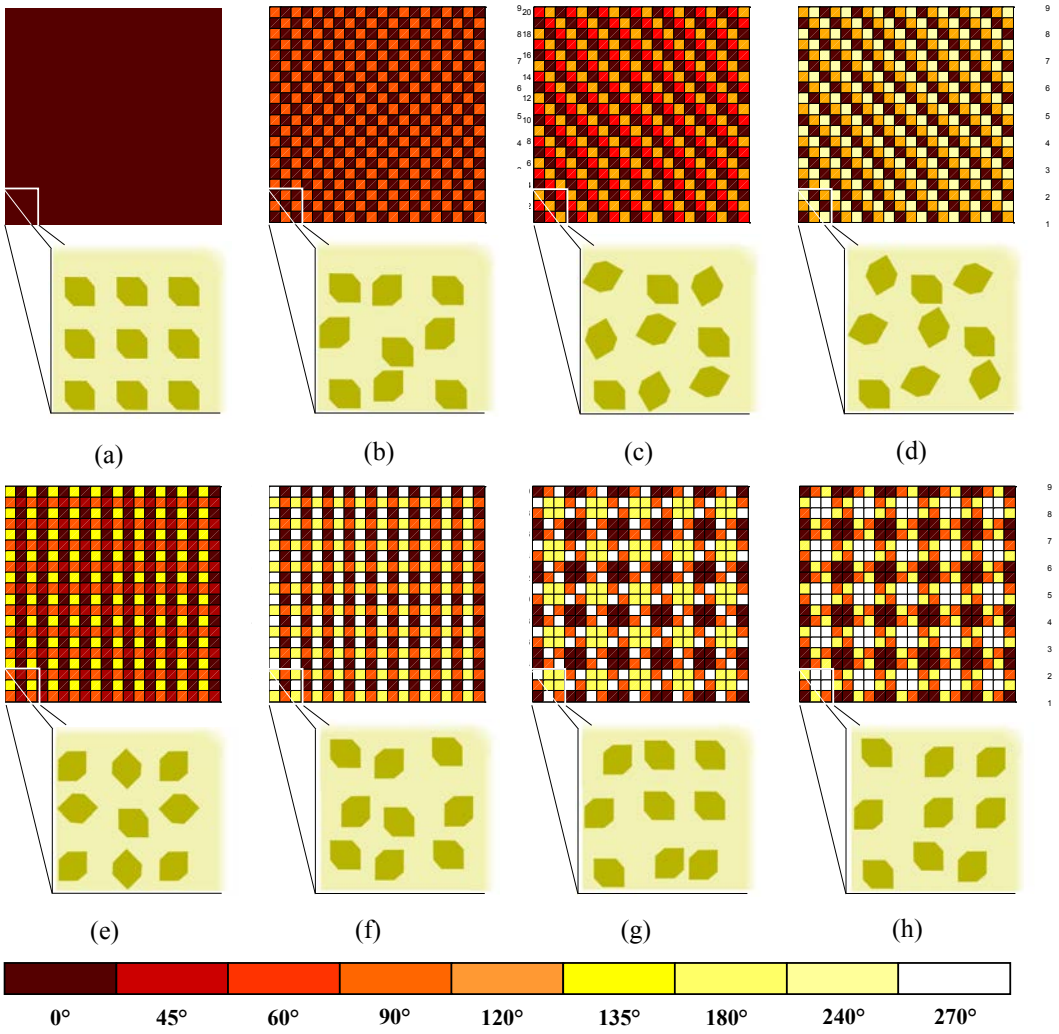

Figure 2.16: Scheme of sequential rotations applied to the transmitting layer of the transmitarray: without rotations (a); with rotations of 0°/90° (b) in a chessboard arrangement; with rotations of 0°/60°/120° (c), 0°/120°/240° (d) in a diagonal arrangement; with rotations of 0°/45°/90°/135° (e), 0°/90°/180°/270° (f) in a clockwise arrangement; with rotations of 0°/90°/180°/270° in two different rotated sub-array arrangements (g, h). The corresponding receiving layers are formed by different arrangements of linearly-polarized patch antennas rotated by $\psi_l = 0°$,180° accordingly with Eqns. 2.13, 2.14.

Table 2.4: Simulated radiation characteristics at 30 GHz of a 400-elements transmitarray with the sequential rotation schemes of Fig. 2.16. AR and XPD calculated on a 10% fractional bandwidth.

T	1	2	3	
p	1	1	1	2
Rotations (°)	-	0/90	0/60/120	0/120/240
Distribution	(a)	(b)	(c)	(d)
Arrangement	w/o rotations	chessboard	diagonal	
Relative Gain (dB)	-	-0.5	-0.4	-0.4
Max SLL (ϕ=0°, 45°)(dB)	-21.0,-16.0	-22.0,-20.0	-16.6,-18.6	-19.6,-15.6
Max AR (dB)	5.0	1.25	0.61	0.75
Min XPD (dB)	11	23	29	28

Table 2.5: Simulated radiation characteristics at 30 GHz of a 400-elements transmitarray with the sequential rotation schemes of Fig. 2.16. AR and XPD calculated on a 10% fractional bandwidth.

T	4			
p	1	2		
Rotations (°)	0/45/90/135	0/90/180/270		
Distribution	(e)	(f)	(g)	(h)
Arrangement	clockwise		sub-array I	sub-array II
Relative Gain (dB)	-0.5	-0.5	+0.3	-0.2
Max SLL (dB)	-16.5,-19.5	-21.5,-18.5	-18.0,-14.0	-19.9,-20.9
Max AR (dB)	0.7	0.15	0.22	0.3
Min XPD (dB)	28.5	40	38	36

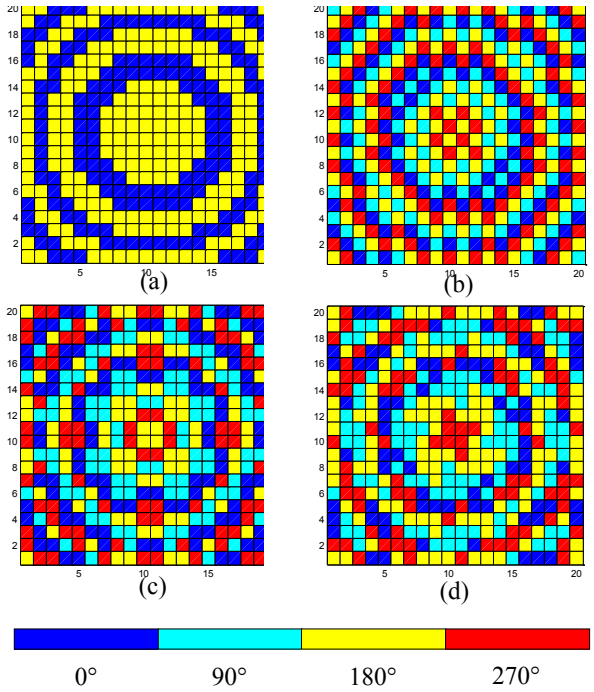

Figure 2.17: Phase distributions applied to the transmitarray surface with the different schemes of rotations (w/o rotations (a), clockwise (b), 4-element sub-array (c, d) rotations). These schemes correspond to the rotation configurations (a), (f), (g) and (h) of Fig. 2.16, respectively.

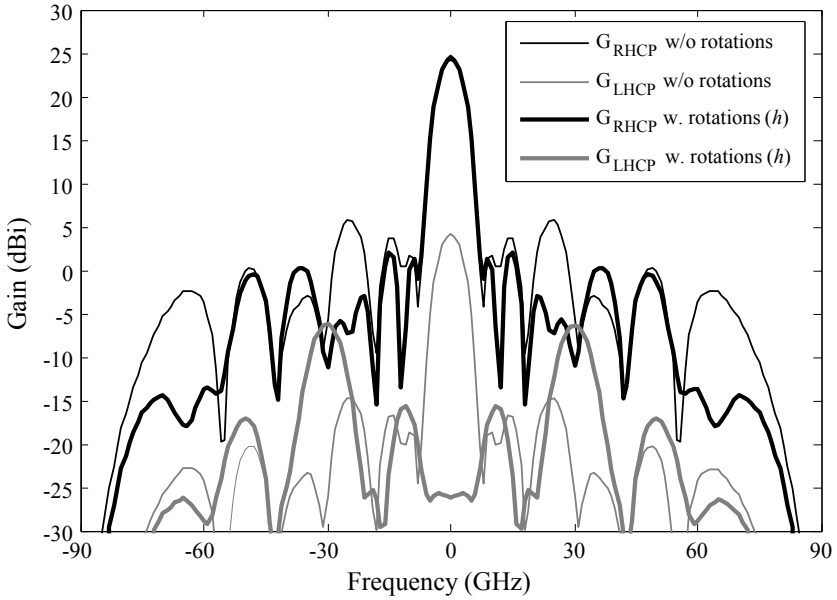

Figure 2.18: Radiation pattern in the horizontal plane w/o rotations and with rotation scheme in the last configuration (Fig. 2.16h).

2.5 Mutual Coupling

The simplest setup used for the unit-cell radiation pattern takes into account the mutual coupling between the elements in a regular lattice (i.e. without considering the rotations of the neighbour unit-cells). Only the transmitting layer of a single unit-cell is simulated and is excited with a lumped port placed in the gap between the via and the ground plane. Proper periodic and radiation conditions are applied at the boundaries to calculate the radiation pattern (Fig. 2.19 a). The directivity calculated in RHCP and LHCP for the $\phi = 0°$ plane are plotted in Fig. 2.21(a, b) (solid bold lines). The radiation pattern calculated in this way is the same in magnitude for each unit-cell of the array as if no rotations were applied. The phase of Fig. 2.21(c) is shifted by $\psi_l = 180°$ for the corresponding 180°-state unit-cell.

However, rotation of angles ψ_c have been considered in the previous paragraph for the improvement of the circular polarization purity. In that case, the irregular lattice generated on the transmitting layer must be taken into account for an accurate embedded pattern calculation. Then, a different setup must be considered in order to increase the accuracy of the proposed model. In fact, the accuracy in the radiation pattern of each individual unit-cell is essential to predict correctly the radiation performance of the array [81]. Moreover, as already shown for phased array antennas [82], the effectiveness of the sequential rotation technique is highly sensitive to variations of the single element radiation pattern. This setup, shown in Fig. 2.19(b), is formed by 4×4 sub-arrays of sequentially rotated transmitting layer patches, which is the periodicity of the selected arrangement shown in Fig. 2.16(h). Only one patch is fed with a lumped port, as already shown in Fig. 2.10, and all the others are closed on a matched load. Periodic conditions are applied at the boundaries. Four different simulations have been performed for the four different angles of rotations (ψ_c), taking into account the real environment and mutual couplings of each patch antenna, as shown in Fig. 2.20. The obtained directivity is shown in Fig. 2.21 for the different values of ψ_c. Asymmetries in the co-polarized pattern (RHCP) and significantly higher cross-polarized levels (LHCP) are the main observed effects if compared with the setup used to calculate the embedded pattern of a transmitarray without rotations. The worst case corresponds to the unit-cell with $\psi_c = 180°$ (solid grey line in Fig. 2.21(b)) for which the cross-polarized gain is 22 dB higher at broadside if compared to the results given by the first simulation setup (black bold line in Fig. 2.21(b)). Moreover, there is an error in the phase difference of the RHCP electric field between the four cells, mainly outside the angular region (-30°, 30°), as shown in Fig. 2.21(c). Both of the effects are due to the mutual coupling between the CP antennas in the irregular lattice. With the transmitarray simulation technique and the radiation patterns of the unit-cells in their sub-array environment, an optimal focal distance of 52 mm ($F/D = 0.52$) at 30 GHz has been found as a best trade-off between spillover loss and illumination tapering.

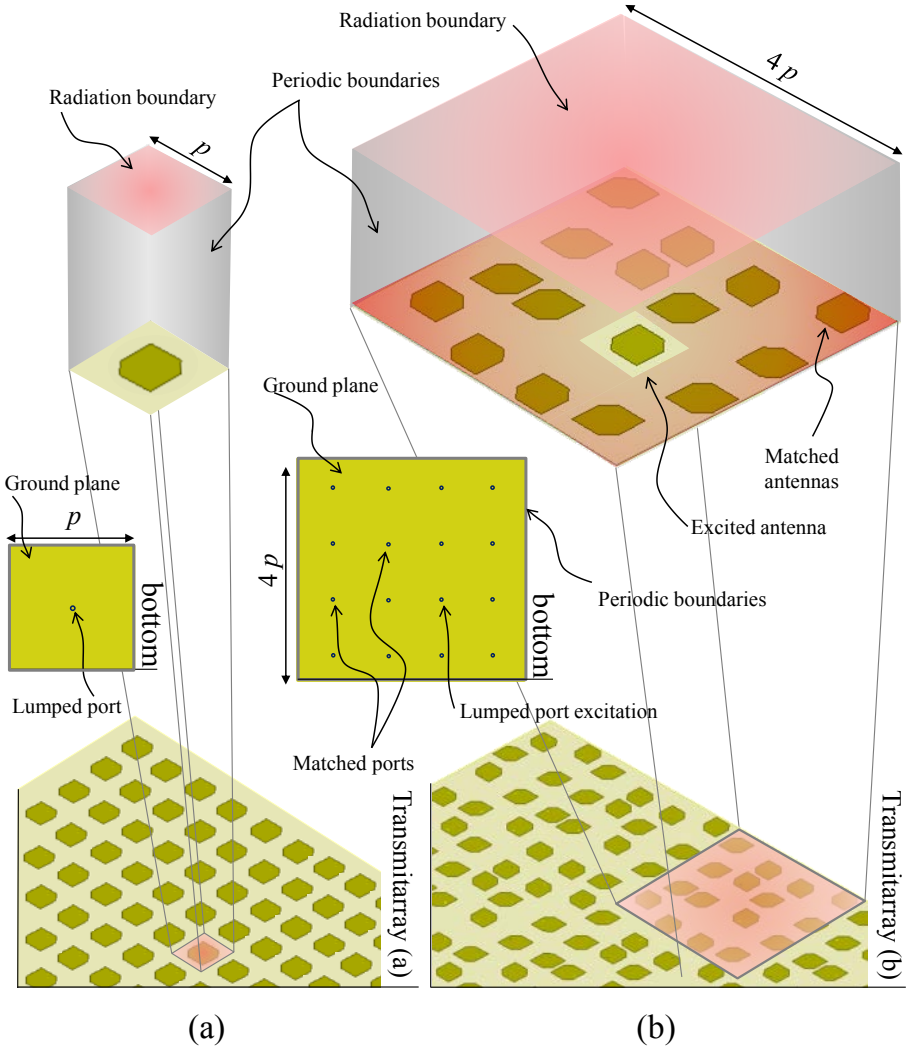

Figure 2.19: Simulation setup considered for the calculation of the embedded pattern of a transmitarray without (a) and with (b) sequential rotations.

Considering the transmitarray without the rotations and the unit-cell simulation setup of Fig. 2.19(a) for the radiation pattern calculations, the simulated broadside RHCP gain is 24.2 dBi at 30 GHz and the broadside axial ratio is under 3 dB between 29.2 and 30.5 GHz, as shown in Figs. 2.22, 2.24 (dashed lines). The corresponding directivity, spillover losses and power efficiency equal 25.8 dBi, 1.4 dB and 69.5%, respectively. In the configuration with the rotations (h) of Fig. 2.16 and the unit-cell simulation setup of Fig. 2.19(b) for the radiation pattern calculations, a maximum gain of 23.2 dBi with a broadside axial ratio under 3 dB between 27 and 35 GHz have been found, as shown in Figs. 2.22, 2.24 (markers lines). The corresponding directivity equals 24.8 dBi. As expected, the use of the sequential rotations leads to an improvement of the axial ratio 3-dB bandwidth, which increases from 4% to 25%. The 1-dB lower gain obtained in this case is due to the lower gain of the active patterns of the rotated patches (Fig. 2.21 a, b) and to the phase errors between the rotated

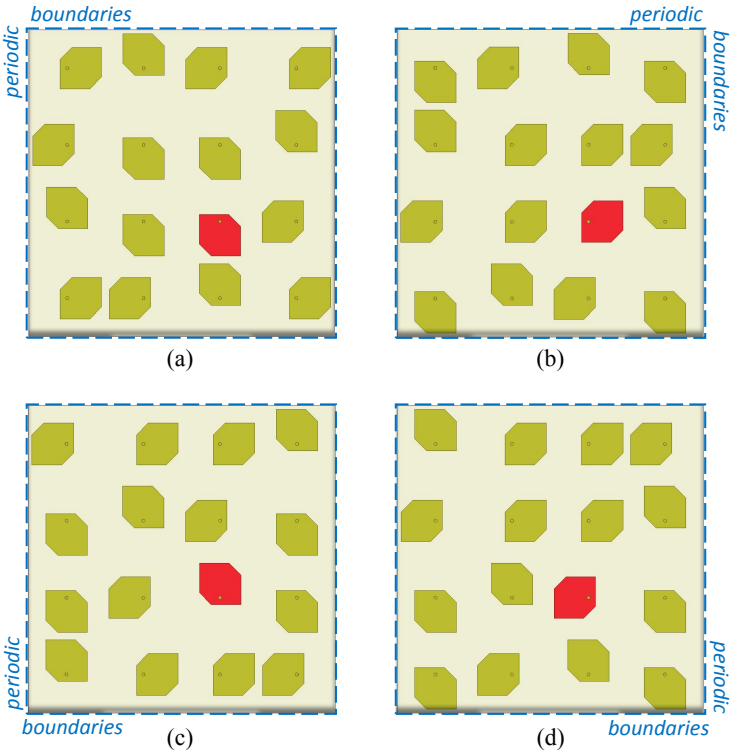

Figure 2.20: Full-wave simulation setup (top view of the transmitting layer) considered for the calculations of the embedded pattern of thetransmitarray with sequential rotations: $\psi_c = 0°$ (a), $\psi_c = 90°$ (b), $\psi_c = 180°$ (c), $\psi_c = 270°$ (d). The patch antenna drawn in red is the excited one; all the others are closed to a matched load.

patches (Fig. 2.21 c) introduced by the mutual couplings taken into account in the setup of Fig. 2.19(b).

The proposed new analysis setup for transmitarrays allows to take into account the mutual coupling between neighbours unit-cells in a non-regular arrangement, such as the ones generated with the sequential rotation technique, without significantly affecting the simulation time and allowing a fast and efficient prediction of the radiation performances. The contribution given by the proposed approach is fundamental when the radiating elements are characterized by high levels of coupling, such as in the case of circularly-polarized elements proposed here.

2.6 Experimental results

The transmitarray (B) with the sequential rotations designed in the previous section has been manufactured and tested in anechoic chamber (Fig. 2.23a). Photographs of the transmitting and receiving layers are shown in Fig. 2.23(b and c). The measured co-polarization broadside gain (RHCP) is equal to 22.8 dBi at 30 GHz with XPD of 17.2 dB, as shown in Fig. 2.22. The resulting power efficiency equals 63.1%. The power budget and the main radiation pattern

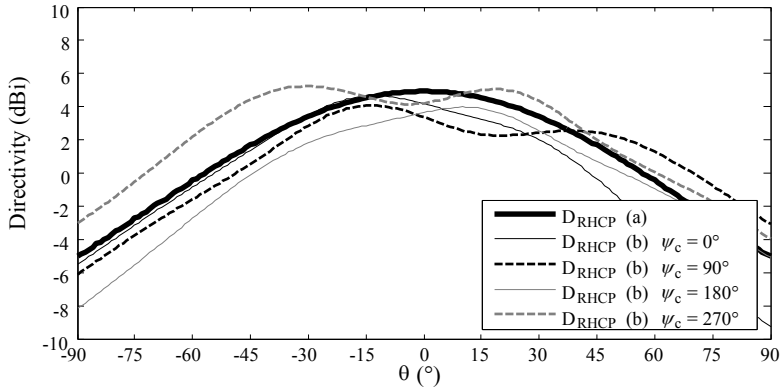

(a)

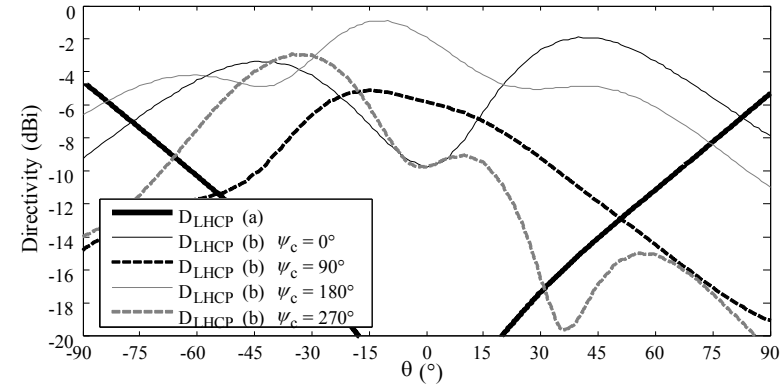

(b)

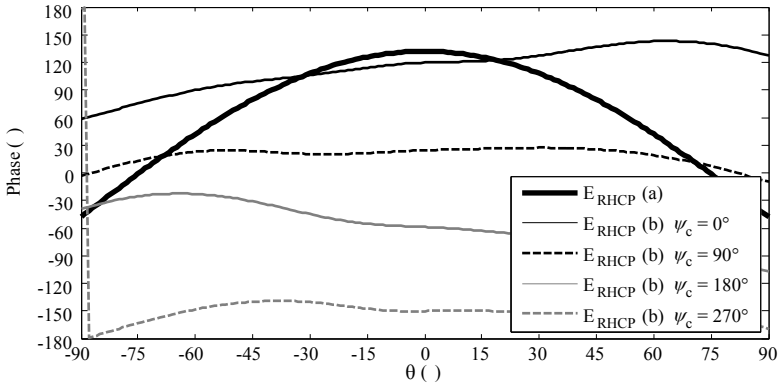

(c)

Figure 2.21: Embedded pattern of the single unit-cell calculated at 30.0 GHz with the setup shown in Fig. 2.19; Co-polar (a) and cross-polar (b) magnitudes, co-polar phases (c).

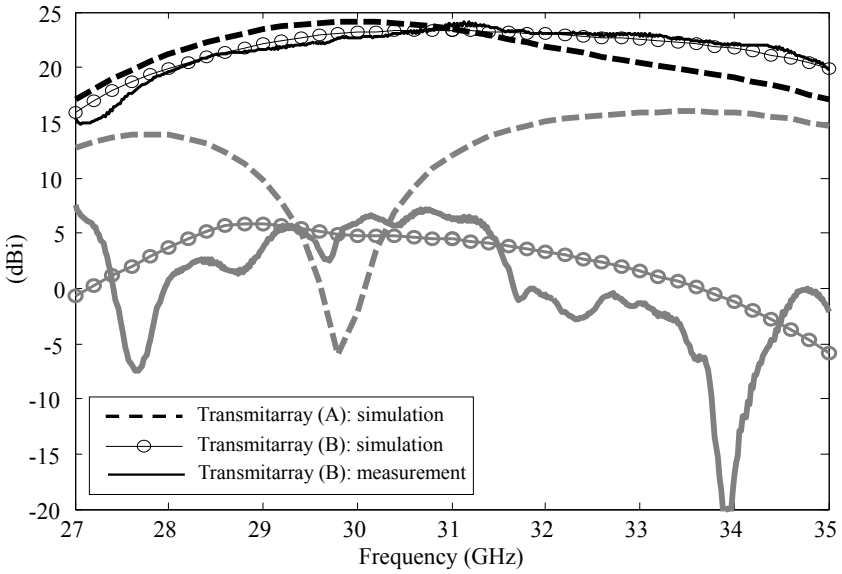

Figure 2.22: Co- and cross-polarized broadside CP gains for the transmitarray without rotations (A; Fig. 2.16a) and for the transmitarray with sequential rotations (B; Fig. 2.16h). The unit cell embedded patterns have been calculated with the two setups of Fig. 2.19 for the two transmitarrays, respectively.

characteristics at 30 GHz are reported in Table 2.6. The experimental results are in good agreement with the numerical predictions. The co-polarized gain at broadside in RHCP has a 3-dB bandwidth of 20% (28.5-35.0 GHz), and the axial ratio is below 3 dB between 27.4 and 35.0 GHz (24.4%), as shown in Figs. 2.22, 2.24. The axial ratio remains under 3 dB in angular range of the main beam (3-dB beamwidth) in all the bandwidth (Fig. 2.25). The 1-dB gain bandwidth is about 10%. The radiation patterns measured at 30 GHz in the horizontal and diagonal cut-planes are plotted in Figs. 2.26, 2.27. The asymmetrical behavior which can be observed on both the simulation and measurement results is due to the mutual coupling. As discussed in the previous paragraph, it has a significant impact on the embedded radiation patterns in terms of AR and it generates the asymmetries. A good agreement between the measurements (solid bold lines) and the numerical results (dashed lines) can be observed in the main beam direction and in the angular region corresponding to the 3-dB beamwidth, which is equal to 7°, for both the co- and cross-polar components. Moderate discrepancies can be observed for the side lobes inside the angular region between -45° and +45°. However, the maximum measured side lobe level (SLL), which is equal to -16.9 dB, -17.0 dB, -17.3 dB in the horizontal, vertical and diagonal planes, respectively, is predicted with a maximum error of 1 dB. Further differences outside this angular range are mainly due to the spillover losses, which are not taken into account in the simulated results presented above. Similar considerations can be done for the radiation patterns at 29, 31 and 32 GHz, shown in Figs. 2.28, 2.29 and 2.30, respectively, in the horizontal plane.

In order to take into account the spillover radiation effects, a full-wave simulation of the

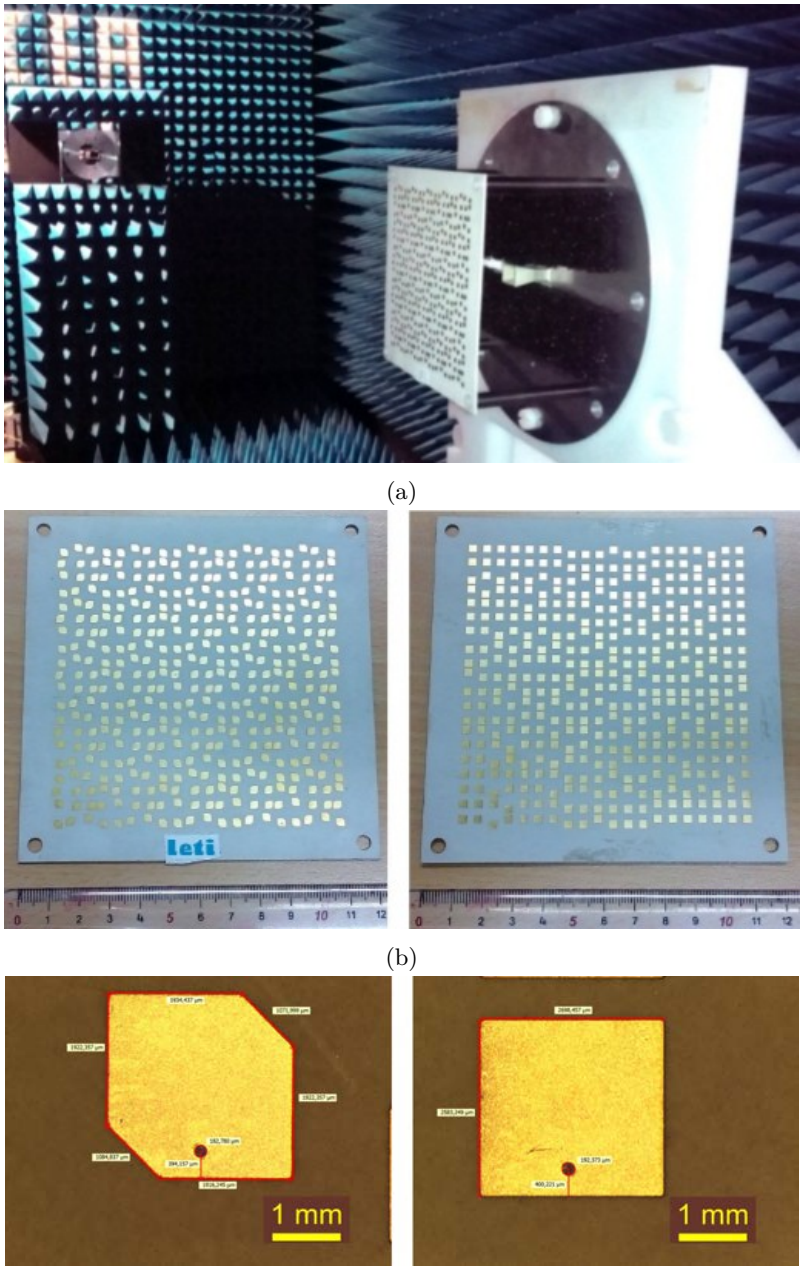

(a)

(b)

(c)

Figure 2.23: Photograph of the measurement setup in anechoic chamber (a). Photographs of the realized prototype (receiving and transmitting layer) (b) and microscope images of the single unit-cell on the array surface (c).

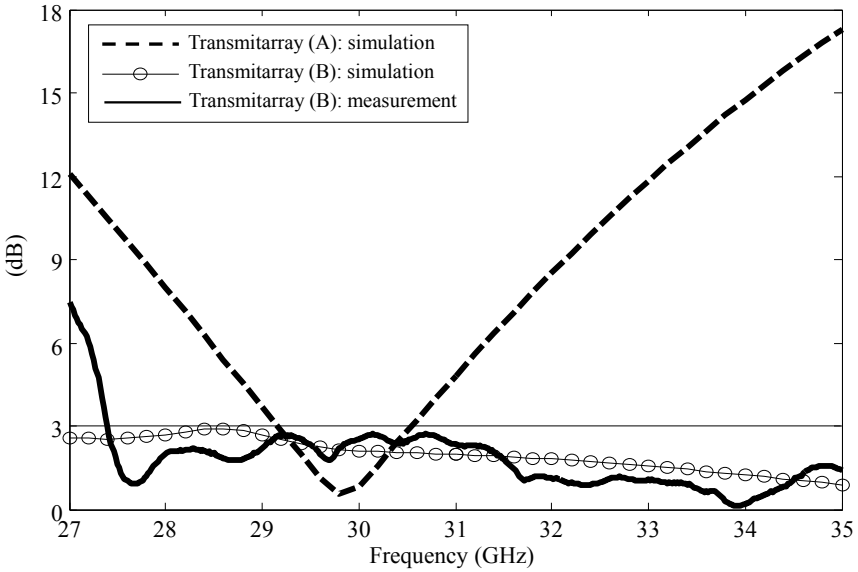

Figure 2.24: Broadside axial ratio for the transmitarray without rotations (A; Fig. 2.16a) and for the transmitarray with sequential rotations (B; Fig. 2.16h). The unit cell embedded patterns have been calculated with the two setups of Fig. 2.19 for the two transmitarrays, respectively.

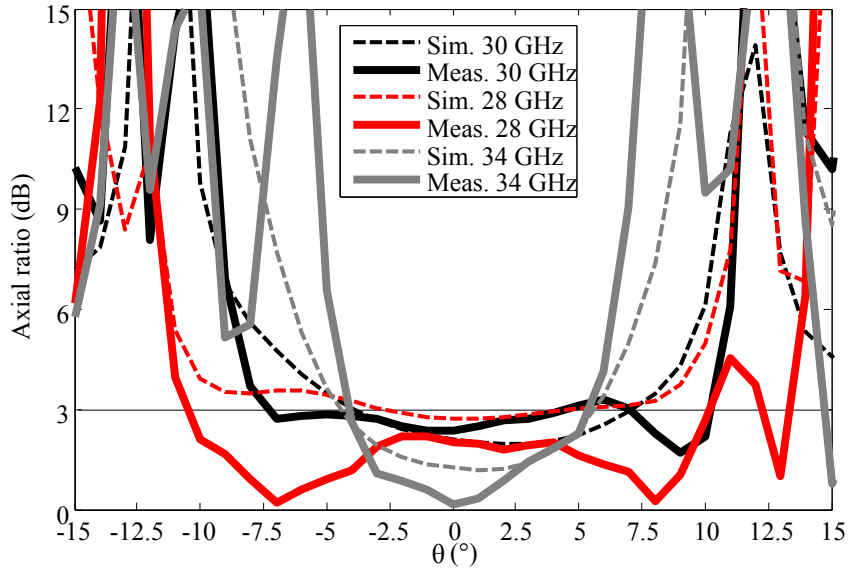

Figure 2.25: Simulated and measured axial ratio for the transmitarray with rotations (B; Fig. 2.16h) in the main beam region (15°,15°) at 28, 30 and 32 GHz.

Table 2.6: Power budget and radiation characteristics at 30 GHz for the realized prototype with sequential rotation (h) of Fig. 2.16.

	Simulation	Measurement
Focal source gain at broadside	11.7 dBi	11.7 dBi
Broadside directivity (RHCP)	24.8 dBi	-
Spillover loss	1.4 dB	-
Broadside gain (RHCP)	23.2 dBi	22.8 dBi
Power efficiency	69.5%	63.1%
Broadside XPD	17.0 dB	17.2 dB
Max SLL ($\phi = 0°$)	-17.9	-16.9
Max SLL ($\phi = 45°$)	-16.5	-17.0
Max SLL ($\phi = 90°$)	-18.3	-17.3

whole transmitarray has been performed using Ansys HFSS with the hybrid integral solver [80]. The obtained radiation patterns at 30 GHz are shown in Figs. 2.26, 2.27, for the co- and cross-polarization components (solid lines). The patterns at 29, 31 and 32 GHz are shown in Figs. 2.28, 2.29 and 2.30, respectively. These results confirm the electromagnetic performance predicted with the hybrid model and provide a better agreement with the measurements at angles beyond 45° from broadside. Even if they better fit the measurements, it is worth to notice that including the full-wavee simulations of the full array in the design process is actually difficult in terms of simulation time and becomes impossible for larger arrays.

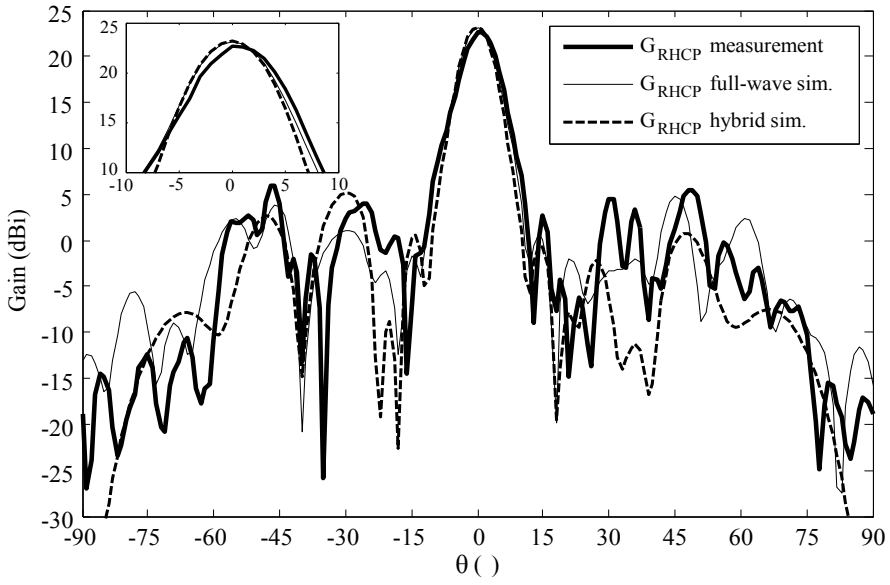

(a)

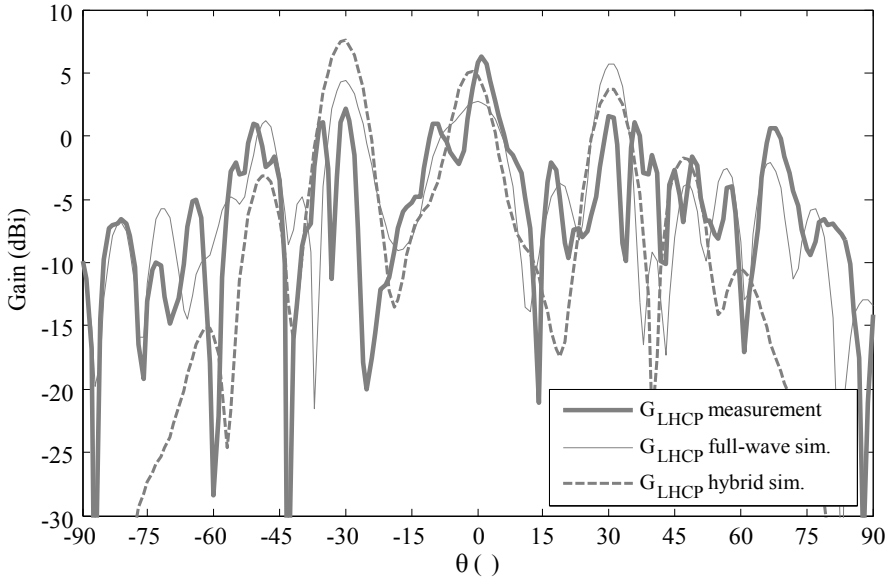

(b)

Figure 2.26: Simulated and measured radiation patterns (co-polar and cross-polar components in circular polarization) in the horizontal plane at 30 GHz.

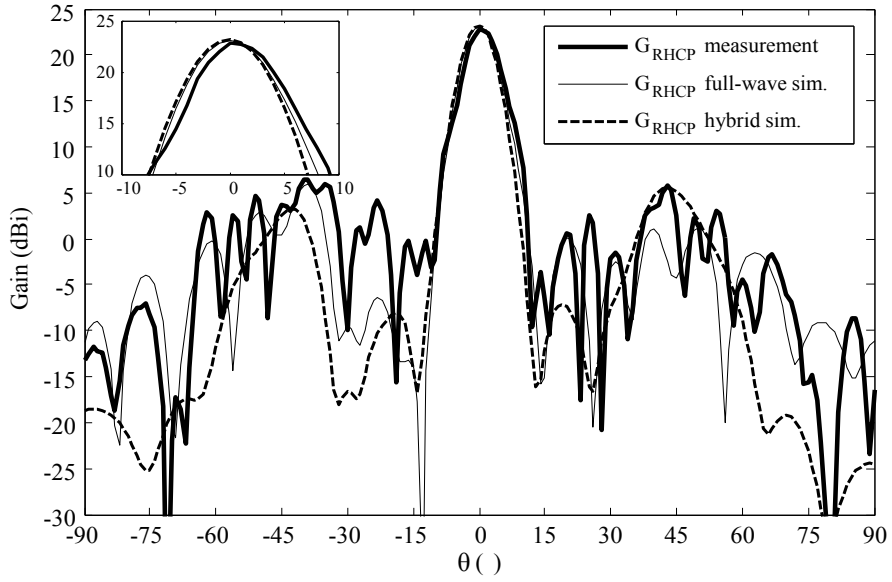

(a)

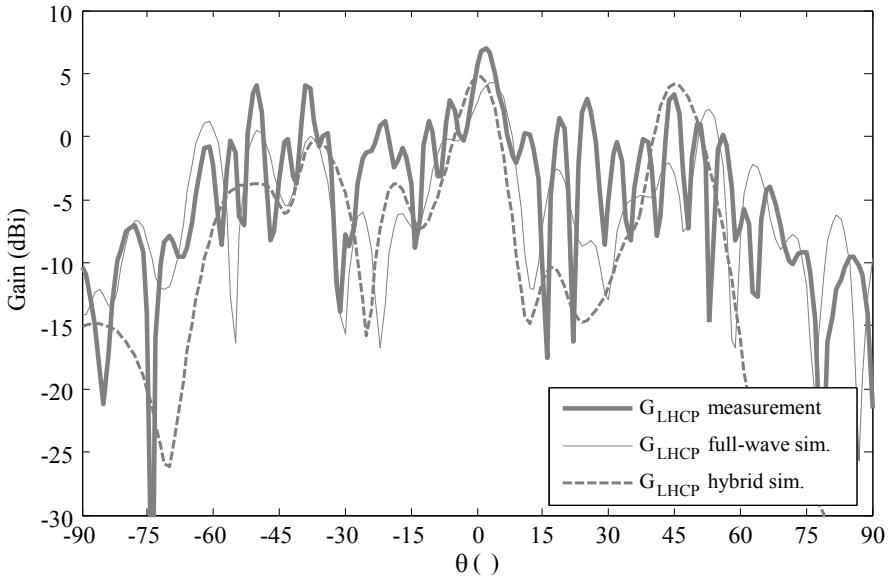

(b)

Figure 2.27: Simulated and measured radiation patterns (co-polar and cross-polar components in circular polarization) in the diagonal plane at 30 GHz.

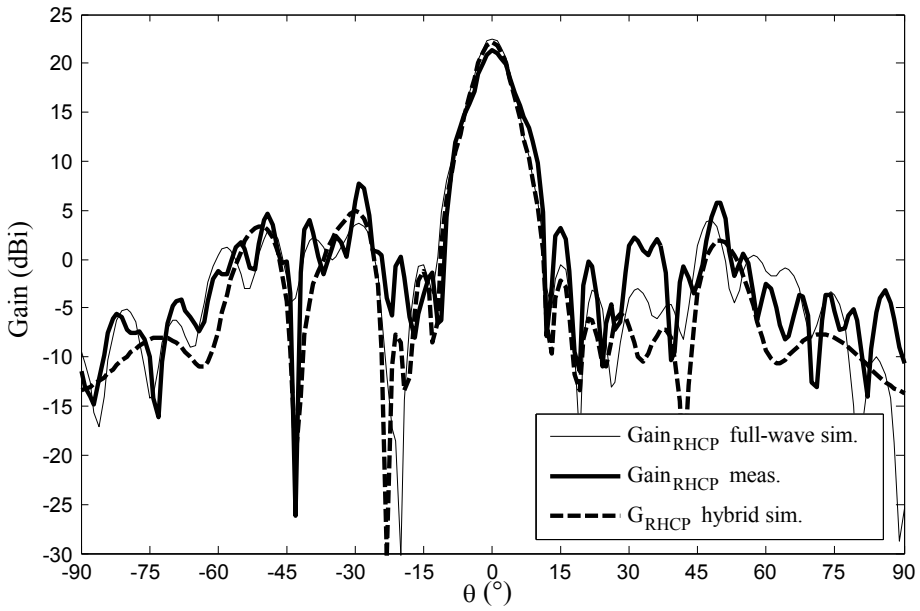

(a)

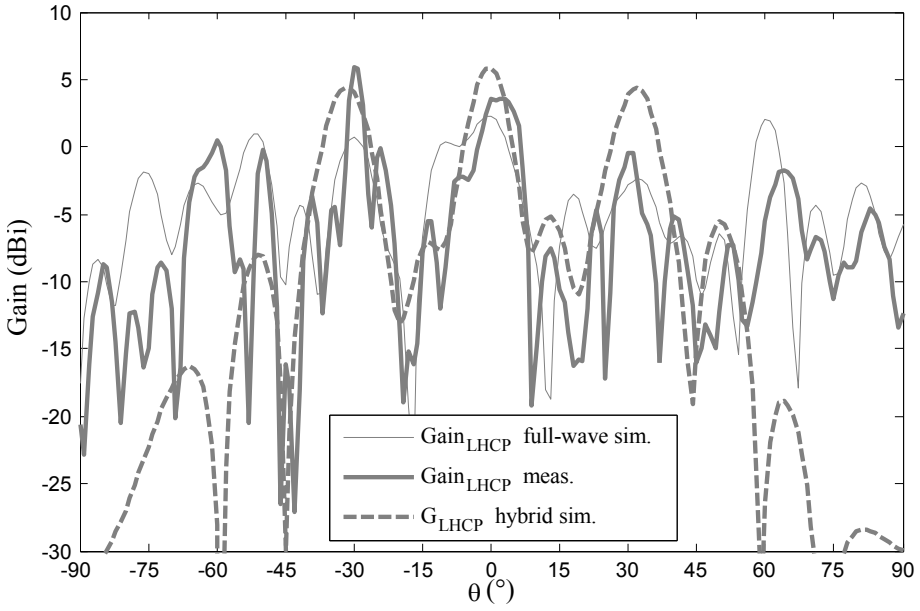

(b)

Figure 2.28: Simulated and measured radiation patterns (co-polar and cross-polar components in circular polarization) in the horizontal plane at 29 GHz.

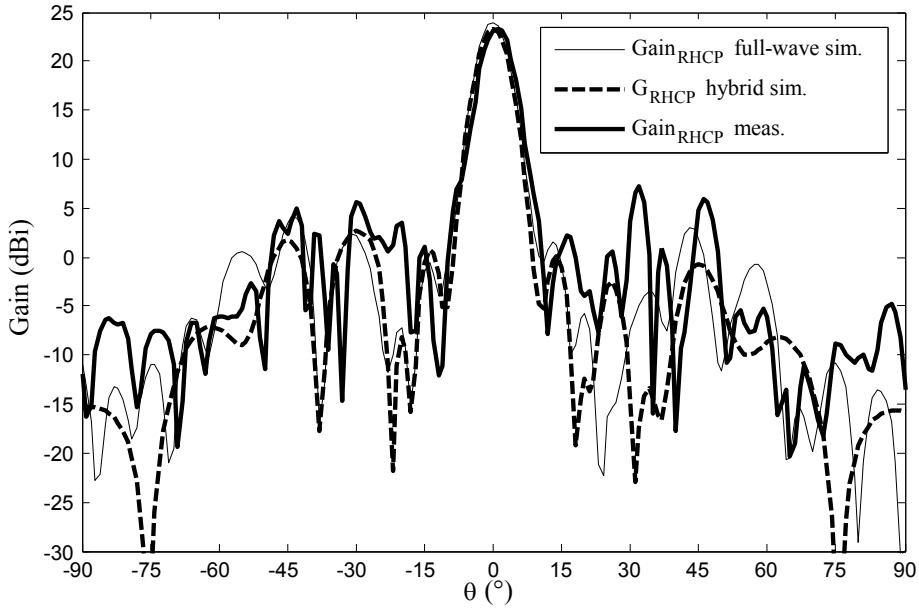

(a)

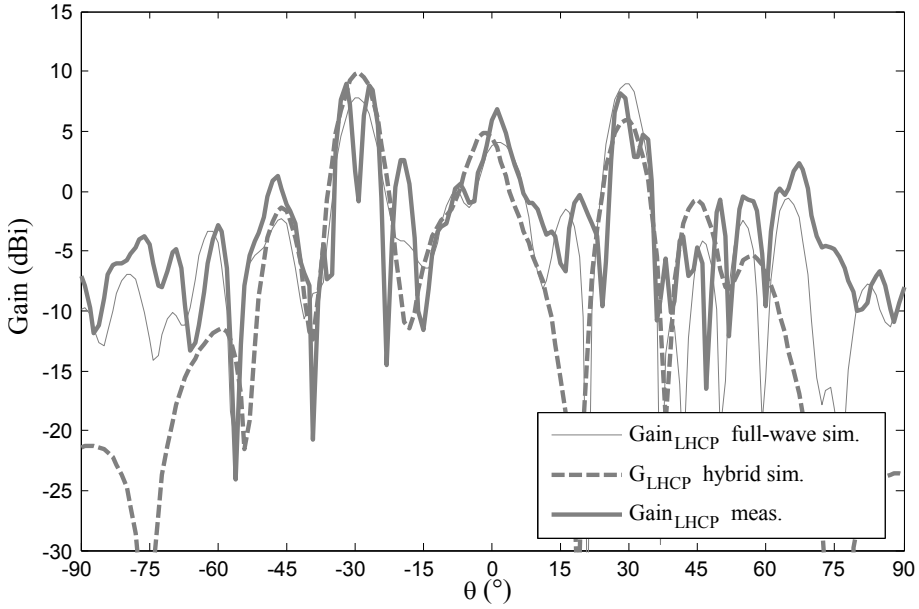

(b)

Figure 2.29: Simulated and measured radiation patterns (co-polar and cross-polar components in circular polarization) in the horizontal plane at 31 GHz.

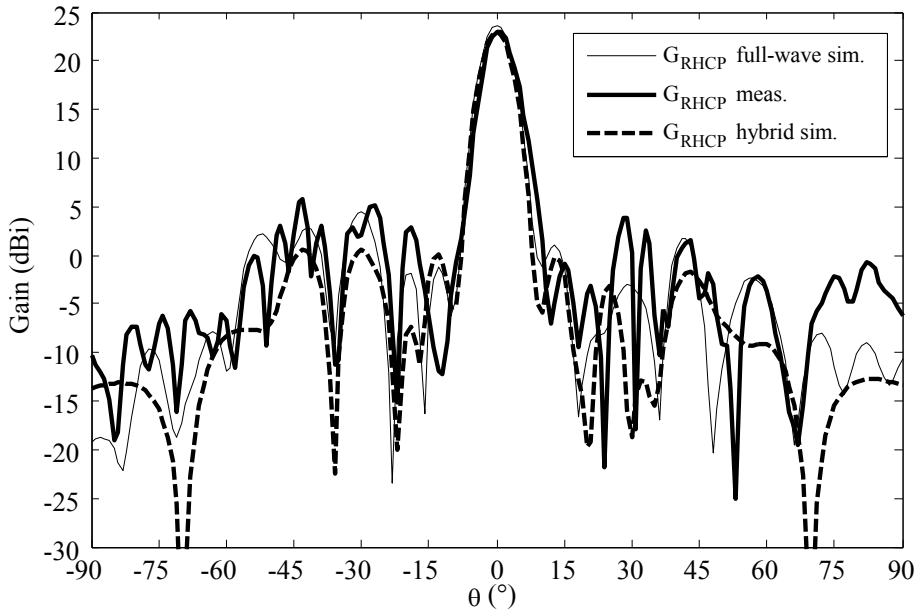

(a)

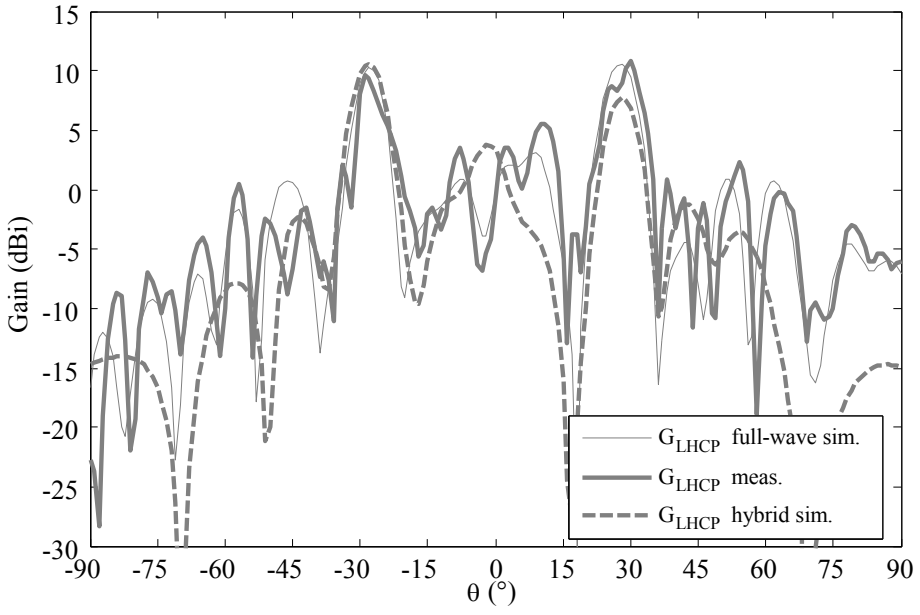

(b)

Figure 2.30: Simulated and measured radiation patterns (co-polar and cross-polar components in circular polarization) in the horizontal plane at 32 GHz.

2.7 Conclusions

In this chapter, the design, modelling and characterization of circularly-polarized transmitarrays with sequential rotations in Ka-band are presented. The sequential rotation technique is investigated and applied to transmitarray antennas. Several rotation angles in different schemes have been considered and subarrays of four elements ($T = 4$) demonstrated a dramatic improvement of the circular polarization generated by the array. In order to validate the numerical results, a passive prototype has been designed.

The unit-cell is formed by a linearly-polarized rectangular patch connected to a CP square patch with truncated corners. Full-wave simulations with Floquet port excitation showed an insertion loss of 0.2 dB at 30 GHz and a 1-dB transmission bandwidth of 10%. A phase resolution of 1 bit is achieved by rotating the linearly-polarized patch in the receiving layer by 180°.

A 400-elements transmitarray with 2×2 rotated sub-arrays based on the proposed unit-cell has been designed. An accurate simulation model which takes into account the mutual couplings between the rotated patch antennas has been presented. With this method, the isolated unit cell is simulated with periodic boundary conditions in order to calculate its scattering parameters. Then, sub-arrays of 4×4 unit-cells are considered for the embedded pattern calculations taking into account the effects of the rotations in the inter-element mutual coupling estimation. This configuration has been compared with the non-rotated version and a significant improvement in the broadside axial ratio performance has been demonstrated.

The realized prototype has a broadside RHCP gain of 22.8 dBi at 30 GHz with an axial ratio lower than 3 dB between 27.4 and 35 GHz (24.4%). A good agreement with the numerical results has been demonstrated. Finally, full-wave simulations of the full transmitarray successfully validated the measurements and the hybrid simulation results. The small discrepancies found in the radiation patterns calculated with the hybrid tool mainly outside the main beam region are attributed to spillover radiation. A possible improvement of the method of analysis proposed here is considering the spillover radiation in the pattern calculation.

Chapter 3

Reconfigurable unit-cell in Ka-band

In this chapter, the design of a reconfigurable unit-cell in Ka-band working in linear polarization is presented with the objective of a full transmitarray realization. The 1-bit phase resolution is achieved by integrating two p-i-n diodes in the design. It is inspired from the design developed in [39] in X-band. Among the addressed challenges, there are the high-frequency characterization of the p-i-n diodes, their modelling and integration on the PCB structure, and the design of the bias network with up to ten bias lines in close vicinity of the radiating elements. A sensitivity analysis is also carried out with full-wave simulations. The experimental setup used for the characterization is presented and measurements results are discussed.

3.1 P-i-n diode characterization

P-i-n diodes (MA4AGP907 from M/ACOM [83]) have been selected as active devices for their low insertion losses and small size (see Fig. 3.1). Two-port measurements of their scattering parameters on a coplanar transmission line fabricated on a FR4 substrate have been performed up to 35 GHz with the SOLT (Short-Open-Load-Through) calibration kit Picoprobe CS-9, manufactured by GGB Industries [84] in order to extract their equivalent lumped-element models. The coplanar line dimensions are selected in order to accommodate the diodes and use microwave probes with ground-signal-ground configuration and 350 μm of pitch. The measurement setup used is shown in Fig. 3.2. The measured scattering parameters are reported in Fig. 3.3. In the forward (I_{bias} = 10 mA) and reverse (V_{bias} = 1.2 V) states, the device is modelled with the circuits shown in Fig. 3.4. A series L-R circuit (R_{ON} = 4.2 Ω, L_{ON} = 0.05 nH) and a shunt R-C circuit (R_{OFF} = 300 kΩ, C_{OFF} = 42 fF)

are used for the two states, respectively. These values have been found by de-embedding the coplanar test structure shown in Fig. 3.2. In particular, this setup has been studied with full-wave simulations with proper excitation and the diode has been replaced by the equivalent circuits for the two states.

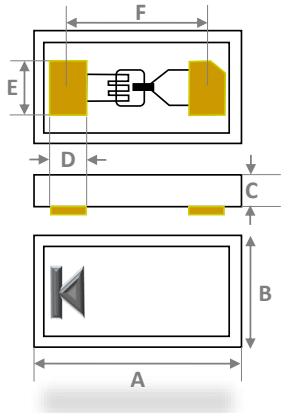

	Min.	Max.
A	0.6604	0.6858
B	0.3429	0.3683
C	0.1651	0.1905
D	0.1092	0.1346
E	0.1727	0.1854
F	0.4623	0.4877

Figure 3.1: Scheme and geometrical dimensions (in millimetres) of the p-i-n diode Flip-chip packaging MA4AGP907 manufactured by M/ACOM technologies [83].

The experimental value of R_{ON}, which mainly determines the insertion losses, corresponds to the specification of the manufacturer [83]. The other parameters differ from these specifications, due to different characterization conditions, but are in line with the results obtained earlier at lower frequencies [39]. The agreement in magnitude and phase for both the forward and reverse states is good (Fig. 3.3).

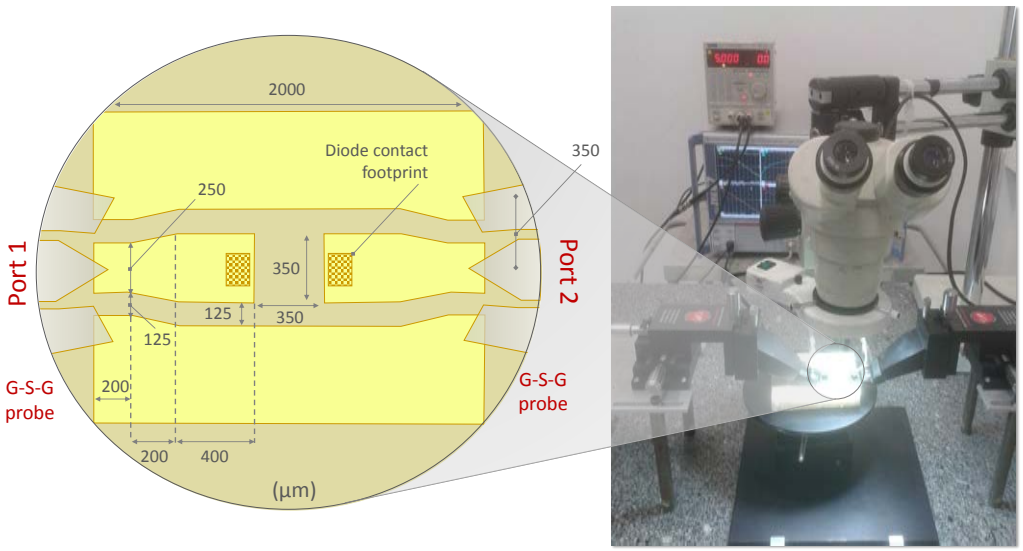

Figure 3.2: Photograph of the setup used for the characterization of the p-i-n diode. It includes: a diode mounted on a coplanar line, two microwave probes (GSG configuration with 350 μm of pitch), a VNA and a DC power supply.

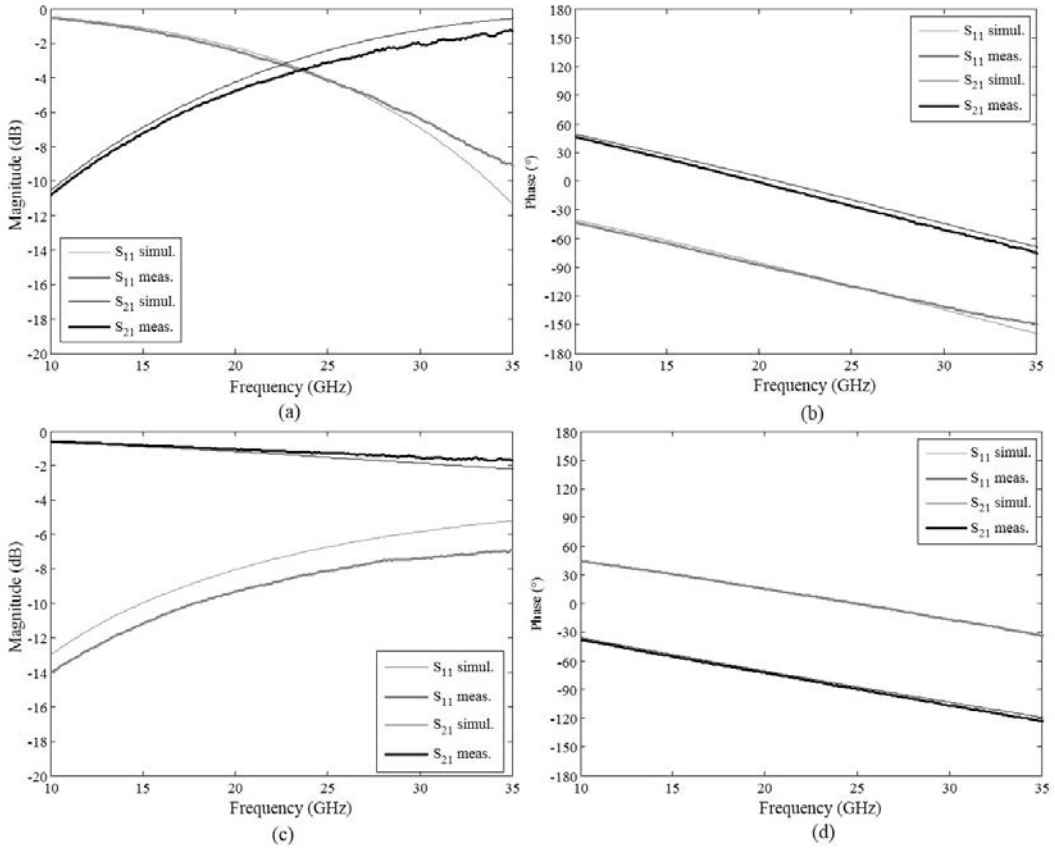

Figure 3.3: Simulated and measured scattering parameters (magnitudes (a, c) and phases (b, d)) of the p-i-n diode in the reverse (a, b) and forward (c, d) states.

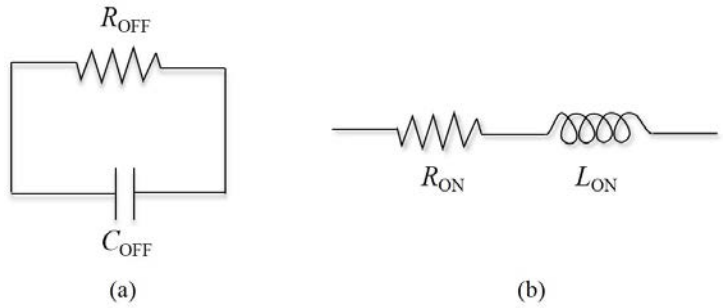

Figure 3.4: Equivalent circuit model for a p-i-n diode in the reverse (a) and forward (b) states. $R_{ON} = 4.2\ \Omega$, $L_{ON} = 0.05$ nH, $R_{OFF} = 300$ kΩ, $C_{OFF} = 42$ fF.

The measured insertion losses are between 1.0 and 2.0 dB in the frequency range of 25.0-35.0 GHz. It is worth to notice that these losses are partly due to the setup considered for the characterization which includes several tapered transitions in coplanar technology on a FR4 substrate. In addition, the characteristic impedance of these sections is not 50 Ohms and then additional losses due to the impedance mismatch with the microwave probes calibrated on 50 Ohms should be considered. For this reason, a simulation in which all the coplanar setup with 50-Ohms lumped-port excitation has been considered. Poor isolation is also observed in the same frequency range. This aspect will be taken into account in the unit-cell design and a phase shifting method independent from the active device isolation will be presented in the next sections.

3.2 Unit-cell design

The proposed unit-cell, whose dimensions are 5.1×5.1 mm^2 (i.e. half-wavelength in free-space at 29.4 GHz), consists of four metal layers (Fig. 3.5), two identical substrates of Rogers Duroid RT6002 ($h_s = 508$ μm, $\epsilon_r = 2.94$, tan$\delta = 0.0012$) [78] and one bonding film of Arlon CuClad 6700 ($h_f = 114$ μm, $\epsilon_r = 2.35$, tan$\delta = 0.0025$) [79]. The receiving layer (Fig. 3.5(b)) is composed of a rectangular patch loaded by a U-shaped slot, while the transmitting layer (Fig. 3.5(d)) contains a rectangular patch loaded by an O-shaped slot and the two p-i-n diodes.

In the EM simulator, these active devices are modelled as a Gallium-Arsenide block (ϵ_r = 12.9, $0.686 \times 0.368 \times 0.19\,\text{mm}^3$) and a lumped-element equivalent circuit extracted from the measurements presented in the previous section. This active patch is connected to the passive one with a metallized via hole ($d_V = 200$ μm) placed at the center of the unit-cell. A ground plane occupies one of the two intermediate layers. The other inner layer, shown in Fig. 3.5(c), contains the biasing lines. All geometrical dimensions are defined in Fig. 3.5 and reported in Table 3.1.

3.2.1 Bias network

In the proposed unit-cell structure, one p-i-n diode is biased in the forward state with a 10-mA current. The 1.2-V threshold voltage of this diode is sufficient to maintain the other diode, mounted in anti-parallel configuration, in its reverse state. Thus, only one bias line is necessary for each unit-cell, facilitating thereby the layout and routing of the bias network in very large array configurations [73]. The bias line is 100-μm wide and is connected to the active patch by using two symmetric metallic via connections (d_B = 150 μm). Since d_B is significantly large compared to the edges ($(W_l - W_{g1})/2 = 0.51$ mm, Fig. 3.5) of the transmitting patch and cannot be reduced to lower values when using

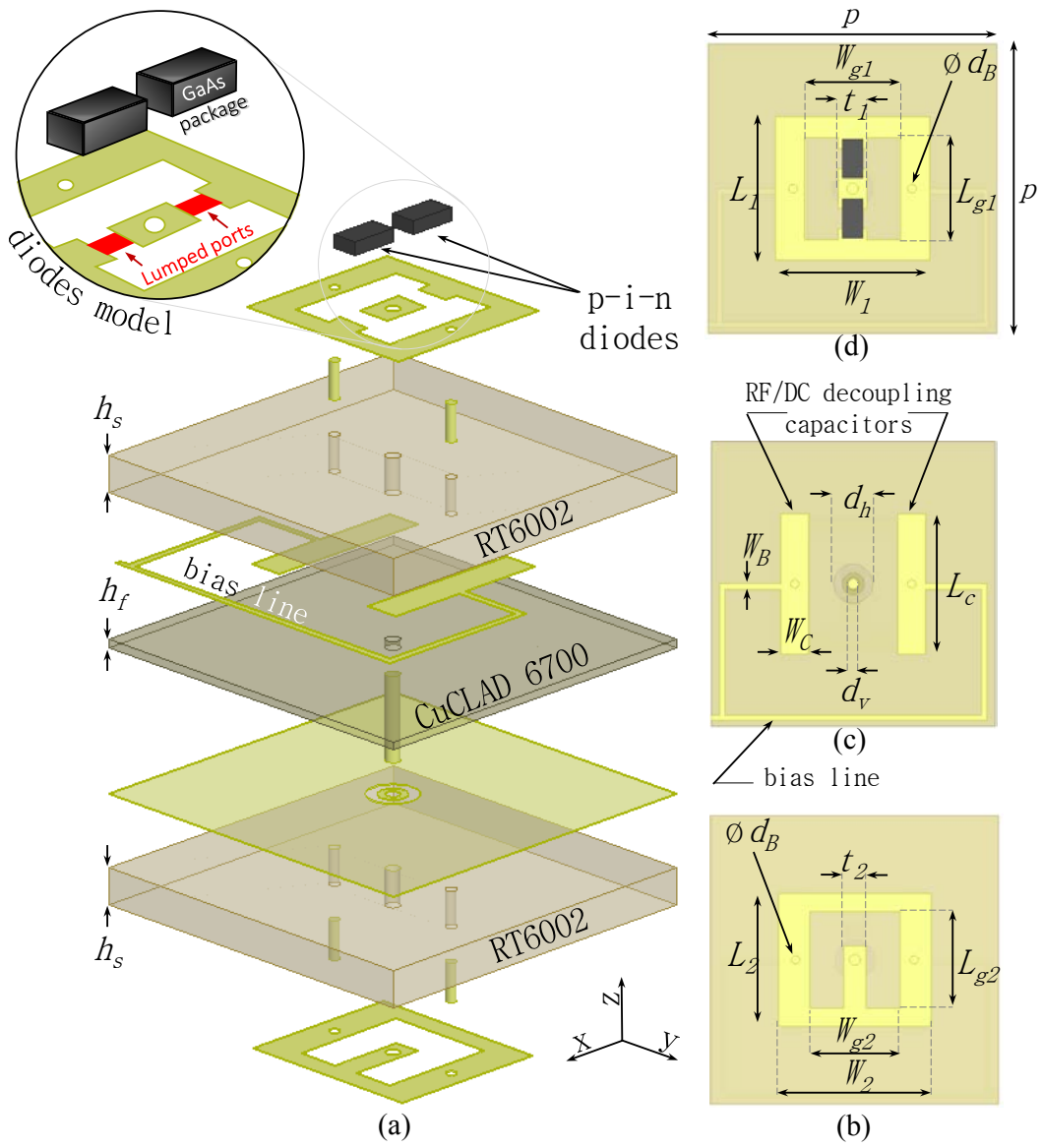

Figure 3.5: Scheme of the unit-cell architecture. Exploded view (a), receiving layer (b), biasing layer (c) and transmitting layer (d). Details of the model used for the diodes in the full wave simulations are given in the circular inset.

Table 3.1: Unit-cell geometrical dimensions of Fig. 3.5 in millimetres.

	value		value		value
p	5.1	L_C	2.5	L_2	2.33
L_1	2.52	W_C	0.5	W_2	2.7
W_1	2.72	d_V	0.2	L_g2	1.8
L_{g1}	1.8	d_h	0.7	W_{g2}	1.6
W_{g1}	1.7	d_B	0.15	t_2	0.4
t_1	0.5	W_B	0.1	h_s	0.508
				h_f	0.114

standard manufacturing techniques, the currents on the patch can be perturbed by these vias; therefore a RF/DC decoupling circuit must be designed in order to avoid a significant part of the RF signal leaking through the bias lines.

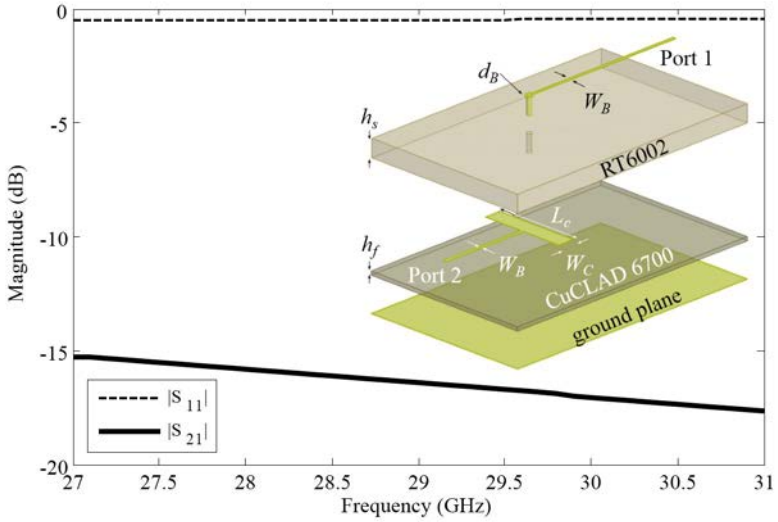

Figure 3.6: Scattering parameters simulated for the RF/DC decoupling circuit formed by a distributed capacitor of area 2.5×0.5 mm^2. Inset: 3D sketch of the simulation setup.

Different solutions have been considered, such as radial stubs, meander lines, resistive films and capacitive loads to filter out the RF signals from the bias lines. The first two solutions have demonstrated poor isolations (i.e. pronounced RF currents on the bias lines) because of the limited available space. The use of films with resistivity of 25/50/100 Ω/sq. has shown very good results in terms of isolation at the cost of higher transmission losses (1.3/0.7/0.5 dB of additional losses) of the unit-cell. Finally, a distributed capacitor of 2.5×0.5 mm^2 area, which corresponds to 0.68 pF, has been selected (Fig. 3.5c). The optimization has been carried out with full-wave simulations in Ansys HFSS v.15 [80]. The considered setup, shown in the inset of Fig. 3.6, includes the shunt capacitor connected with

a transmission line composed of the bias line, a metallized via (diameter d_B) and a microstrip line of width W_B on the top layer. Two waveguide ports feed the transmission lines. The simulated return loss is lower than 0.5 dB, and the isolation between both ports is better than 15 dB between 27.0 and 31.0 GHz (Fig. 3.6). Finally, the full unit-cell, with two symmetric bias lines and capacitive loads, was simulated, and the minor impact of the bias lines on its electromagnetic performances was confirmed.

3.2.2 Numerical results

Scattering parameters

The unit-cell has been simulated using the commercial software Ansys HFSS v.15 [80] with periodic boundary conditions and Floquet port excitations to take into account the mutual couplings with the surrounding unit-cells. The full-wave simulations under normal incidence give the scattering parameters calculated for the two phase states (Fig. 3.7).

The reflection coefficient S_{11} from the diode-loaded patch side (port 1) is lower than -10 dB between 27.7 GHz and 29.8 GHz for the 0°-state and between 27.5 GHz and 30.1 GHz for the 180°-state. The -10 dB matching bandwidth from the other port (port 2, S_{22}) spans between 27.9 GHz and 29.5 GHz for the 0°-state and between 27.7 GHz and 29.7 GHz for the 180°-state. The minimum insertion loss is only 0.9 dB at 29 GHz with a 3-dB transmission bandwidth of 27.5-30.8 GHz for the 0°-state and 27.2-31.3 GHz in the 180°-state. The phase difference between the two states is around 180° with a maximum error of 13°, as shown in Fig. 3.7(c). This error is mainly due to the non-symmetrical geometry of the passive patch and the relative positions of the two patch antennas. This is also confirmed by the reflection coefficients (Fig. 3.7) which are different from the two receiving and transmitting sides.

Despite the poor isolation of the p-i-n diodes used in the design, the phase shifting function is obtained. This is due to the specific accommodation of these devices on the patch antenna. In fact, the structure can be seen as an antenna charged with two different circuits, one inductive (for the ON state) and one capacitive (for the OFF state), placed symmetrically along its axis in the E-plane. Switching the two states is equivalent to mirroring the loads and the whole patch antenna producing a 180° constant and broadband phase shift. For this reason, the proposed approach could enable simple and effective unit-cell design even at higher frequencies.

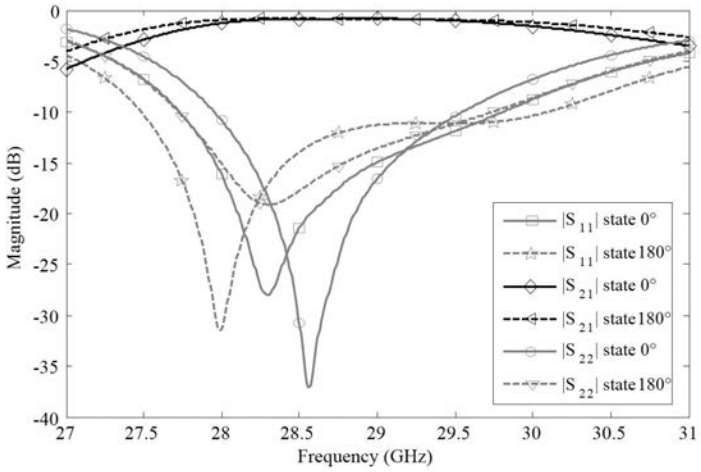

(a)

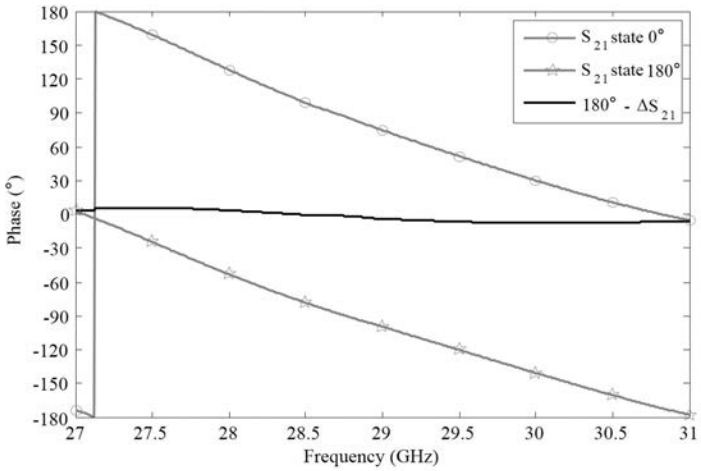

(b)

Figure 3.7: Scattering parameters (magnitude (a) and phases (b)) of the unit-cell simulated with periodic boundary conditions and Floquet port excitation.

Radiation Patterns

The simulation setup of Fig. 3.8 is considered for the radiation pattern calculation. It is different from the one proposed in Chapter 2 based on a half-cell excited with a lumped port. In fact, it includes the whole unit-cell structure, excited with a Floquet port on one side and terminated on a radiation boundary on the opposite side. In this way, all the losses can be taken into account when evaluating the realized gain of the unit-cell.

The simulated radiation patterns of the active layer patch antenna are shown at 29.2 GHz in H-plane in Fig. 3.9(a) for the 0°/180° states. The realized gain at broadside reaches 4.0 dBi and the 3-dB beam-width is 86°. As shown in Fig. 3.9(b), the broadside co-polarized realized gain (along x) is between 1.9 and 4.1 dBi between 27.5 and 31 GHz. The cross polarization discrimination is greater than 40 dB within this bandwidth.

The passive layer patch antenna exhibits a realized gain at broadside of 4.1 dBi and it

is higher than 1.6 dBi between 27.5 and 31 GHz, as shown in Fig. 3.10(a). The cross polarization discrimination is higher than 50.0 dBi. The 3-dB beam-width is 86° (Fig. 3.10(b)). The slight difference between the two radiation characteristics are due to the asymmetries which characterize this architecture, as already discussed for the scattering parameters.

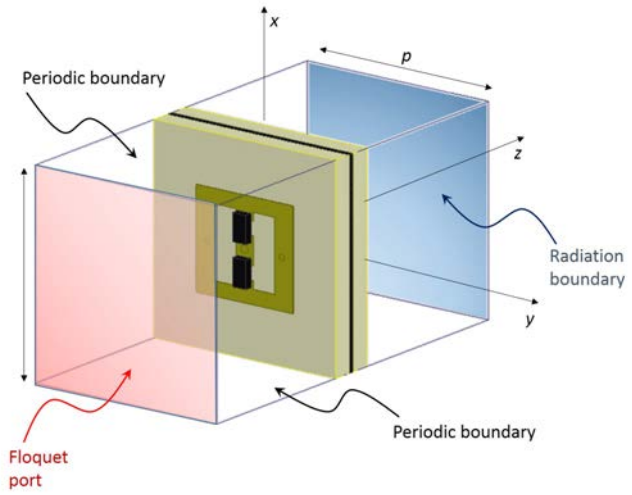

Figure 3.8: 3D sketch of the simulation setup used for the radiation pattern calculation. A Floquet port is placed in front of the active patch antenna side. A radiation boundary is placed in front of the active patch side. For the calculation of the radiation pattern from the opposite side these two conditions are inverted.

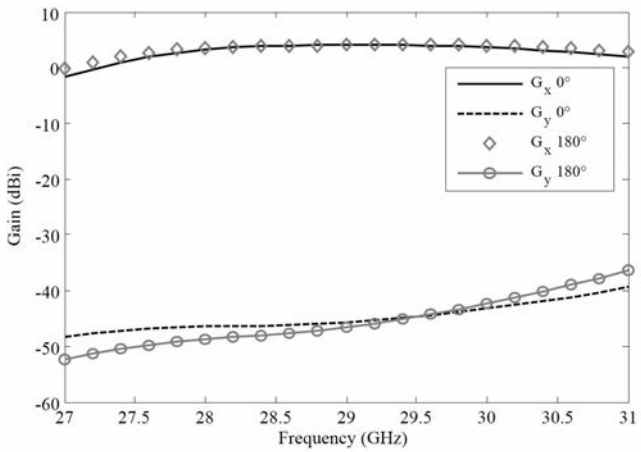

(a)

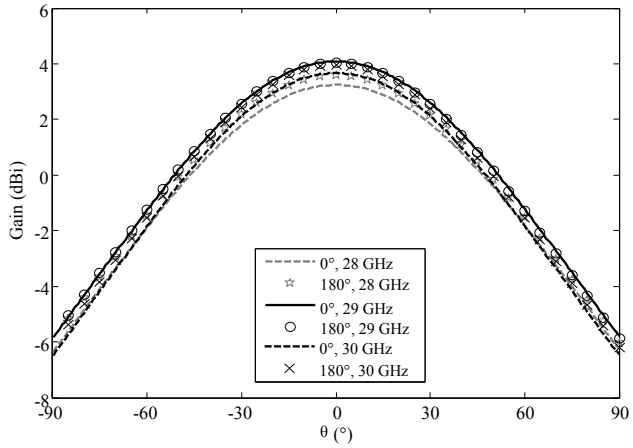

(b)

Figure 3.9: Broadside realized gain (a) and radiation pattern at 28.0, 29.0 and 30.0 GHz (b) in the H-plane of the unit-cell active layer. A Floquet port is placed in front of the passive patch antenna side. A radiation boundary is placed in front of the active patch side.

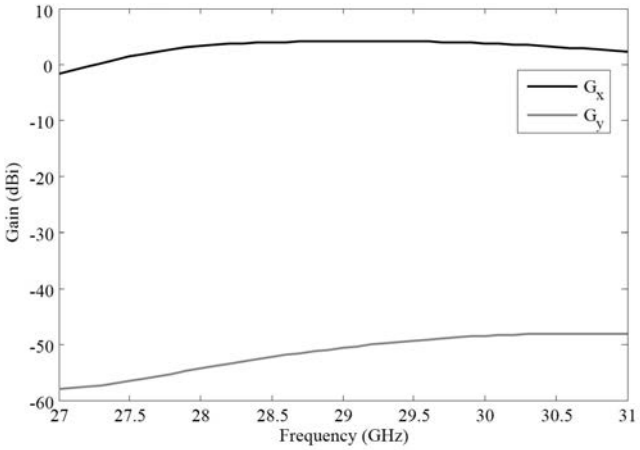

(a)

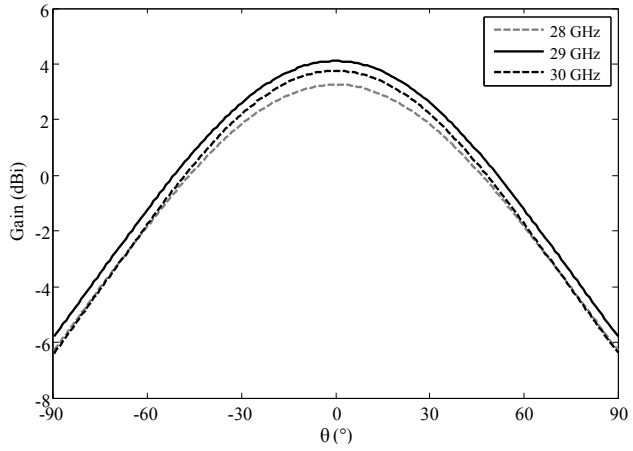

(b)

Figure 3.10: Broadside realized gain (a) and radiation pattern at 28.0, 29.0 and 30.0 GHz (b) in the H-plane of the unit-cell passive layer. A Floquet port is placed in front of the active patch antenna side. A radiation boundary is placed in front of the passive patch side.

3.2.3 Oblique incidence

The effect of an oblique incidence is investigated with a proper set of full-wave simulations with periodic boundary conditions. In particular, the Floquet port excitation is maintained on the surfaces in front of and behind the unit-cell and the master/slave periodic conditions have been defined for each incidence angle. In this way, the correct Floquet modes are excited in the structure. Only the unit-cell in the 0° state is considered in this study. Similar considerations are valid for the other phase state. With angles between 10° and 40° in the E-plane, the simulated reflection and transmission coefficients are shown in Fig. 3.11. The reflection coefficient (Fig. 3.11(a)) from the port 1 (active patch) is under -10 dB within the nominal bandwidth for all the incidence angles. This bandwidth is extended by about 900 MHz towards lower frequencies for an incidence of 40°. Similar considerations are valid for the reflection coefficient on the opposite side (Fig. 3.11(c)). The minimum insertion loss (Fig. 3.11(b)) increases with the angle of incidence but it is always lower than 1.2 dB within the nominal bandwidth (27.5 - 31.0 GHz). With angles between 10° and 40° in the H-plane, the simulated reflection and transmission coefficients are shown in Fig. 3.12. The reflection coefficient (Fig. 3.12(a)) from the port 1 is under -10 dB within the nominal bandwidth for incidence angles up to 30°. This bandwidth is extended by about 900 MHz towards lower frequencies for 30° incidence. With 40° incidence, the reflection losses are higher with a minimum of 7 dB in the nominal bandwidth. Similar considerations are valid for the reflections on the opposite side (Fig. 3.11(c)). The minimum insertion loss (Fig. 3.11(b)) increases with the angle of incidence and it is lower than 1.7 dB for angles of incidence up to 30° within the nominal bandwidth. With 40°, the losses increase significantly but the 3-dB bandwidth is always larger than the nominal bandwidth.

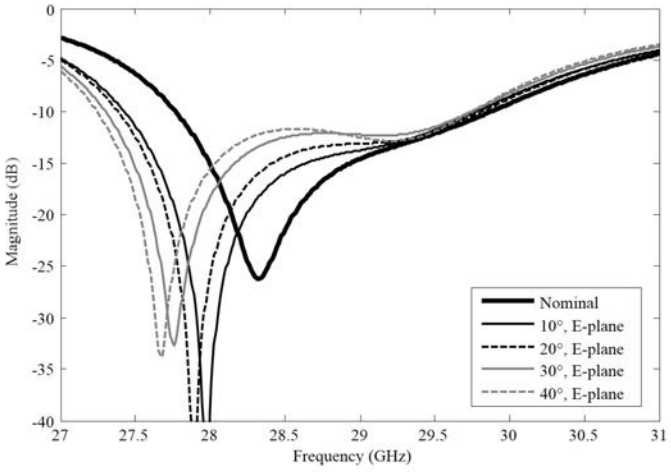

(a)

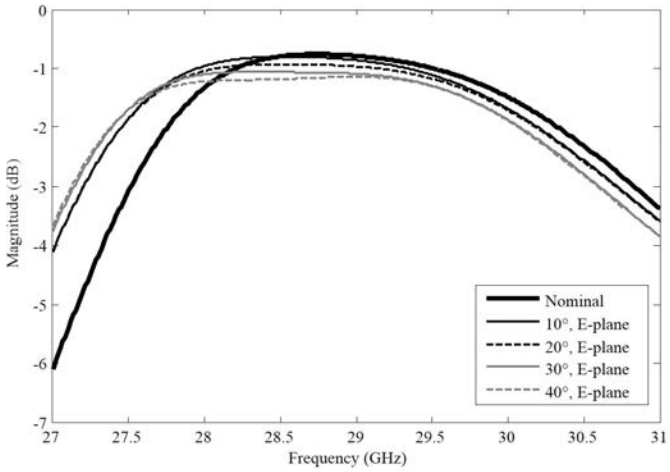

(b)

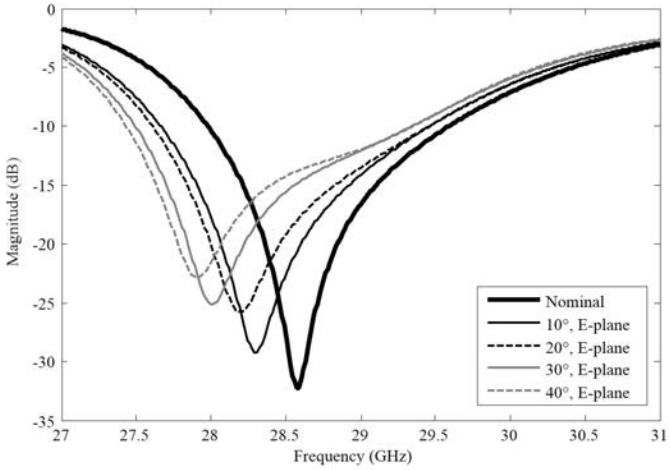

(c)

Figure 3.11: Scattering parameters simulated with different incidence angles in the E-plane: S_{11} (a), S_{21} (b), S_{22} (c).

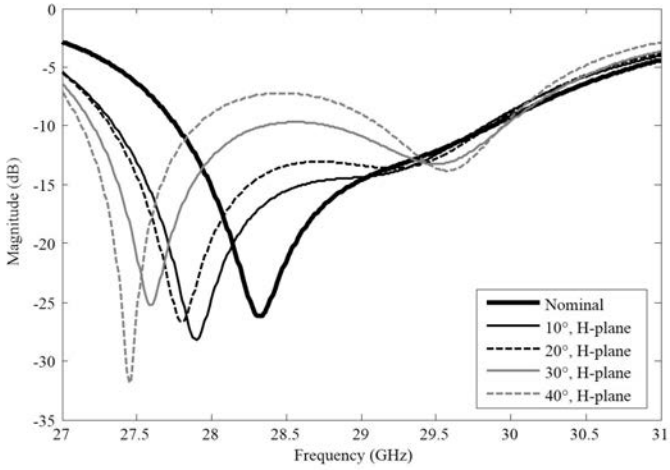

(a)

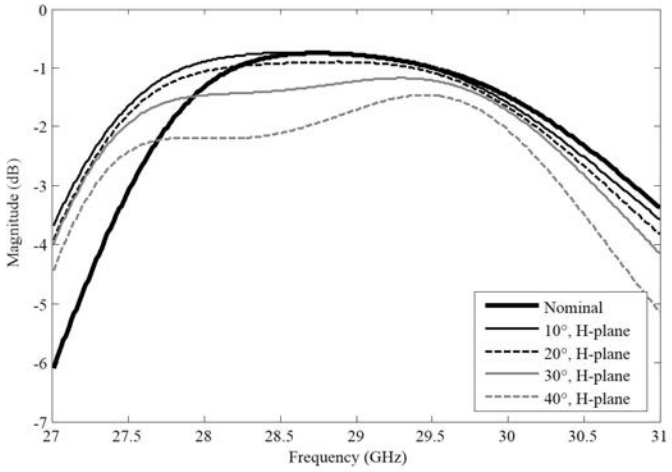

(b)

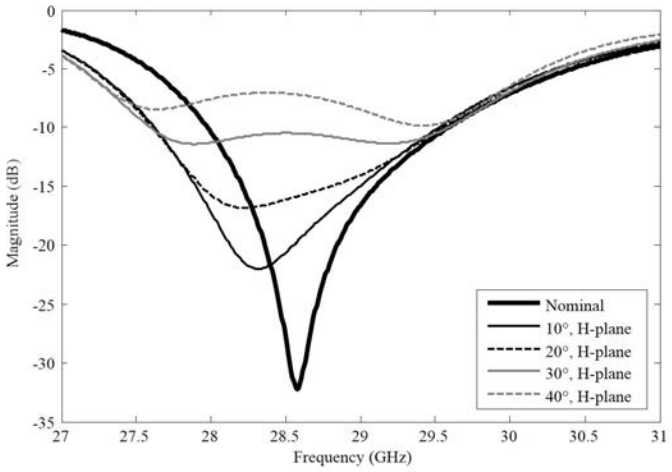

(c)

Figure 3.12: Scattering parameters simulated with different incidence angles in the H-plane: S_{11} (a), S_{21} (b), S_{22} (c).

3.2.4 Sensitivity analysis

In order to investigate the feasibility of the proposed architecture with standard PCB technologies, a sensitivity simulation study has been carried out. The parameters taken into account are the patch resonant lengths L_1 and L_2 on both layers and the diameter d_V of the metallized via. Indeed, an exhaustive parametric study, omitted here for the sake of brevity, including all the variables reported in Table 3.1 and misalignments between layers, has shown that these three parameters have the most important impact on the unit-cell scattering parameters. A variation of ± 30 μm, which is a reasonable maximum error for PCB technology, has been selected. The unit-cell in the 0°-phase state with periodic boundary conditions and normal incidence has been considered. The magnitudes of the scattering parameters are plotted in Fig. 3.13. A variation of ± 30 μm of L_1 shifts in frequency the reflection coefficients S_{11} and S_{22} by about ± 50 MHz (Fig. 3.13(a)) and ± 100 MHz (Fig. 3.13(c)), respectively.

The same variation on L_2 produces a frequency shift of ±200 MHz (Fig. 3.13(a)) on S_{11} and ±300 MHz (Fig. 3.13(c)) on S_{22}. The 10-dB return loss bandwidth is reduced by 300 MHz in the worst case ($L_1 - 30$ μm).

A maximum shift of 300 MHz (about 1%) can be observed on the 3-dB transmission band, as shown in Fig. 3.13(b). However, the obtained minimum insertion loss is similar to the nominal case (0.9 dB). A variation of -30 μm in the diameter of the metallized via (d_V), which connects the two patch antennas placed in the center of the unit-cell, produces similar effects as a +30 μm variation of L_2. In all the considered cases, the frequency behaviour of the proposed structure is preserved with minimum insertion losses and 3-dB transmission bandwidth similar to the nominal design presented in the previous section.

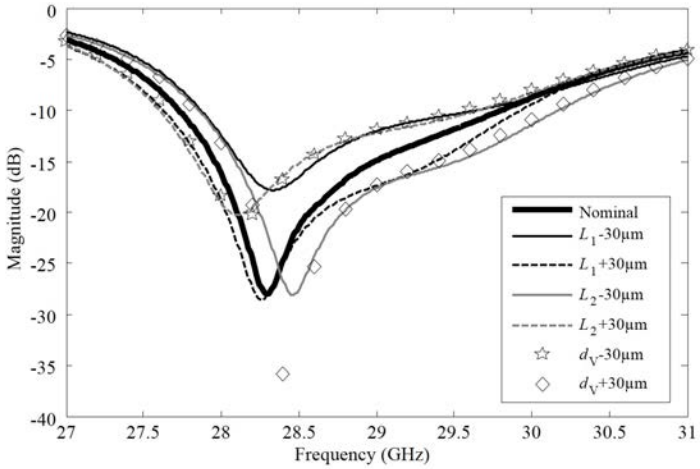

(a)

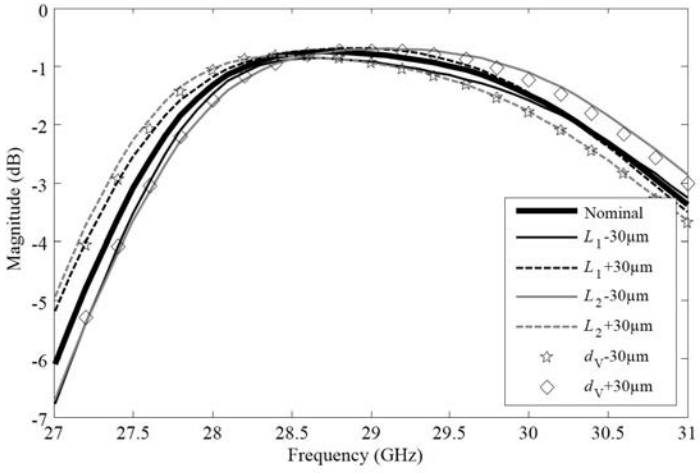

(b)

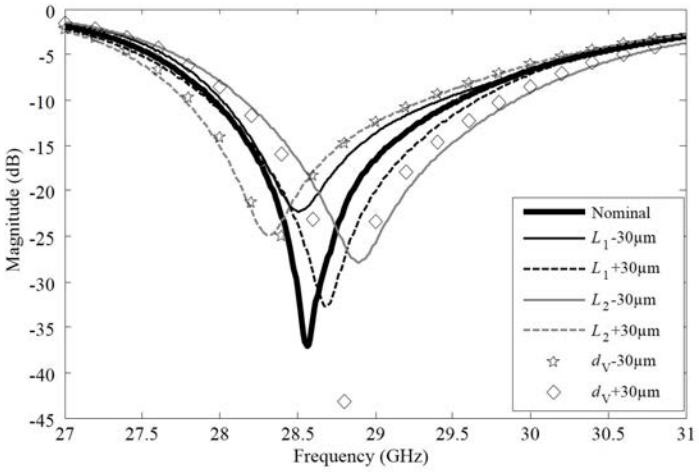

(c)

Figure 3.13: Simulated scattering parameters magnitudes (S_{11} (a), S_{21} (b), S_{22} (c)) of the unit-cell for different values of L_1, L_2 and L_3.

3.3 Characterization setup

The unit-cell has been characterized in a waveguide simulator based on standard WR-28 waveguides (7.112×3.556 mm^2). It is formed by two coax-to-WR-28 adaptors, two WR-28 straight waveguide sections and two tapered transitions between the rectangular section of the waveguides and the square section of the unit-cell; these transitions have an optimized length of 1.2 mm ($\lambda_0/8.6$) to minimize the impedance mismatch.

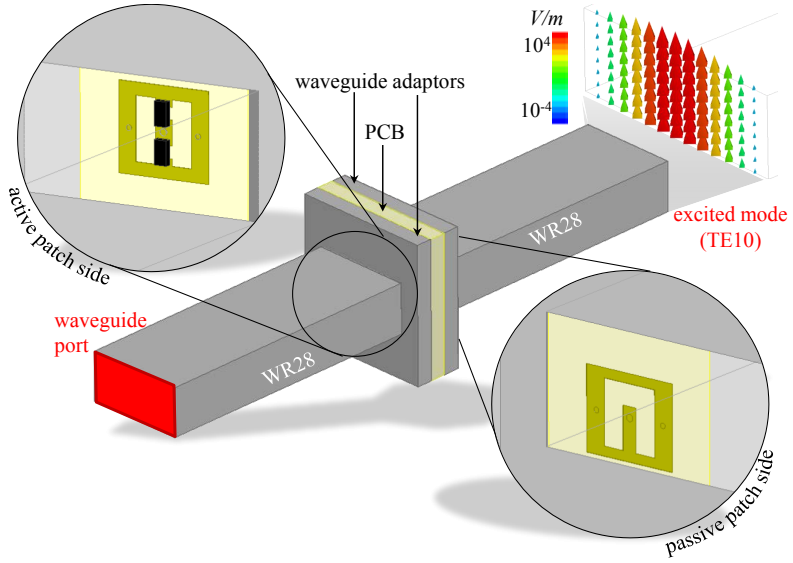

Figure 3.14: Full-wave simulation setup of the unit-cell in waveguide.

The simulated scattering parameters of the unit-cell with the setup of Fig. 3.14 are plotted in Figs. 3.15, 3.16 (dashed bold lines). As expected, there is a difference between these

results and the scattering parameters calculated with periodic boundary conditions and normal incidence (Fig. 3.7). In particular, we can observe a 500-MHz shift towards lower frequencies. This is mainly due to the oblique incidence of the waves in the waveguide simulator. The equivalent angle is given by the following equation [85]:

$$\sin(\theta) = \frac{\lambda_0}{\lambda_g} \tag{3.1}$$

where λ_0 is the free-space wavelength and λ_g is the cut-off guided wavelength. For the fundamental mode (TE10) in rectangular waveguide, it is given by

$$\lambda_g = 2a \tag{3.2}$$

where a is the waveguide larger side (a=7.112 mm for the WR-28). At 29 GHz, with the WR-28 standard rectangular waveguide, this ratio gives a value of about 45° for θ. Indeed, a simulation of the unit-cell with periodic boundary conditions and a 45° oblique incidence in E-plane (Figs. 3.15, 3.16, solid lines) leads to a very good agreement with the simulation of the actual waveguide setup. The slight difference between the curves is due to the square-to-rectangular transitions. The experimental results will be compared with these curves, where the entire waveguide environment is correctly taken into account. The reflection coefficient from the active patch (port 1) is lower than -10 dB between 27.2 GHz and 29.4 GHz for the 0°-state and between 27.0 GHz and 28 GHz for the 180°-state. The minimum insertion loss is 0.87 dB at 28 GHz and the 3-dB transmission bandwidth equals 27.0-30.5 GHz for the 0°-state and 26.8-30.7 GHz in the 180°-state. These values, summarized in Table 3.2, are similar to the nominal values given in previous sections, despite the 500 MHz frequency shift due to the waveguide environment.

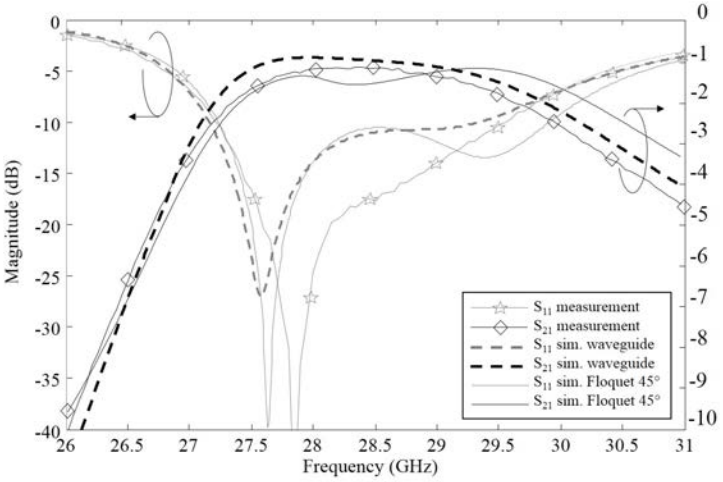

(a)

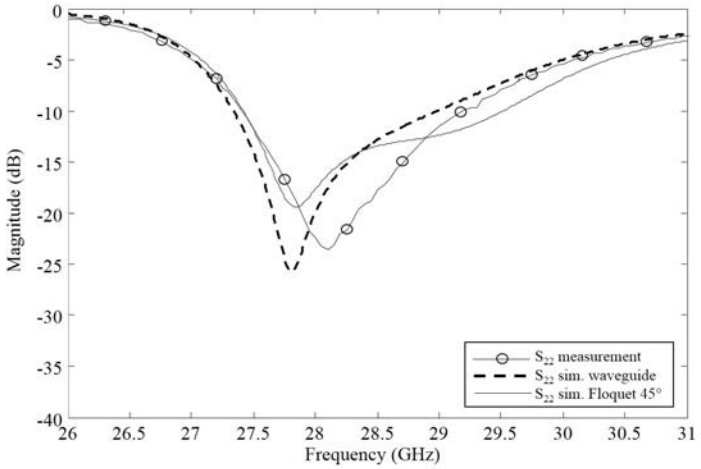

(b)

Figure 3.15: Simulated and measured scattering parameters magnitudes (0° state) in WR-28 waveguide: S_{11}, S_{21} (a) and S_{22} (b).

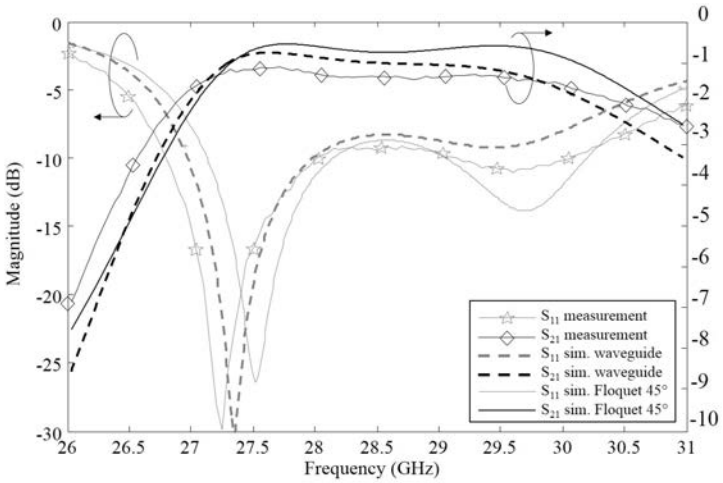

(a)

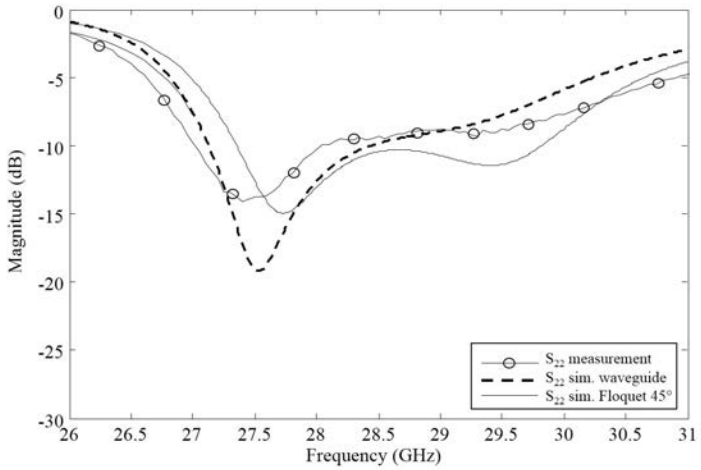

(b)

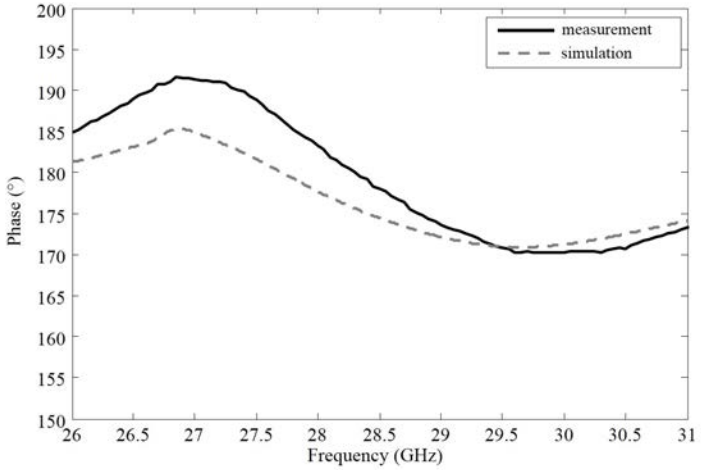

(c)

Figure 3.16: Simulated and measured scattering parameters magnitudes (180° state) in WR-28 waveguide: S_{11}, S_{21} (a) and S_{22} (b). Simulated and measured phase difference between the two states (c).

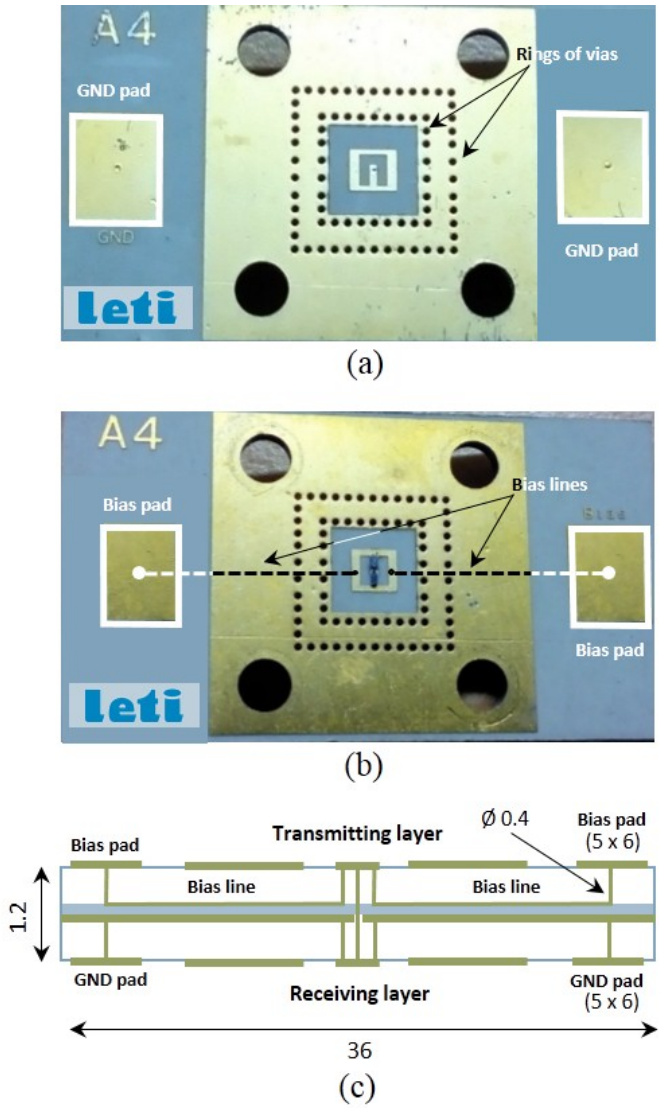

Figure 3.17: Photograph of the unit-cell prototype (receiving (a) and transmitting (b) layers) and cut-view on the horizontal axis of the structure. Dimensions are given in millimeters.

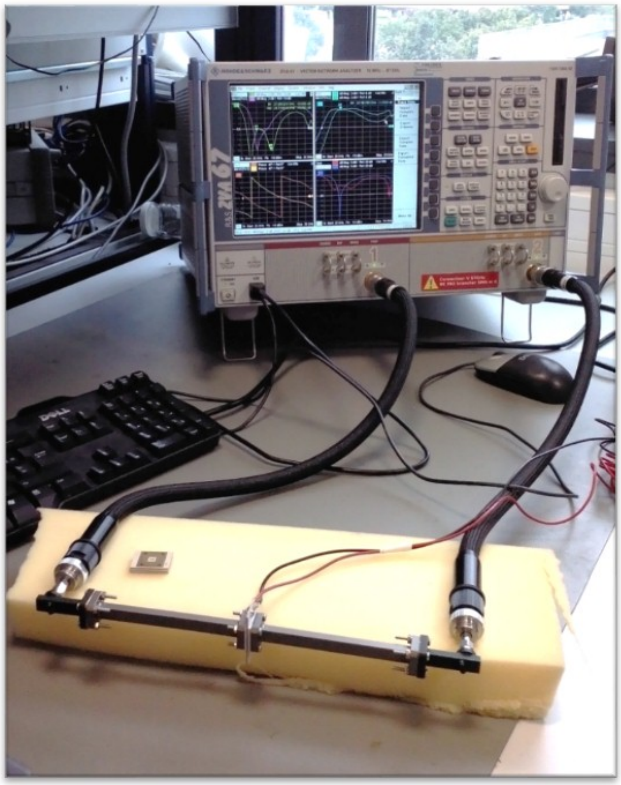

Figure 3.18: Photograph of the full measurement setup in standard waveguide WR-28 used for the characterization.

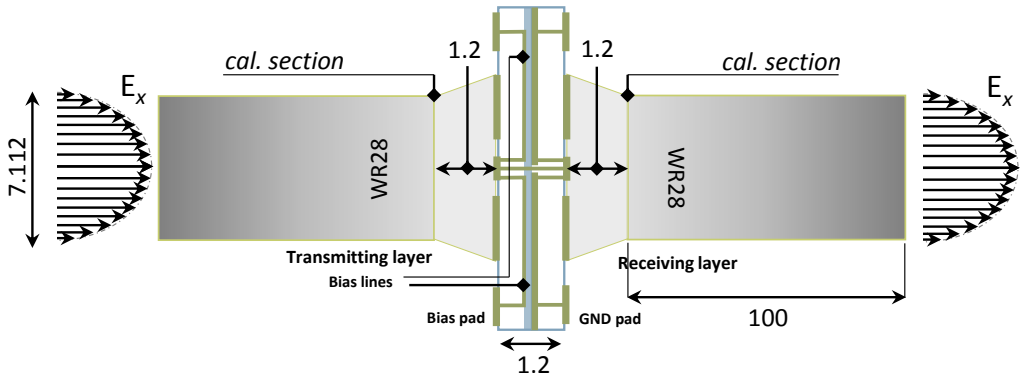

Figure 3.19: Scheme of the waveguide setup used to test the unit-cell. Dimensions are given in millimeters.

3.4 Measurements

The realized prototype of the unit-cell is shown in Fig. 3.17(a, b). The original design is surrounded by two rings ($6 \times 6\,\mathrm{mm}^2$ and $9 \times 9\,\mathrm{mm}^2$) of metallized vias with a diameter of $500\,\mu$m. These rings associated with the metallic areas in contact with the WR-28 flanges warranty the continuity of the waveguide walls and avoid the propagation of substrate modes outside the unit-cell. Two bias lines, passing through the two rings of vias, and pads for the ground connections are included on the boards, as shown in Fig. 3.17(c). Further full-wave simulation studies performed with the complete setup have shown their negligible impact on the frequency response of the unit-cell.

This prototype has been tested in the waveguide simulator shown in Figs. 3.18, 3.19. In order to de-embed the waveguide sections and coax-to-waveguide adaptors from the unit-cell scattering parameters, a TRL calibration with waveguide standards has been performed. The two thin ad-hoc transitions from the WR-28 sections to the square unit-cell sections are not deembedded. Indeed, the unit-cell section (5.1×5.1 mm^2) does not allow the propagation of the fundamental TE10 mode at 29 GHz (its cut-off frequency is 29.4 GHz) so that the transitions cannot be included in the calibration process. The measured scattering parameters show minimum insertion losses of 1.09 dB and 1.29 dB for the 0°- and 180°-states, respectively (Figs. 3.15, 3.16). The absolute 3-dB transmission bandwidth is 27.0-30.2 GHz and 26.7-31.2 GHz in the 0°- and 180°- phase states, respectively. The relative 3-dB transmission bandwidth (i.e. with the minimum insertion loss as reference) is 26.8-30.8 GHz and 26.7-32.0 GHz in the 0°- and 180°- phase states, respectively. The additional losses of about 0.3 dB, when compared to the simulations, are attributed to the fabrication uncertainties and the neglected adaptor sections during the deembedding process. The measured phase difference between the two transmission states equals 180° at 28.5 GHz and the maximum error in the transmission bandwidth is 13° ($\pi/14$) at 26.8 GHz (Fig. 3.16). The agreement between the simulated and the measured scattering parameters is very good, as summarized in Table 3.2.

Table 3.2: Simulated and measured performance in the waveguide setup. The simulation setup of Fig. 3.14 has been considered.

	0°		180°	
	Simul. (GHz)	Meas. (GHz)	Simul. (GHz)	Meas (GHz)
S_{21} 2-dB BW	27.2-29.9	27.3-29.7	27.0-30.1	26.9-30.3
S_{21} 3-dB BW	27.0-30.5	27.0-30.2	26.8-30.7	26.7-31.0
S_{11} 10-dB BW	27.2-29.3	27.2-29.5	27.0-28.0	26.8-28.0
S_{22} 10-dB BW	27.3-29.0	27.4-29.3	27.1-28.5	27.0-28.1

3.5 Bias lines

In order to use the proposed architecture as a building block of large transmitarrays, the possibility to accomodate more than one bias line inside the unit-cell period must be investigated.

First, a simulation study has been carried out. The single unit-cell design presented in the previous sections has been modified by inserting up to ten bias lines (six on the bias layer and four on the top layer), as shown in Fig. 3.20(a, b). The simulated scattering parameters are shown in Fig. 3.20(c). As we can observe, the effect of this modification is negligible. This is mainly due to the orientation of these lines parallel to the cross-polarized field and the decoupling circuit formed by the two distributed capacitors defined in the design. Passing bias lines on the top layer requires also the use of via connections. In order to investigate this effect, three unit-cells with the bias network layout shown in Fig. 3.21(a,b) are simulated with periodic boundary conditions and Floquet mode excitation. The S parameters of Fig. 3.21(c) show negligible effects on the frequency response of the unit-cell.

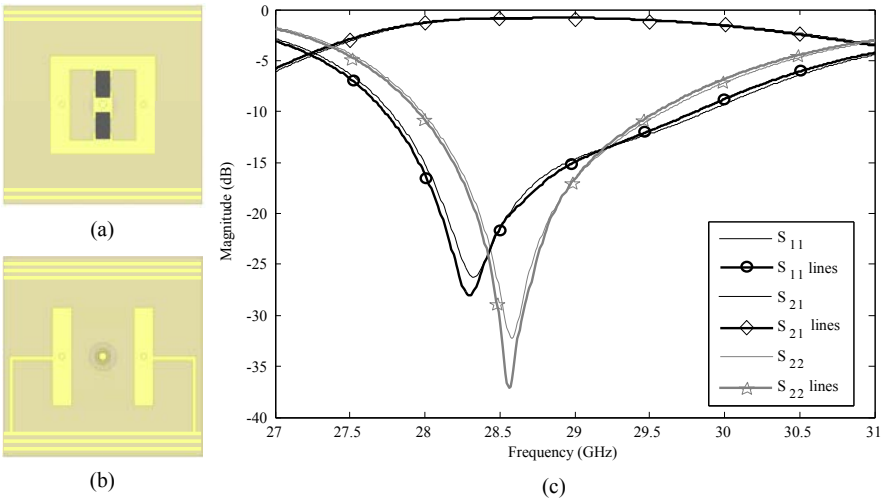

Figure 3.20: Unit-cell with ten bias lines accommodated in the transmitting (a) and biasing (b) layers. Scattering parameters magnitudes for the single unit-cell without and with ten bias lines (c).

The modified unit-cell has been realized and tested in the waveguide setup already introduced. Two configurations are considered: a first with the connection to the bias signal realized at the center of the unit-cell (Fig. 3.22a, b) and a second one with side connections (Fig. 3.22c,d). Photographs of the realized prototypes are shown in Fig. 3.25. The scattering parameters for the first configuration are shown in Fig. 3.23. For the second configuration, the S-parameters are shown in Fig. 3.24. In both cases, a good agreement with the numerical results obtained by considering the setup of Fig. 3.14 has been found.

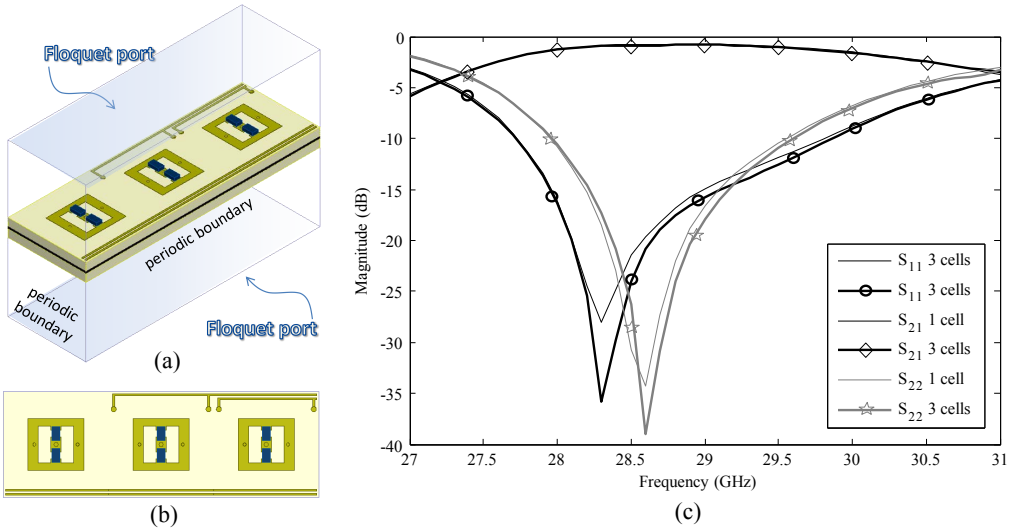

Figure 3.21: Simulation setup used to evaluate the effects of the bias lines on the unit-cell frequency response: 3D sketch (a) and transmitting (b). Scattering parameters magnitudes for three unit-cells with bias lines compared to the single unit-cell (c).

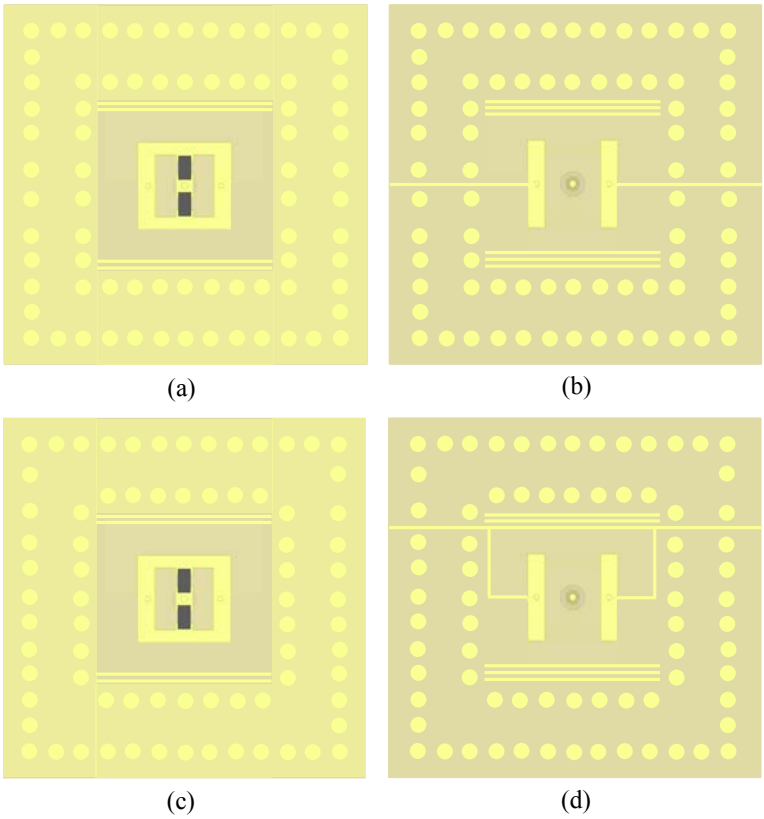

Figure 3.22: Schemes of the unit-cell with ten bias lines connected to the center (a, b) or to the side (c, d) tested in waveguide.

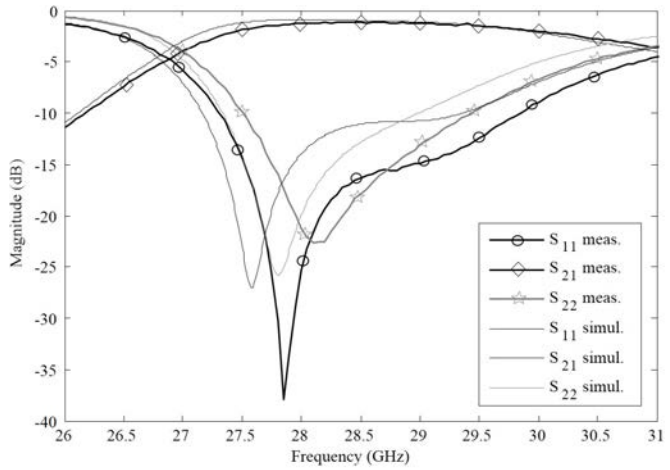

(a)

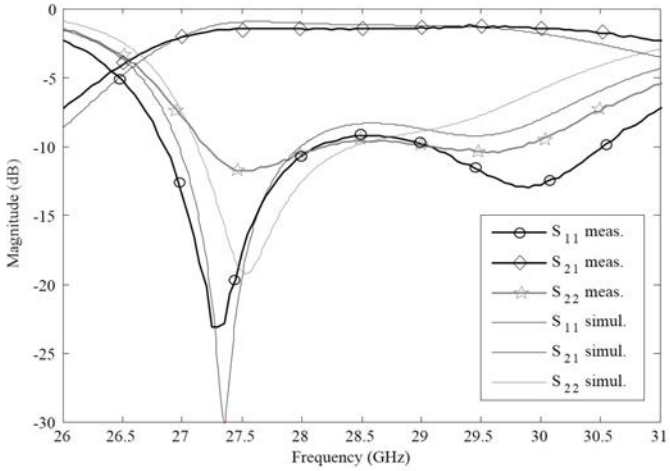

(b)

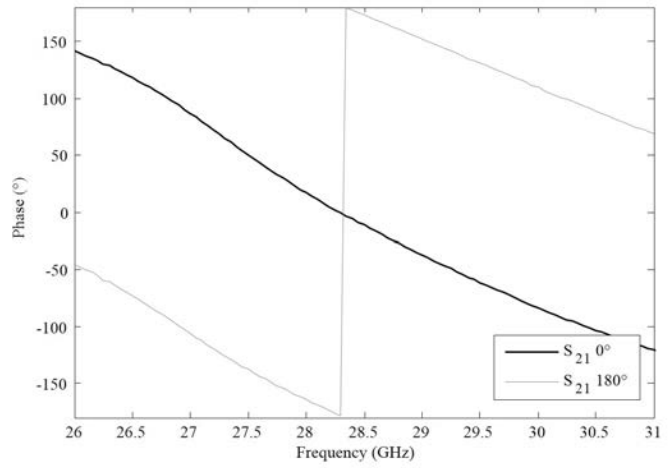

(c)

Figure 3.23: Measured scattering parameters magnitudes (a, b) and phases (c) of the single unit-cell in waveguide with ten bias lines and a center bias signal connection.

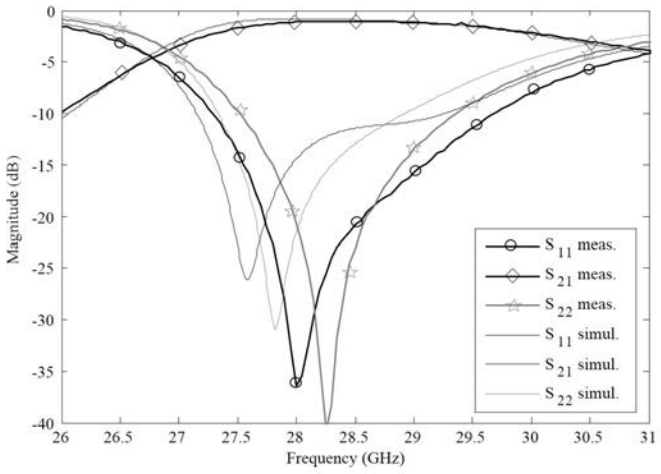

(a)

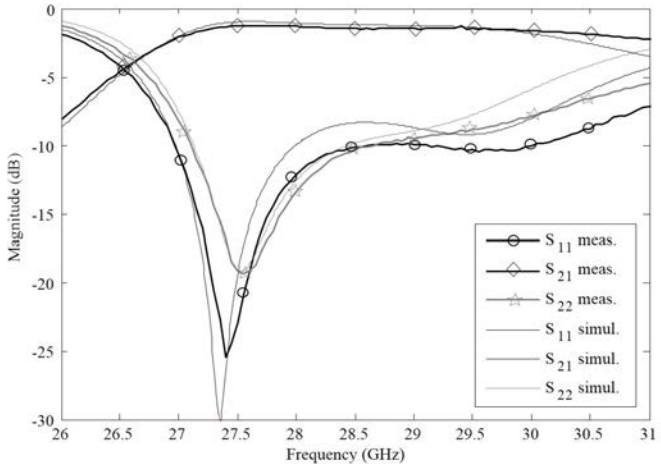

(b)

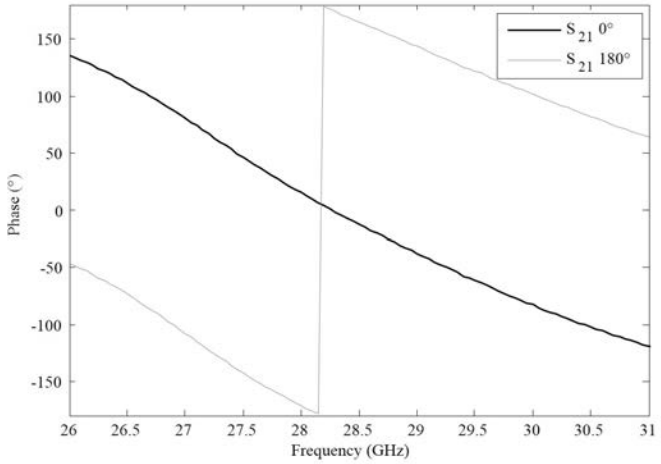

(c)

Figure 3.24: Measured scattering parameters magnitudes (a, b) and phases (c) of the single unit-cell in waveguide with ten bias lines and a side bias signal connection.

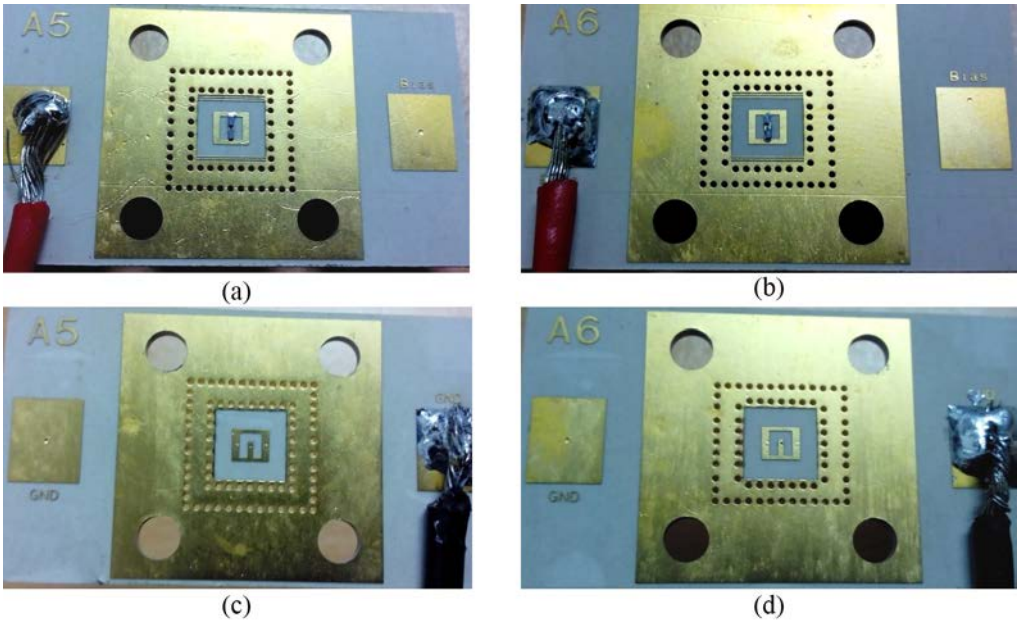

Figure 3.25: Photographs of the tested unit-cell prototypes with integrated bias lines: center (a, c) and side (b, d) connections.

3.6 Rotation of the transmitting patch

The unit-cell considered until now was characterized by two patch antennas, one on the receiving and one on the transmitting layers, which generate a linearly-polarized field aligned in the same direction. In this paragraph, the effects of a rotation on the transmitting layer passive patch is studied. The receiving layer configuration remains unchanged, as well as the configuration of the bias lines.

The simulated scattering parameters in magnitude for the two phase states are reported in the graphs of Fig. 3.26 (a, b). As expected, the performances are very similar to the nominal design without the rotations. This unit-cell, which includes also ten bias lines, has been fabricated and tested in waveguide (Fig. 3.27). Photographs of the realized prototype are shown in Fig. 3.28. The setup considered for the characterization is similar to the one presented previously except for a rotation of 90° of the waveguide assembly on one side in order to allow the propagation of the TE10 mode excited from the rotated patch antenna. The measurement results are shown in Fig. 3.26. A good agreement has been found for both the 0° and 180° states with the numerical results obtained by considering the waveguide setup of Fig. 3.14. The discrepancies are attributed to the error of alignments between the rotated waveguides. The measured phase response, shown in Fig. 3.26(c), demonstrates the phase shift between the two states.

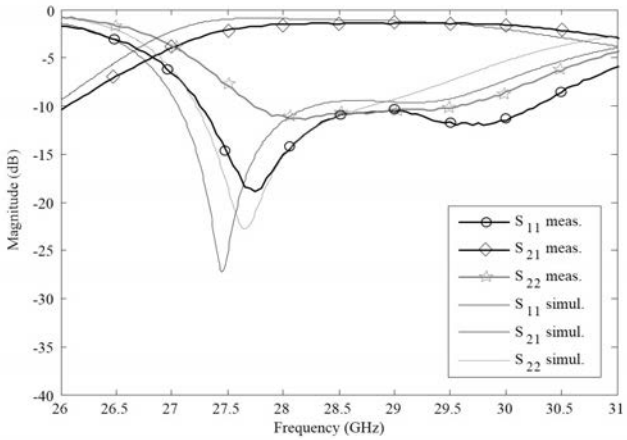

(a)

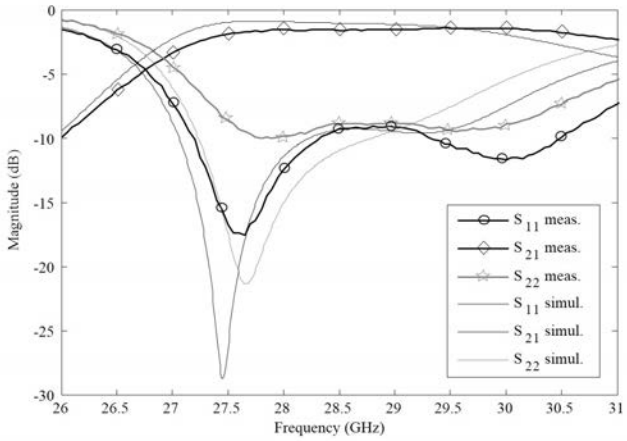

(b)

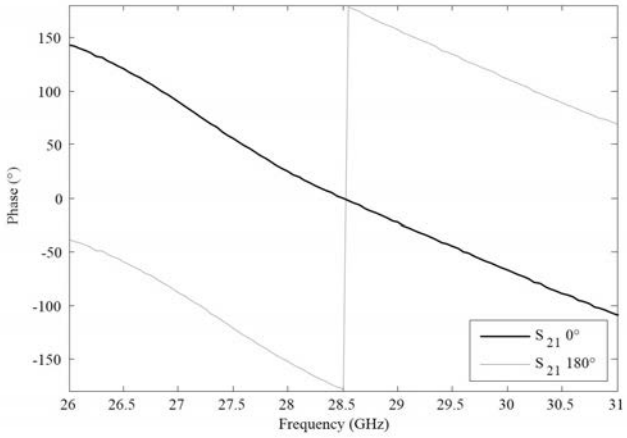

(c)

Figure 3.26: Measured scattering parameters magnitudes (a, b) and phases (c) of the single unit-cell in waveguide with ten bias lines and passive patch rotated by 90°.

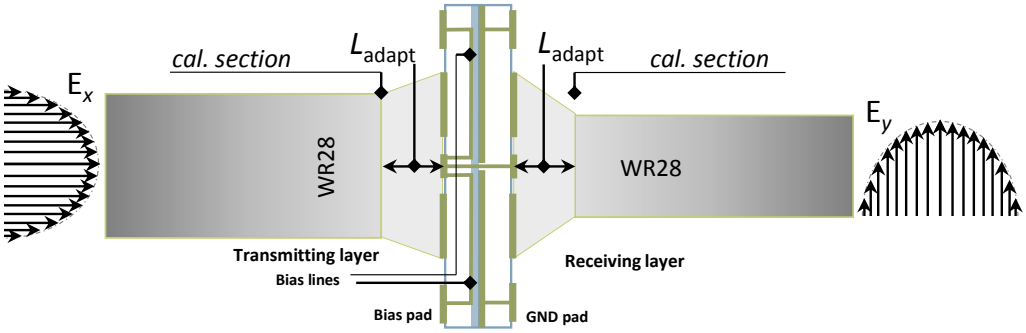

Figure 3.27: Scheme of the waveguide setup used to test the unit-cell with 90° rotated patch.

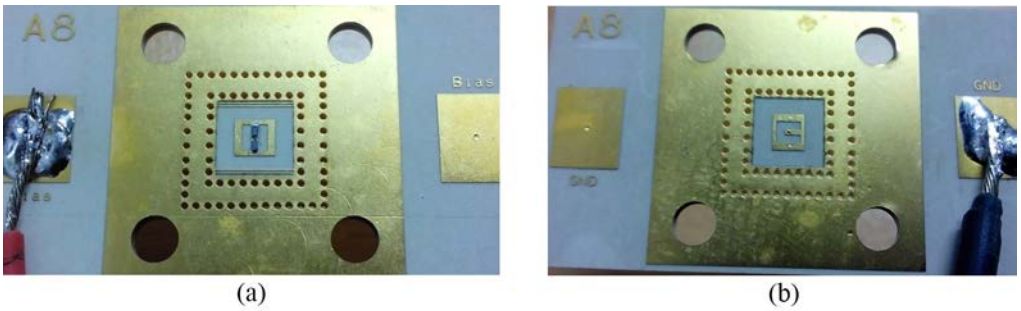

(a) (b)

Figure 3.28: Photographs of the tested unit-cell prototypes with integrated bias lines and a 90° rotation of the passive patch: active (a) and passive (b, d) patch layers.

3.7 Conclusions

In this chapter, an electronically reconfigurable 1-bit unit-cell has been presented for transmitarray applications in Ka-band.

The proposed design is conceived for manufacturing with a standard PCB technology and it is formed by four metallized layers, two substrates and one bonding film. On the transmitting layer, two p-i-n diodes are mounted on a slot-loaded patch antenna. The diodes have been modelled with an equivalent lumped-element circuit for the forward and reverse states. The values of the lumped elements have been defined by fitting the measurements done with microwave probes on a coplanar setup. The unit-cell design includes an RF/DC decoupling circuit formed by two capacitors implemented in microstrip technology. The oblique incidence on both the E- and H-plane has been investigated and shows no major performance change.

The realized prototype has been tested in a WR-28 ad-hoc waveguide simulator. Insertion losses of 1.09 dB and 1.29 dB at 29 GHz have been measured for the 0°- and 180°-phase states, respectively, with a 3-dB bandwidth around 11%. A very good agreement with the full-wave simulation has been demonstrated. The effects of additional bias lines and patch antenna rotation of 90° have been investigated with numerical results and validated with waveguide measurements.

Compared to the 1-bit design presented in [39] at 10 GHz, the proposed unit-cell exhibits minimum insertion losses reduced by about 0.5 dB maintaining similar 3-dB bandwidth. It is one of the lower-loss unit-cell, if compared with the works based on other technologies proposed in the literature. For instance, in [38], the 2-bit MEMS-based unit-cell has simulated minimum IL between 2.0 and 2.9 dB in Ka-band. In [31], the varactor-based unit-cell had an average IL of 3.4 dB in C-band.

The proposed unit-cell architecture will be used for the design of a reconfigurable transmitarray presented in Chapter 4.

Chapter 4

Reconfigurable transmitarrays in Ka-band

In this chapter, the design of reconfigurable transmitarrays based on the unit-cell demonstrated in Chapter 3 is presented. Both linear and circular polarizations are considered. In the latter case, the sequential rotation technique, already presented in Chapter 2, is applied with different rotation schemes to the transmitting layer which is composed of passive linearly-polarized patch antennas.

Numerical simulations have been used to analyse the performances of the different configurations and select the best one. A prototype of 400-elements working in LH/RH circular polarization has been manufactured and tested in anechoic chamber. The measurement results are discussed.

4.1 Transmitarray in linear polarization

A square array of 400 unit-cells is analysed by using the analytical/numerical in-house method proposed in Chapter 2 in order to reduce the computational effort [39]. The focal source considered is the one used in Chapter 2 (a standard WR34 waveguide horn with 10 dBi of nominal gain). The optimal focal distance ($F = 60\,\text{mm}$, $F/D = 0.6$, Fig. 4.1) and the corresponding phase distribution shown in Fig. 4.2 have been calculated at 29.0 GHz. This value of F has been selected in order to maximize the broadside gain and it corresponds to a trade-off between the losses due to the spillover and the losses due to the illumination tapering. The maximum broadside gain is 23.8 dBi and the side lobe level (SLL) is better than -19.0 dB on the horizontal plane. The cross-polarization level is under 30 dB at broadside. The simulated frequency response of Fig. 4.3 shows a 1-dB gain bandwidth of about 8.5% (28.0-30.5 GHz). The radiation patterns at 27.4 and 31.0 GHz are shown in Fig. 4.4.

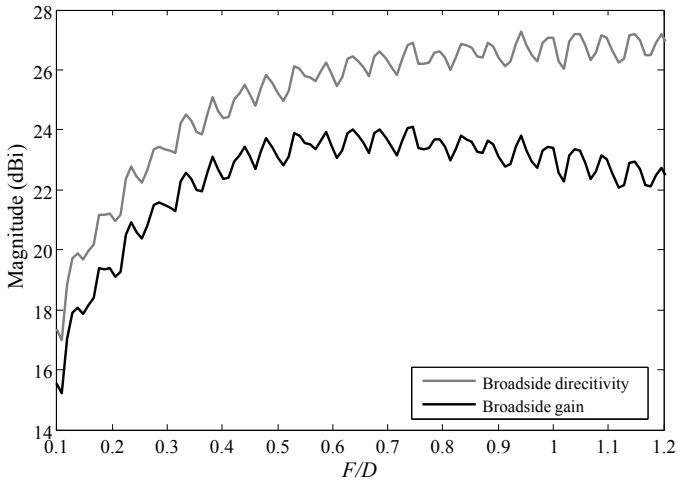

Figure 4.1: Simulated broadside gain and directivity of a 400-elements transmitarray based on the unit-cell of Chapter 3 and working in linear polarization.

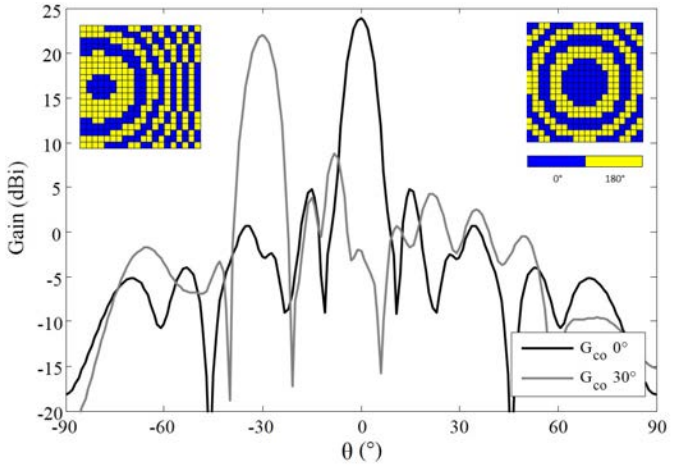

Figure 4.2: Radiation patterns in the $\phi = 90°$ plane at 29.0 GHz for the co-polar linear polarization of a 400-elements transmitarray formed by the unit-cell design proposed in Chapter 3. Main beam at broadside and at -30° with the corresponding phase distribution.

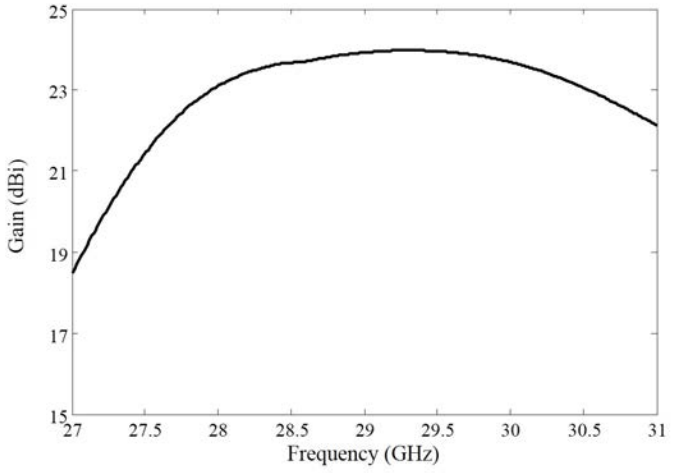

Figure 4.3: Frequency response for the broadside beam configuration shown in Fig. 4.2.

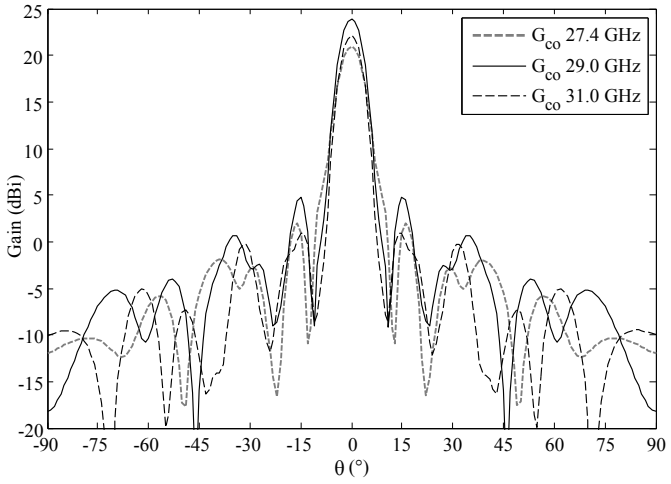

Figure 4.4: Radiation patterns in the $\phi = 90°$ plane for the co-polar linear polarization at 27.4, 29.0 and 31.0 GHz of a 400-elements transmitarray formed by the unit-cell design proposed in Chapter 3.

Table 4.1: Radiation characteristics of a 400-elements transmitarray working in linear polarization.

Angle	Directivity (dBi)	Gain (dBi)	SLL (dB)
0°	26.2	23.8	-19.0
-10°	25.9	22.8	-16.0
-20°	25.0	22.6	-17.2
-30°	24.4	22.0	-13.3
-40°	23.4	21.0	-13.1
-50°	22.8	19.8	-12.3

By introducing a proper phase shift [39] in the unit-cell distribution, tilted beams in any cut-plane can be obtained. The phase distribution required to obtain a tilt of -30° in the horizontal plane is shown in the inset of Fig. 4.2. The corresponding radiation pattern is shown in the same figure (grey line). The maximum gain is 22.0 dBi and the SLL is -13.3 dB in this configuration.

The main radiation characteristics of the antenna with electronic beam steering up to -40° in the $\phi = 90°$ plane are summarized in Table 4.1. The maximum gain decreases from 23.8 dBi (broadside) to 19.8 dBi (θ_0 = -50°) because of the unit-cell gain variation in the same angular range (see Chapter 3).

4.2 Transmitarray in circular polarization

The same linearly-polarized unit-cell used in the previous section can be used to build transmitarrays in circular polarization as well. In this case, a sequential rotation scheme

can be applied to the transmitting layer of the transmitarray, as discussed and demonstrated in Chapter 2 (Section 2.4, Figures 2.15-2.16, Tables 2.4-2.5). The negligible effect of the rotations applied to the passive patches on the unit-cell nominal performances has been investigated and discussed with numerical simulations and waveguide measurements in the Chapter 3. The use of a linearly-polarized unit-cell leads to about 3-dB lower gain if compared with an array built with circularly-polarized elements [69, 86]. However, it allows to generate both right-handed or left-handed circular polarizations depending on the phase distribution, which is a very interesting functionality for many systems.

Clockwise and sub-array rotated arrangements of unit-cells in which the passive patch antenna is rotated by 0°, 90°, 180° and 270° of rotation angle (the case $T = 4$, $p = 2$ presented in Chapter 2) will be considered. The best results were obtained with these schemes in the analysis of passive transmitarrays proposed in Chapter 2.

It is worth to notice that the active unit-cell side loaded by p-i-n diodes is placed on the receiving layer and the rotation is applied to the passive unit-cell side (transmitting layer). This leads to a very simple handling of the bias lines in the active unit-cell side since they all remain parallel to each other. The bias lines arrangement inside each unit-cell have been discussed in Chapter 3 and the final array layout is presented Section 4.3.

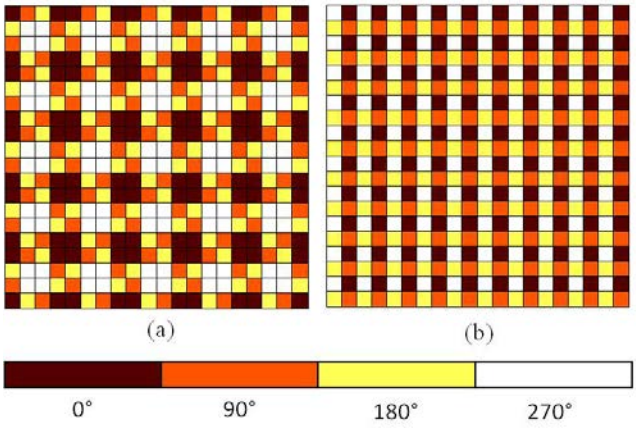

Figure 4.5: Sequential rotations schemes considered in the transmitting layer: 4×4 sub-array (a) and clockwise (b) arrangements.

A 400-elements transmitarray configuration has been studied with the hybrid analytical/numerical method proposed in Chapter 2. First, a 4×4 sub-array rotated arrangement of Fig. 4.5(a) has been selected. This is the distribution used for the realized passive transmitarray with circularly-polarized unit-cells tested in Chapter 2. A sketch of the receiving and transmitting layers for this configuration is shown in Fig. 4.6(a). The radiation patterns in the $\phi = 90°$ plane and in all cut-planes and the corresponding phase distribution are shown in Fig. 4.7(a). The phase compensation has been calculated, as already explained in Chapter 2, by considering the angle of rotation applied on the transmitting layer (ψ_m) and

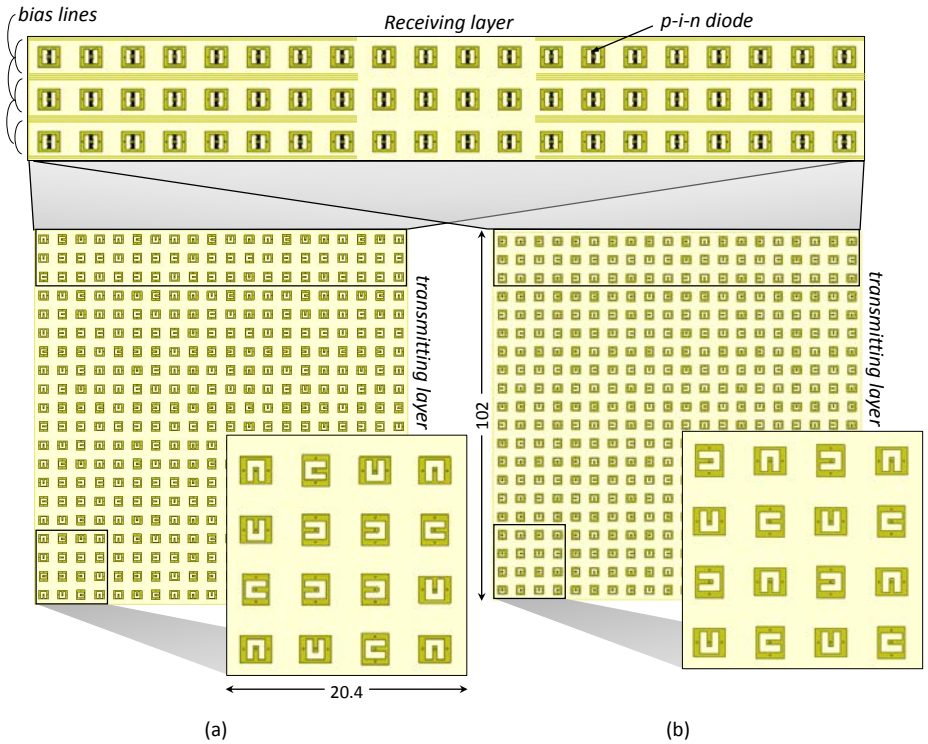

Figure 4.6: Layouts of the receiving and transmitting layers corresponding to the schemes of Fig. 4.5: 4×4 sub-array (a) and clockwise (b) arrangements.

the phase of the incident wave coming from the source on the receiving layer (ϕ_m) with the following relation:

$$\Delta\phi_m = \psi_m, \text{ if } \phi_m - \psi_m < \pi, \tag{4.1}$$

$$\Delta\phi_m = \psi_m + \pi, \text{ if } \phi_m - \psi_m > \pi. \tag{4.2}$$

The 2D radiation patterns for the co-polar and cross-polar circularly-polarized components are shown in Fig. 4.7(b,c) at 29.0 GHz. The maximum broadside gain is 20.8 dBi in right-handed circular polarization with a power efficiency of 58%. The co-polarized side lobes are 20.0 dB below. The left-handed CP component is 28.0 dB below at broadside, as summarized in Table 4.2. The antenna power budget is given in Table 4.3. However, the use of linearly-polarized unit-cells instead of circularly-polarized ones leads to high cross-polarized side lobes (-10.4 dB at 30°, Fig. 4.7) in the two cardinal planes ($\phi = 0°$, $\phi = 90°$).

In order to improve these performances, the clockwise distribution of Fig. 4.5(b) has been considered. The phase distribution is given in Fig. 4.8(a). A sketch of the receiving and transmitting layers for this configuration is shown in Fig. 4.6(b). The states of the p-i-n diodes mounted on the receiving antenna are calculated accordingly with this phase distribution and the rotation scheme (Fig. 4.5(b)) and the resulting mask is shown in Fig. 4.9(a).

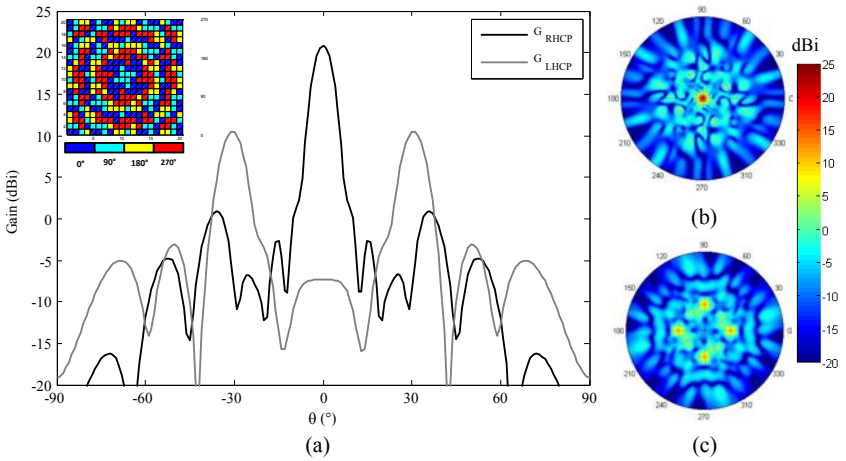

Figure 4.7: Simulated radiation patterns (realized gains in circular polarization) in the $\phi = 90°$ plane (a) and 2D maps (b,c) with the main beam at broadside and the rotation scheme shown in Fig.4.5(a). The calculated optimal phase distribution on the transmitting layer at 29.0 GHz is shown in the inset.

The radiation pattern at 29.0 GHz is shown in Fig. 4.10. The radiation performances and power budget are summarized in Tables 4.2, 4.3.

The 2-D radiation patterns are shown in Figs. 4.10(b,c) for the co- and cross-polar components. The cross-polarized side lobes are lower and better performances are obtained as compared to the sub-array scheme.

By replacing the phase law of Eqn. 4.1, only in correspondence of the 90° and 270° rotated cells with the following equations

$$\Delta\phi_m = \psi_m, \text{ if } \phi_m - \psi_m > \pi, \tag{4.3}$$

$$\Delta\phi_m = \psi_m + \pi, \text{ if } \phi_m - \psi_m < \pi, \tag{4.4}$$

a left-handed circularly-polarized beam can be generated. In fact, this operation is equivalent to invert the sense of rotation of the patch antennas in the array arrangement, allowing the generation of both RHCP and LHCP beams by changing electronically the phase compensation mask applied to the transmitarray. The new phase distribution is shown in Fig. 4.8(b) and the corresponding receiving layer states are shown in Fig. 4.9(b). The radiation patterns for the broadside main beam direction is shown in Figs. 4.10.

With the distribution (a), the RHCP gain is 20.6 dBi at broadside with XPD of 30.3 dB in the main beam direction. The maximum side lobe level (SLL) is -22.0 dB in the $\phi = 90°$ plane. With the distribution (b), the LHCP gain is 20.6 dBi with XPD and SLL similar to the previous case.

Tilted angles up to -40° in the two cardinal planes are obtained by considering the proper delay in the phase shift calculations. In the $\phi = 90°$ plane, a tilt of -20° and -40° is

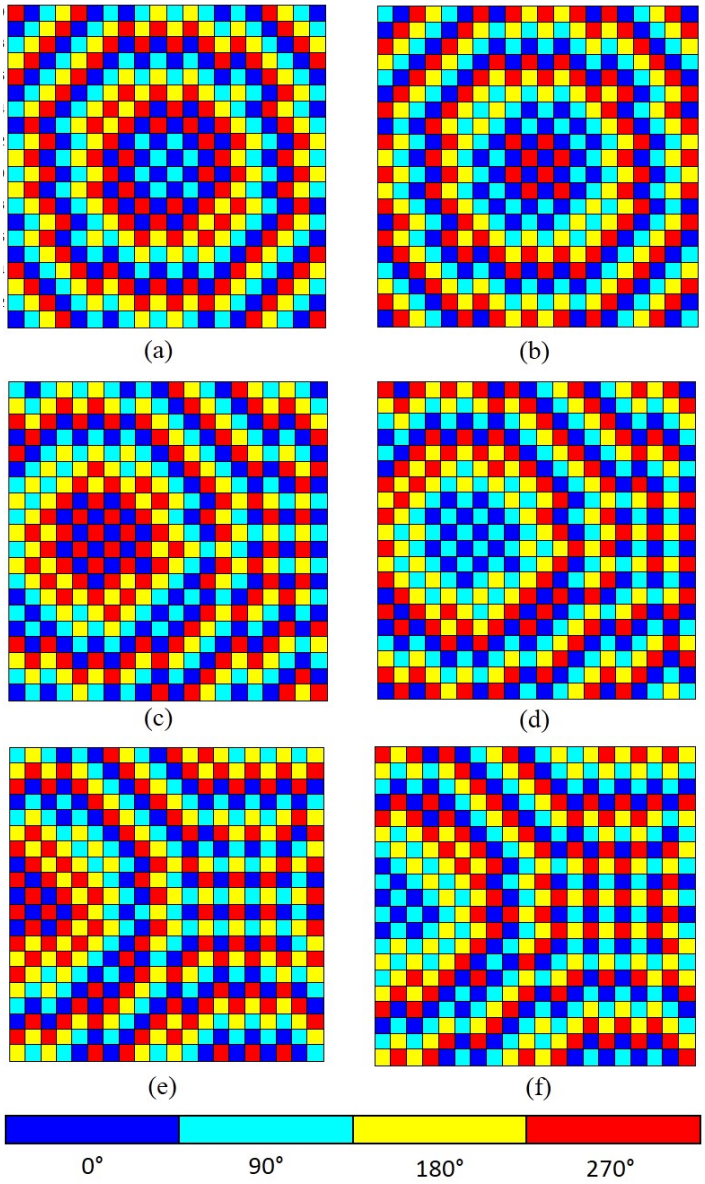

Figure 4.8: Phase distributions calculated for the clockwise rotation scheme (Fig. 4.5(a)) with 0° (a, b), -20° (c, d) and -40° (e, f) tilted beams in the ϕ=90° plane. Right-handed (a, c, e) and left-handed (b, d, f) circularly-polarized main beams. The receiving layer distributions, realized with the proper states of p-i-n diodes, for the configurations (a) and (b) are shown in Fig. 4.9.

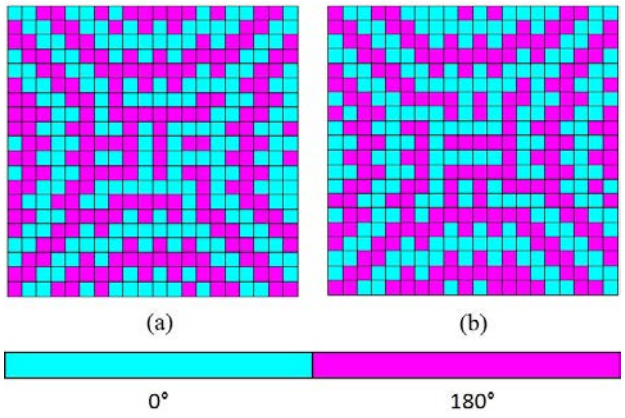

Figure 4.9: Receiving layer compensation masks for the phase distributions shown in Fig 4.8(a, b).

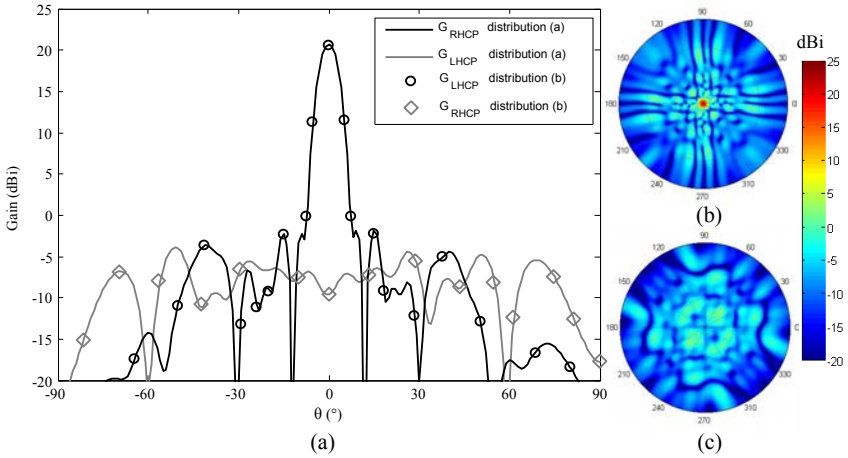

Figure 4.10: Simulated radiation patterns (a) (realized gain) in the $\phi = 90°$ plane and 2D maps (b,c) for the phase distributions (a) (solid lines) and (b) (markers) of Fig. 4.8.

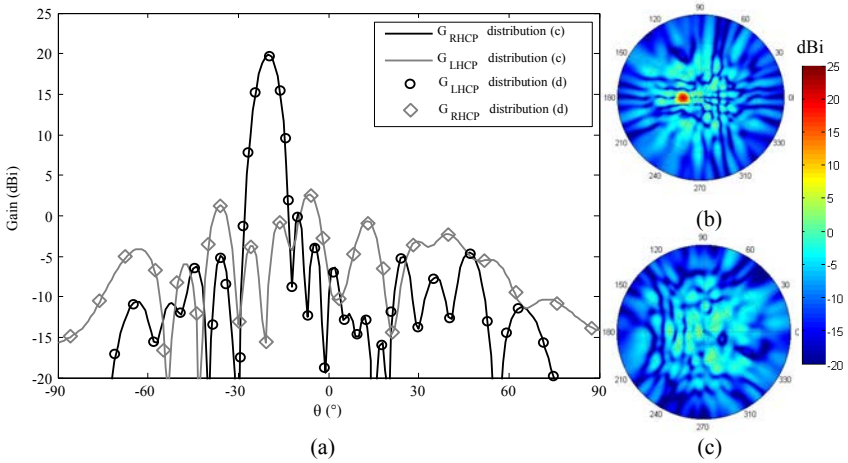

Figure 4.11: Simulated radiation patterns (realized gain) in the $\phi = 90°$ plane (a) and 2D maps (b,c) for the phase distributions (c) (solid lines) and (d) (markers) of Fig. 4.8.

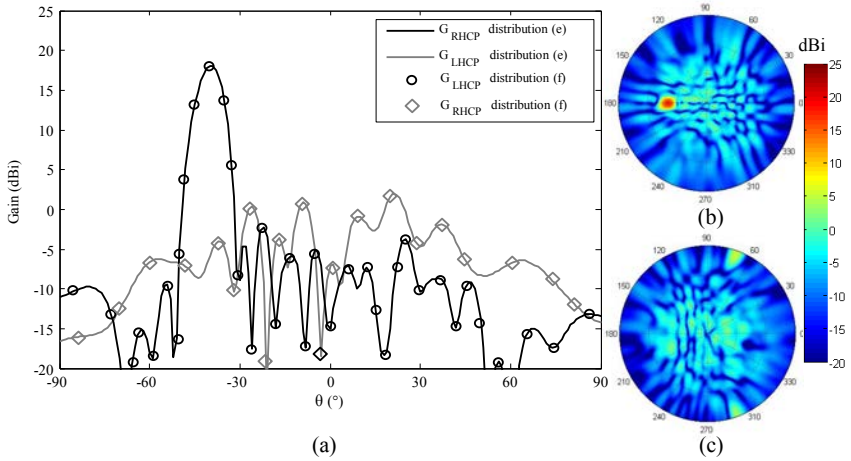

Figure 4.12: Simulated radiation patterns (realized gain) in the $\phi = 90°$ plane (a) and 2D maps (b,c) for the phase distributions (e) (solid lines) and (f) (markers) of Fig. 4.8.

considered. The phase compensations are shown for the left-handed and right-handed CP beams in Fig 4.8(c, d) and (e, f). The radiation patterns in the same plane are shown in Figs. 4.11, 4.12.

With the distribution (c), which corresponds to a main beam direction of -20°, the RHCP gain is 19.9 dBi at broadside with XPD of 28.5 dB in the main beam direction. The maximum side lobe level (SLL) is -19.6 dB in the $\phi = 90°$ plane. With the distribution (d), the LHCP gain is 19.9 dBi with XPD and SLL similar to the previous case. With the distribution (e), which corresponds to a main beam direction of -40°, the RHCP gain is 18.1 dBi at broadside with XPD of 23.7 dB in the main beam direction. The maximum side lobe level (SLL) is -20.3 dB in the $\phi = 90°$ plane. With the distribution (f), the LHCP gain is 18.0 dBi with XPD and SLL similar to the previous case.

In order to verify the tilting capabilities of the proposed solution, a 45° azimuthal plane is considered. Tilted beams at -20°, -30° and -40° are shown in Figs. 4.13, 4.14, 4.15, respectively . The optimized phase distributions are shown in the insets of each figure.

In the -20° case, the maximum RHCP gain is 20.0 dBi with XPD of 24.6 dB in the main beam direction. The maximum co-polar side lobe level (SLL) is -16.8 dB in the $\phi = 45°$ plane. In the -40° case, the maximum RHCP gain is 17.6 dBi with XPD of 26.0 dB in the main beam direction. The maximum co-polar side lobe level (SLL) is -14.5 dB in the $\phi = 45°$ plane.

Beyond 30° of beam tilt, a spurious cross-polarized (LHCP) lobe of radiation appears in the opposite quadrant (Fig. 4.16). In the -30° case, its magnitude is 14.6 dBi (-4.5 dB if compared with the main beam) at $\theta = 68°$. In the -40° case, its magnitude is 16.0 dBi (-1.6 dB if compared with the maximum RHCP gain) at $\theta = 52°$.

An almost symmetrical phase distribution is obtained in the case of a 45° tilted beam

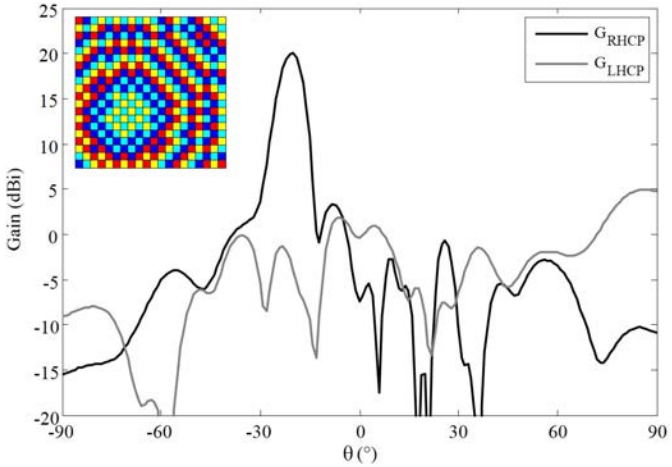

Figure 4.13: Simulated radiation pattern (realized gain) in the $\phi = 45°$ plane with main beam tilted at -20° in the same azimuthal plane. Inset: optimal phase distribution.

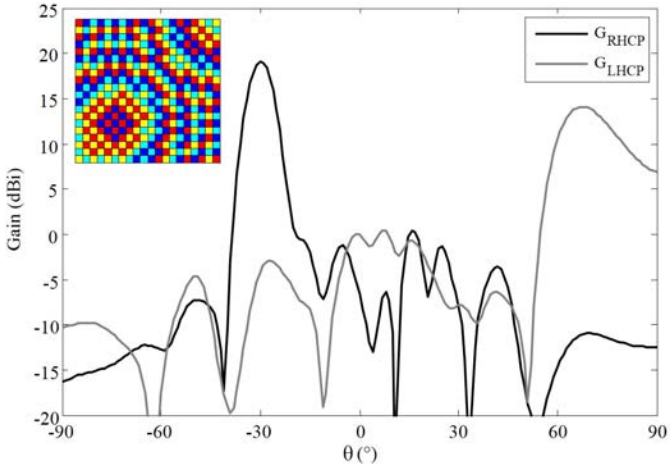

Figure 4.14: Simulated radiation patterns (realized gain) in the $\phi = 45°$ plane with main beam tilted at -30° in the same azimuthal plane. Inset: optimal phase distribution.

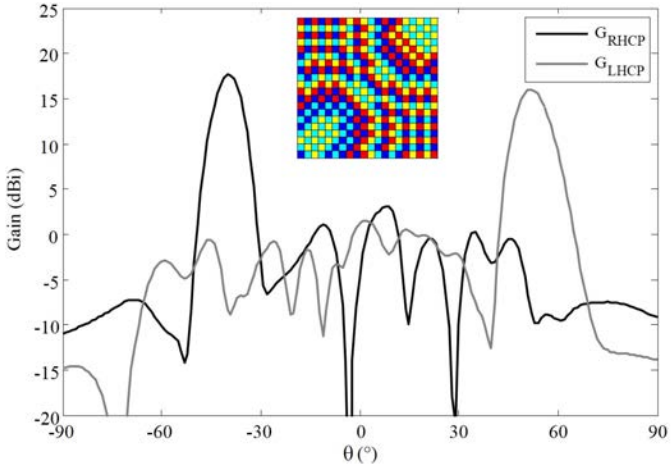

Figure 4.15: Simulated radiation patterns (realized gain) in the $\phi = 45°$ plane with main beam tilted at -40° in the same azimuthal plane. Inset: optimal phase distribution.

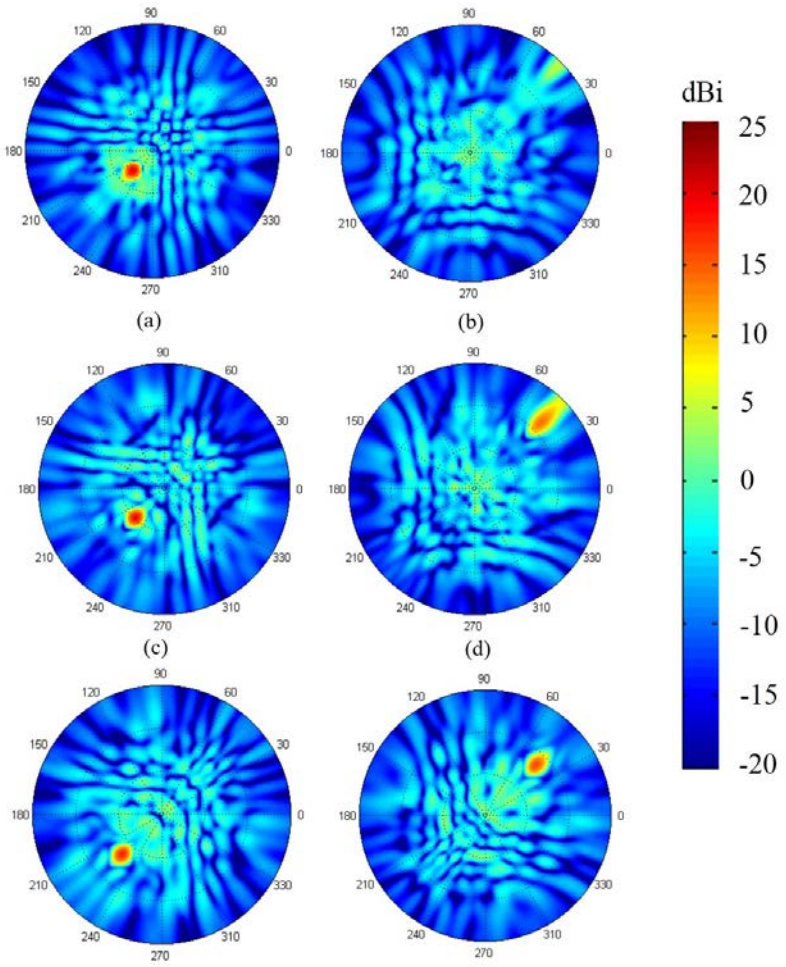

Figure 4.16: Simulated 2D radiation patterns (realized gain) with main beam tilted at -20° (a, b), -30° (c, d), -40° (e, f) in the $\phi = 45°$. Co-polar RHCP (a, c, e) and cross-polar LHCP (b, d, f) components.

in the same plane (Fig. 4.17). The LHCP spurious lobe magnitude is 16.9 dBi (-0.3 dB if compared with the maximum RHCP gain) at $\theta = 45°$.

Similar effects can be observed in any azimuthal plane, except for the cardinal planes ($\phi = 0°, 90°$), with tilting angles greater than 30°. This is the case in the example shown in Fig. 4.18 where the main beam has been steered at θ = -40° in the plane ϕ = 20° and a spurious cross-polarized lobe appeared in the plane ϕ = -110°. This is mainly due to the symmetric phase distribution generated on the array distribution (insets of Figs. 4.14, 4.15 and 4.17). The transmitarray with this configuration of rotations and linearly-polarized unit-cells has limited tilting capabilities to a cone of 40°-50°. In the cardinal planes, this range can be extended up to 80° without occurrence of spurious lobes in cross circular polarization.

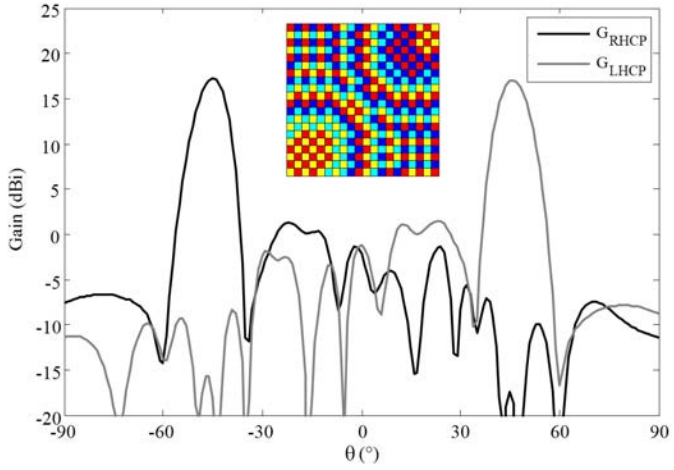

Figure 4.17: Simulated radiation patterns (realized gain) in the $\phi = 45°$ plane with the main beam tilted at -45° in the same azimuthal plane. Inset: optimal phase distribution.

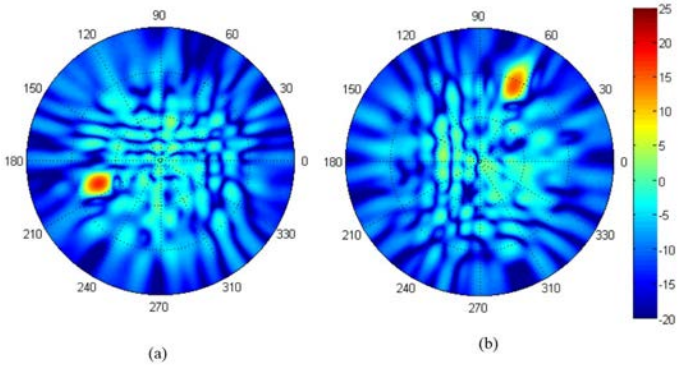

Figure 4.18: Simulated 2D radiation patterns (realized gain) with the main beam tilted at -40° in the $\phi = 20°$ plane. Co- (a) and cross-polar (b) components.

Table 4.2: Radiation characteristics of a 400-elements transmitarray working in RHCP circular polarization with the sequential rotation schemes of Fig 4.5.

θ_0	ϕ_0	Rotations	Gain (dBi)	XPD (dB)	Max X-pol. SLL (dB)	SLL (dB)
0°	90°	(a)	20.8	28.0	-10.4	-20.0
0°	90°	(b)	20.6	30.0	-24.0	-17.0
-20°	90°	(b)	19.9	28.5	-16.9	-19.6
-40°	90°	(b)	18.1	23.7	-16.1	-20.3
-20°	45°	(b)	20.0	24.6	-15.0	-16.8
-30°	45°	(b)	19.1	23.3	-4.5	-18.7
-40°	45°	(b)	17.6	26.0	-1.6	-14.5
-45°	45°	(b)	17.2	35.4	-0.2	-14.5

Table 4.3: Power budget and radiation characteristics at 29.0 GHz for the transmitarray configurations of Fig. 4.5.

	Rotations (a)	Rotations (b)
Focal source gain at broadside	11.7 dBi	11.7 dBi
Broadside directivity (RHCP)	23.2 dBi	23.0 dBi
Spillover loss	1.5 dB	1.5 dB
Broadside gain (RHCP)	20.8 dBi	20.6 dBi
Power efficiency	58.7%	58.7%

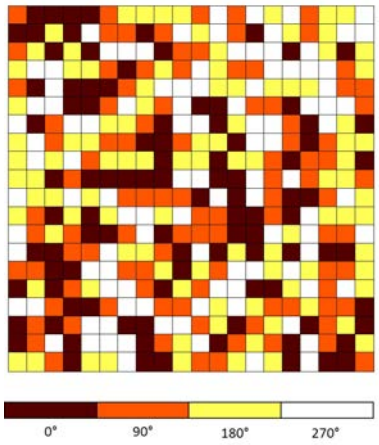

Figure 4.19: Random sequential rotation scheme applied to the transmitting layer of the transmitarray.

4.2.1 Random sequential rotations

In order to improve the tilting capabilities of the transmitarray, a random distribution of rotations (Fig. 4.19) has been considered. Four angles of rotation are used, as in the case of the distributions proposed in the previous paragraph.

As studied in [67, 68] for a phased array configuration of printed dipoles, this technique can improve the side lobe level of a sequentially-rotated array of linearly-polarized elements. The behaviour of this solution is similar to a sparse array arrangement [87] with the advantages of a regular lattice. In the case of transmitarrays, the application of this concept is very easy and can be seen as an extension of the regular periodic rotation schemes proposed in Chapter 2 and in the previous section. In fact, the absence of a corporate feed network removes any constraint on the element rotation and leads to a simple implementation of any kind of rotation scheme.

Several random distributions have been generated automatically with a routine inside the analysis code presented in Chapter 2. The best configuration is chosen by considering the maximum broadside gain and the corresponding XPD. The maximum cross-polarized side lobe levels has been also monitored. The best phase distribution calculated for a broadside beam is given in the inset of Fig. 4.20. The radiation patterns in the three principal planes at 29.0 GHz are shown in Fig. 4.20. The gain is 20.8 dBi at broadside with a XPD greater than 35 dB in the main beam direction. The maximum SLL is -18.5 dB, -18.7 dB, -16.9 dB in the $\phi = 0°$, $45°$, $90°$, respectively. The frequency response is shown in Fig. 4.21. The co-polar gain is greater than 18.0 dBi between 27.5 and 31 GHz, as in the case of a regular clockwise distribution (markers). A minimum cross polarization discrimination of 33.0 dB is maintained in the same bandwidth.

The capability to switch the polarization of the main beam is preserved as demonstrated

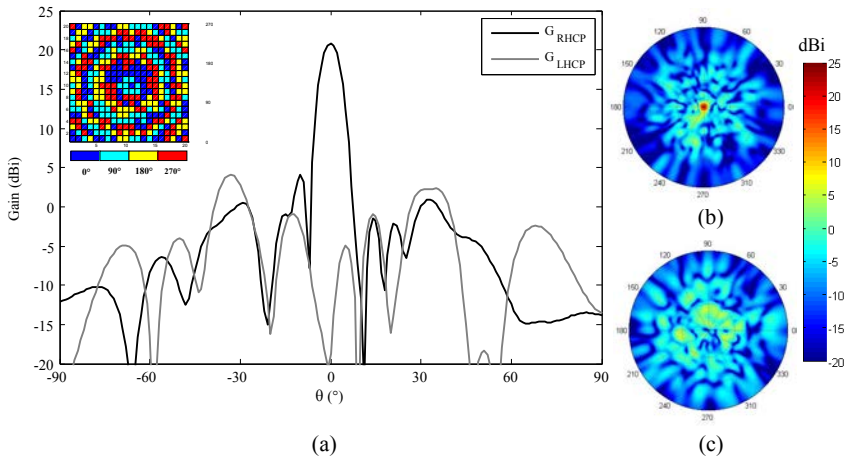

Figure 4.20: Simulated radiation patterns (realized gain) in the $\phi = 90°$ plane (a) and 2D maps (b,c). Inset: optimal phase distribution.

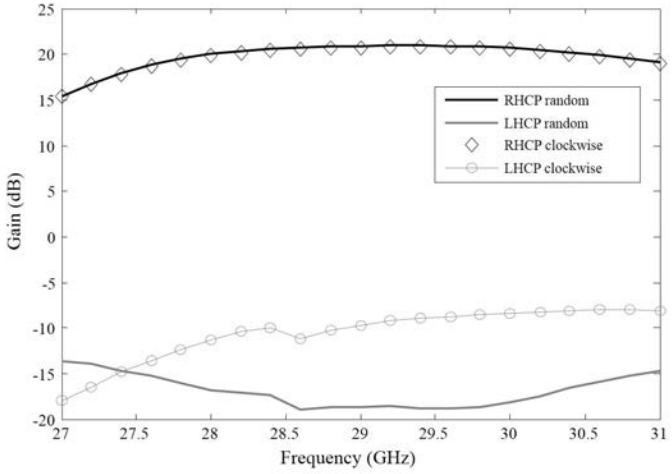

Figure 4.21: Frequency response of the 400-elements transmitarray with a broadside beam with the clockwise (markers) and random (solid lines) sequential rotation schemes of Fig. 4.5(b) and Fig. 4.19, respectively.

at broadside in Fig. 4.22. The maximum gain is 20.8 dBi with SLL of -17.8 dB in the $\phi = 90°$ plane. The XPD is greater than 35 dB.

Tilted beams are calculated in this cardinal plane (Figs. 4.23, 4.24). In the -20° case, the maximum RHCP gain is 20.0 dBi with XPD of 23.9 dB in the main beam direction. The maximum side lobe level (SLL) is -16.5 dB in the $\phi = 90°$ plane. In the -40° case, the maximum RHCP gain is 18.5 dBi with XPD of 16.0 dB in the main beam direction. The maximum side lobe level (SLL) is -17.0 dB in the $\phi = 90°$ plane.

In order to verify the tilting capabilities of the proposed solution, a 45° azimuthal plane is considered. Tilted beams at -20°, -30° and -40° are shown in Figs. 4.25, 4.26, 4.27. The optimized phase distributions are shown in the insets of each figure.

In the -20° case, the maximum RHCP gain is 20.4 dBi with XPD of 20.0 dB in the main

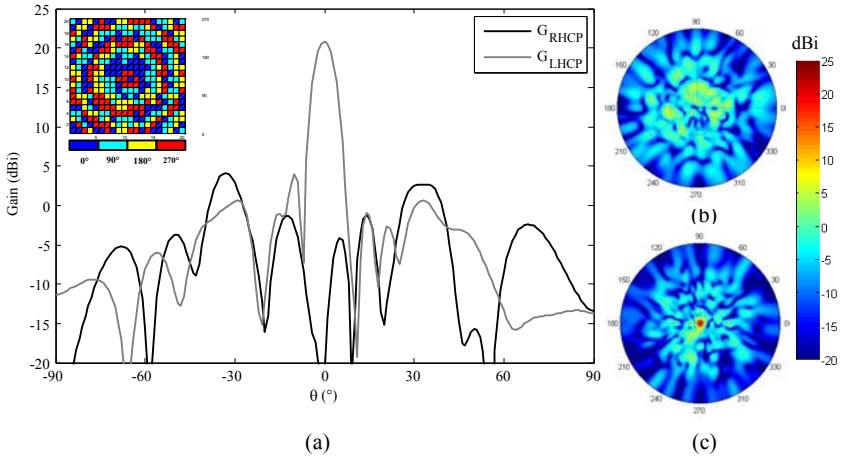

Figure 4.22: Simulated radiation patterns (realized gain) in the $\phi = 90°$ plane. Inset: optimal phase distribution calculated with the random rotation scheme of Fig. 4.19.

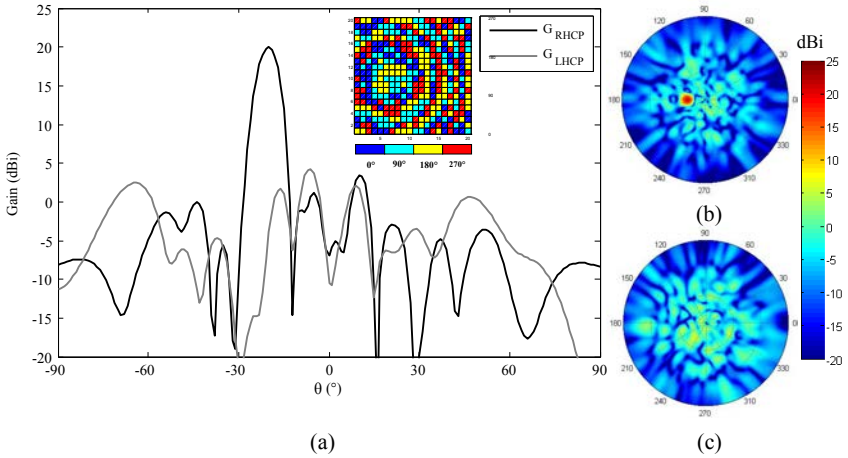

Figure 4.23: Simulated radiation patterns (realized gain) with tilted beam at -20°: $\phi = 90°$ plane (a) and 2D maps (b,c). Inset: optimal phase distribution.

beam direction. The maximum SLL is -17.3 dB in the $\phi = 45°$ plane. In the -30° case, the maximum RHCP gain is 19.2 dBi with XPD of 19.9 dB in the main beam direction. The maximum SLL is -14.2 dB in the $\phi = 45°$ plane.

The spurious cross-polarized lobe is cancelled, as shown in Figs. 4.25, 4.26, 4.27. Even in the case of tilted beams in the other cut-planes, good performances are obtained, as shown in (Fig. 4.28).

4.2.2 Cross polarization reduction

The radiation patterns presented in the previous section are obtained with a reference phase of 0°. At a first order, this parameter has no impact on the radiation performances since only the phase differences between the array elements determine the radiation patterns. However, it has been demonstrated that the variation of this parameter can have an impact

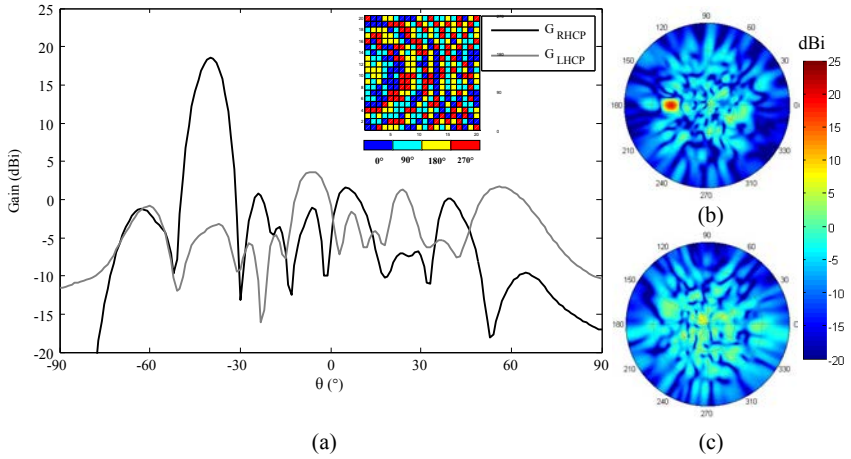

Figure 4.24: Simulated radiation patterns (realized gain) with tilted beam at -40°: $\phi = 90°$ plane (a) and 2D maps (b,c). Inset: optimal phase distribution.

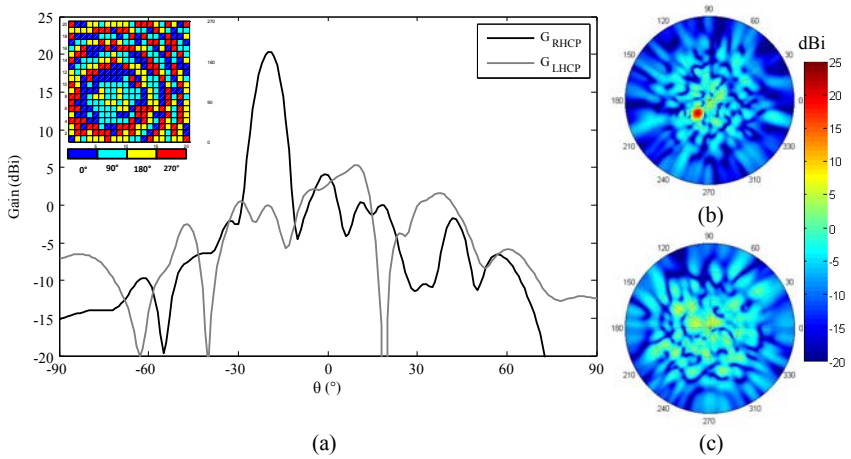

Figure 4.25: Simulated radiation patterns (realized gain) in the $\phi = 45°$ plane (a) and 2D maps (b,c) with the main beam tilted at -20° in the same azimuthal plane. Inset: optimal phase distribution.

on the cross-polarization levels in the main beam direction due to the differences between the unit-cells [88].

We considered the case of random rotations and a main beam tilted at -40° in the diagonal plane. The variation of the main beam co-polar gain and the cross-polarization level as a function of the phase offset at 29.0 GHz has been analyzed by calculating the radiation performance for values of phase offset between 0° and 360° with a step of 1°. In general, any parameter, such as the side lobe levels and the 3-dB bandwidth, can be considered studying the impact of the phase offset variation and optimizing the transmitarray configuration. The results are shown in Fig. 4.29. We observe a small variation in the main beam magnitude ($<$ 0.5 dB, black line) and an optimal value of 220°, where the cross-polarization discrimination is maximized (markers). It is worth to notice that the maximum level of cross polarization

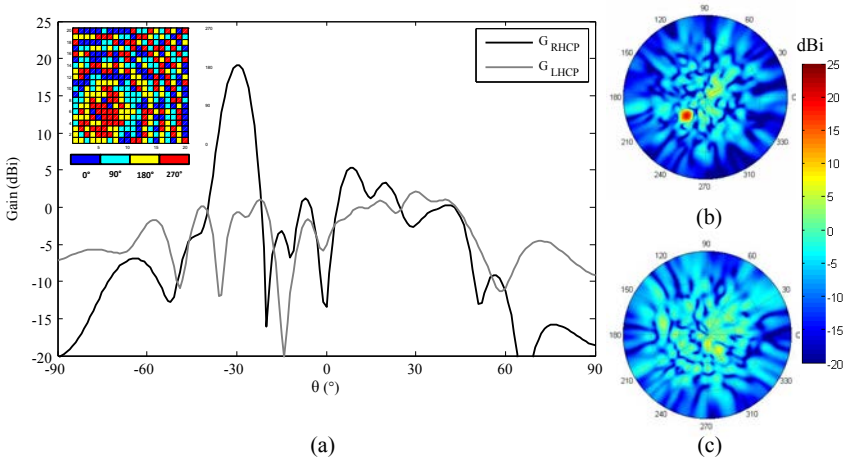

Figure 4.26: Simulated radiation patterns (realized gain) in the $\phi = 45°$ plane (a) and 2D maps (b,c) with the main beam tilted at -30° in the same azimuthal plane. Inset: optimal phase distribution.

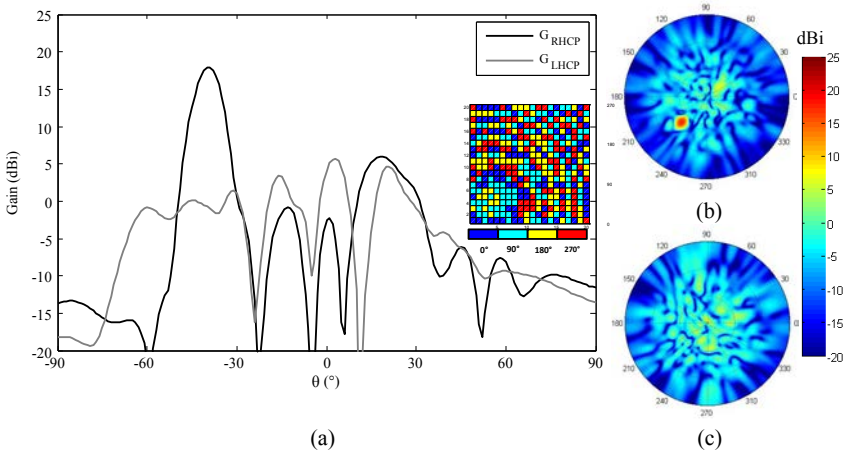

Figure 4.27: Simulated radiation patterns (realized gain) in the $\phi = 45°$ plane (a) and 2D maps (b,c) with the main beam tilted at -40° in the same azimuthal plane. Inset: optimal phase distribution.

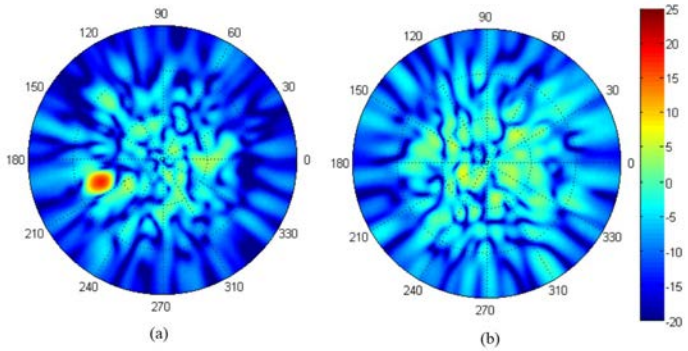

Figure 4.28: Simulated radiation patterns (realized gain) in the $\phi = 20°$ plane with the main beam tilted at -40° in the same azimuthal plane. Inset: optimal phase distribution.

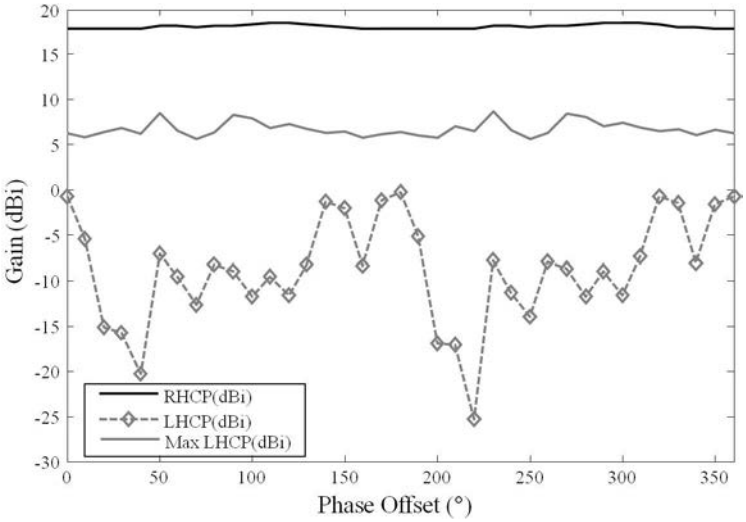

Figure 4.29: Simulated co-polar (black curve) and cross-polar (markers) realized gain in correspondence of the main beam tilted at -40° in the $\phi = 45°$ plane as a function of the phase offset. Maximum cross-polar gain (gray curve) in all cut-planes as a function of the phase offset.

radiation in all the azimuthal planes are similar for all values of phase offset (grey line, Fig. 4.29). Then, the variation of this parameter does not affect the maximum level of the cross-polarized side lobe and, for this reason, the regular arrangements previously analyzed are not considered here.

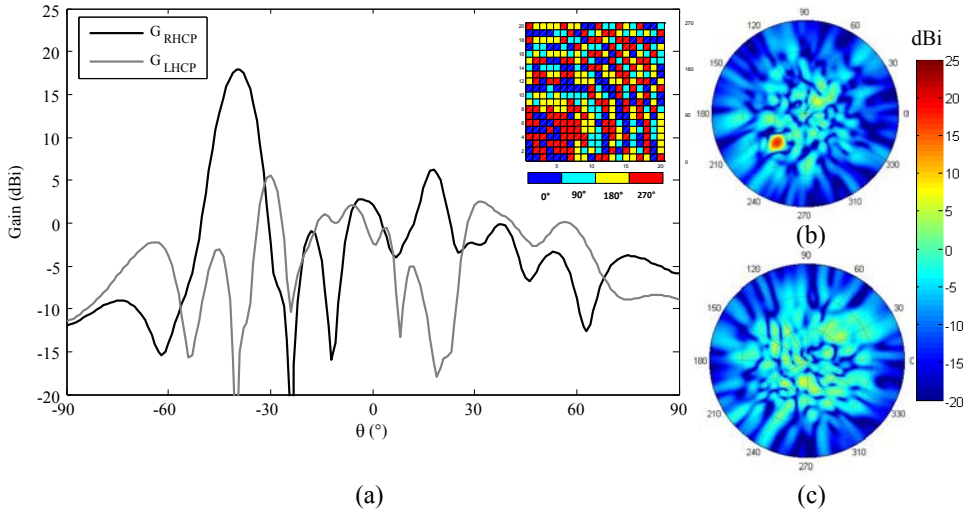

Figure 4.30: Simulated radiation pattern (realized gain) in the $\phi = 45°$ plane with main beam tilted at -40° in the same azimuthal plane. Inset: optimal phase distribution with optimized phase offset (220°).

The obtained phase distribution and radiation patterns are shown in Fig. 4.30. The maximum RHCP gain is 17.9 dBi with XPD greater than 35.0 dB in the main beam direction. The maximum side lobe level (SLL) is -11.9 dB in the $\phi = 45°$ plane.

A significant improvement of the cross polarization levels in the main beam direction is obtained. This technique has been validated numerically. Practically, for each value of main beam direction, an optimal phase offset has been selected spanning between 0° and 360°. The XPD is monitored during the numerical simulations and the optimal value is selected.

In practice, this optimization should be carried out for each desired angle of tilt and the value of phase offset with corresponding phase distribution saved on a database. The embedded control system will have the access to this information for a proper antenna configuration.

4.3 Prototype architecture

The array configuration with random sequential rotations, studied in the previous section, has been considered for a prototype realization. First, a bias lines arrangement in the receiving layer has been defined (Figs. 4.31, 4.33) inside a quarter of the transmitarray (10×10 unit-cells). Symmetries allow to cover the full array area with the same architecture. The corresponding transmitting layer is shown in Fig. 4.32. Only the passive patch antennas with the random sequential rotation are realized on this layer.

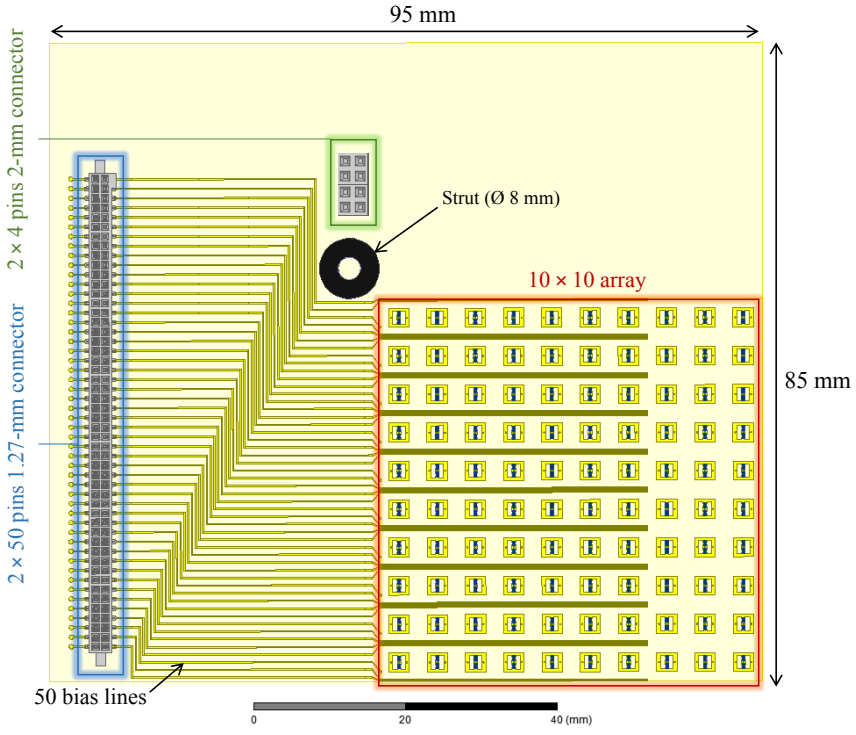

Figure 4.31: Quarter of the final array configuration (10×10 unit-cells), view of the receiving layer with 50 bias lines connected to the 2×50 pins 1.27-mm SMT connector with 2×50 pins.

A 2×50 pins 1.27-mm SMT connector manufactured by SAMTEC [89] is used to interconnect the array with the control logic boards. Half of the bias lines (50 lines) are routed

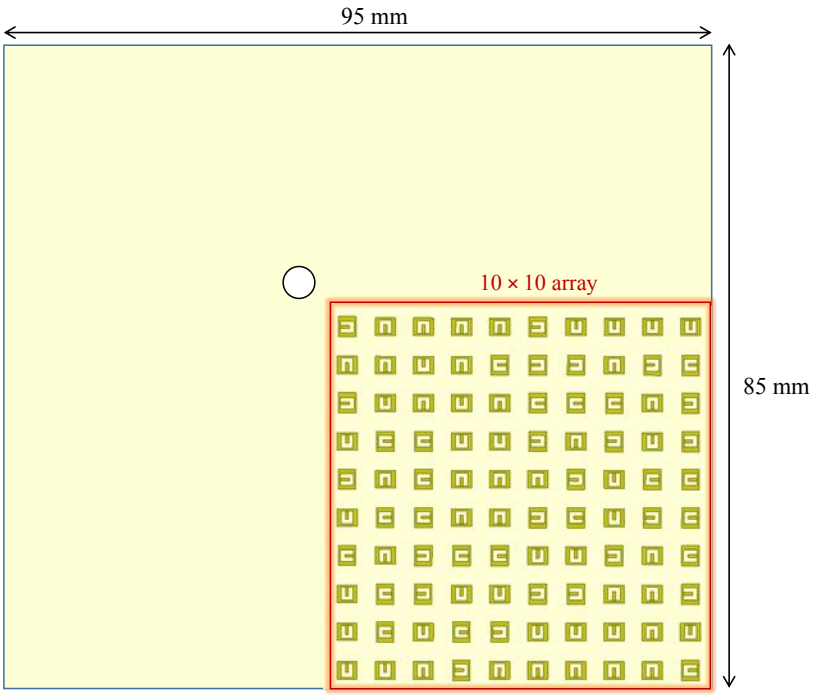

Figure 4.32: Quarter of the final array configuration (10×10 unit-cells), view of the transmitting layer.

on the top (receiving) layer while the other half are routed on the inner metal layer in order to minimize the occupied area and respect the line spacing constraints. The bias lines connection order is shown in Fig. 4.34. This sequence has been taken into account in the programming sequence of the control boards (Appendix B).

The layout obtained for the full array of Figs. 4.35, 4.36 has been manufactured and the 800 p-i-n diodes have been soldered on the receiving layer. In order to select the diodes states of each unit-cell, a positive or a negative current must be applied on each bias line. Four control boards, whose dimensions are 150×150 mm^2 [39] are used, one for each quarter of the transmitarray, which includes 100 unit-cells. Each board is formed by 13 shift registers and 25 4×4 switches. Chip resistors are used to obtained $\pm$ 10 mA of current on each bias line at the output of the switches. The total power consumption of the p-i-n diodes is about 4.8 W. The whole system, including the control boards, has a consumption of 20 W, due to the required voltage of the components used on these boards. Additional details on these PCB architecture are given in Appendix B. In order to minimize the possible influence of these circuits on the radiation pattern, they will be placed behind the focal plane and connected to the transmitarray receiving layer with four DC ribbon cables. In order to check the functionality of these control boards and the input program sequence, some tests are carried out with an array of 800 Light Emitting Diodes (LEDs) (Fig. 4.37). In correspondence of each cell of this test structure, two LEDs of different colors are connected, replicating the

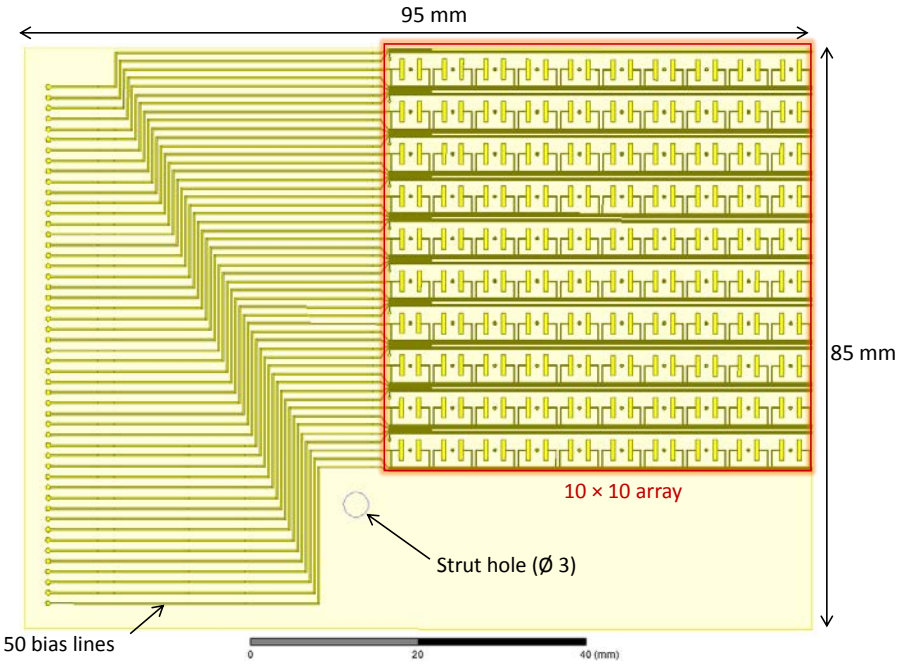

Figure 4.33: Quarter of the final array configuration (10×10 unit-cells), view of the biasing layer with 50 bias lines arrangement.

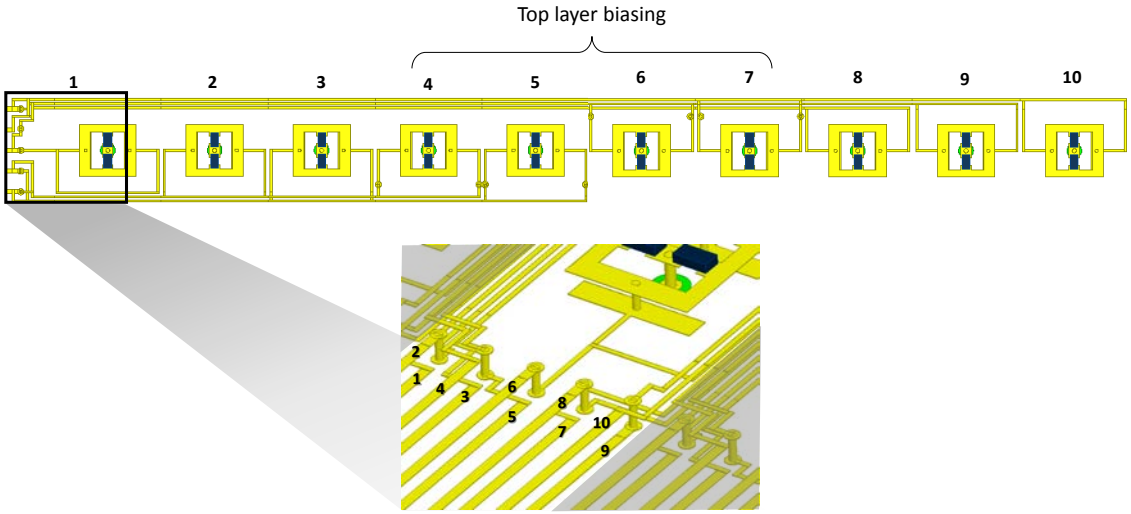

Figure 4.34: Bias line arrangement on a half transmitarray row (both the receiving and biasing layers are visible).

electrical configuration of the p-i-n diodes on the real unit-cell. Some photographs of the final prototype are shown in Fig. 4.38.

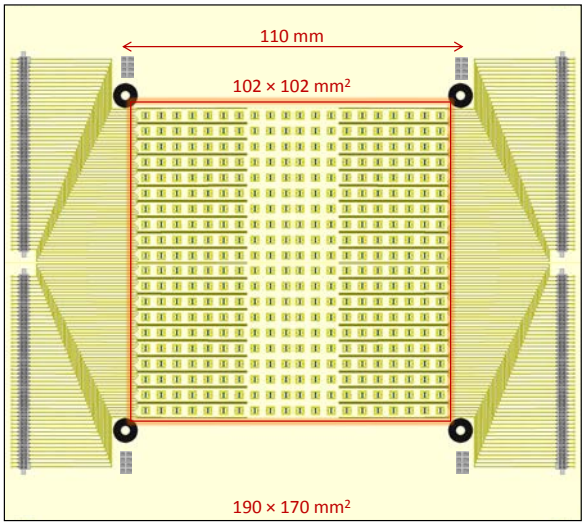

Figure 4.35: Scheme of the complete transmitarray prototype (receiving layer).

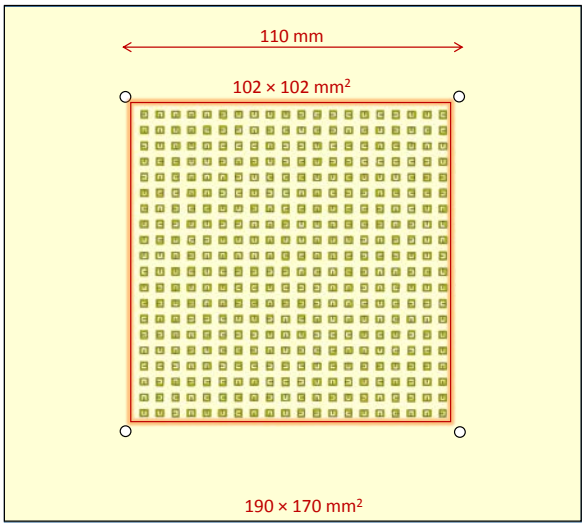

Figure 4.36: Scheme of the complete transmitarray prototype (transmitting layer).

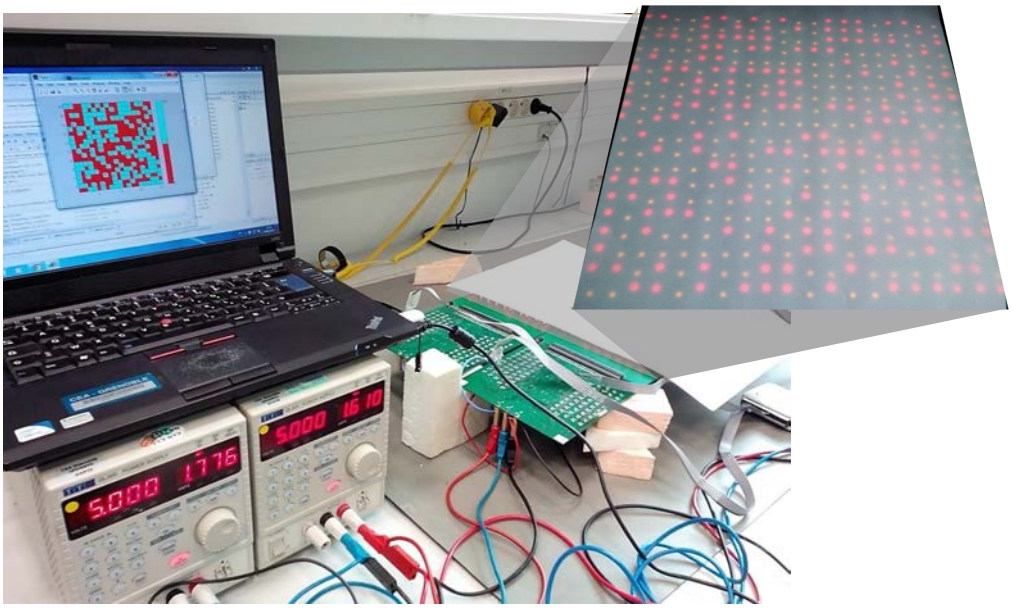

Figure 4.37: Photograph of the setup used to test the control boards.

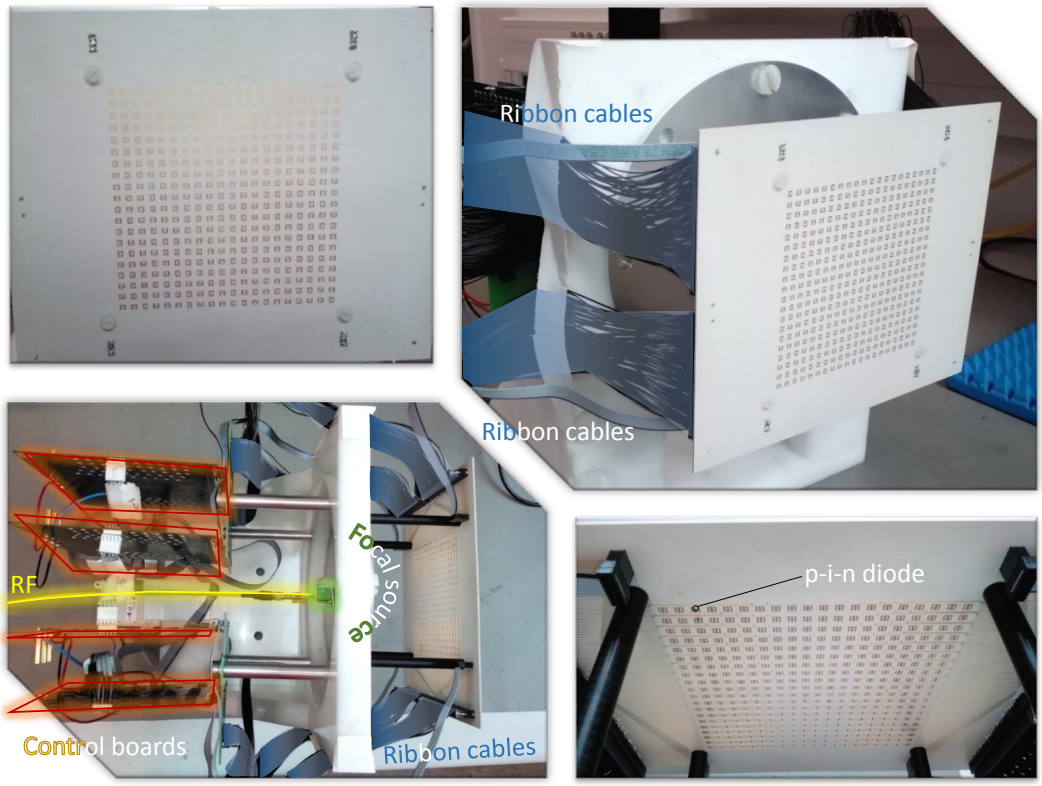

Figure 4.38: Photographs of the realized transmitarray prototype in Ka-band.

4.4 Experimental results

The prototype realized has been tested in anechoic chamber with the setup of Fig. 4.39. The broadside frequency response (Fig. 4.40) exhibits cross polarization levels below 0.0 dBi with a maximum broadside gain of 20.9 dBi in circular polarization. The measured 3-dB gain bandwidth goes from 27.4 to 31.7 GHz (14.6%) and a good agreement with the simulations has been found. The broadside axial ratio is lower than 1.8 dB in all this bandwidth (Fig. 4.40). The variation of the axial ratio in the (-15°,+15°) angular region is shown in Fig. 4.43 for different frequencies (27.4, 29.0 and 31.0 GHz) in the 3-dB bandwidth. It is under 3 dB in the main beam region in all the cases.

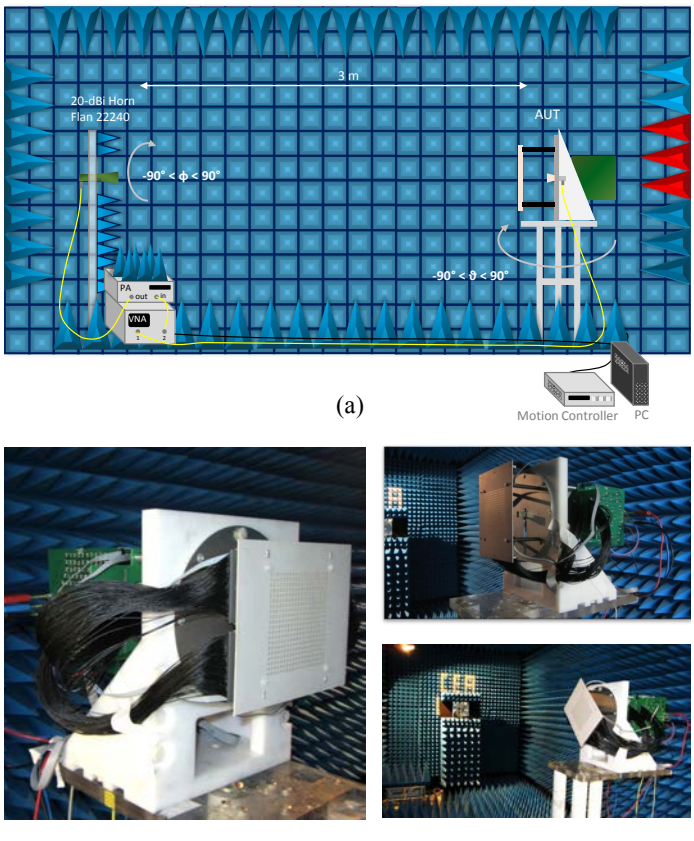

Figure 4.39: Sketch of the setup used for the characterization (a) and photographs (b) of the realized prototype in anechoic chamber.

The antenna power budget is summarized in Table 4.4. The aperture efficiency of the antenna is 9.5% (-10.2 dB) and is calculated as the difference between the measured gain (20.8 dBi) and the maximum directivity (31 dBi) expected from a uniform aperture of $10\,\lambda \times 10\,\lambda$. About 3 dB of losses are due to the use of linearly-polarized unit-cells in the sequential rotation scheme. In fact, with linearly-polarized patches placed on the transmitting layer, each antenna radiates half of its power in the intended circular polarization and the other

half in the cross-polarized component. The cross-polarized circular components interfere destructively in the boresight direction but they add constructively in other angular directions away from boresight. The 1-bit phase resolution leads to 3.5 dB of quantization losses. The illumination tapering of about 10 dB generated by the horn antenna placed at 60 mm from the receiving layer gives 1.2 dB of additional losses. Spillover (1.5 dB) and unit-cell insertion losses (1 dB) are added. The radiation patterns in circular polarization on the vertical plane of Figs. 4.41, 4.42 demonstrate almost the same performances achieved for both the LH and RH polarizations.

Steering angles between -60° and +60° have been considered in the horizontal plane. With tilted beams at -30° in the horizontal plane (Figs. 4.44, 4.45), a maximum LHCP gain of 19.1 dBi has been measured. The XPD is 33.5 dB in the same direction. In the RHCP mode, the measured XPD is 38.3 dB. The radiation patterns for a tilted beam at +40° in the same plane are shown in Figs. 4.46, 4.47. The values of gain, XPD and SLL in this case and for all the tested configurations in the horizontal plane are summarized in Tables 4.5, 4.6.

A range of ±50° has been considered on the vertical plane. With a tilted LH beam at -30° in this plane (Figs. 4.48, 4.49), the maximum measured gain is 19.9 dBi with XPD of 40.5 dB. In RH mode, the gain is 19.0 dBi and the XPD is 23 dB. Tilted beams at +40° in the vertical plane are shown in Figs. 4.50, 4.51. The performances for all the tested configurations are summarized in Tables 4.7, 4.8. Tilted beams up to ±40° are considered in the diagonal plane (Figs. 4.52, 4.53, 4.55, 4.56 and Tables 4.9, 4.10). A good agreement between measurements and simulations has been obtained in all the cases. Good axial ratios are maintained in the main beam regions within the working bandwidth (Fig. 4.54).

All the measured (co-polar circularly-polarized component) configurations are shown in Figs. 4.57, 4.59, 4.61 for the LHCP beams and in Figs. 4.58, 4.60, 4.62 for the RHCP beams.

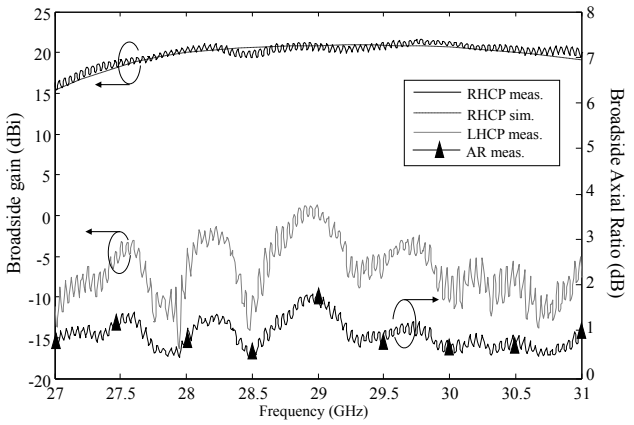

Figure 4.40: Simulated (solid lines) and measured (solid bold lines) realized gains in RHCP and LHCP at broadside and measured broadside axial ratio (markers).

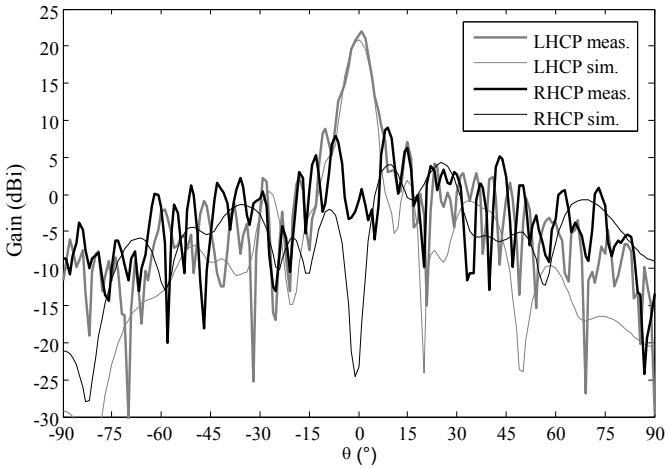

Figure 4.41: Simulated (solid lines) and measured (solid bold lines) radiation patterns (realized gain) at 29.0 GHz in the vertical plane. LHCP beam at broadside (vertical plane).

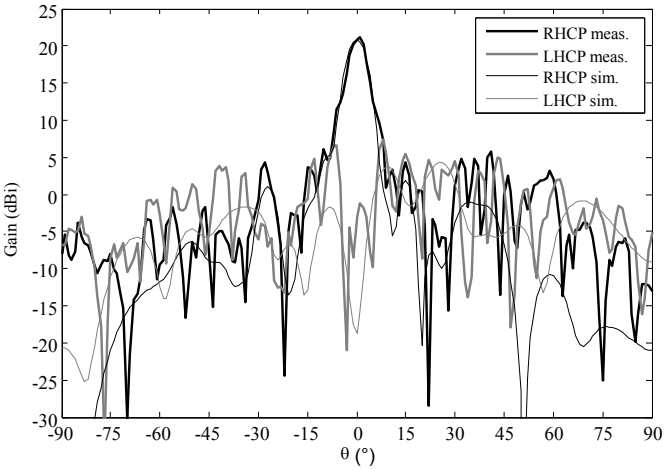

Figure 4.42: Simulated (solid lines) and measured (solid bold lines) radiation patterns (realized gain) at 29.0 GHz in the vertical plane. RHCP beam at broadside (vertical plane).

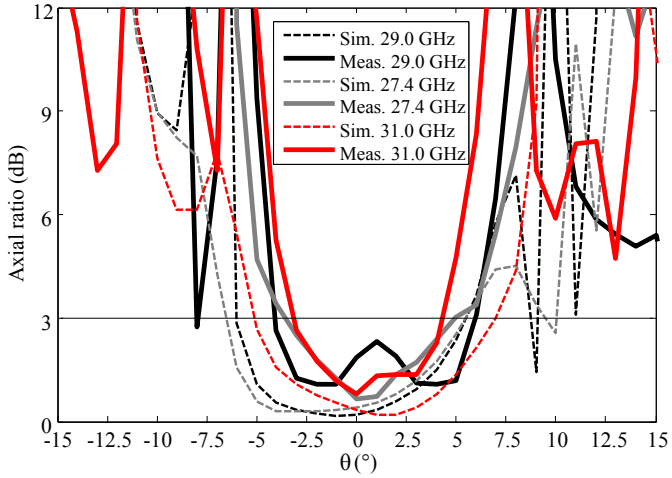

Figure 4.43: Simulated and measured axial ratio in the main beam angular region (broadside configuration) at 27.4, 29.0 and 31.0 GHz.

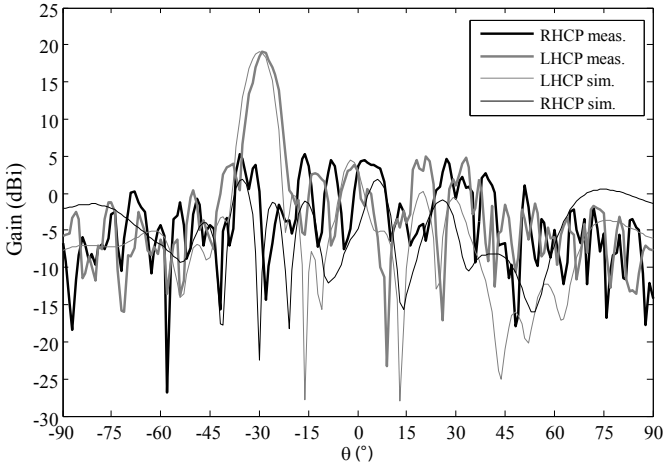

Figure 4.44: Simulated (solid lines) and measured (solid bold lines) radiation patterns (realized gain) at 29.0 GHz in the horizontal plane. LHCP beam at -30^o (horizontal plane).

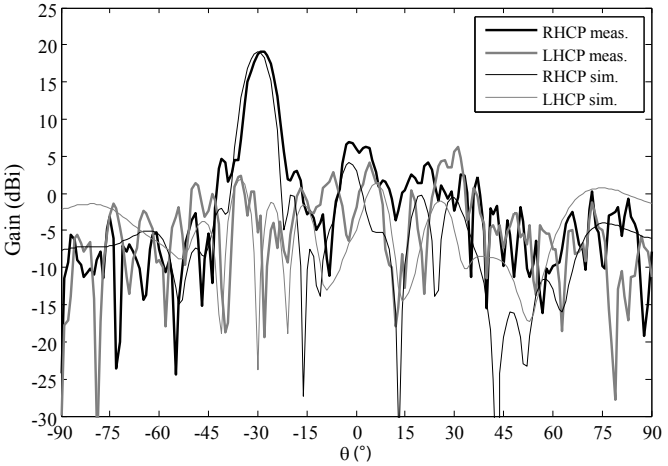

Figure 4.45: Simulated (solid lines) and measured (solid bold lines) radiation patterns (realized gain) at 29.0 GHz in the horizontal plane. RHCP beam at -30^o (horizontal plane).

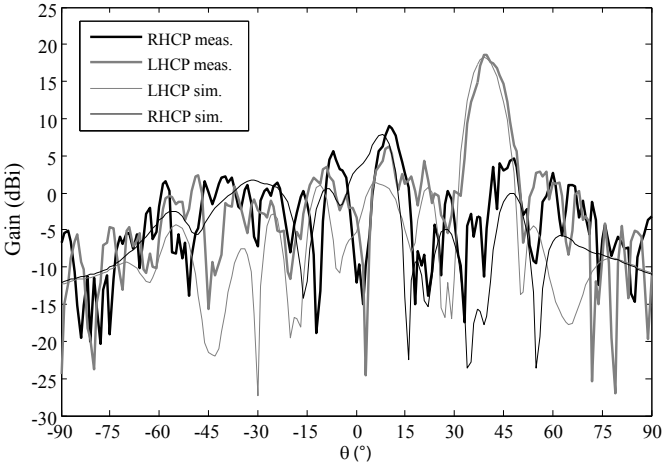

Figure 4.46: Simulated (solid lines) and measured (solid bold lines) radiation patterns (realized gain) at 29.0 GHz in the horizontal plane. LHCP beam at 40^o (horizontal plane).

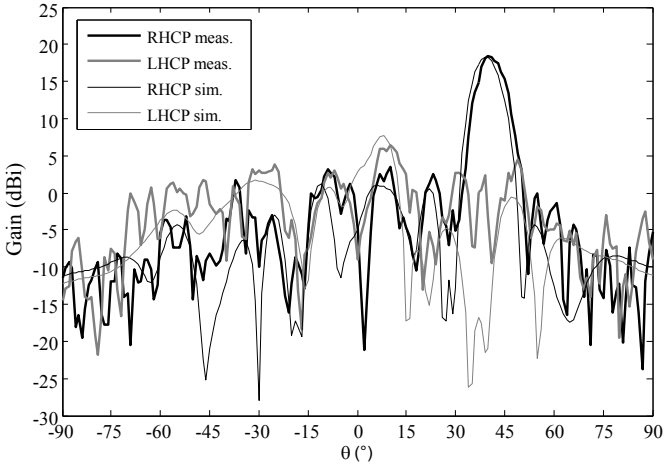

Figure 4.47: Simulated (solid lines) and measured (solid bold lines) radiation patterns (realized gain) at 29.0 GHz in the horizontal plane. RHCP beam at 40^o (horizontal plane).

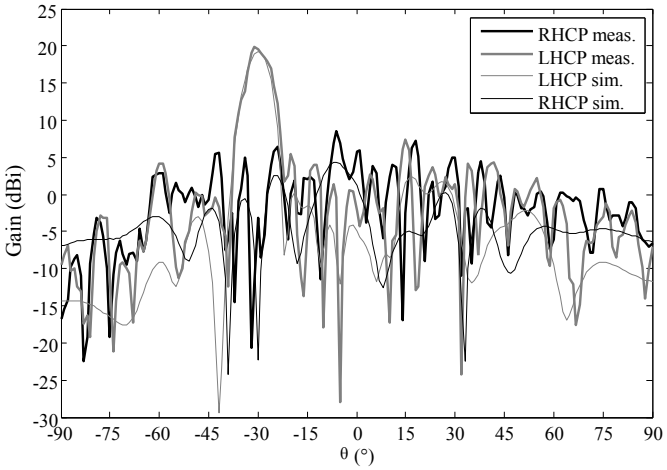

Figure 4.48: Simulated (solid lines) and measured (solid bold lines) radiation patterns (realized gain) at 29.0 GHz in the vertical plane. LHCP beam at -30^o (vertical plane).

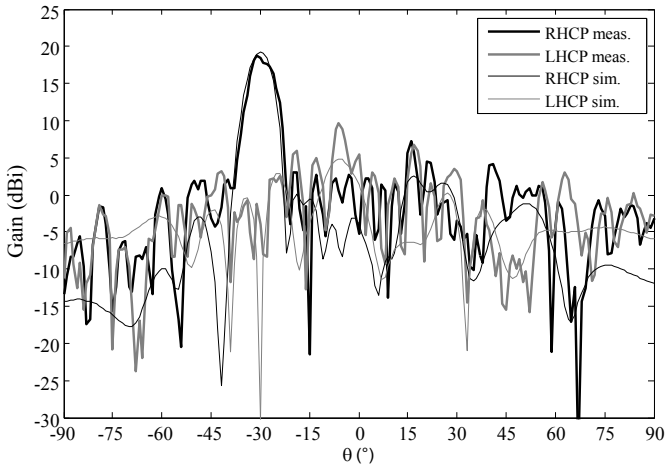

Figure 4.49: Simulated (solid lines) and measured (solid bold lines) radiation patterns (realized gain) at 29.0 GHz in the vertical plane. RHCP beam at -30^o (vertical plane).

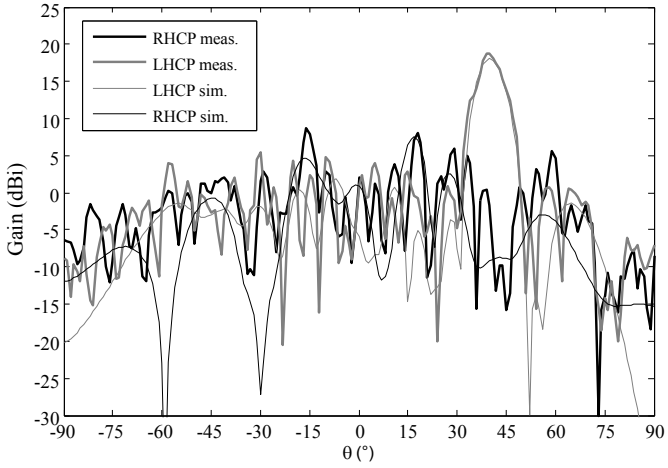

Figure 4.50: Simulated (solid lines) and measured (solid bold lines) radiation patterns (realized gain) at 29.0 GHz in the vertical plane. LHCP beam at 40^o (vertical plane).

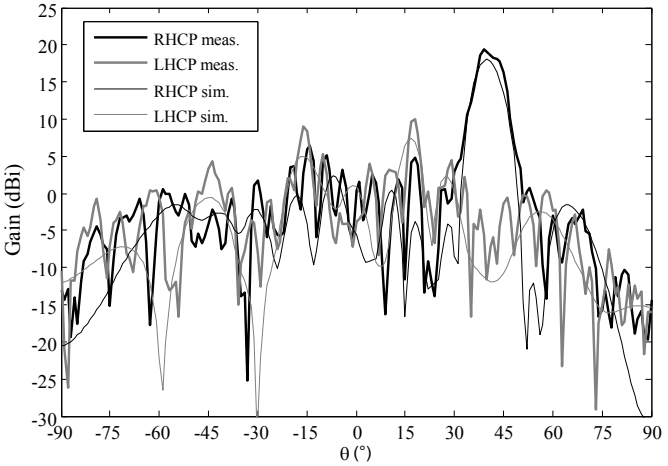

Figure 4.51: Simulated (solid lines) and measured (solid bold lines) radiation patterns (realized gain) at 29.0 GHz in the vertical plane. RHCP beam at 40^o (vertical plane).

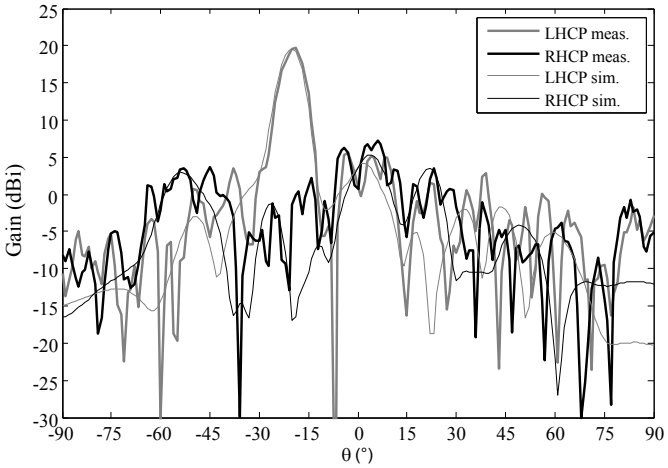

Figure 4.52: Simulated (solid lines) and measured (solid bold lines) radiation patterns (realized gain) at 29.0 GHz in the diagonal plane. LHCP beam at -20^o (diagonal plane).

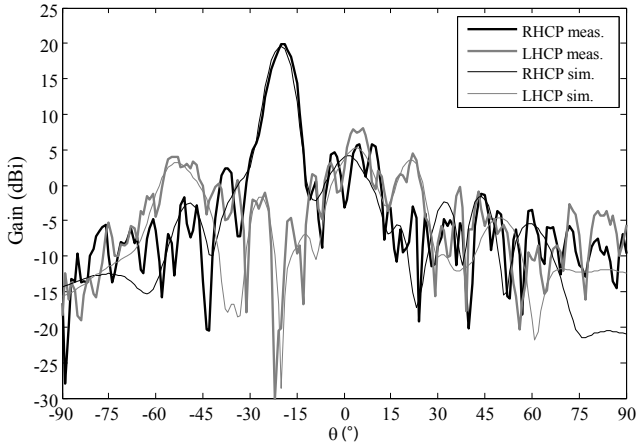

Figure 4.53: Simulated (solid lines) and measured (solid bold lines) radiation patterns (realized gain) at 29.0 GHz in the diagonal plane. RHCP beam at -20^o (diagonal plane).

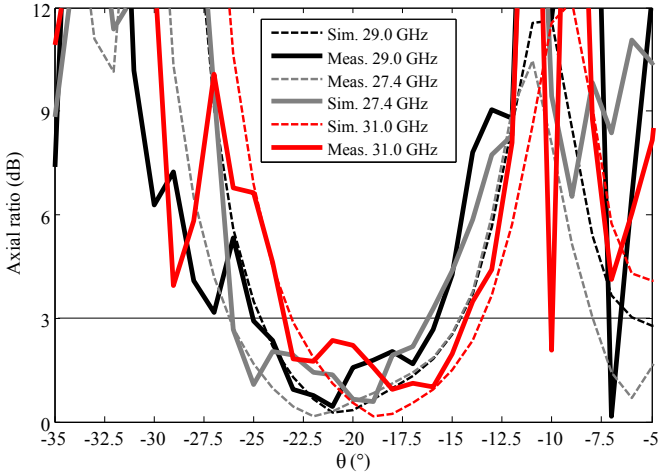

Figure 4.54: Simulated and measured axial ratio in the main beam angular region (-20^o tilted beam in the diagonal plane) at 27.4, 29.0 and 31.0 GHz.

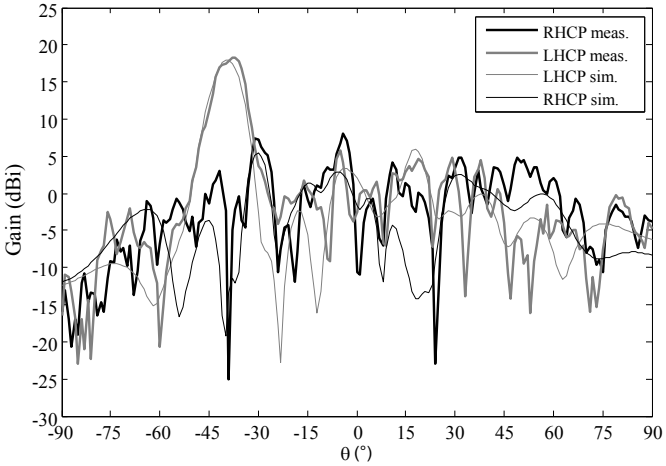

Figure 4.55: Simulated (solid lines) and measured (solid bold lines) radiation patterns (realized gain) at 29.0 GHz in the diagonal plane. LHCP beam at -40^o (diagonal plane).

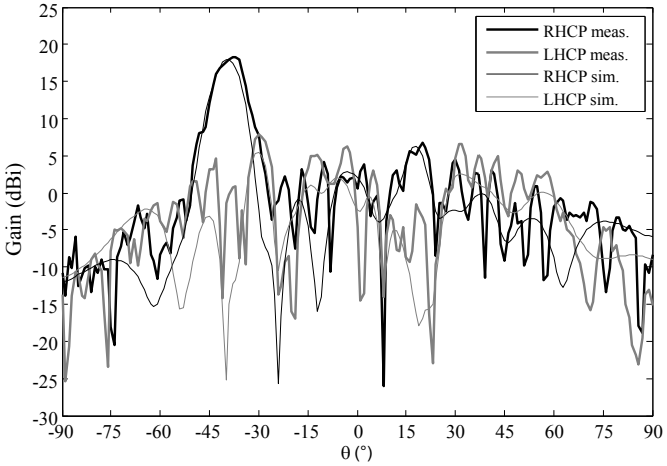

Figure 4.56: Simulated (solid lines) and measured (solid bold lines) radiation patterns (realized gain) at 29.0 GHz in the diagonal plane. RHCP beam at -40^o (diagonal plane).

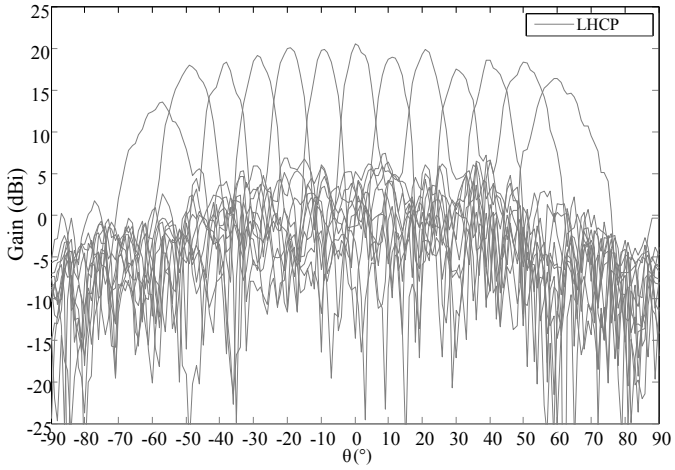

Figure 4.57: Measured radiation patterns (LHCP realized gain) at 29.0 GHz in the horizontal plane with different steering angles.

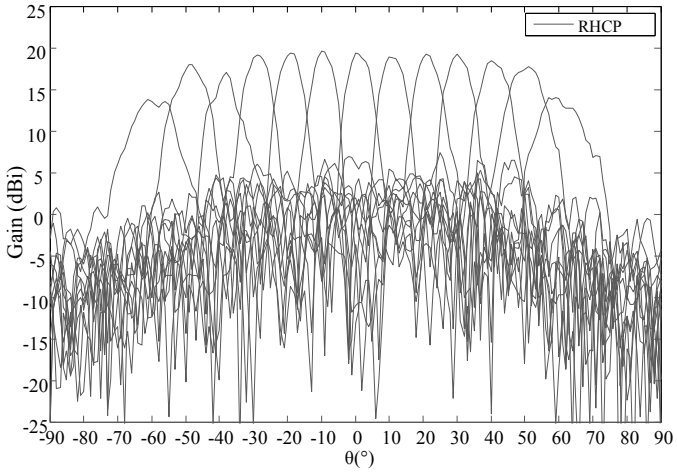

Figure 4.58: Measured radiation patterns (RHCP realized gain) at 29.0 GHz in the horizontal plane with different steering angles.

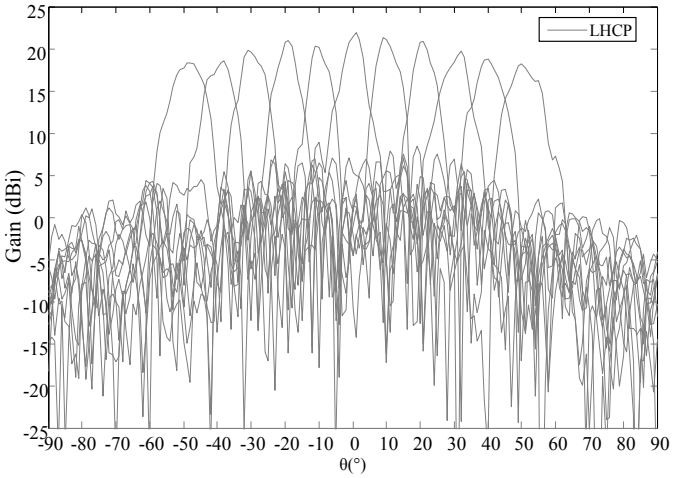

Figure 4.59: Measured radiation patterns (LHCP realized gain) at 29.0 GHz in the vertical plane with different steering angles.

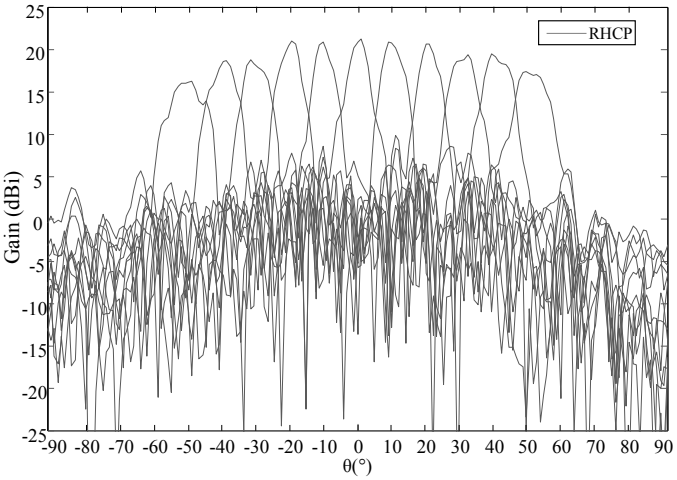

Figure 4.60: Measured radiation patterns (RHCP realized gain) at 29.0 GHz in the vertical plane with different steering angles.

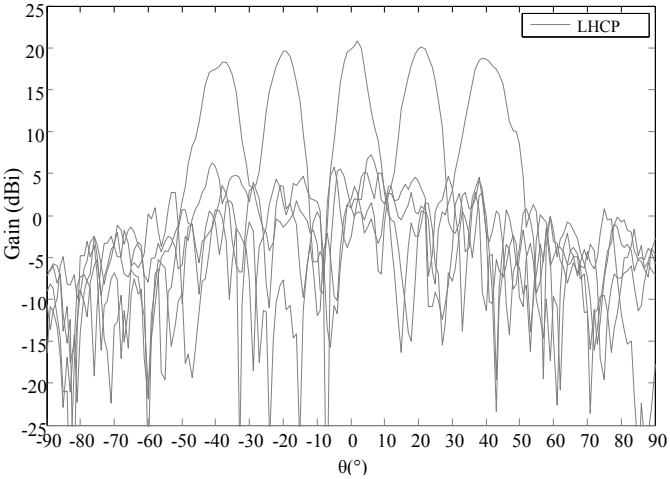

Figure 4.61: Measured radiation patterns (LHCP realized gain) at 29.0 GHz in the diagonal plane with different steering angles.

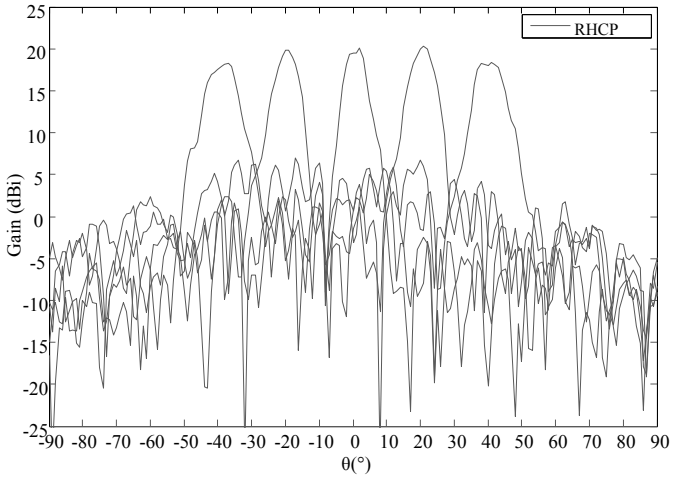

Figure 4.62: Measured radiation patterns (RHCP realized gain) at 29.0 GHz in the diagonal plane with different steering angles.

Table 4.4: Power budget and radiation characteristics at 29.0 GHz for the realized prototype at broadside.

	Simulation	Measurement
Focal source gain at broadside	11.7 dBi	11.7 dBi
Theoretical directivity of a uniform aperture	31.0 dBi	-
Quantization loss	3.5 dB	-
Linearly-polarized unit-cells losses	3.0 dB	-
Tapering loss	1.2 dB	-
Broadside directivity (RHCP)	23.3 dBi	-
Spillover loss	1.5 dB	-
Unit-cells I.L.	1 dB	-
Broadside gain (RHCP)	20.8 dBi	20.8 dBi
Power efficiency	58.7%	58.7%
Aperture efficiency	9.5%	9.5%

Table 4.5: Simulated and measured radiation characteristics of the tested reconfigurable transmitarray at 29.0 GHz. LHCP beams in the horizontal plane.

Angle	Gain (dBi)		XPD (dB)		SLL (dB)	
	Sim.	Meas.	Sim.	Meas.	Sim.	Meas.
-60°	15.2	13.5	36.2	18.5	-12.2	-8.8
-50°	18.0	17.3	36.0	25.7	-11.6	-15.5
-40°	17.8	18.3	40.0	24.3	-16.6	-12.5
-30°	19.1	19.1	40.0	33.5	-14.7	-14.0
-20°	19.8	20.1	38.0	24.6	-18.2	-14.3
-10°	20.6	19.8	30.0	20.6	-19.0	-14.0
0°	20.9	21.0	40.0	22.5	-16.9	-14.8
10°	20.1	18.9	37.5	21.3	-16.1	-12.9
20°	20.3	19.8	44.3	32.4	-16.8	-12.5
30°	19.5	17.3	40.0	41.5	-18.1	-12.6
40°	18.1	18.5	30.1	17.1	-16.8	-11.8
50°	17.1	18.3	39.1	26.3	-15.1	-16.4
60°	15.3	16.4	37.3	23.4	-14.0	-11.4

Table 4.6: Simulated and measured radiation characteristics of the tested reconfigurable transmitarray at 29.0 GHz. RHCP beams in the horizontal plane.

Angle	Gain (dBi)		XPD (dB)		SLL (dB)	
	Sim.	Meas.	Sim.	Meas.	Sim.	Meas.
-60°	15.2	13.8	35.2	10.8	-12.6	-8.8
-50°	17.3	18.0	35.3	19.2	-15.5	-13.0
-40°	17.7	17.1	40.0	20.1	-9.9	-12.4
-30°	19.1	19.1	42.0	38.3	-17.3	-12.8
-20°	19.9	19.4	49.0	42.6	-17.6	-13.0
-10°	20.7	19.7	30.0	17.6	-16.3	-14.8
0°	20.9	20.8	39.0	24.0	-16.9	-14.8
10°	20.0	18.9	39.5	21.1	-16.9	-14.3
20°	20.4	19.2	44.2	29.9	-16.9	-15.0
30°	19.5	19.2	40.5	22.2	-19.0	-13.2
40°	18.2	18.5	30.1	21.5	-17.6	-15.1
50°	17.1	17.6	38.0	27.6	-15.3	-14.0
60°	15.5	14.0	44.0	16.4	-14.2	-7.6

Table 4.7: Simulated and measured radiation characteristics of the tested reconfigurable transmitarray at 29.0 GHz. LHCP beams in the vertical plane.

Angle	Gain (dBi)		XPD (dB)		SLL (dB)	
	Sim.	Meas.	Sim.	Meas.	Sim.	Meas.
-50°	17.1	18.3	38.0	19.5	-14.7	-8.6
-40°	18.6	18.0	38.0	28.2	-14.4	-9.5
-30°	19.2	19.9	41.2	40.5	-14.9	-11.4
-20°	20.0	20.9	45.0	27.9	-14.6	-13.9
-10°	20.1	20.3	32.0	25.0	-18.7	-16.0
0°	20.9	21.0	40.0	22.5	-19.0	-16.0
10°	20.7	21.4	31.1	20.0	-17.9	-15.0
20°	19.8	20.8	21.8	38.0	-16.7	-14.4
30°	19.2	19.7	40.0	32.7	-17.8	-13.3
40°	18.0	18.7	27.0	27.6	-16.4	-13.0
50°	18.2	16.8	37.0	24.0	-16.9	-10.0

Table 4.8: Simulated and measured radiation characteristics of the tested reconfigurable transmitarray at 29.0 GHz. RHCP beams in the vertical plane.

Angle	Gain (dBi)		XPD (dB)		SLL (dB)	
	Sim.	Meas.	Sim.	Meas.	Sim.	Meas.
-50°	17.0	18.3	34.6	19.6	-14.0	-11.1
-40°	18.0	18.7	34.0	24.0	-13.5	-12.2
-30°	19.2	19.0	40.0	23.0	-16.8	-12.0
-20°	20.0	21.0	45.0	26.0	-16.0	-14.0
-10°	20.2	20.8	32.0	31.4	-18.7	-16.5
0°	20.9	20.8	39.0	24.0	-18.8	-16.4
10°	20.7	20.8	36.0	22.0	-17.7	-15.0
20°	19.8	20.6	38.0	27.0	-16.5	-10.8
30°	19.3	19.3	43.0	28.7	-17.4	-13.1
40°	18.0	19.4	28.0	30.0	-11.0	-10.0
50°	16.9	17.3	45.0	30.3	-13.0	-11.0

Table 4.9: Simulated and measured radiation characteristics of the tested reconfigurable transmitarray at 29.0 GHz. LHCP beams in the diagonal plane.

Angle	Gain (dBi)		XPD (dB)		SLL (dB)	
	Sim.	Meas.	Sim.	Meas.	Sim.	Meas.
-40°	17.9	18.3	37.0	43.0	-14.5	-13.0
-20°	19.8	19.6	35.0	32.0	-15.4	-14.4
0°	20.9	21.0	40.0	22.5	-19.3	-16.2
20°	19.9	20.1	29.8	19.0	-17.2	-14.5
40°	18.4	18.7	40.0	23.2	-15.4	-11.5

Table 4.10: Simulated and measured radiation characteristics of the tested reconfigurable transmitarray at 29.0 GHz. RHCP beams in the diagonal plane.

Angle	Gain (dBi)		XPD (dB)		SLL (dB)	
	Sim.	Meas.	Sim.	Meas.	Sim.	Meas.
-40°	17.9	18.3	37.0	43.0	-11.7	-11.9
-20°	19.8	19.6	45.0	39.0	-15.6	-11.5
0°	20.9	20.8	39.0	24.0	-19.5	-14.5
20°	20.0	20.3	31.8	22.0	-17.3	-14.5
40°	18.4	18.4	45.0	37.4	-15.2	-14.1

4.5 Conclusions

In this Chapter, the design, realization and experimental characterization of a 400-elements reconfigurable transmitarray working in circular polarization in Ka-band has been presented. The design is based on the unit-cell proposed in Chapter 3 in linear polarization.

The sequential rotation technique studied in Chapter 2 has been applied to the passive transmitting layer in order to generate the circular polarization. Several rotation schemes have been considered. Numerical simulations have shown that the regular ones give good results in terms of axial ratio for steering in the two cardinal planes, but generate spurious cross-polarized side lobes when other cut-planes are considered. In the worst case (at 45° in a diagonal plane), a spurious beam almost at the same gain as the main beam is generated. In order to avoid this spurious beam, random rotations are applied. The extensive numerical analysis of this configuration has shown good performances in terms of polarization purity in the main beam region without causing any spurious lobe. The effects of the phase reference for the transmitarray distributions has been studied; the cross polarization levels in the main beam direction can be further reduced by changing this parameter. The proposed configuration has been realized and tested in anechoic chamber. A broadside gain of 20.8 dBi in circular polarization is obtained with a XPD of about 25 dB. The LHCP/RHCP switching capability has been demonstrated. In all the tested cases, a good agreement with the simulations and a beam-steering capability of ±60°,±50°,±40° have been demonstrated on the horizontal, vertical and diagonal planes, respectively.

Comparing the obtained results with the literature, the proposed configuration is the first one that operates in circular polarization with electronic beam-steering in all the azimuthal planes. It is among the few examples that permit to control also the polarization (LHCP/RHCP) and it is the first one that implements the sequential rotations.

In addition, it exhibits a power efficiency of about 58%. The aperture efficiency is about 10%.

The use of multiple planar sources leads to a dramatic reduction of the focal distance F and then the proposed architecture can be more easily integrated on mobile platforms. Some numerical and experimental results are given in Appendix C. Further studies can include designs with increased phase resolutions in order to improve the aperture efficiency and reduce the Side Lobe Level.

Chapter 5

Reconfigurable circularly-polarized unit-cell in Ka-band

In Chapters 3 and 4, the circular polarization of the radiated beam has been obtained by using linearly-polarized (LP) reconfigurable unit-cells with the sequential rotation technique. In order to increase the antenna directivity and gain, and then improve the aperture efficiency, one possibility is to generate the circular polarization (CP) directly with each unit-cell. This leads to a 3-dB higher gain if the unit-cell losses are unchanged. However, the capability of switching between LHCP and RHCP is irremediably lost.

With this objective, the design of a reconfigurable unit-cell in Ka-band working in circular polarization is presented in this chapter. Handling the transmission phase shift and generating at the same time a good circular polarization (Axial Ratio < 3 dB) is the main addressed challenge. The proposed architecture works in linear polarization in the receiving layer and the circular polarization is generated on the transmitting layer. A 1-bit phase resolution is considered and achieved by integrating two p-i-n diodes in the design, following the approach proposed in Chapter 3. The required bias network design is discussed in detail. Finally, an *ad-hoc* characterization setup in waveguide suitable for CP unit-cells is presented.

5.1 Unit-cell design

The proposed unit-cell, whose dimensions are 5.1×5.1 mm^2 (i.e. half-wavelength in free-space at 29.4 GHz), is designed on the same substrate stack as the linearly-polarized unit-cell described in Chapter 3. There are four metal layers (Fig. 5.1), two identical substrates of

Table 5.1: Unit-cell geometrical dimensions in millimetres.

	value		value		value
p	5.1	L_C	2.5	L_2	1.91
L_1	2.6	W_C	0.5	W_2	0.54
W_1	2.78	d_V	0.2	L_g2	1.5
L_{g1}	1.8	d_h	0.7	W_{g2}	1.1
W_{g1}	1.8	d_B	0.15	t_2	0.74
t_1	0.5	W_B	0.1	h_s	0.508
				h_f	0.114

Rogers Duroid RT6002 ($h_s = 508$ μm, $\epsilon_r = 2.94$, tan$\delta = 0.0012$) [78] and one bonding film of Arlon CuClad 6700 ($h_f = 114\mu$m, $\epsilon_r = 2.35, tan\delta = 0.0025$). As in the architecture of Chapter 3, the receiving layer (Fig. 5.1(d)) is composed of a rectangular patch loaded by an O-shaped slot and the two p-i-n diodes; this active patch is linearly-polarized. It is worth to notice that this choice allows the use of simple and wideband focal sources and at the same time a simple handling of the bias lines required to polarized the two diodes, as discussed in Chapter 3. In the transmitting layer, a square patch with truncated corners loaded by a U-shaped slot is designed in order to generate the circular polarization.

In the EM simulator, the two p-i-n diodes are modelled as a Gallium-Arsenide block (ϵ_r = 12.9, $0.686 \times 0.368 \times 0.19$ mm^3) and a lumped-element equivalent circuit extracted from the measurements presented in Chapter 3. The active patch is connected to the passive one with a metallized via hole ($d_V = 200$ μm) placed at the center of the unit-cell. A ground plane occupies one of the two intermediate layers. The other inner layer, shown in Fig. 5.1(d), contains the biasing lines. All geometrical dimensions are defined in Fig. 5.1 and reported in Table 5.1.

5.1.1 Bias network

The two diodes are polarized with a RF/DC decoupling circuit formed by two distributed capacitors in microstrip technology. Their dimensions are the same as for the linearly-polarized unit-cell of the transmitarray presented in Chapter 4. As already analyzed in Chapter 3, these structures allow to obtain a good isolation ($>$ 15 dB) while minimizing the space occupied. In the unit-cell of Chapter 3, the passive patch worked in linear polarization and it is used for the ground connection required for the polarization of the two p-i-n diodes. In particular, two metallized vias were placed on the horizontal axis of the patch antenna (in correspondence of the center of the non-radiating edges) in order to minimize the impact on the electric field of the TM01 fundamental mode. In the architecture proposed here, the

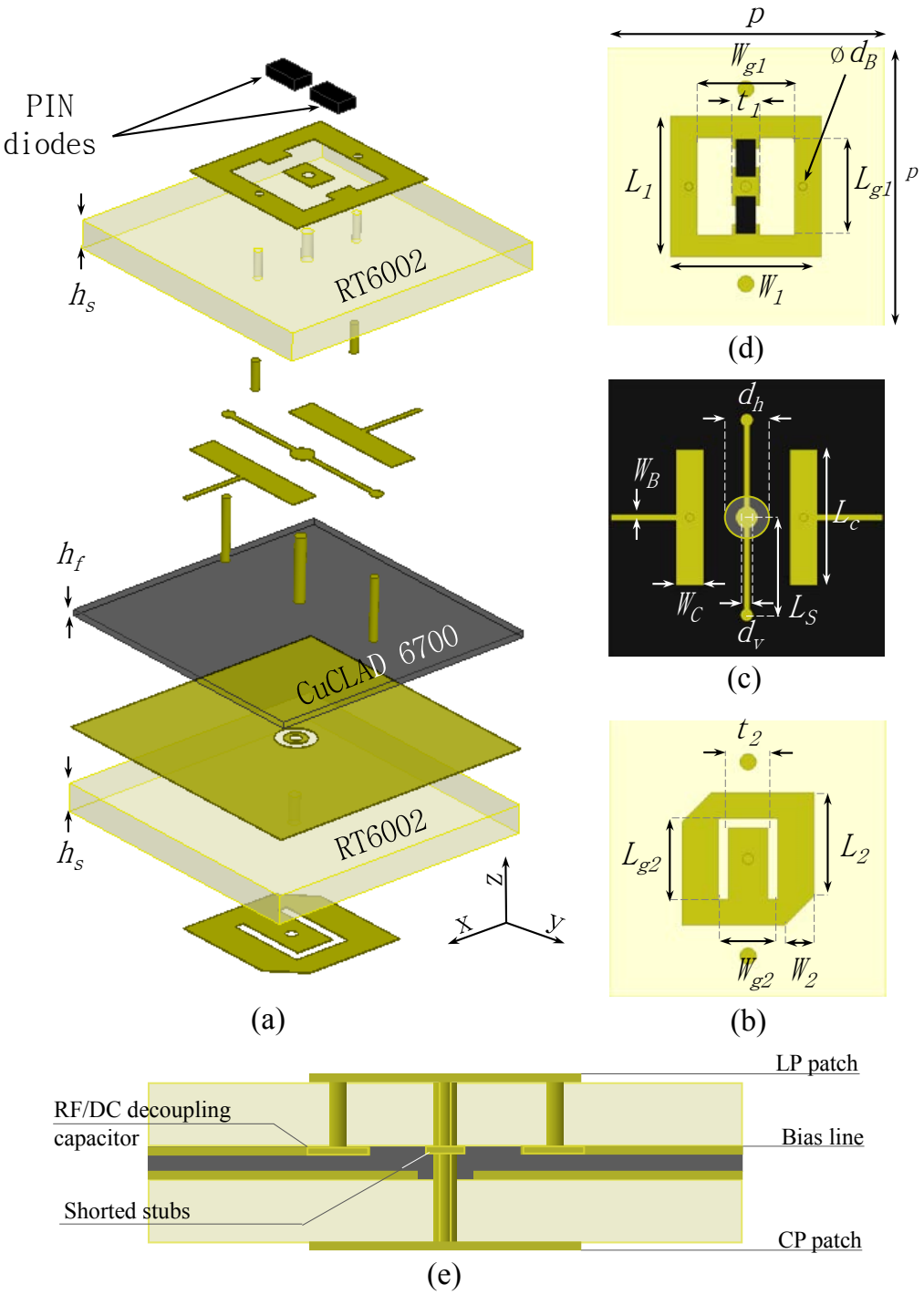

Figure 5.1: Scheme of the unit-cell architecture. Exploded view (a), transmitting layer (b), biasing layer (c), receiving layer (d) and cut view (e).

passive patch antenna is circularly-polarized and then placing one or more metallized vias directly on this patch without perturbing the two excited orthogonal modes is hardly possible. In any case, this would increase drastically the sensitivity to the fabrication errors (drilling diameter and misalignments between layers). For these reasons, the ground connection is realized here by using two short-circuited quarter-wavelength stubs connected to the center metallized via (Fig. 5.1(c)). This solution enables the use of the truncated-corners square patch on the transmitting layer and reduces drastically the dependence of the polarization purity to the manufacturer constraints.

5.1.2 Numerical results

Scattering parameters

The unit-cell has been simulated using the commercial software Ansys HFSS v.15 [80] with periodic boundary conditions and Floquet port excitations to take into account the mutual couplings to the surrounding unit-cells, as already done in Chapter 3 (Fig. 5.2). The full-wave simulations under normal incidence give the scattering parameters associated to the circular polarization (see Appendix A) calculated for the two phase states (Fig. 5.3).

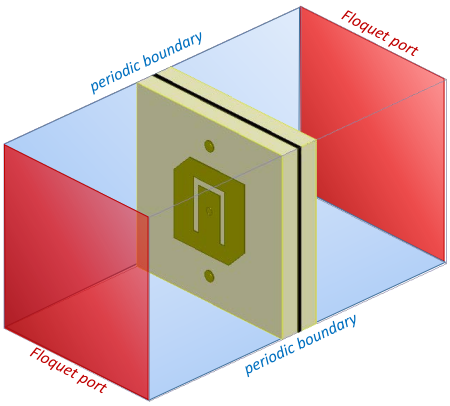

Figure 5.2: Scheme of the HFSS model used to calculate the scattering parameters for the unit-cell of Fig. 5.1.

The reflection coefficient S_{11} from the diode-loaded patch side (port 1) is lower than -10 dB between 27.4 GHz and 30.9 GHz for the 0°-state and between 27.3 GHz and 31.0 GHz for the 180°-state. The -10 dB matching bandwidth from the other port (port 2, S_{22}) spans between 27.8 GHz and 31.0 GHz for the 0°-state and between 27.4 GHz and 31.0 GHz for the 180°-state. The minimum insertion loss is only 1.02 dB at 29 GHz with a 3-dB transmission bandwidth of 27.4-30.9 GHz for the 0°-state and 27.4-31.0 GHz in the 180°-state. The phase difference between the two states is around 180° with a maximum error of 6°, as shown in

Fig. 5.3(b). This error is mainly due to the non-symmetrical geometry of the two patches and their relative positions.

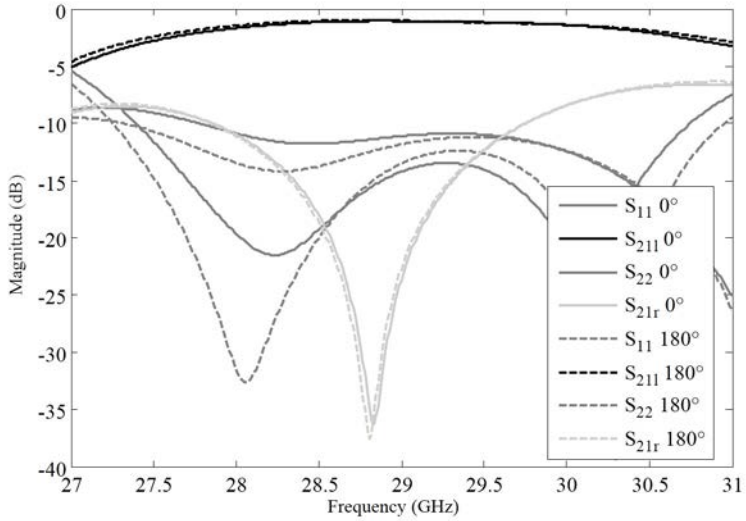

(a)

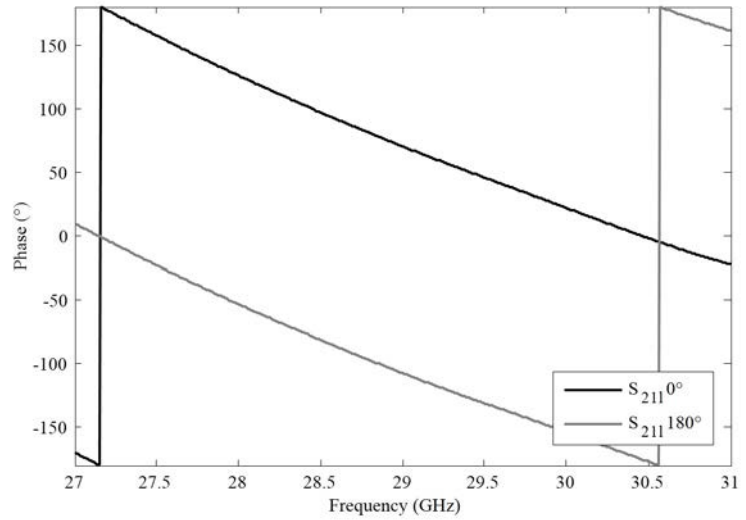

(b)

Figure 5.3: Scattering parameters (magnitude (a) and phase (b)) of the unit-cell simulated with periodic boundary conditions and Floquet port excitation. S_{11} and S_{22} are the reflection coefficients calculated from the linearly-polarized and circularly-polarized layers, respectively. The transmission coefficients S_{21l}, S_{21r} are referred to the circular polarization and they have been calculated as reported in Appendix A.

Radiation Patterns

The simulated radiation patterns of the transmitting layer patch antenna are shown at 29.2 GHz in Fig. 5.4(a) for the 0°/180° states in the E-plane. The gain at broadside reaches 3.77 dBi and the 3-dB beam-width is 88°. As shown in Fig. 5.4(a), the broadside co-polarized realized gain is between 1.68 and 3.79 dBi between 27.5 and 31 GHz. The broadside axial

ratio is lower than 3 dB between 28.4 GHz and 29.2 GHz (about 2.8%). This bandwidth is mainly limited by the truncated-corner patch antenna and can be enlarged by considering different stacking or patch shapes to generate the circular polarization. However, the axial ratio can be improved by applying the sequential rotation technique in the transmitting layer, as analysed and demonstrated with the passive prototype of Chapter 2.

If compared to the linearly-polarized unit-cell presented in Chapter 3, the proposed design working in circular polarization exhibits similar performances in terms of minimum insertion loss, 3-dB bandwidth and realized gain.

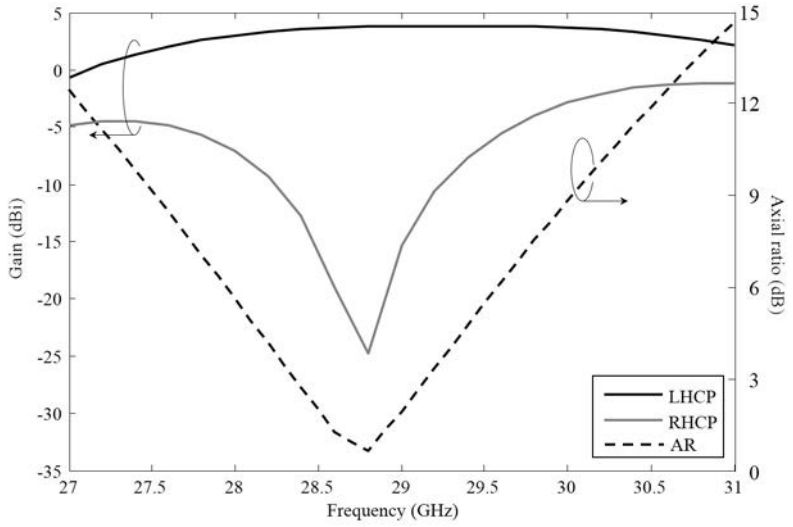

(a)

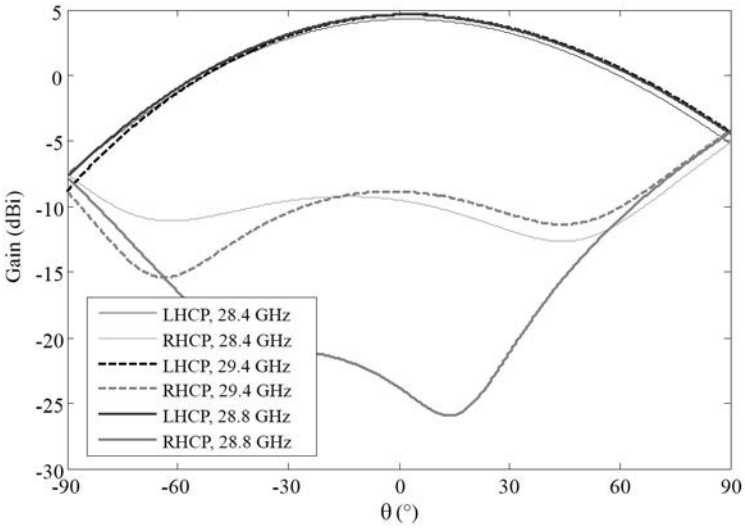

(b)

Figure 5.4: Broadside realized gains, axial ratio (a) and radiation pattern at 28.4, 28.8 and 29.4 GHz (b) of the unit-cell simulated with periodic boundary conditions.

5.1.3 Oblique incidence

The effect of an oblique incidence are investigated with a proper set of full-wave simulations with periodic boundary conditions (Fig. 5.2). Only the unit-cell in the state 0° is considered in this study. Similar considerations are valid for the other phase state. With angles between 10° and 40° in E-plane (considering the receiving layer patch orientation as reference) the simulated reflection and transmission coefficients are shown in Fig. 5.5. The reflection coefficient (Fig. 5.5(a)) from the port 1 (active patch) is under -10 dB within the nominal bandwidth for incidence angles up to 30°. This bandwidth is extended by about 500 MHz towards lower frequencies in the 40° case. For the reflection coefficient on the opposite side (Fig. 5.5(c)), the S_{22} is under -8 dB for all the incidence angles. As expected, the minimum insertion loss (Fig. 5.5(b)) increases with the angle of incidence but it is always lower than 1.5 dB. The 3-dB bandwidth covers always the nominal frequency band (27.5 - 31.0 GHz). With angles between 10° and 40° in H-plane (considering the receiving layer patch orientation as reference), the simulated reflection and transmission coefficients are shown in Fig. 5.6. The considerations on the reflection coefficients done for the E-plane oblique incidence are still valid in the H-plane (Fig. 5.6(a, c)). The minimum insertion loss (Fig. 5.5(b)) increases with the angle of incidence but it is lower than 1.6 dB for all the angles of incidence. The 3-dB bandwidth covers the nominal bandwidth up to 30°. At 40°, the losses increase significantly between 29.0 and 30.0 GHz and the 3-dB bandwidth is reduced by about 300 MHz.

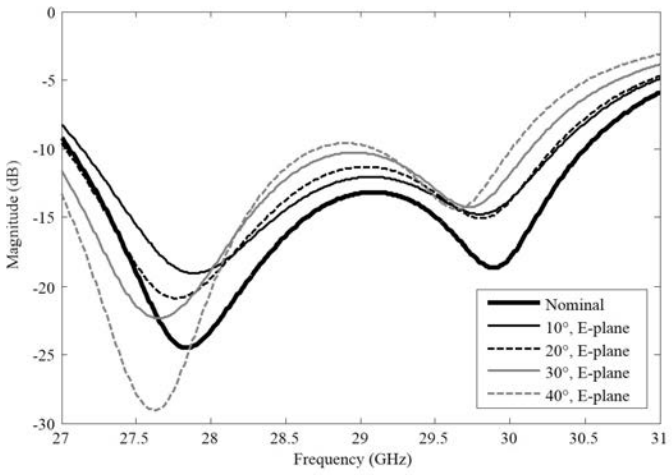

(a)

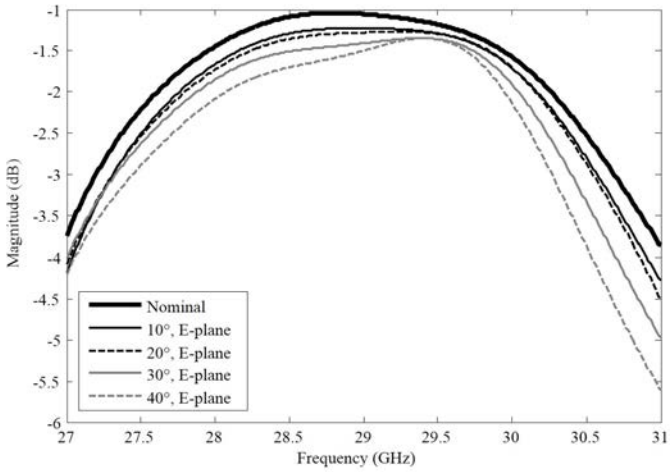

(b)

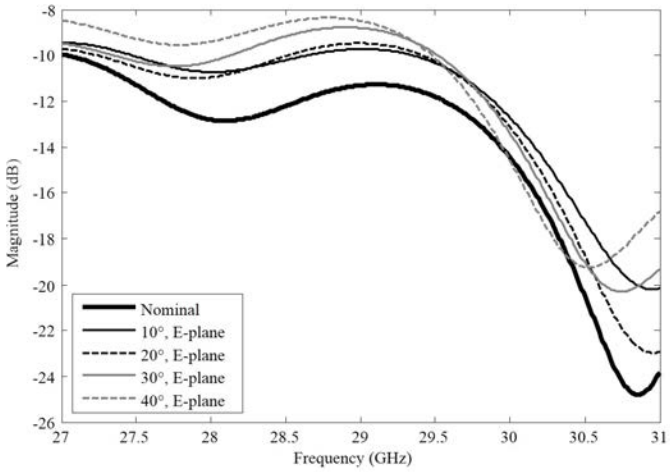

(c)

Figure 5.5: Scattering parameters simulated with different incidence angles in the E-plane: S_{11} (a), S_{21} (b) and S_{22} (c).

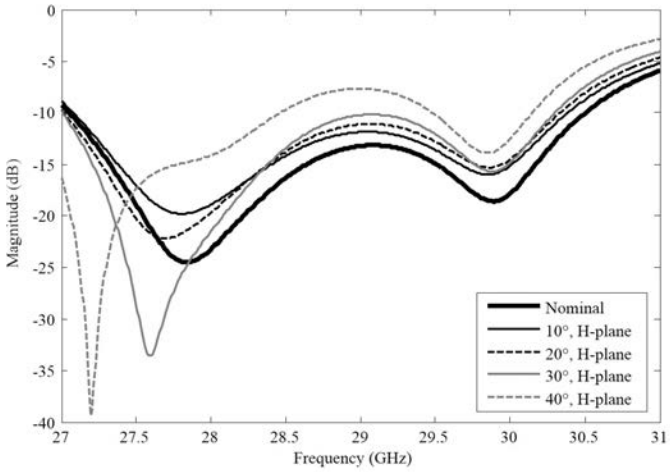

(a)

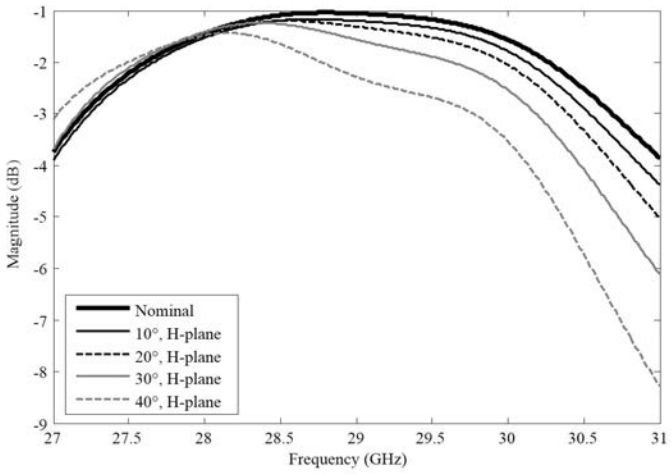

(b)

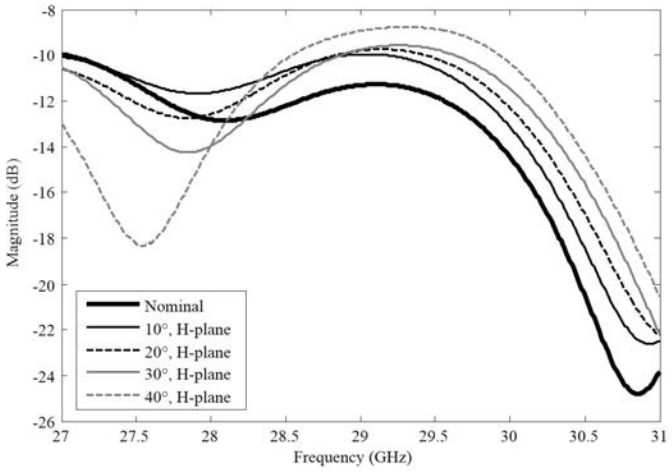

(c)

Figure 5.6: Scattering parameters simulated with different incidence angles in the H-plane: S_{11} (a), S_{21} (b) and S_{22} (c).

5.1.4 Sensitivity analysis

In order to investigate the feasibility of the proposed architecture with standard PCB technologies, a sensitivity simulation study has been carried out, similarly to the one done in Chapter 3. Among the parameters taken into account, there are the circularly-polarized patch resonant lengths along x and along y. The corresponding parameters are labelled $L_2(x)$ and $L_2(y)$. Furthermore, the U-slot dimensions (L_{g2} and W_{g2}) and width (t_2) on the same layer are taken into account. Finally, the resonant length of the receiving layer patch (L_1) and the center metallized via diameter (d_V) are considered. Indeed, an exhaustive parametric study, including all the variables reported in Table 5.1 and misalignments between layers, has shown that these three parameters have the most important impact on the unit-cell frequency response. A variation of ± 30 μm, which is a reasonable maximum error for PCB technology, has been selected. The unit-cell in the 0°-phase state with peri-

odic boundary conditions and normal incidence has been considered. The magnitudes of the scattering parameters are plotted in Fig. 5.7 for $L_2(x)$ and $L_2(y)$ variations. A variation of ± 30 μm of L_2 along x and y does not have an important effect on the reflection coefficients S_{11} and S_{22}. Only the variation $L_2(x) + 30\mu$m increases the return loss by about 5 dB from port 1 and 3 dB from port 2 at 29 GHz (Fig. 5.7(a, c)). The variation of $\pm 30\mu$m along x and along y produces a frequency shift of ± 100 MHz on S_{21} (Fig. 5.7(b)) in the transmission bandwidth, with 0.5-dB increased insertion losses in the case of the $+30\mu$m variation.
The magnitudes of the scattering parameters are plotted in Fig. 5.8 for L_{g2} and W_{g2} variations. There is no significant variation on the reflection coefficients S_{11} and S_{22}. Only the variation $W_{g2}(x) - 30\mu$m degrades the return loss from port 2 (Fig. 5.8(a, c)). The same variation increases the insertion losses by about 0.5 dB, which is the most important effect (Fig. 5.8(b)).

A variation of +30 μm of t_2 increases the reflection coefficient S_{11}, but the 10-dB bandwidth still covers the nominal bandwidth (Fig. 5.9(a)). The same variation on S_{22} increases the reflection coefficients which are still below -9 dB (Fig. 5.9(c)). The insertion losses are higher with a +30 μm variation (Fig. 5.9(b)).
Similar considerations for both the reflection and transmission coefficients are valid for the resonant length of the linearly-polarized patch L_1 on the receiving layer (Fig. 5.9). Finally, the sensitivity analysis on the center metallized via diameter d_V are shown in Fig. 5.10. The performances are worse in the case $d_V + 30\mu$m. In particular, the insertion losses are increased by about 0.5 dB (Fig. 5.10). The variation of the broadside axial ratio for the different values of L_2, L_{g2}, w_{g2}, L_1, t_2 and d_V is shown in Fig. 5.11. A maximum frequency shift of 500 MHz can be observed with similar bandwidth and minima in all the cases. In addition, it is almost independent from the central via diameter variations.

In all the considered cases, the frequency behaviour of the proposed structure is preserved with a minimum insertion loss and a 3-dB transmission bandwidth similar to the nominal design presented in the previous section.

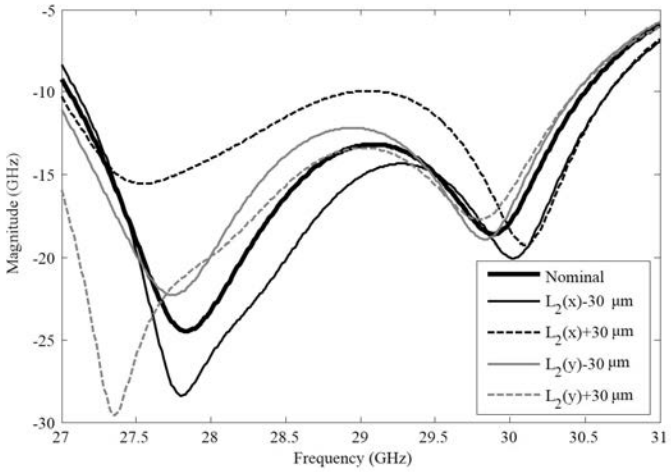

(a)

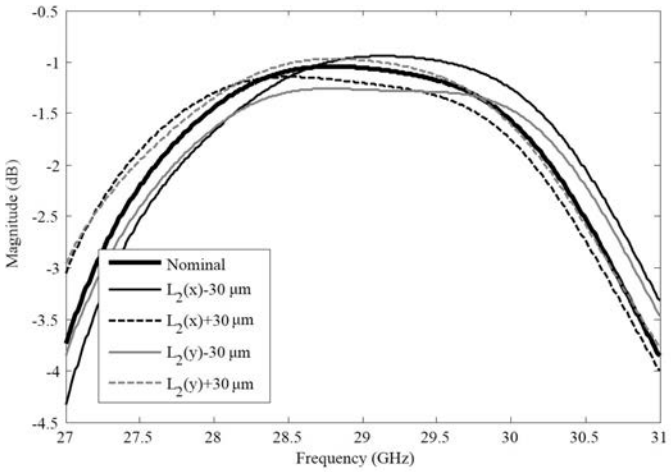

(b)

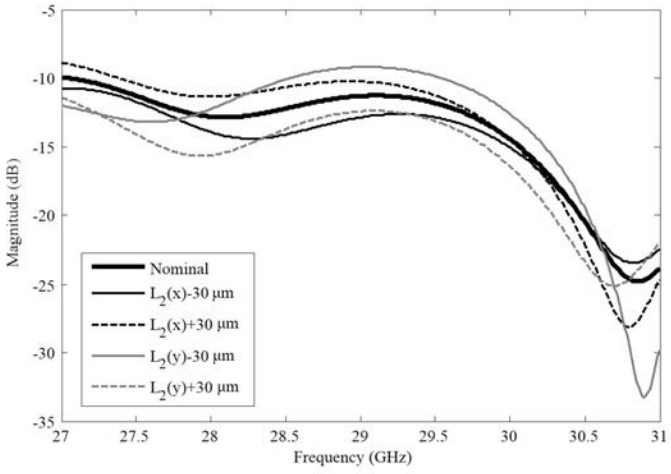

(c)

Figure 5.7: Simulated scattering parameters magnitudes (S_{11} (a), S_{21} (b), S_{22} (c)) of the unit-cell for different values of L_2.

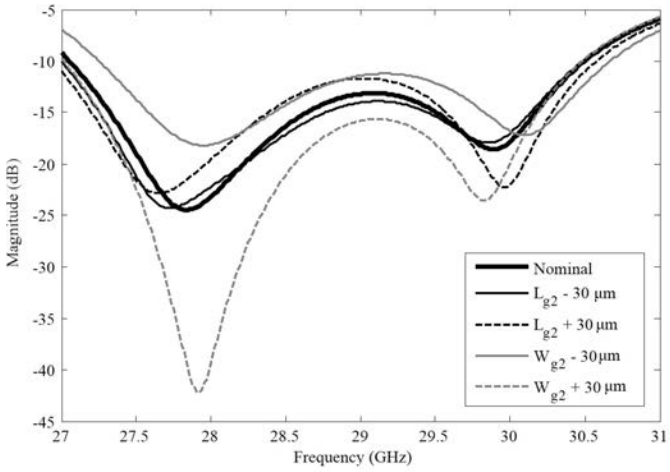

(a)

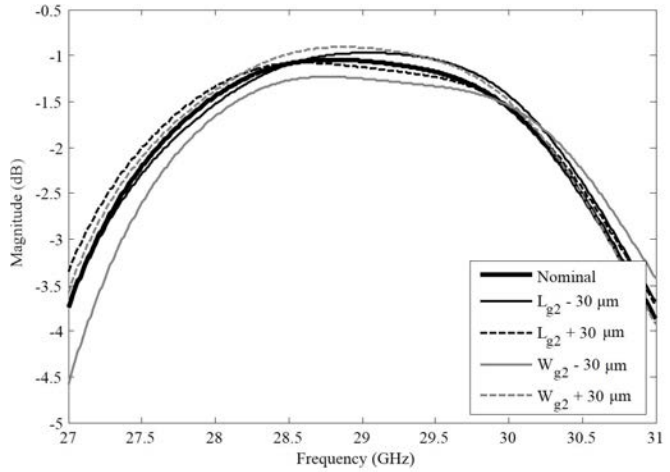

(b)

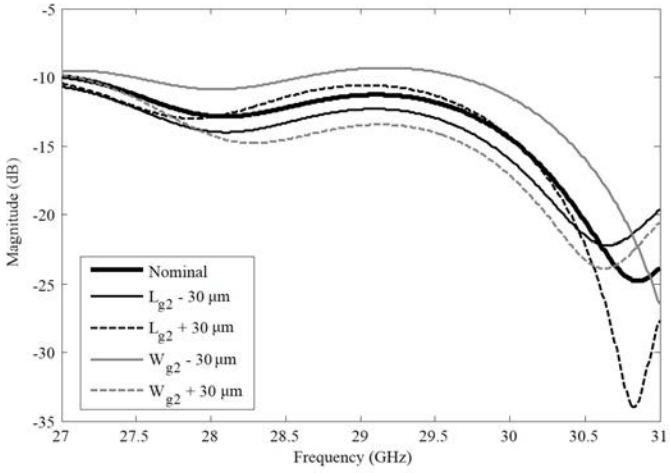

(c)

Figure 5.8: Simulated scattering parameters magnitudes (S_{11} (a), S_{21} (b), S_{22} (c)) of the unit-cell for different values of L_{g2} and w_{g2}.

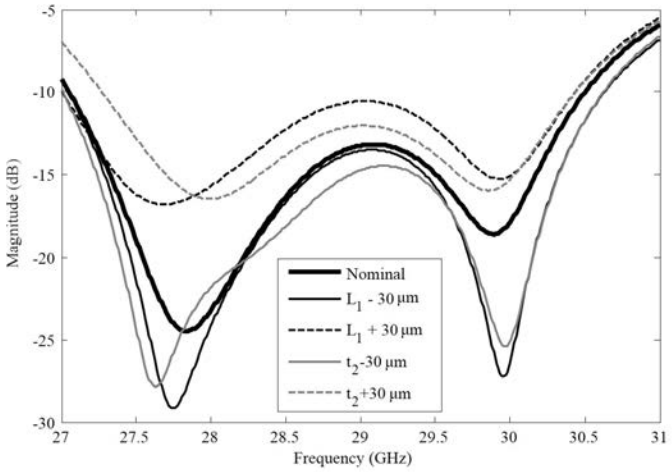

(a)

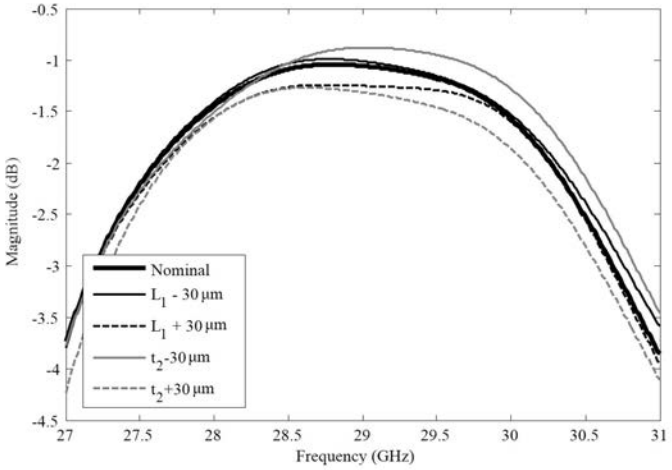

(b)

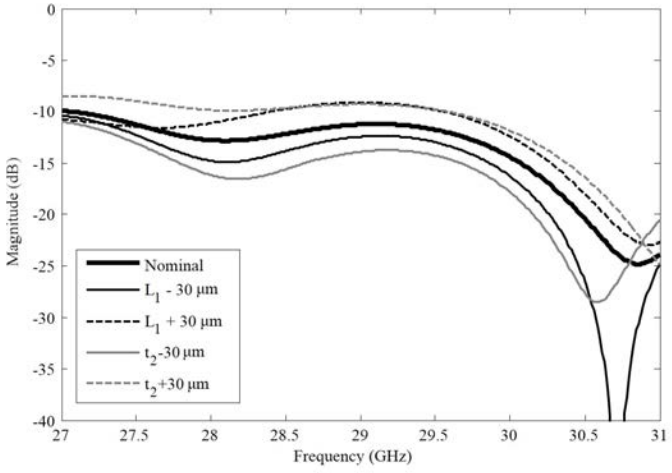

(c)

Figure 5.9: Simulated scattering parameters magnitudes (S_{11} (a), S_{21} (b), S_{22} (c)) of the unit-cell for different values of L_1 and t_2.

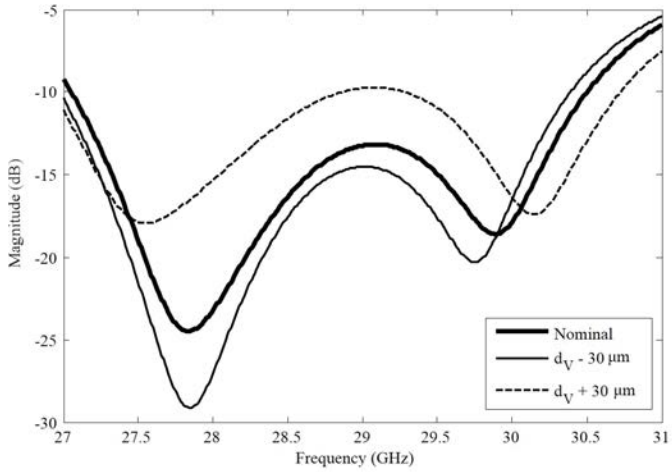

(a)

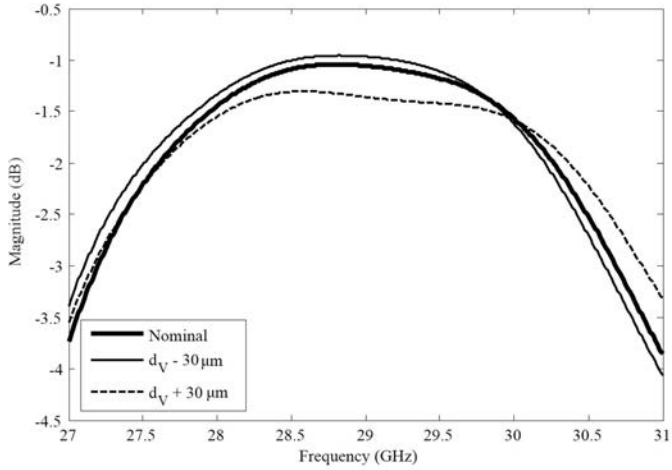

(b)

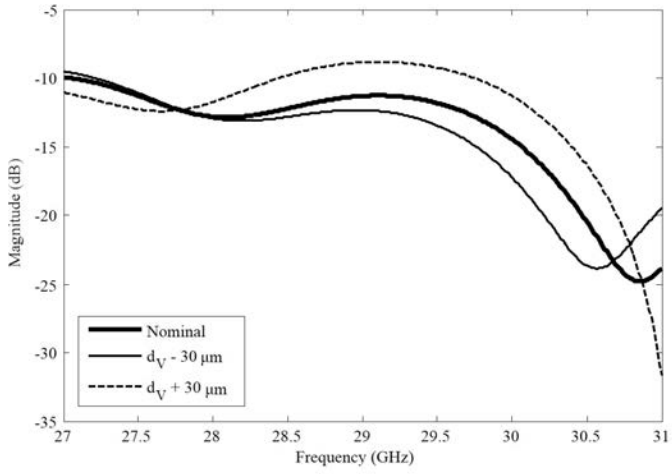

(c)

Figure 5.10: Simulated scattering parameters magnitudes (S_{11} (a), S_{21} (b), S_{22} (c)) of the unit-cell for different values of d_V.

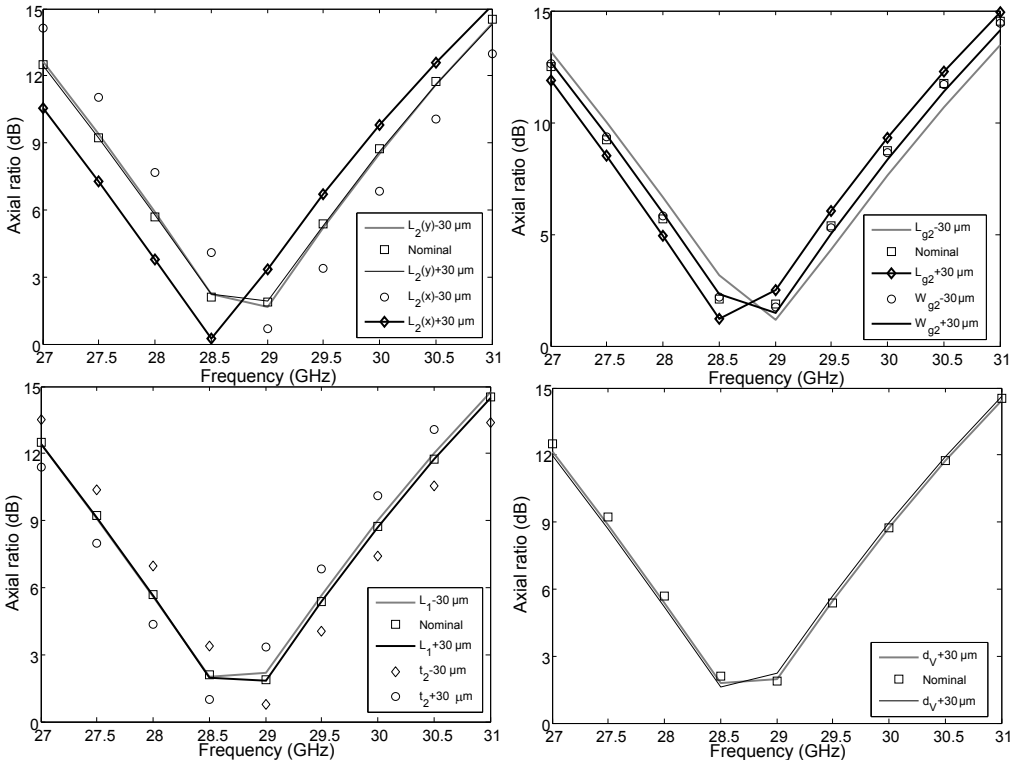

Figure 5.11: Simulated broadside axial ratio of the unit-cell Fig. 5.1 for different values of L_2, L_{g2}, w_{g2}, L_1, t_2, d_V.

5.2 Alternative solutions

Some alternative solutions have been considered in order to generate the circular polarization in the transmitting layer. In all cases, the receiving layer structure is the same as considered above, only the geometrical dimensions have been adjusted and optimized. The first design, labelled unit-cell B, is directly derived from the presented unit-cell, labelled here unit-cell A. The truncated-corner square patch is coupled with a parasitic square patch realized on a superstrate of Rogers Duroid RT5880 [78] (Fig. 5.12). In this case, the performances are shown in Table 5.2. Another Arlon CuCLAD film ([79]) is considered for bonding the new substrate with the RT6002 on the transmitting layer (Fig. 5.12). The minimum insertion losses decrease by about 0.2 dB and a similar RL bandwidth is obtained, if compared to the design A. The AR 3-dB bandwidth becomes 1.5 GHz almost twice the bandwidth of unit-cell A, as summarized in Table 5.2.

Another option investigated in this study is formed by a square patch loaded by an asymmetrical slot coupled with a parasitic square patch (unit-cell C of Fig. 5.12). In this case, the bandwidth of the axial ratio increases up to 2.2 GHz (Table 5.2). Similar results are obtained by considering a rectangular patch coupled with a parasitic patch rotated by 45° (unit-cell D, Table 5.2). The simulated scattering parameters in a periodic environment for the 0° phase state are shown in Fig. 5.13. In all the cases, a larger bandwidth in terms of

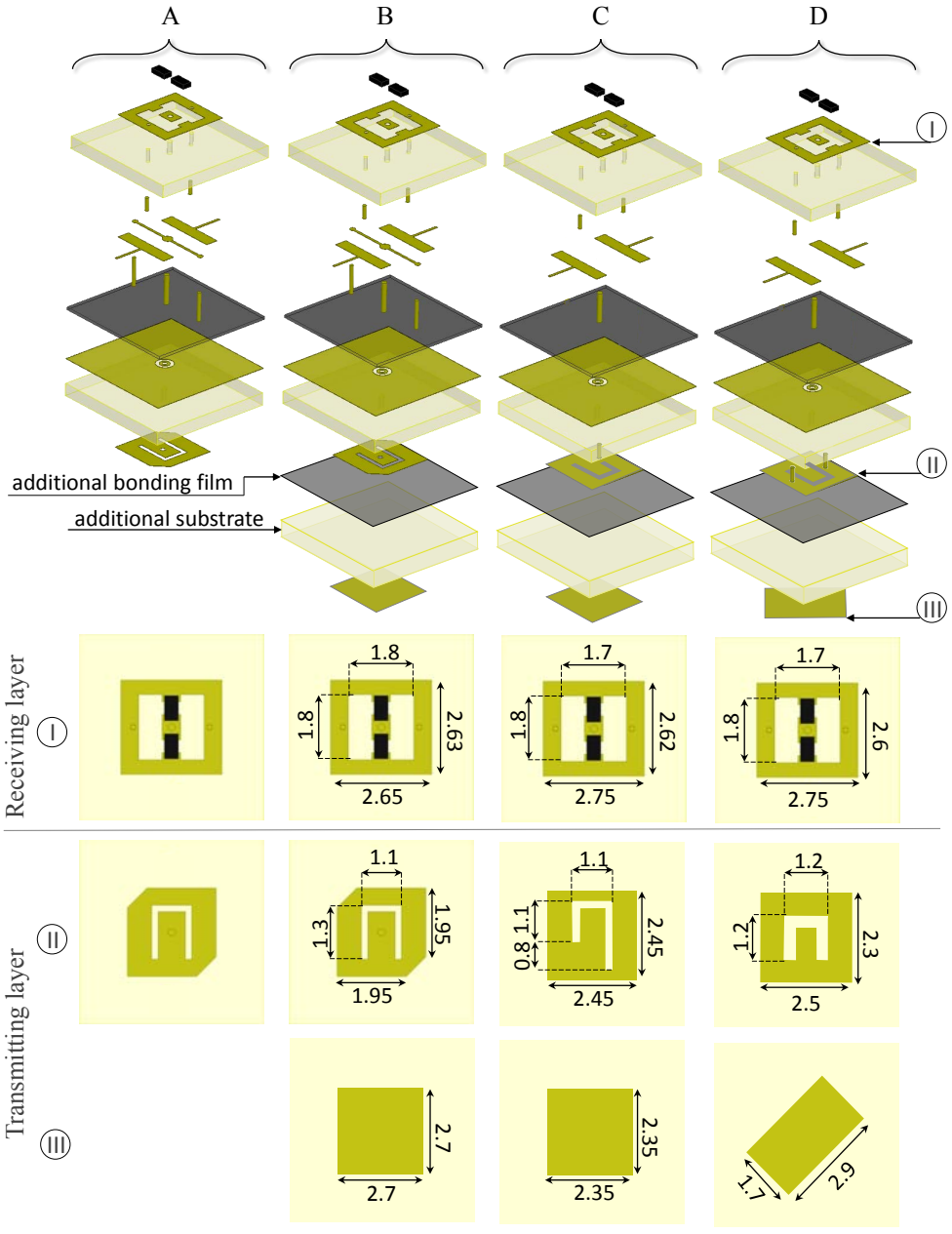

Figure 5.12: Scheme of the four unit-cell architectures considered for generating the circular polarization in the transmitting layer. Dimensions are given in millimeters.

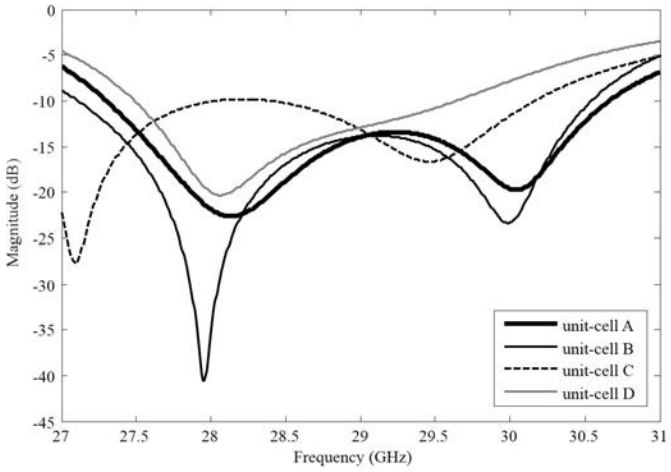

(a)

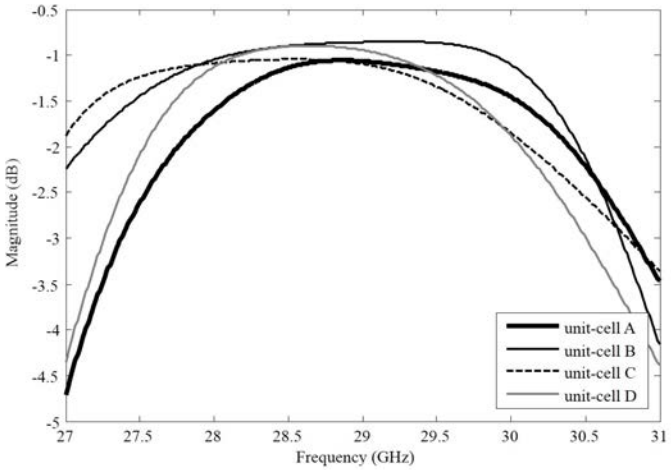

(b)

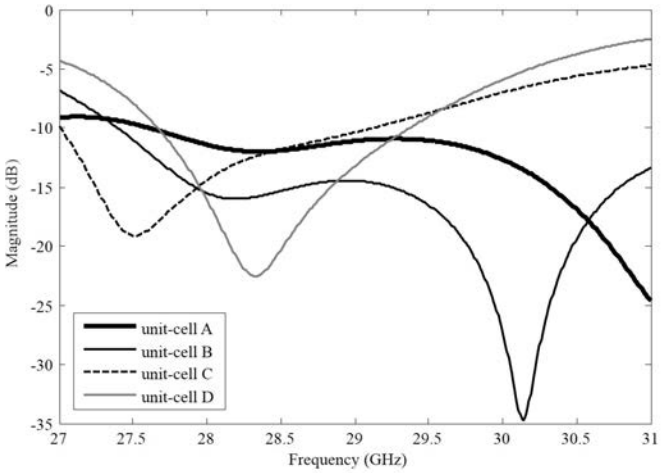

(c)

Figure 5.13: Simulated scattering parameters magnitudes (S_{11} (a), S_{21} (b), S_{22} (c)) of the different unit-cells shown in Fig. 5.12.

axial ratio is obtained. However, the use of the sequential rotation technique increases this bandwidth, as demonstrated in Chapter 2. Therefore, only the first solution is considered for a prototype realization and characterization in waveguide as it is the simplest structure to fabricate.

Table 5.2: Unit-cells simulated performance in the 0° state.

	Unit-cell A	Unit-cell B	Unit-cell C	Unit-cell D
Min. IL	1.08 dB	0.85 dB	1 dB	0.9 dB
RL bandwidth	27.4-30.7 GHz	27.0-30.5 GHz	26.7-30.0 GHz	27.5-30.0 GHz
2-dB IL	27.8-30.5 GHz	27.0-30.5 GHz	27.0-30.0 GHz	27.5-29.6 GHz
3-dB AR	800 MHz	1.5 GHz	2.2 GHz	2.15 GHz

5.3 Characterization setup

The unit-cell has been characterized in a waveguide simulator based on a standard WR28 waveguide (7.112×3.556 mm^2) on the receiving layer side (linear polarization) and a square non-standard waveguide on the transmitting layer side (circular polarization). In fact, the generation of the circular polarization in this layer implies the use of a waveguide in which the two orthogonal modes can propagate in the same conditions. Both circular and square waveguide sections have been considered. A square waveguide with a side of 6.5 mm has been selected. In addition, an orthomode transducer (OMT) is needed. An OMT is a three-ports waveguide component which allows to separate and combine the two orthogonal polarizations. One of the three ports must accept the two modes and its section can be square or circular. In general, the other two are connected to rectangular waveguides with propagating TE10 fundamental mode. These functionalities are realized with different architectures and different technologies. In waveguide, turnstile and Boifot junctions are the most used. A commercial OMT with nominal working band between 27.0 and 31.0 GHz fabricated by MM microwave [90] has been considered in the present work. It has two waveguide ports in WR-28 and one circular port with diameter 7.112 mm. With this OMT and a matched load, three two-port measurements can be carried out to characterize the unit-cell. Ad-hoc waveguide adaptors are considered between the unit-cell section and the rectangular standard waveguide and between the unit-cell section and the square waveguide. The optimized length of both adaptors is 1.2 mm ($\lambda_0/8.6$). Then, the vertical and horizontal components will be measured independently by using a matched load at one of the two ports of the OMT. The junction 1 is formed by the rectangular waveguide and the adaptor to the unit-cell on the receiving side and the junction 2 is formed by the adaptor to the square waveguide, the square waveguide section and the OMT.

5.3.1 Calibration procedure

First, a two-port TRL calibration is performed to de-embed the coaxial adaptors and the WR-28 sections. Considering the setup of Figs. 5.14-5.16, the junction 2 must be de-embedded with an ad-hoc procedure. In fact, the square waveguide in which the two orthogonal modes are combined from the OMT makes the characterization of this waveguide section more difficult. The variable short circuit method is considered and performing several 1-port and 2-ports measurements, the following scattering parameters of this junction S_{J2} can be obtained.

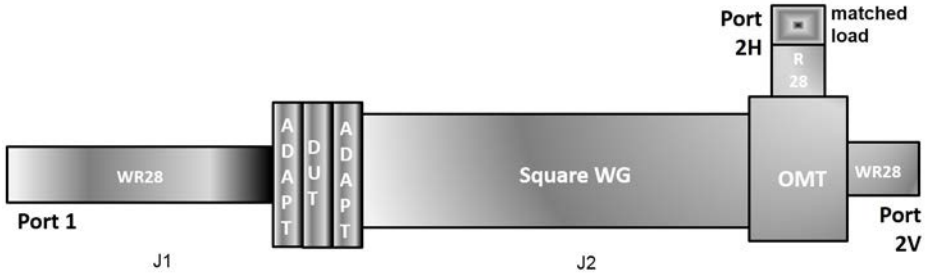

Figure 5.14: Scheme of the waveguide setup for the first measurement in which the scattering parameters associated to the vertical polarization are measured.

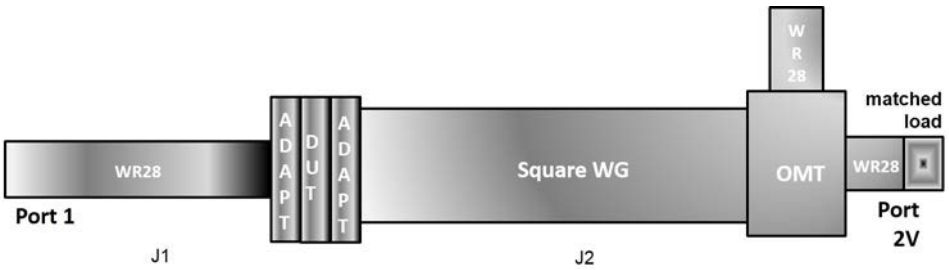

Figure 5.15: Scheme of the waveguide setup for the second measurement in which the scattering parameters associated to the horizontal polarization are measured.

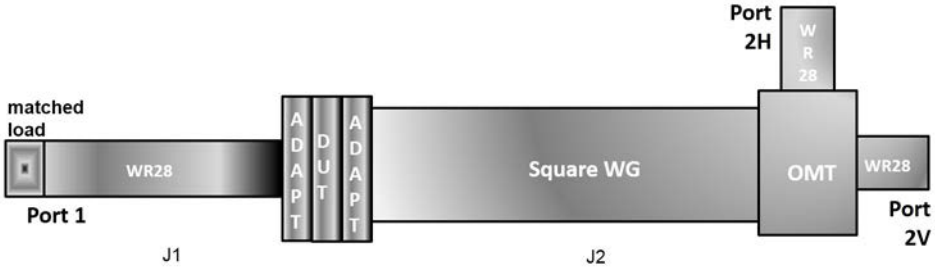

Figure 5.16: Scheme of the waveguide setup for the third measurement in which the scattering parameters associated to the transmission between the vertical and horizontal polarization are measured.

$$S^{J2} = \begin{pmatrix} S^{J2}_{1H1H} & S^{J2}_{1H2H} & 0 & 0 \\ S^{J2}_{2H1H} & S^{J2}_{2H2H} & 0 & 0 \\ 0 & 0 & S^{J2}_{1V1V} & S^{J2}_{1V2V} \\ 0 & 0 & S^{J2}_{2V1V} & S^{J2}_{2V2V} \end{pmatrix} \tag{5.1}$$

The null elements in the previous matrix are due to the hypothesis that the OMT has infinite isolation. More details about the procedure are given in the Appendix D.

5.3.2 Measurement procedure

Once the scattering parameters of the junction J2 are known, the following S parameters must be measured in order to characterize the unit-cell:

$$S^{cell} = \begin{pmatrix} S^{cell}_{2H2H} & S^{cell}_{2H1V} & S^{cell}_{2H2V} \\ S^{cell}_{1V2H} & S^{cell}_{1V1V} & S^{cell}_{1V2V} \\ S^{cell}_{2V2H} & S^{cell}_{2V1V} & S^{cell}_{2V2V} \end{pmatrix} \tag{5.2}$$

For this purpose, three 2-ports measurements must be carried out, as shown in Figs. 5.14-5.16:

- Measurement V, in which the parameters $S^{cell}_{1V1V}, S^{cell}_{1V2V}, S^{cell}_{2V1V}, S^{cell}_{2V2V}$ associated to the vertical polarization are extracted (Fig. 5.14);
- Measurement H, in which the parameters $S^{J2}_{1H1H}, S^{J2}_{1H2H}, S^{J2}_{2H1H}, S^{J2}_{2H2H}$ associated to the horizontal polarization are extracted (Fig. 5.15);
- Measurement VH, in which the parameters $S^{J2}_{2H2H}, S^{J2}_{2H2V}, S^{J2}_{2V2H}, S^{J2}_{2V2V}$ associated to the horizontal and vertical polarizations are extracted (Fig. 5.16).

In the first measurement (Fig. 5.14), we can define the 2×2 matrices associated to the junction 2 and to the unit-cell as

$$S^{cell}_{meas,V} = \begin{pmatrix} S^{cell}_{1V1V} & S^{cell}_{1V2V} \\ S^{cell}_{2V1V} & S^{cell}_{2V2V} \end{pmatrix}, \tag{5.3}$$

and

$$S^{J2}_{meas,V} = \begin{pmatrix} S^{J2}_{1V1V} & S^{J2}_{1V2V} \\ S^{J2}_{2V1V} & S^{J2}_{2V2V} \end{pmatrix}. \tag{5.4}$$

The measured scattering parameters $S_{meas,V}$ are used to calculate the related transmission parameters $T_{meas,V}$ (see Appendix D). Then, the transmission matrix related to the unit-cell $T^{cell}_{meas,V}$ is calculated as

$$T^{cell}_{meas,V} = T_{meas,V} \cdot (T^{J2}_{meas,V})^{-1}. \tag{5.5}$$

A similar procedure can be defined for the measurement H (Fig. 5.15). For the third measurement (VH) (Fig. 5.16), the unit-cell scattering matrix $S^{J2}_{meas,VH}$ is defined as

$$S^{cell}_{meas,VH} = \begin{pmatrix} S^{cell}_{2H2H} & S^{cell}_{2H2V} \\ S^{cell}_{2V2H} & S^{cell}_{2V2V} \end{pmatrix}. \tag{5.6}$$

The transmission matrix related to the unit-cell can be calculated as function of $T_{meas,VH}$ as follows:

$$T^{cell}_{meas,VH} = \left(T^{J2}_{meas,V}\right)^{-1} \cdot (T_{meas,VH}) \cdot (T_{meas,H})^{-1}. \tag{5.7}$$

Further details and a numerical validation on the this procedure applied to the proposed unit-cell architecture are given in Appendix D.

5.4 Conclusions

In this chapter, an electronically reconfigurable 1-bit circularly-polarized unit-cell has been presented for transmitarray applications in Ka-band.

The phase control is obtained on the receiving layer with the same method proposed in Chapter 3 and based on the use of p-i-n diodes. The generation of the circular polarization is realised on the transmitting layer by considering passive planar antennas of different typologies. In this way, the electronic control of the phase is completely separated from the polarization of the radiated field and then very good polarization purity can be achieved. In addition, sequential rotations schemes can be easily applied in order to broaden the axial ratio bandwidth.

Different solutions are proposed for the transmitting layer layout. The first one is based on a square patch with truncated corners and loaded by a slot. The ground connection has been realized with quarter-wavelength stubs independent from the patch antenna obtaining a better robustness to the fabrication errors. An axial ratio under 3 dB in a 4% band-

width is obtained with insertion losses of about 1 dB. Alternative solutions include square patch with asymmetrical slots and rectangular parasitic patches rotated by 45°. In that way, larger axial ratio bandwidth can be obtained (up to 8%) at the cost of more complex stacking. However, the sequential rotation technique can be applied to the simplest unit-cell in a transmitarray configuration improving significantly the axial ratio performances, as demonstrated in Chapters 2 and 3.

A characterization setup with an ad-hoc calibration procedure based on rectangular and square waveguides and an ortho-mode transducers has been also presented and validated numerically (Appendix D). Prototypes of the proposed unit-cell architecture are under test in the presented waveguide setup at the time when this manuscript is written.

Chapter 6

Radiation pattern synthesis for monopulse radar

In this chapter, the design of a monopulse radar antenna based on a reconfigurable transmitarray is presented. After a general introduction on monopulse radars, two techniques used to generate sum (Σ) and difference (Δ) patterns will be presented. The first one is based on the optimization of the phase distributions. The second one is based on the use of multi-source illumination. Both techniques are validated by numerical and experimental results using a linearly-polarized reconfigurable transmitarray working in X-band. The experimental setup used for the characterization is presented and measurements results are discussed in detail.

6.1 Radar techniques

The objective of a radar system is to detect and individuate the coordinates of an electromagnetic scatterer (i.e. a target object) in the antenna beam. In this system, the transmitter generates waveforms of electromagnetic radiation at a regular rate. The antenna radiates the transmitter output into space typically in a directional pattern that concentrates most of the power into a major lobe in one or two angular dimensions. The same antenna is in general used for reception. The received signals are converted from radio frequency to intermediate frequency, amplified and filtered and then processed for the information extraction. The antenna receives an echo if the target is in the beam direction. The target distance (range) is estimated by considering the delay between the transmitted pulse and the received echo.

A first way to determine the angular position of a target is to steer the antenna beam and note the pointing direction that gives the maximum echo amplitude. This method is used in many search radars where measurement precision on the order of $1/10B$, where B is the

beamwidth, is sufficient, but it cannot be used if a higher precision is needed. In addition, it does not support a closed-loop tracking angle, because of the absence of directional or sense information. The need of continuous, accurate angle and range measurements led to the development of tracking radars.

The tracking radar is a radar that automatically keeps the antenna beam axis aligned with the target. Any deviation of the target from the beam axis produces a correction signal (called error signal) for one or each coordinate, approximately proportional to the angular deviation in that coordinate, with a sign that indicates the sense of deviation. Different techniques are used:

- Sequential lobing;
- Monopulse.

In this paragraph, a review of these techniques with their applications is presented.

6.1.1 Sequential lobing

The oldest tracking radar technique is the lobe-switching [91]. The radar beam, instead of pointing directly at the target, points slightly to one side and then to the other one, alternating rapidly. This working principle is shown in Fig. 6.3 for only the elevation angle. If the target is above or below the axis, the echoes are unequal. If the target is above the crossover axis, the echo on lobe 1 is greater than from lobe 2. The difference between the two signals is positive indicating that the antenna must point at higher elevation. The same operation can be done in both angular coordinates by switching between four beams. By switching between more beams, mechanically or electronically, a rotation around the tracking axis is realized, resulting in a conical scan (Fig. 6.2). Lobe switching and conical scan are included in the sequential lobing technique.

This technique is used where moderate precision is required. The principal source of error is the fluctuation that occurs in the echoes of most targets. It results in an error due to the target displacement from the antenna axis. Another disadvantage is the limitation imposed on the data rate. This could be a serious limitation especially for targets with high angular acceleration. Furthermore, if the beam switching is realized mechanically (conical scan), the mechanical vibrations introduce an error in the tracking axis. The solution to overcome these problems is the monopulse technique, also called simultaneous lobing.

6.1.2 Monopulse

The earliest description of the monopulse radar technique appeared in [92]. Two categories of monopulse radars can be individuated:

- amplitude-comparison;

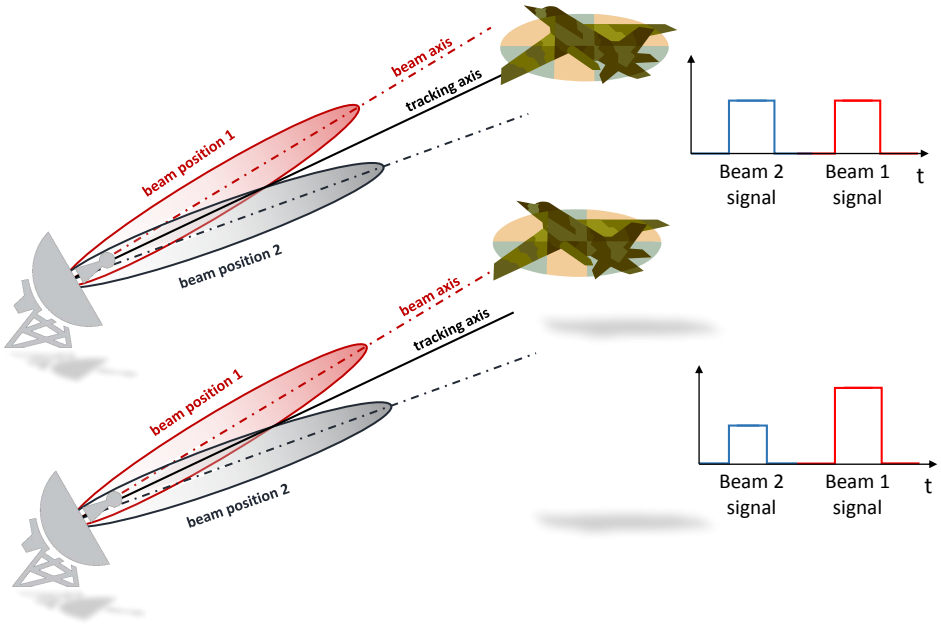

Figure 6.1: 3D sketch of the sequential-lobing tracking radar principle. Only two beams for the tracking in elevation angle are considered for the sake of simplicity.

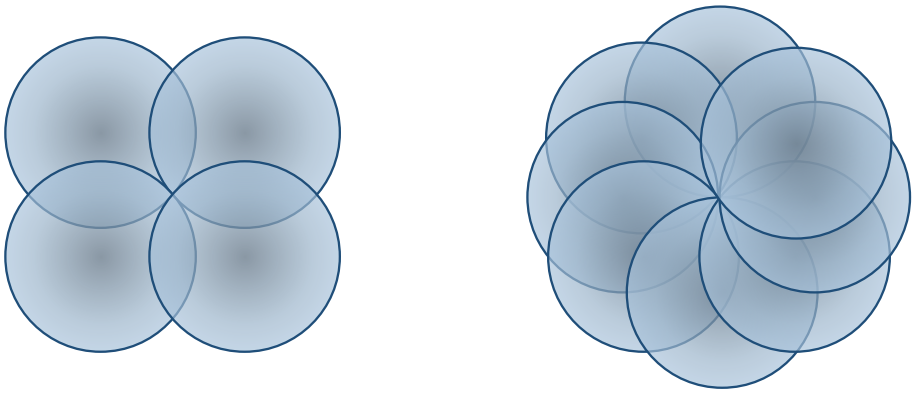

Figure 6.2: Schemes of the lobes sequentially generated in the sequential-lobing radar. Four beams and conical scan.

- phase comparison.

The first one is similar in concept to lobe switching, but the four receiving beams (for both elevation and azimuth detections) are formed simultaneously by the antenna and the comparison is done between the received signals associated to each beam. A scheme of the working principle is shown in Fig. 6.3. In the first step, we consider the target aligned with the Σ-lobe. When its position changes entering in a lobe of the Δ-pattern, the amplitude of the signal received in the corresponding Δ-channel increases. The phase-comparison is slightly different, but the principle of the simultaneous lobing is preserved. In both cases, the real-time comparison between the signals on the Σ- and Δ-channels is required. Since the angle information is available from every received pulse instead of a sequence of different impulses, the monopulse technique can provide higher data rates than sequential lobing.

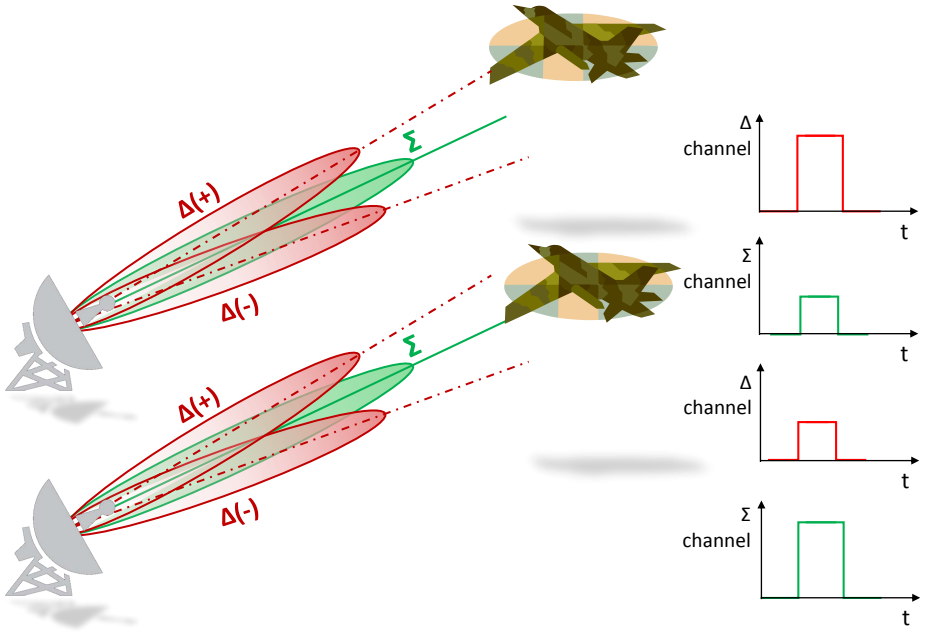

Figure 6.3: 3D sketch of the monopulse tracking radar principle. Only two beams for the tracking in elevation angle are considered for the sake of simplicity.

These systems are ideally free of errors due to the fluctuations between pulses in target echo strength. In practice, due to design and cost constraints, these errors are not null but greatly reduced. These advantages are obtained at the cost of greater equipment complexity and costs. In fact, the system includes multiple receivers, as shown in the scheme of Fig. 6.4, where only a two-quadrant system (detection in only one plane) is considered.

However, most of the tracking radars used today are of the monopulse type. They perform a variety of functions, such as [91]:

- Missile launching and guidance;

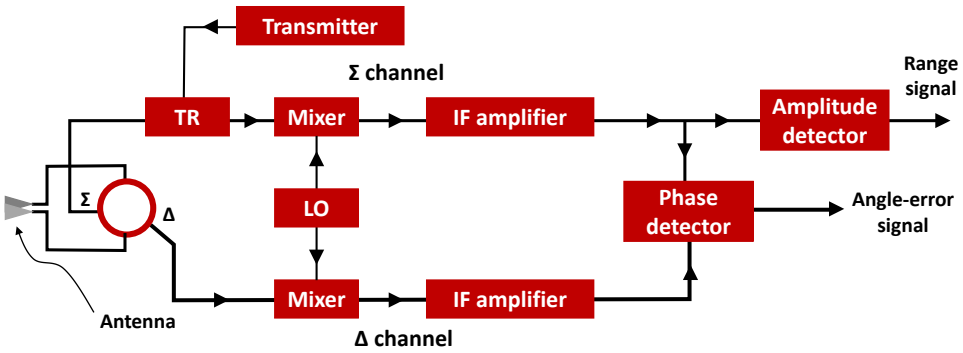

Figure 6.4: Scheme of the receiver needed for a two-quadrant monopulse tracking radar with amplitude comparison.

- Strategic military applications, such as homeland security;
- Space applications, including tracking of space vehicles and satellites;
- Intelligence applications;
- Support applications (instrumentation radars) with accuracy of $1/200\ B$.

Many monopulse radar antennas alternative to the classical parabolic reflectors have been proposed in the last years such as planar printed phased arrays [93, 94, 95, 96], slot arrays in waveguide and in substrate integrated waveguide technology [97, 98, 99]. Reflect-arrays [100] and dielectric lens-based systems [101] have been also investigated. In [95], a phased array of microstrip patch antennas working in Ku band (14 GHz) is proposed for monopulse applications. It includes 4 sub-arrays of 64 elements in a square lattice and a feeding network with hybrid coupler and phase shifter to generate the two kinds of beams required. In particular, the four subarrays are connected to the four ports of a comparator formed by four 3-dB hybrid junctions and the required phase delays are realized with "snake" microstrip lines. All this network is realized on the same layer of the microstrip patch antenna, making the design difficult because of the mutual coupling. In addition, spurious radiation is generated. In [99], a similar architecture is proposed in W-band (94 GHz) by using an array of slots in substrate integrated waveguide (SIW) technology. The feeding network and the hybrid coupler are all realized in this technology. Each port is connected to a cascade of two hybrid couplers. A first 90° phase shift is obtained with a simple SIW waveguide section. The second one is realized with SIW waveguides of different widths. The fabrication errors generate unbalances in the Δ-lobes magnitude. In [100], a monopulse system based on a dielectric lens is proposed in W band (94 GHz). The lens is illuminated with four sources (CPW slot antennas) and the signals are recombined to obtain a Σ-pattern, a Δ-pattern in elevation and a Δ-pattern in azimuth (four-quadrant system). It allows the integration of the systems only at high frequencies due to the dielectric lens thickness (12 mm in this case). All the systems presented above generate a fixed multi-beam pattern and

require an additional rotational mechanism for the target tracking like in the first monopulse radars based on parabolic reflectors. The capability to change electronically the main beam direction leads to a quick detection and improved performance. Some designs have been investigated in the last years.

In [102], a Rotman lens is used to obtain a discrete beam steering. A RF-circuit based on p-i-n diodes mounted on the feeding network of the two horn antennas connected after the Rotman lens are used to introduce the 180° of phase shift required to generate the delta patterns. The antenna works in Ka band (37 GHz) and tilted beams at discrete angles are obtained for both the sum and difference patterns by changing the input port of the Rotman lens up to 60°. Only one plane can be considered and this limits the application of this architecture to only two-quadrant systems. In addition, continuous beam-scanning cannot be achieved. In [103], a travelling wave antenna architecture is proposed. An array of slot antennas in waveguide technology is used and fed with different input lines. By shifting and recombining these signals, the Σ and Δ patterns are obtained as already proposed for the planar design in [99]. The use of this kind of antennas here allow the beam steering by changing the working frequency of the system. However, this functionality is complex to handle because the frequency-dependence of the steering angle must be taken into account in the detection system. Limited steering capabilities can be obtained because of the antenna bandwidth. In [104], a similar structure is proposed and the steering capability is achieved in frequency in only one plane and with traditional phased-array techniques on the other plane, increasing the system complexity and costs.

6.2 Reconfigurable transmitarray in X-band

The unit-cell adopted to implement the electronically reconfigurable transmitarray was proposed and fully characterized in [39]. The 1-bit unit-cell working principle is similar to the one explained in Chapter 3. Its dimensions are 15 x 15 mm^2 (half-wavelength in free space at 10 GHz). It has been tested in standard WR-90 waveguide setup with ad-hoc adaptors. The measurements show a minimum insertion loss of 1.8 dB and a bandwidth of 10% [39]. The described unit-cell is used to build a linearly-polarized 400-elements transmitarray configuration shown in Fig. 6.5 [39]. The simulation and measurements of single beams in the horizontal and vertical planes performed in [73] showed a maximum broadside gain of 22.7 dBi and tilting capabilities $\pm 50°$ and $\pm 70°$ in the vertical and horizontal planes, respectively. The possibility to use this antenna in order to generate Σ/Δ patterns for monopulse radar applications has been investigated in this work. With this purpose, two configurations have been considered (Fig. 6.6), namely a single-source and a four-sources configurations which are presented in the following sections.

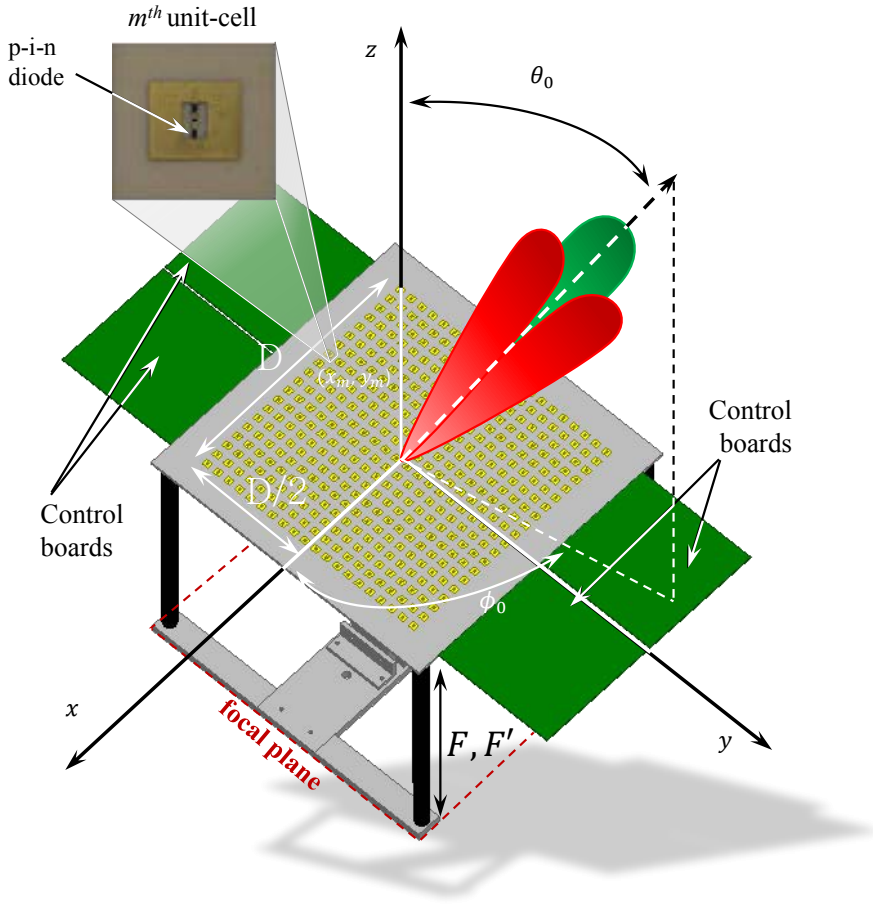

Figure 6.5: 3D sketch of the reconfigurable transmitarray for monopulse radar applications.

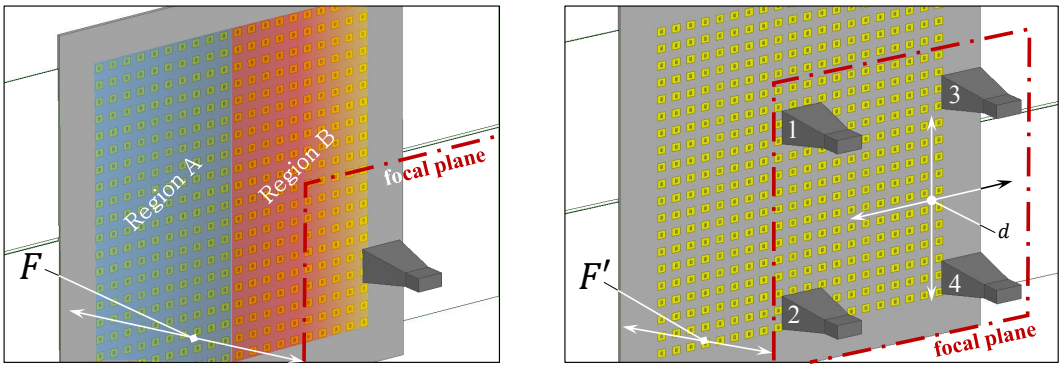

Figure 6.6: 3D sketch of the focal source plane of the single- and multiple- source configurations.

6.3 Single-source configuration

In order to generate a Δ pattern with the transmitarray presented in the previous section and already tested for the single-beam (Σ) patterns in [73], it is necessary to change the phase synthesis procedure considered in the previous work. In particular, the array surface must be divided in two halves (A, B) in which the phase law can be assigned.

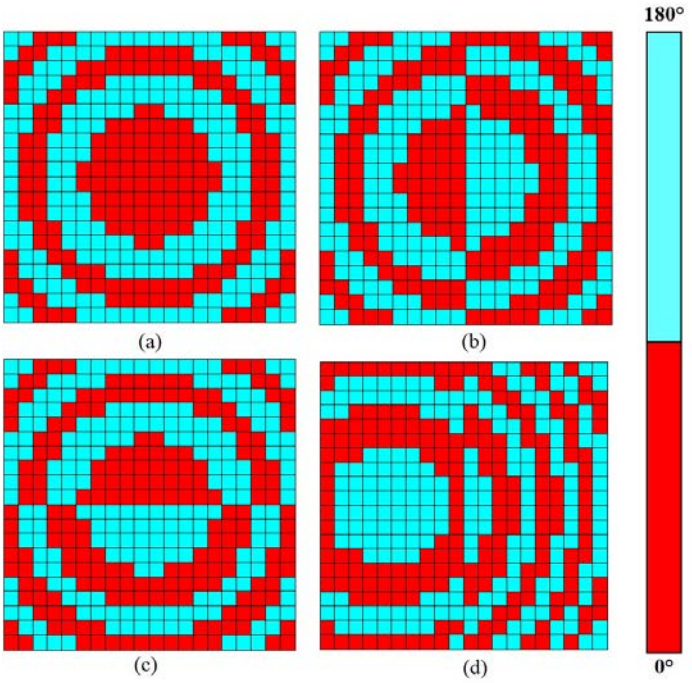

Figure 6.7: Optimized phase distributions for the single-source configuration with main beam direction at broadside ($\Sigma(a), \Delta$ (b,c) patterns) and tilted at 20° in the horizontal plane (Δ-pattern) (d).

The distribution shown in Fig 6.7(a), used to obtain a Σ pattern at broadside has been calculated as shown in Chapter 2, with the following relations

$$\Delta\phi_m = 0, \tag{6.1}$$

if $|\phi_m - \delta_m| < \pi/2$, otherwise

$$\Delta\phi_m = \pi, \tag{6.2}$$

where m denotes the generic unit-cell of the array, ϕ_m is the phase of the incident wave on the receiving layer and δ_m is the delay required for tilting the beam in an arbitrary direction, calculated with the well-known relation

$$\delta_m = k_0(x_m \sin\theta_0 \cos\phi_0 + y_m \sin\theta_0 \sin\phi_0), \tag{6.3}$$

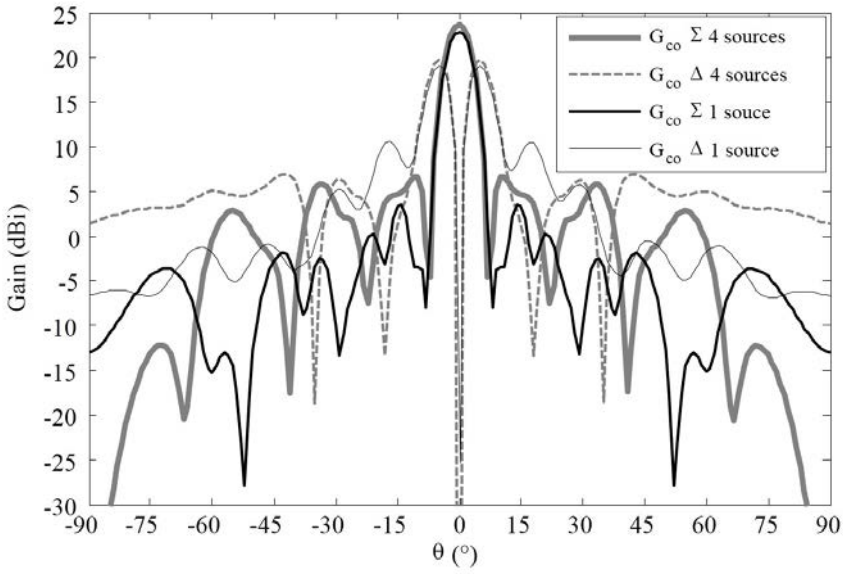

Figure 6.8: Simulated radiation pattern in the horizontal plane at 10 GHz with Σ and Δ patterns generated with the two proposed transmitarray configurations.

where k_0 is the propagation constant in free space and (x_m, y_m) are the Cartesian coordinates of the m-th unit-cell, θ_0, ϕ_0 denote the desired main beam direction. To obtain a Δ pattern in the horizontal plane, the phase law in region A is the same reported in eqs. 6.1, 6.2. The phase law in the second region (B) can be written by inverting the conditions defined in eqs. 6.1, 6.2. In this way, a phase difference of 180° is maintained between the two regions and a null is obtained in the desired direction. The resulting distribution is shown in Fig. 6.7. In this way, a Δ pattern has been generated in the $\phi = 90°$ cut-plane, as shown in Fig. 6.8. By changing the orientation of the two regions A and B by 90°, it is possible to obtain a Δ pattern in the vertical plane; any other cut-plane can be chosen accordingly to the orientation of the frontier between the regions A and B. Moreover, Δ patterns with a null steered at any 2-D angle can be generated by applying the eq. 6.3 to the calculated phase distributions in the two regions.

The experimental characterization of the new phase distributions has been performed in anechoic chamber. Different Δ patterns and different cut-planes have been considered. The results for a broadside beam and a 20°-tilted beam are shown in Fig. 6.10 and 6.11 in the horizontal plane. For the broadside case, a measured Δ-lobe gain of 20.0 dBi with a side lobe level (SLL) of -11.4 dB in the horizontal plane have been measured. The null depth is 22.0 dB. In the 20°-tilted beam case, a measured Δ-lobe gain of 19.1 dBi with SLL of -10.3 dB in the horizontal plane have been measured. The null depth is 22.6 dB. The frequency response of the Δ patterns for both configurations are shown in Fig. 6.12. Δ-lobes within all the bandwidth are obtained and a beam-squint of ±2° is observed in the 20°-tilted beam case. The antenna has been also tested with tilted beams up to 40° in the

two cardinal planes. The cross-polarization component is under 30 dB in all the measured configurations. The measured results compared with the simulated ones are reported in Table 6.2, 6.3, 6.4. A good agreement has been obtained between the simulations and the measurements. The discrepancies are partly attributed to the spillover radiation, which is not taken into account in the simulation method, especially for large steering angles. In addition, the null of the Δ patterns are difficult to measure because high-precision alignment is required. Simultaneous generation of a Σ and a Δ patterns for receiving both the signal and detect a target on a plane (two-quadrant systems) can be realized by using multi-mode horn antennas for this transmitarray illumination [105]. In this case, the fundamental and two higher modes inside the horn antenna used as focal source are exploited. By combining the signal associated to the different modes, signals associated to the Σ and Δ patterns can be extracted. However, this configuration has not been investigated in detail due to the complexity and high realization costs of this kind of focal antenna.

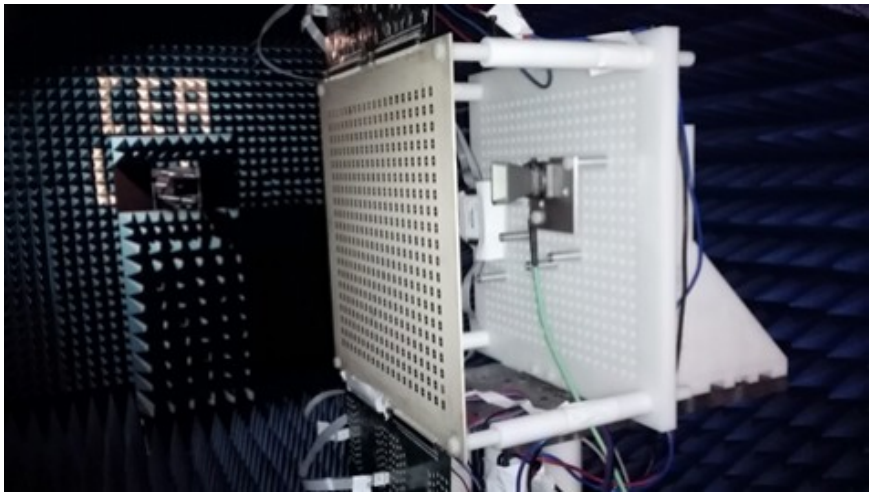

Figure 6.9: Photograph of the X-band monopulse radar based on a transmitarray antenna architecture in anechoic chamber.

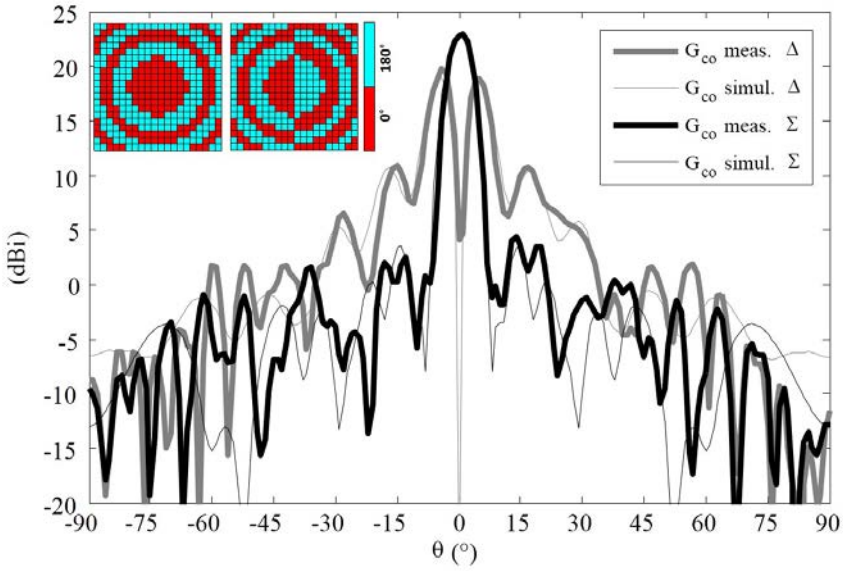

Figure 6.10: Simulated and measured Σ and Δ radiation patterns at 10 GHz for the single source configuration with a broadside beam.

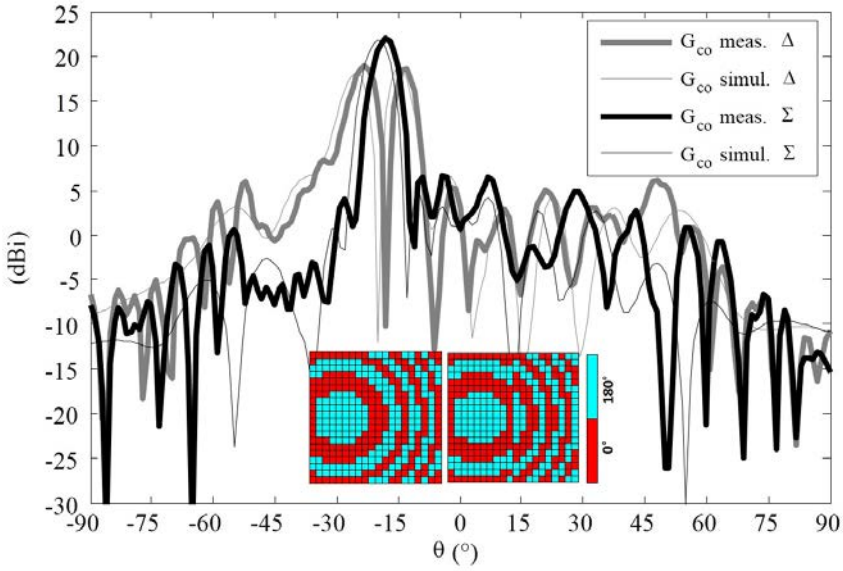

Figure 6.11: Simulated and measured Σ and Δ radiation patterns at 10 GHz for the single source configuration with a 20° tilted beam.

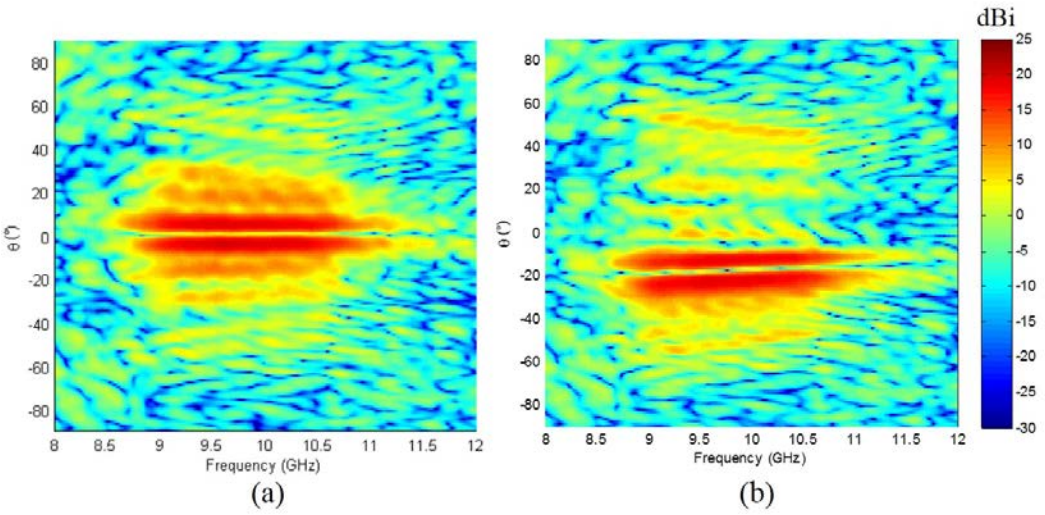

Figure 6.12: Measured Δ radiation patterns for the single source configuration with a broadside beam (a) and a 20° tilted beam (b) as a function of the frequency.

6.4 Four-sources configuration

The second configuration considered is formed by the same array used in the previous section illuminated by four horn antennas with 10 dBi of nominal gain. The setup considered is shown in Fig. 6.6. The focal distance and the distances between the sources have been optimized using the same method of analysis and synthesis illustrated in Chapter 2. The optimization process was reported in [40, 106]. The optimal focal distance is $F' = 119$ mm and the distance between the sources is $d = 113$ mm. The focal distance is reduced by a factor of two as compared to the single-source case, which is a first advantage of this configuration.

The optimal phase distribution at broadside is shown in the inset of Fig. 6.16. With this distribution, a Σ pattern at broadside can be obtained. In order to obtain a Δ pattern in the horizontal plane, it is sufficient to consider a phase shift of 180° between the sources 1, 2 and 3, 4. For the vertical plane, the same shift must be maintained between the sources 1, 3 and 2, 4, as summarized in Table 6.1. It is worth to notice that a Σ pattern and two Δ patterns (one for each cardinal plane) can be simultaneously generated with this configuration (four-quadrant system). The simulation results are shown in Fig. 6.8 for broadside beams in the horizontal plane. The Σ pattern has a maximum gain of 23.5 dBi with SLL of -16.5 dB. They correspond to 0.6-dB higher gain and 0.7-dB higher SLL if compared with the same beam generated with a single source in the configuration illustrated in the previous section. Both the effects are due to the different incident power distribution provided by the multiple focal source illumination [40, 106]. Tilted beams can be obtained with proper phase distributions by considering the proper phase delay and maintaining the phase excitations of the four

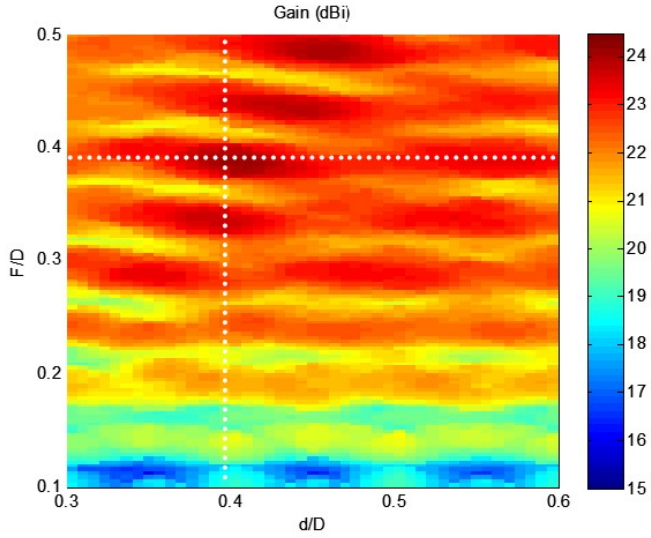

Figure 6.13: Simulated realized gain as a function of the focal distance F and of the distance between the sources d in the focal plane.

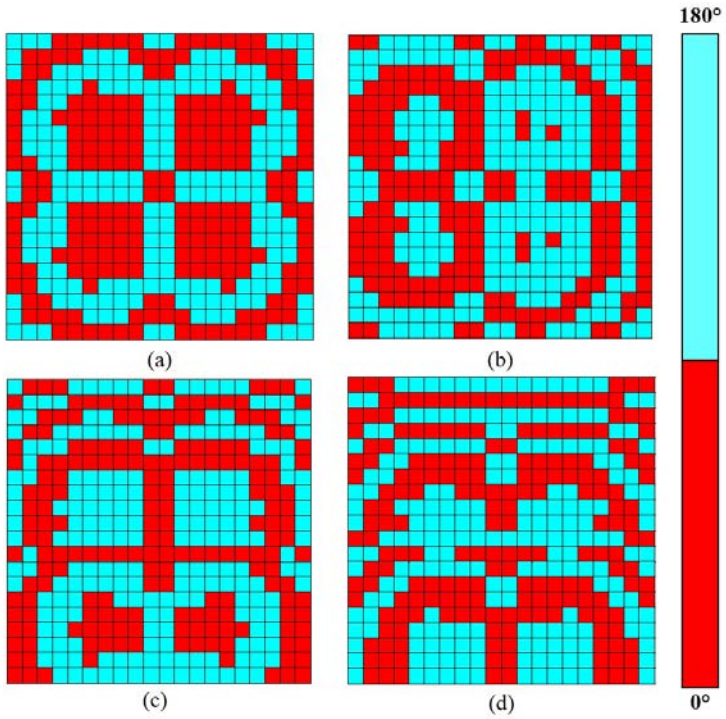

Figure 6.14: Optimized phase distributions for the multisource configurations with a beam direction at broadside (a) and tilted by 20° (b) in the horizontal plane and 30° (c), 40° (d) in the vertical plane.

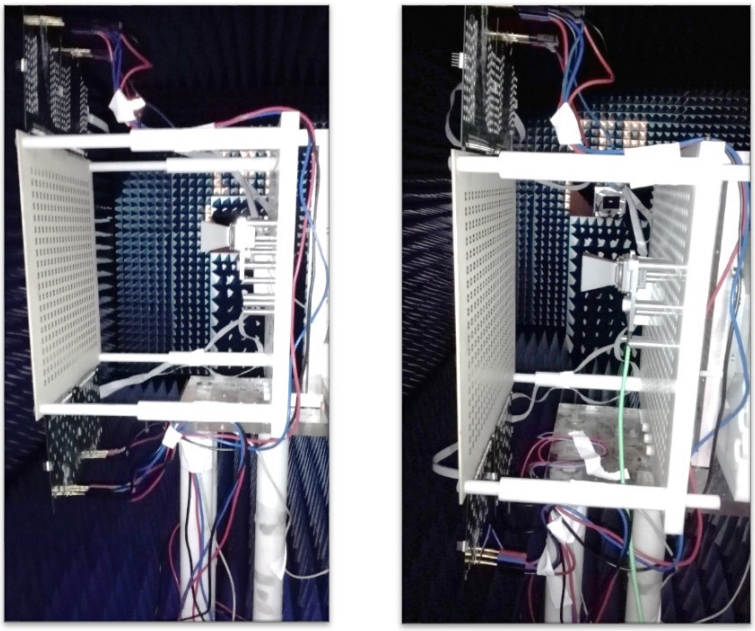

Figure 6.15: Photograph of the X-band monopulse radar based on a transmitarray antenna architecture in anechoic chamber in the single and four sources configurations.

feeds reported in Table 6.1. The maximum gain of the two Δ lobes is 20 dBi with null depth of 40 dB at broadside, as shown in Fig. 6.8. The Δ patterns are generated on both cardinal planes allowing the detection of the target angular position in a 2D space.

The four-sources configuration has been tested in four steps with only one horn at a same time placed in one of the optimized positions in the focal plane (Fig. 6.15). Co-polar and cross-polar components have been measured for several phase distributions in order to obtain tilted beams in the different cut-planes. The obtained radiation patterns for each focal source have been recombined with a normalization constant and the phase weights of Table 6.1 to obtain the Σ and Δ patterns in the horizontal and vertical planes. The results for the broadside and -20° tilted-beam in the horizontal plane are shown in Fig. 6.16, 6.17. For the broadside case, a Σ-lobe gain of 23.2 dBi with SLL of -14.4 dB and a Δ-lobe gain of 19.3 dBi with SLL of -10.6 dB in the horizontal plane have been measured. The null depth is 22.7 dB. The frequency behavior is shown in Fig. 6.18. The other configurations tested in anechoic chamber with scan angles up to -40° in both cardinal planes are summarized in Tables 6.5, 6.6, 6.7. A good agreement has been obtained between measurements and simulations. The discrepancies, mainly in the null depth estimation, are attributed to errors in the positioning of each source in the focal plane during the measurements. In order to complete the proposed radar systems, a network formed by four hybrid junctions (rat-race couplers) is required to feed the sources. Moreover, proper RF circuits are needed for the final estimation of the azimuth and elevation angle (Fig. 6.19). This part of the system go beyond the objectives of this work.

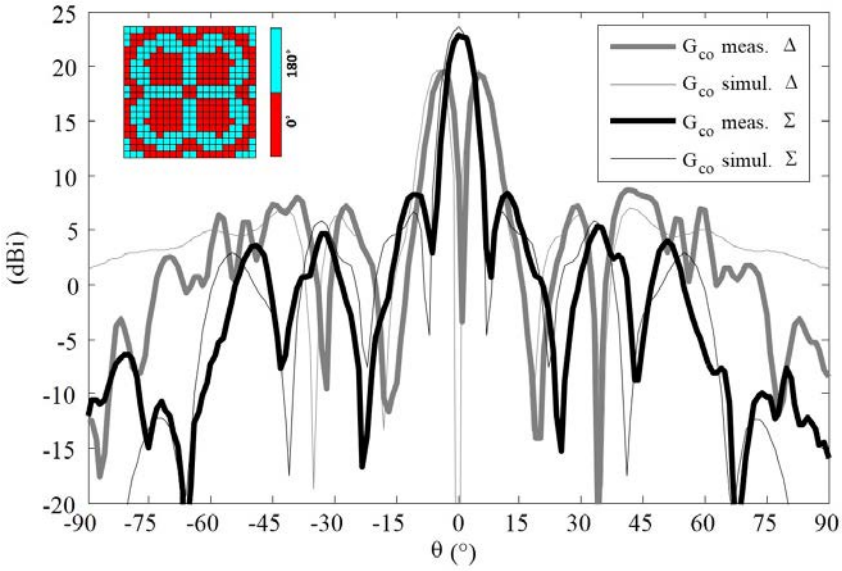

Figure 6.16: Simulated and measured Σ and Δ radiation patterns at 10 GHz for the four-sources configuration with a broadside beam.

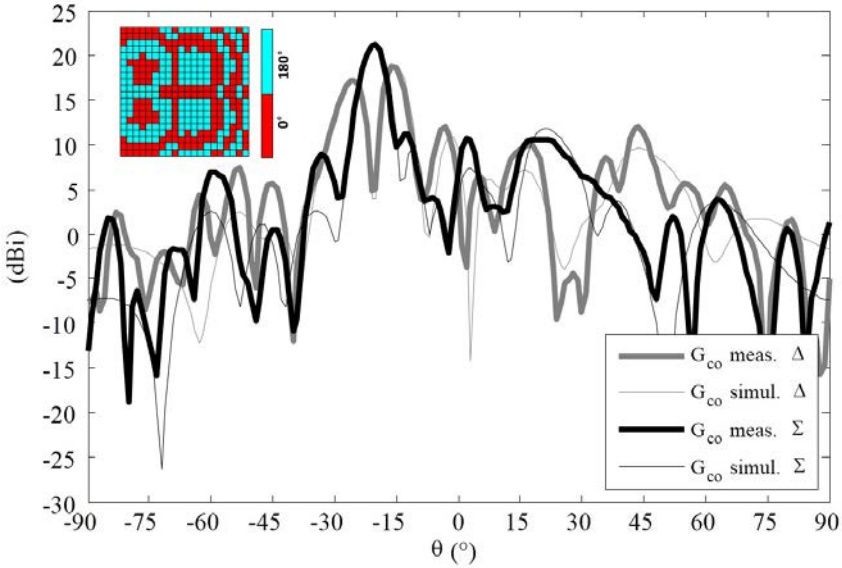

Figure 6.17: Simulated and measured Σ and Δ radiation patterns at 10 GHz for the four-sources configuration with a 20° tilted beam.

Table 6.1: Focal source excitation phase for Δ-pattern generation in the four-sources configuration.

Source 1	Source 2	Source 3	Source 4	Pattern
α	α	α	α	Σ
α	α	$\alpha+\pi$	$\alpha+\pi$	Δ horizontal
α	$\alpha+\pi$	$\alpha+\pi$	α	Δ vertical

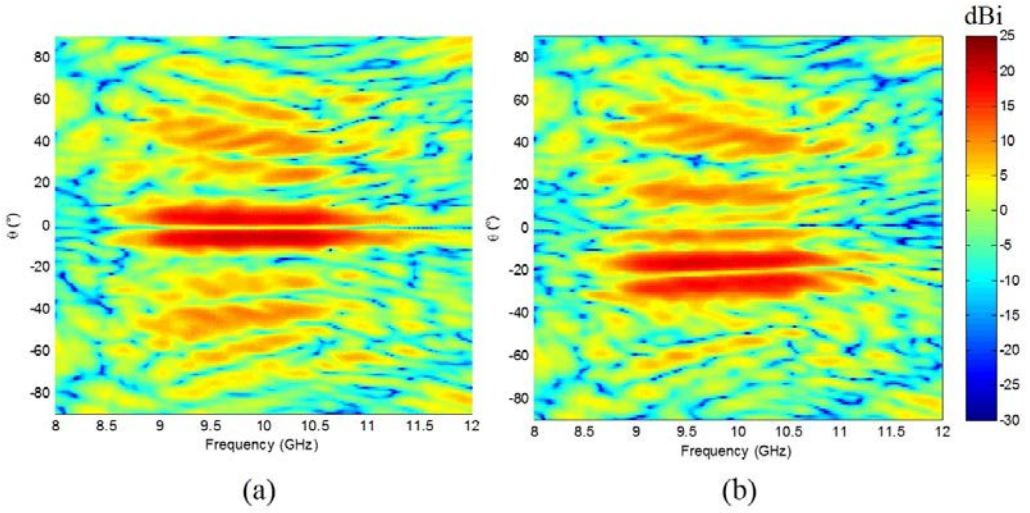

Figure 6.18: Measured Δ radiation patterns for the four-sources configuration with a broadside (a) and a 20° tilted (b) beam as a function of the frequency.

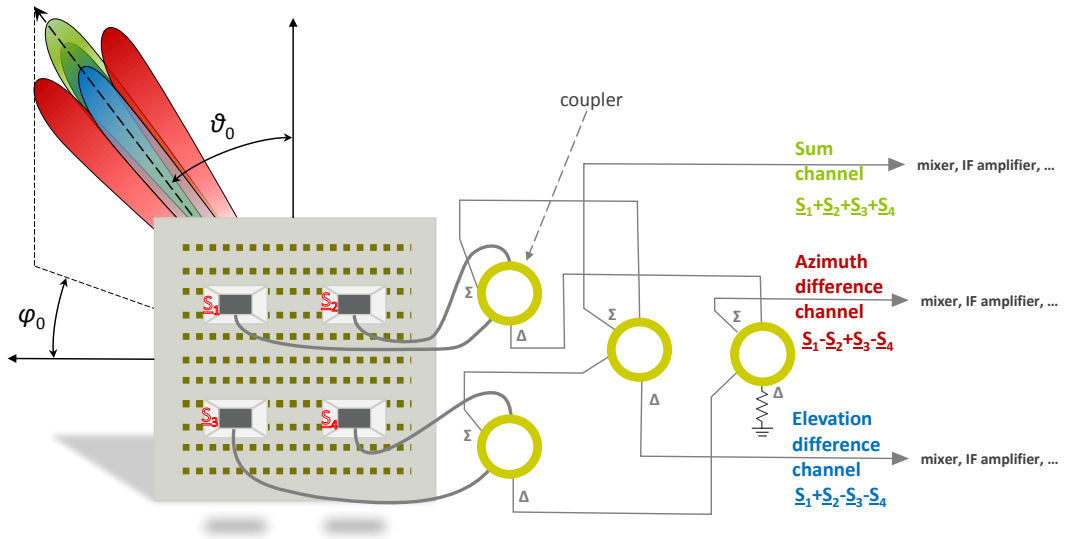

Figure 6.19: Scheme of the feeding network for the four-sources configuration in order to realize a four-quadrant monopulse radar system.

Table 6.2: Simulated and measured Σ-radiation pattern characteristics at 10 GHz for the single-source configuration.

	E-plane				H-plane			
	Gain (dBi)		SLL (dB)		Gain (dBi)		SLL (dB)	
	Sim.	Meas.	Sim.	Meas.	Sim.	Meas.	Sim.	Meas.
0	22.9	23.2	-17.2	-19.7	22.9	23.0	-19.4	-18.6
10	22.2	23.0	-12.8	-12.7	22.3	22.5	-13.8	-11.1
20	21.8	22.2	-16.8	-15.3	21.8	22.0	-16.5	-15.5
30	20.7	21.5	-14.9	-15.2	20.6	21.2	-14.0	-14.0
40	19.4	20.5	-12.7	-13.9	19.5	20.0	-14.5	-12.6

Table 6.3: Simulated and measured Δ-radiation pattern characteristics at 10 GHz for the single-source configuration in the E-plane.

	E-plane					
	Gain (dBi)		SLL (dB)		Null depth (dB)	
	Sim.	Meas.	Sim.	Meas.	Sim.	Meas.
0	19.1	20.0	-8.3	-11.4	44.0	22.0
10	20.1	20.3	-9.8	-10.0	20.7	22.0
20	18.8	19.1	-12.0	-10.3	30.3	22.6
30	17.8	18.2	-8.9	-9.7	24.4	14.2
40	17.0	18.3	-7.5	-9.8	22.0	12.7

Table 6.4: Simulated and measured Δ-radiation pattern characteristics at 10 GHz for the single-source configuration in the H-plane.

	H-plane					
	Gain (dBi)		SLL (dB)		Null depth (dB)	
	Sim.	Meas.	Sim.	Meas.	Sim.	Meas.
0	19.1	19.7	-8.4	-8.9	44.0	28.7
10	20.3	20.7	-10.3	-11.3	21.9	36.2
20	18.8	18.9	-12.3	-12.9	30.8	34.1
30	18.0	18.0	-9.8	-10.5	23.0	18.7
40	16.9	17.7	-7.4	-7.2	22.9	14.9

Table 6.5: Simulated and measured Σ-radiation pattern characteristics at 10 GHz for the four-sources configuration.

	E-plane				H-plane			
	Gain (dBi)		SLL (dB)		Gain (dBi)		SLL (dB)	
	Sim.	Meas.	Sim.	Meas.	Sim.	Meas.	Sim.	Meas.
0	23.5	23.2	-16.5	-11.7	23.5	23.2	-17.0	-14.4
10	21.9	21.7	-12.3	-11.5	22.0	21.0	-11.8	-10.9
20	21.3	21.1	-9.6	-9.9	21.3	20.4	-9.6	-9.3
30	20.9	21.5	-11.1	-12.0	20.9	20.7	-12.0	-12.2
40	20.1	20.7	-7.5	-7.0	20.2	20.1	-7.8	-7.8

Table 6.6: Simulated and measured Δ-radiation pattern characteristics at 10 GHz for the four-sources configuration in the E-plane.

	E-plane					
	Gain (dBi)		SLL (dB)		Null depth (dB)	
	Sim.	Meas.	Sim.	Meas.	Sim.	Meas.
0	19.7	20.1	-12.8	-9.0	55.0	18.0
10	18.6	18.0	-8.2	-5.8	24.2	21.0
20	19.0	18.7	-8.0	-6.9	23.0	13.9
30	17.5	18.8	-5.0	-7.0	17.0	30.0
40	16.7	17.9	-3.4	-3.8	17.5	15.9

Table 6.7: Simulated and measured Δ-radiation pattern characteristics at 10 GHz for the four-sources configuration in the H-plane.

	H-plane					
	Gain (dBi)		SLL (dB)		Null depth (dB)	
	Sim.	Meas.	Sim.	Meas.	Sim.	Meas.
0	19.7	19.3	-13.3	-10.6	55.0	22.7
10	18.7	18.7	-8.4	-7.7	21.4	20.5
20	18.8	19.1	-7.8	-8.1	15.1	19.0
30	18.8	17.7.8	-9.0	-7.6	14.3	19.5
40	16.7	16.5	-3.6	-4.2	17.2	16.0

6.5 Conclusions

This chapter demonstrated the radiation pattern synthesis for monopulse radar applications using a reconfigurable transmitarray at X band. Two configurations have been considered: single source and four sources for the illumination. In the first configuration, the generation of Δ patterns have been obtained by modifying the calculated phase distributions on the array surface. In particular, two regions are defined on the transmitarray surface in which a phase compensation law is defined. In the latter configuration, Σ/Δ patterns in the two cardinal planes are generated simultaneously by exciting with the correct phases the four sources. In both cases, the beams can be tilted in any cut-plane. The two configurations have been successfully tested in anechoic chamber and a good agreement has been obtained with tilted beams up to 40° in the two cardinal planes.

The multisource configuration allows the generation of all the beams required for a four-quadrants systems with electronic beam steering in any cut-plane. These characteristics place the proposed transmitarray at the state-of-the-art among the monopulse systems. In addition, this configuration can work also in sequential-mode (sequential lobing radar technique). In fact, each focal source can be associated to a different beam which can be steered in any arbitrary direction by selecting the phase distribution on the corresponding transmitarray quadrant. The possibility to function in different radar modes (monopulse, sequential lobing) broaden its field of applications.

The obtained performance can be improved by considering higher resolution phase distributions (2 bits of quantization) and then increasing the efficiency of the whole antenna. Polarization diversity is often needed in these systems and can be obtained by considering the same antenna architecture with a dual-polarized transmitarray design.

General conclusions

The design, realization and experimental characterization of transmitarray antennas working in Ka-band have been presented. The implementation of electronic beam-steering and the generation of circular polarization have been tackled using standard PCB manufacturing technology and active devices.

In Chapter 1, the transmitarray operational principle has been illustrated and compared to the traditional technologies (phased arrays and reflectarrays). The advantages of different reconfiguration approaches have been discussed while reviewing the designs proposed in the recent literature. Some major fields of applications, such as satellite communications and wireless networks, have been discussed.

In Chapter 2, the hybrid simulation technique used for the analysis and synthesis of transmitarrays has been reported. It is based on numerical simulations and analytical formulations allowing a significant reduction of the computational cost. The sequential rotation technique has been implemented in this tool for the generation of the circular polarization. Compared to phased arrays, the spatial feeding which characterizes transmitarrays allows to apply this technique without introducing further complexity in the structure. Several rotation distributions have been considered and the radiation performances are compared. The effects of the mutual coupling among neighbour unit-cells have been also discussed. A passive transmitarray has been realized and the measured results validate the developed methodology.

In Chapter 3, a linearly-polarized reconfigurable unit-cell in Ka-band with 1 bit of phase quantization is presented. The p-i-n diodes included in the design have been characterized with microwave probes up to 35 GHz and an equivalent lumped-element model has been extracted. The bias network realized includes a RF/DC decoupling circuit formed by capacitors in microstrip technology. The integration of several bias lines has been studied for the realization of large transmitarray configurations. A sensitivity analysis and the impact of oblique incidences have been also discussed. The realized prototype has been measured in standard WR-28 waveguide. Ad-hoc adaptors are included to reduce the impedance mismatch. A minimum insertion loss of 1.09 dB has been measured with a 3-dB relative bandwidth of 14.7% at 29.0 GHz.

In Chapter 4, the design of a reconfigurable 400-elements transmitarray working in circular polarization in Ka-band is presented. It is based on the unit-cells of Chapter 3. A random sequential rotation is applied to the transmitting layer in order to generate a circularly-polarized beam. The possibility to switch between the left and right circular polarization (LHCP/RHCP) is obtained by changing electronically the phase distribution on the transmitarray. The measurements in anechoic chamber have shown a broadside gain of 20.8 dBi and beam-tilting capabilities of $\pm 60°$.

In Chapter 5, the design of a reconfigurable unit-cell working in circular polarization in Ka-band has been presented. Several architectures are investigated and an ad-hoc characterization setup based on a square waveguide and an orthomode transducer has been proposed.

In Chapter 6, the radiation pattern synthesis for monopulse radar applications has been presented. Two strategies are considered. The first one is based on the generation of difference patterns by defining different regions on the transmitarray and applying different phase distributions. The second one is based on the multisource illumination. In particular, with four horn antennas, the simultaneous generation of a sum pattern and two difference patterns on the two cardinal planes has been achieved. The numerical results have been validated experimentally with anechoic chamber measurements in X band.

The results obtained in this Ph.D. thesis lead to several short- and long-term perspectives. The main short-term objective is increasing the phase resolution of the reconfigurable designs proposed in Chapter 3 and 5. In fact, a 2-bits phase resolution can reduce significantly (about 2 dB) the quantization losses and thereby improve the aperture efficiency. However, this approach is effective only if the higher-resolution architecture does not lead to an increased unit-cell insertion loss. Enhanced controls on the generated beam can be also investigated. In Chapter 5, the circular polarization switching with a 400-elements configuration has been proposed. The possibility to integrate this functionality on each unit-cell can be explored in order to improve the radiation efficiency.

Among the long-term perspectives, increasing the compactness of the antenna is a relevant objective. A significant reduction of the antenna thickness has been demonstrated in Chapter 6 and Appendix C by using multiple planar focal sources illumination. Multifacets and conformal transmitarrays can be considered to further improve their integration on mobile platforms.

Increasing the working frequency is another long-term perspective. Scaling reconfigurable transmitarrays to V- and E-band will probably require the integration of the unit-cell radiating element and active devices (diodes, MEMS, amplifier, etc.) in a monolithic structure, increasing significantly the complexity and the cost of the system.

Appendix A

Scattering parameters in circular polarization

In this appendix, the definition of the scattering parameters associated to the circular polarization is reported. The proposed formulations are applied to the unit-cells design of Chapters II and V, in which the lineraly-polarized wave incident on the receiving layer is transformed to a circularly-polarized wave generated by the transmitting layer.

First, we define the input and output vectors considering the scheme of Fig. A.1, as

$$\underline{e} = \begin{pmatrix} e_{1x} \\ e_{1y} \\ e_{2x} \\ e_{2y} \end{pmatrix}, \underline{f} = \begin{pmatrix} f_{1x} \\ f_{1y} \\ f_{2x} \\ f_{2y} \end{pmatrix}. \tag{A.1}$$

The relation between these two vectors is

$$\underline{f} = \underline{\underline{S}} \cdot \underline{e}, \tag{A.2}$$

where the scattering matrix S is defined by:

$$\underline{\underline{S}} = \begin{pmatrix} S_{11xx} & S_{11xy} & S_{12xl} & S_{12xr} \\ S_{11yx} & S_{11yy} & S_{12yl} & S_{12yr} \\ S_{21lx} & S_{11ly} & S_{22ll} & S_{22rr} \\ S_{21rx} & S_{11ry} & S_{22rl} & S_{22lr} \end{pmatrix}. \tag{A.3}$$

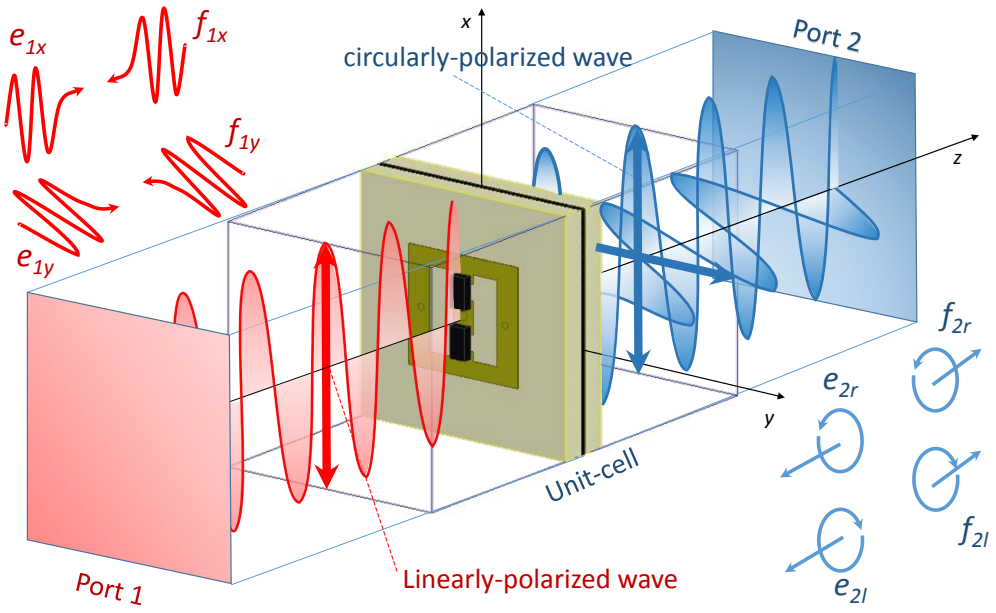

Figure A.1: Scheme of incident and emerging waves considered in the scattering parameters evaluation in circular polarization.

Each element of this matrix is referred to the linear and circular polarizations at ports 1 and 2, respectively, as shown in Fig. A.1. For instance, S_{11xx} is the reflection coefficient at port 1 associated to a linearly-polarized wave incident along x and S_{22ll} is the reflection coefficient at port 2 associated to a left-handed circularly-polarized incident wave.

The relations between the vectors e and f with the vectors $\underline{a}$ and $\underline{b}$ are:

$$\underline{e} = \underline{\underline{H}} \cdot \underline{a}, \underline{f} = \underline{\underline{H}} \cdot \underline{b} \tag{A.4}$$

where

$$\underline{a} = \begin{pmatrix} a_{1x} \\ a_{1y} \\ a_{2x} \\ a_{2y} \end{pmatrix}, \underline{b} = \begin{pmatrix} b_{1x} \\ b_{1y} \\ b_{2x} \\ b_{2y} \end{pmatrix}, \underline{\underline{H}} = \frac{1}{\sqrt{2}} \begin{pmatrix} \sqrt{2} & 0 & 0 & 0 \\ 0 & \sqrt{2} & 0 & 0 \\ 0 & 0 & 1 & j \\ 0 & 0 & 1 & -j \end{pmatrix}. \tag{A.5}$$

The vector of the incident waves $\underline{a}$ is related to the vector of the transmitted waves $\underline{b}$ as follows:

$$\underline{b} = \underline{\underline{S_{xy}}} \cdot \underline{a}, \tag{A.6}$$

where

$$\underline{\underline{S_{xy}}} = \begin{pmatrix} S_{11xx} & S_{11xy} & S_{12xx} & S_{12xy} \\ S_{11yx} & S_{11yy} & S_{12yx} & S_{12yy} \\ S_{21xx} & S_{11xy} & S_{22xx} & S_{22xy} \\ S_{21yx} & S_{11xy} & S_{22yx} & S_{22yy} \end{pmatrix}. \tag{A.7}$$

Then, the scattering matrix $\underline{\underline{S}}$ can be expressed as

$$\underline{\underline{S}} = \underline{\underline{H}} \cdot \underline{\underline{S_{xy}}} \cdot \underline{\underline{H}}^{-1}, \tag{A.8}$$

and their components are given by the following expressions:

$$S_{12xl} = \frac{1}{\sqrt{2}}(S_{12xx} + jS_{12xy}), S_{12yl} = \frac{1}{\sqrt{2}}(S_{12yx} + jS_{12yy}), \tag{A.9}$$

$$S_{12xr} = \frac{1}{\sqrt{2}}(S_{12xx} - jS_{12xy}), S_{12yr} = \frac{1}{\sqrt{2}}(S_{12yx} - jS_{12yy}), \tag{A.10}$$

$$S_{21lx} = \frac{1}{\sqrt{2}}(S_{21xx} + jS_{21yx}), S_{21ly} = \frac{1}{\sqrt{2}}(S_{21xy} + jS_{21yy}), \tag{A.11}$$

$$S_{21rx} = \frac{1}{\sqrt{2}}(S_{21xx} - jS_{21yx}), S_{21ry} = \frac{1}{\sqrt{2}}(S_{21xy} - jS_{21yy}), \tag{A.12}$$

$$S_{22rr} = \frac{1}{2}(S_{22xx} + jS_{22xy} + jS_{22yx} - S_{22yy}), \tag{A.13}$$

$$S_{22rl} = \frac{1}{2}(S_{22xx} - jS_{22xy} - jS_{22yx} - S_{22yy}), \tag{A.14}$$

$$S_{22lr} = \frac{1}{2}(S_{22xx} + jS_{22xy} - jS_{22yx} + S_{22yy}), \tag{A.15}$$

$$S_{22ll} = \frac{1}{2}(S_{22xx} - jS_{22xy} + jS_{22yx} + S_{22yy}). \tag{A.16}$$

Appendix B

Control boards architecture

The four boards used to control the p-i-n diodes mounted on the transmitarray unit-cells were developed in [74] and are shown in Fig. B.1. Each board, whose dimensions are 150×150 mm^2 permits to generate the DC current for the control of 100 bias lines in a quarter of the transmitarray. They are placed behind the focal plane and the connection with the antenna is realized with four ribbon cables. With the code developed in [74], the programmable sequence is sent to each board serially. This data stream is saved on shift registers for a series-to-parallel conversion. As shown in Fig. B.2, these registers are connected to several switches. Each switch is connected to a bias line of the transmitarray and gives a negative $-V_{cc}$ or positive V_{cc} voltage.

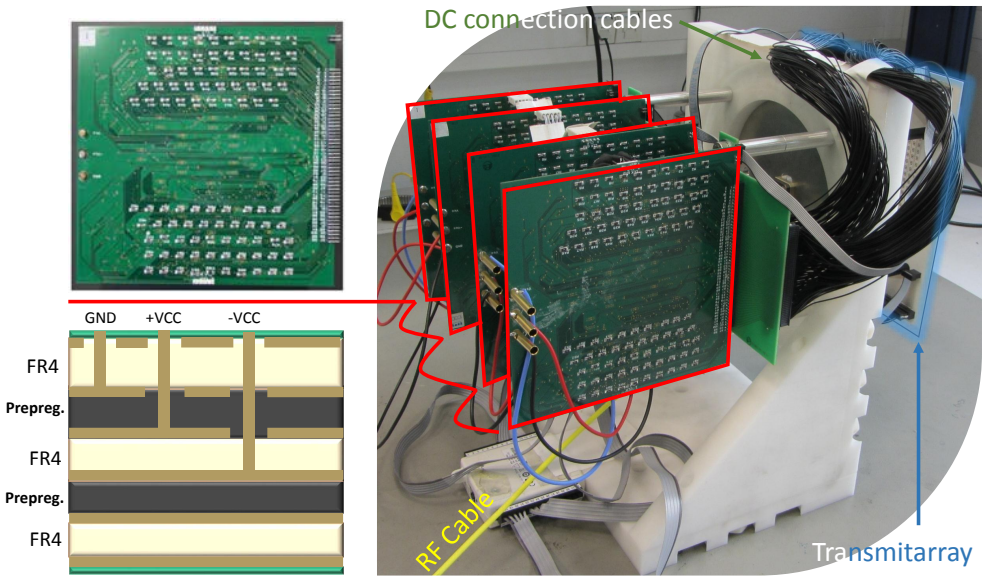

Figure B.1: Photograph of the transmitarray prototype with the four control boards and scheme of their PCB stacking.

The generated currents are determined with 100 chip resistors connected in series with the bias lines.

Each control board contains the following components:

- 13 8-bit shift registers (Texas Instruments SN74HC164D);
- 25 4×4 switches (Analog Devices ADG1434YRUZ);
- 100 chip resistors of 360 Ω, this value is selected to obtain ±10 mA on each bias line with ± 5V.

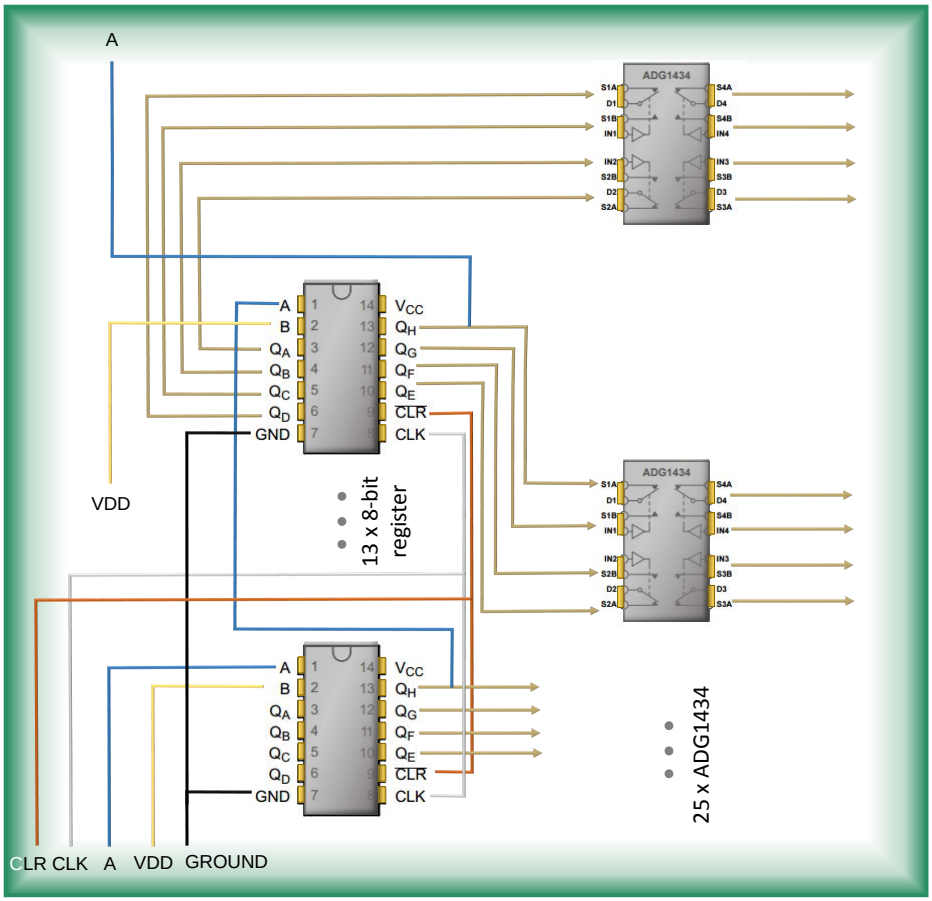

Figure B.2: Scheme of the working principle of each control board.

Appendix C

Reconfigurable transmitarray in Ka-band with planar focal sources

In this part, the objective is to reduce the focal distance, i.e. the distance between the focal source and the array panel, of the antenna configuration proposed in Chapter IV. The value F/D (F is the focal distance, D is the array side) was 0.6 (F = 60 mm). A focal source array in substrate integrated waveguide (SIW) technology is proposed here. A significant reduction (about 50%) of the focal distance will be demonstrated.

C.1 2×2 SIW slot array

First, a single planar source has been designed. Slots array in SIW [107] are selected as a trade-off between the cost, the complexity of the required substrate stacking and the polarization purity. An array of four slots fed with two SIW waveguides and a power splitter in the same technology has been chosen as starting design (C.2). The dimensions of the waveguides, of the slots and the distance between the slot centers and the waveguide end wall are chosen by following the well-known analytical relations proposed in the literature [108, 107]. The SIW waveguide is defined by its width w, the metallized via diameter d and their periodicity p. A standard waveguide of width w_{eq} equivalent to the one in SIW of width w can be defined as follows:

$$w_{eq} = w \cdot s, \tag{C.1}$$

with s defined as

$$s = s_1 + \frac{s_2}{\frac{p}{d} + \frac{s_1 + s_2 - s_3}{s_3 - s_1}}, \tag{C.2}$$

where

$$s_1 = 1.0198 + \frac{0.3465}{\frac{w}{p} - 1.0684}, s_2 = -0.1183 - \frac{1.2729}{\frac{w}{p} - 1.2010}, s_3 = 1.0082 - \frac{0.9163}{\frac{w}{p} - 0.2152}. \quad \text{(C.3)}$$

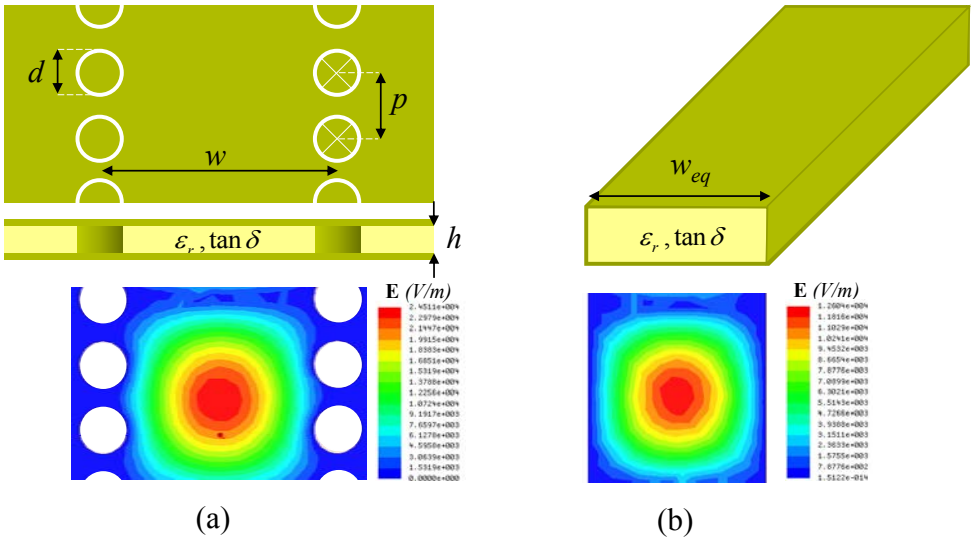

Figure C.1: Sketches of a waveguide in SIW technology (a) and its equivalent standard waveguide (b).

The SIW waveguide on a RT6002 substrate of thickness h =0.584 mm with w =5 mm, d =1 mm and p =1.4 mm is equivalent to a standard waveguide with w =4.2 mm (Fig. C.1). Its cutoff frequency for the fundamental mode TE10 can be easy calculated and it is 20.8 GHz. Considering 1.9 mm as the height of the equivalent waveguide, the higher modes TE20 and TE01 cut-off frequencies are 41 and 46 GHz, warranting its uni-modal operation in Ka band. The substrate configuration is the same used for the fabrication of the transmitarray unit-cells and described in detail in Chapter 3. A fractal-geometry is used for the slot shape in order to extend the bandwidth without increasing the number of layers [109, 110]. Finally, an optimization has been carried out through numerical simulations including in the 3D structure the microstrip transition and an end-launch connector of 50 Ω of characteristic impedance (C.2) [111]. The simulated reflection coefficient of Fig. C.3(a) is under -9.0 dB between 28.0 and 30.9 GHz. The broadside gain is 9.4 dBi at 29 GHz (Fig. C.6(b)) with a simulated radiation efficiency of 89%. The cross polarization discrimination is 22 dB at this frequency. A prototype has been fabricated and tested. The measured reflection coefficient shows a frequency shift of about 300 MHz (1%) due to the tolerances of the fabrication process. The measured radiation pattern shows a maximum gain of 9.5 dBi. The measured radiation patterns as a function of frequency are shown in Fig. C.4.

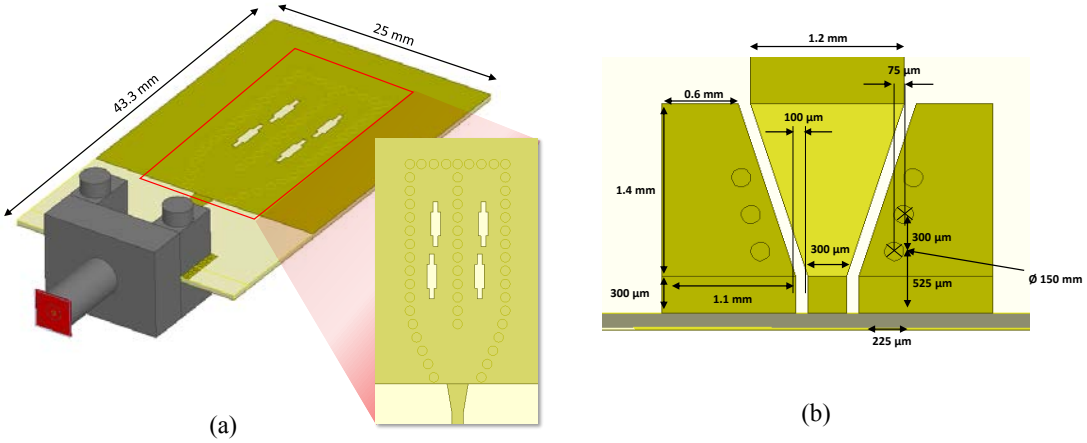

Figure C.2: 3D sketch (a) and microstrip transition detail (b) for the 2×2 array of slot antenna designed in SIW technology.

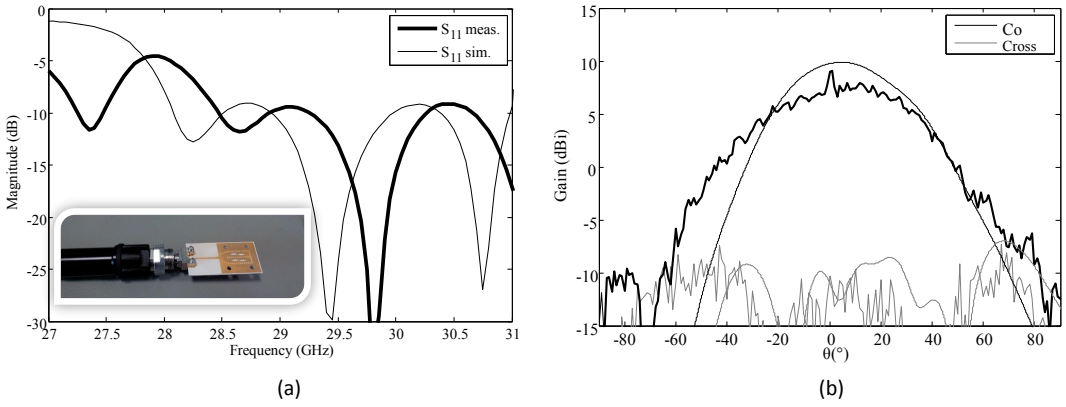

Figure C.3: Measured and simulated reflection coefficient (a) and radiation pattern in the vertical plane (E-plane) at 29 GHz (b) for the 2×2 array of slot antennas designed in SIW technology.

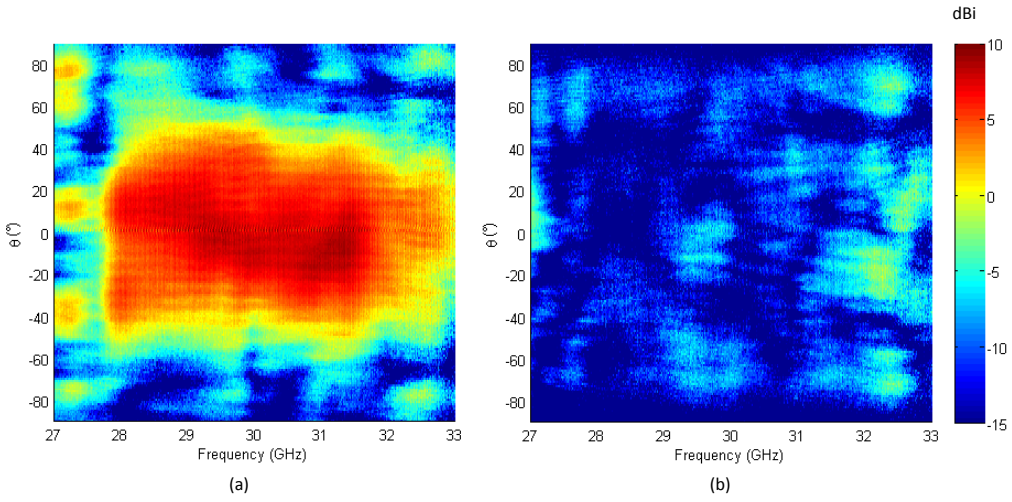

Figure C.4: Measured 2D maps of the co-(a) and cross-polarized components (b) for the 2×2 array of slot antennas designed in SIW technology.

C.2 4×4 SIW slot array

With the design discussed in the previous paragraph, an array of 16 slots has been designed. The distance between the four sub-arrays of 4 elements d and the focal distance F (Fig. C.5) have been optimized at the same time considering the hybrid simulation tool developed in [40],[106], maximizing the broadside gain of the transmitarray of Chapter IV. The results of this analysis gives a distance d of 34 mm and a focal distance F of 36 mm ($F/D = 0.36$ mm).

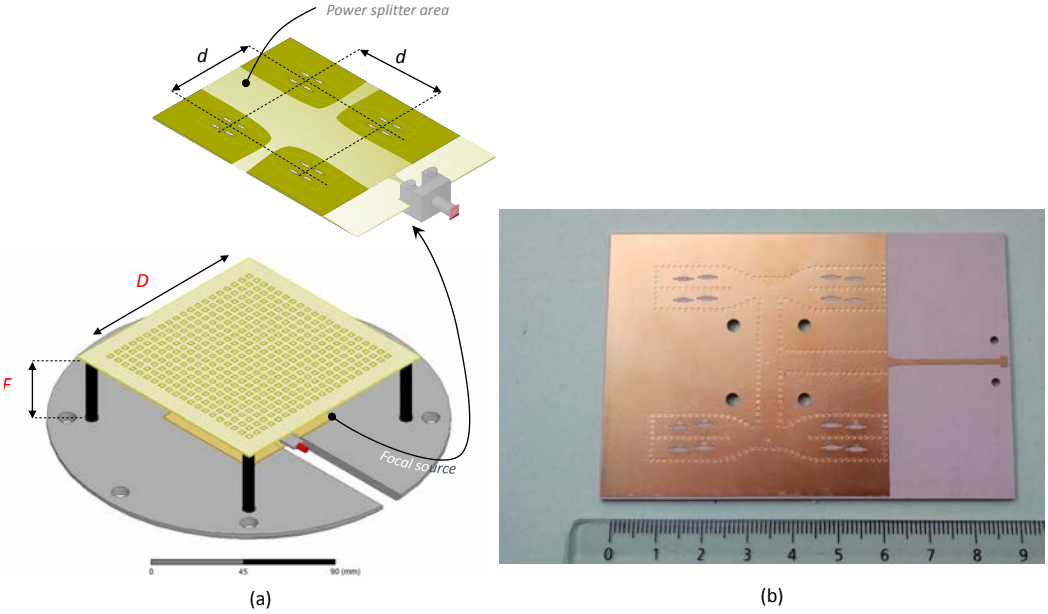

Figure C.5: 3D sketch (a) and photograph (b) of the 4×4 array of slot antenna designed in SIW technology designed as focal source of the transmitarray antenna proposed in Chapter IV.

The distance d has been fixed between the centers of the 4-elements sub-arrays and three 3-dB SIW power splitters are realized (Fig. C.5). The choice of the SIW technology even for the feeding network is due to the fact that a microstrip network realized on the same layer of the antennas could give spurious radiation and reduce the working bandwidth. In addition, a single transition between the SIW waveguide and the microstrip line is required in this case. Shorting inductive posts are inserted in the design to improve the impedance matching. The feeding network and the transition lead to 1-dB of additional losses estimated in the full-wave simulation and a radiation efficiency of 70%.

The simulated and measured reflection coefficients of Fig. C.6 show a matching between 28.0 and 31.0 GHz with a return loss higher than 8.5 dB. A good agreement is obtained between the simulated and measured results in anechoic chamber (Figs. C.6, C.7, C.8) despite a discrepancy of 1.2 dB on the gain (the maximum measured gain is 13.7 dBi at 29.0 GHz).

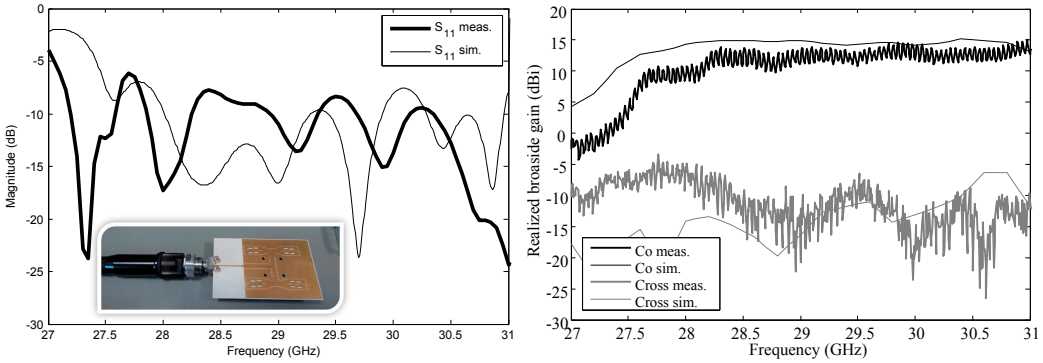

Figure C.6: Measured and simulated reflection coefficient (a) and broadside gain (b) for the 4×4 array of slot antennas designed in SIW technology.

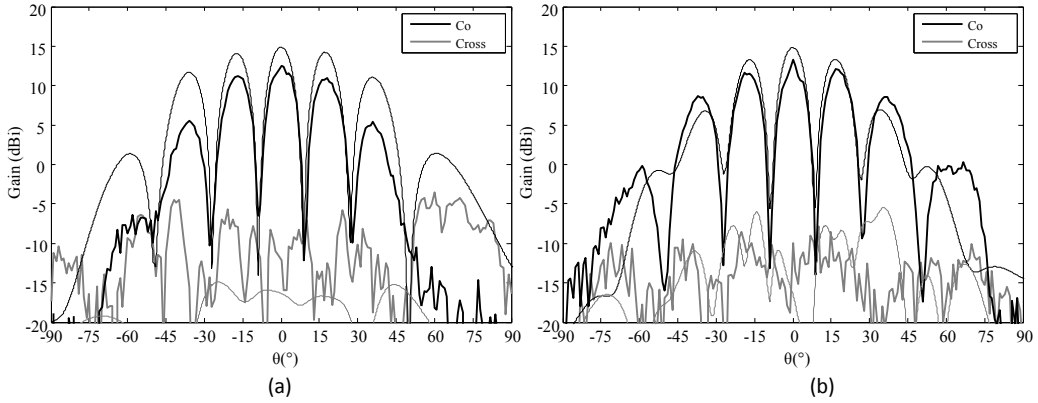

Figure C.7: Measured radiation pattern of the co- and cross-polarized components in the horizontal (a) and vertical (b) planes at 29 GHz for the 4×4 array of slot antenna designed in SIW technology.

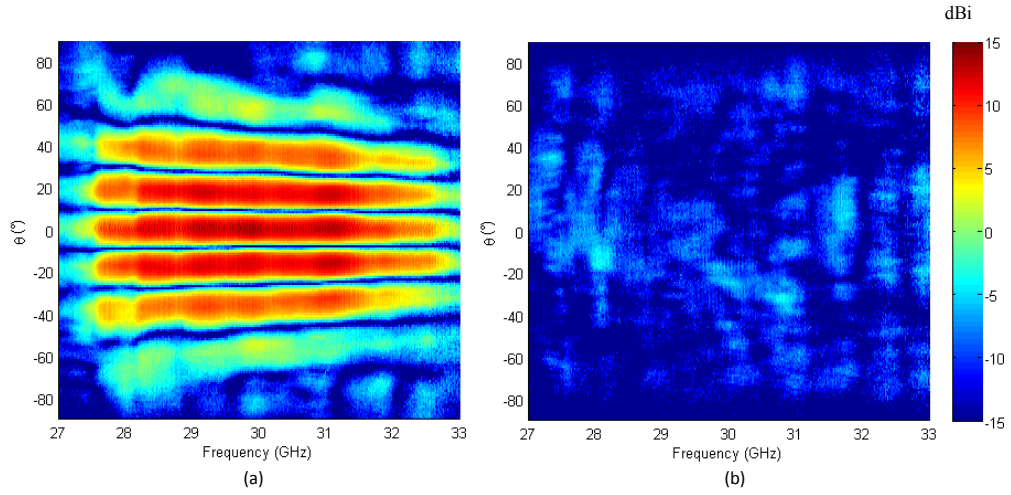

Figure C.8: Measured 2D maps of the co-(a) and cross-polarized components (b) for the 2×2 array of slot antenna designed in SIW technology.

This could be explained by considering additional losses inside the substrate or in the metallized top and bottom layers not well estimated in the simulated model. Further losses could be introduced by the end-launch connector and in the transition between this connector and the microstrip line. The same antenna architectures (arrays of 2×2 and 4×4 slots) have been realized with a coplanar transition to microwave G-S-G (pitch of 350 μm) in order to measure accurately their radiation efficiency and they are under test at the time when the manuscript is written.

C.3 Reconfigurable transmitarray with 4×4 SIW slot focal array

The SIW 16-elements array has been placed at a distance $F = 36$ mm from the transmitarray receiving layer (Fig. C.9). The radiation patterns with a main beam at broadside are shown in Fig. C.10. A very good agreement with the simulation is obtained. As expected, the SLL increases if compared with the single source configuration of Chapter IV. This is mainly due to the uniform power distribution created with the four 2×2 slot array. In fact, with a distance d of 34 mm, each sub-array illuminates almost exclusively a quarter of the transmitarray. The measured maximum gain is 16.2 dBi with a cross polarization discrimination of 27 dB at broadside. This value is lower than the measured one with a single horn antenna (Chapter 4) because the planar focal sources and the required feeding network introduce additional losses.

Tilted beams at -20° and -40° are obtained by changing electronically the phase distribution on the transmitarray panel. The measured radiation patterns of Figs. C.11, C.12 show a very good agreement with the simulations.

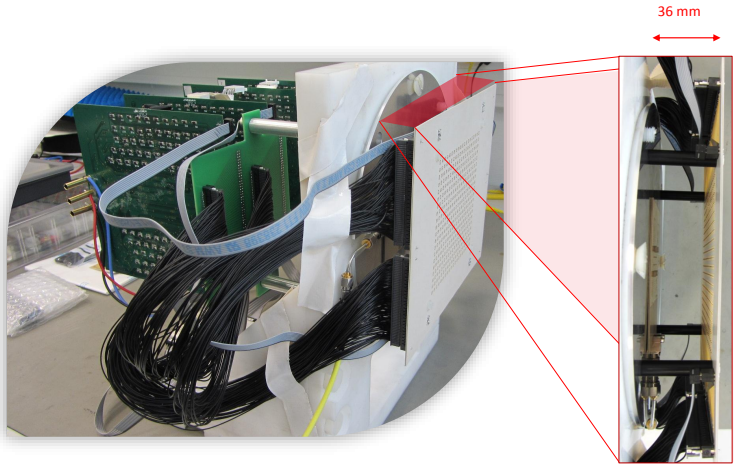

Figure C.9: Photograph of the transmitarray prototype of Chapter IV with the 4×4 array of slot antennas as focal source.

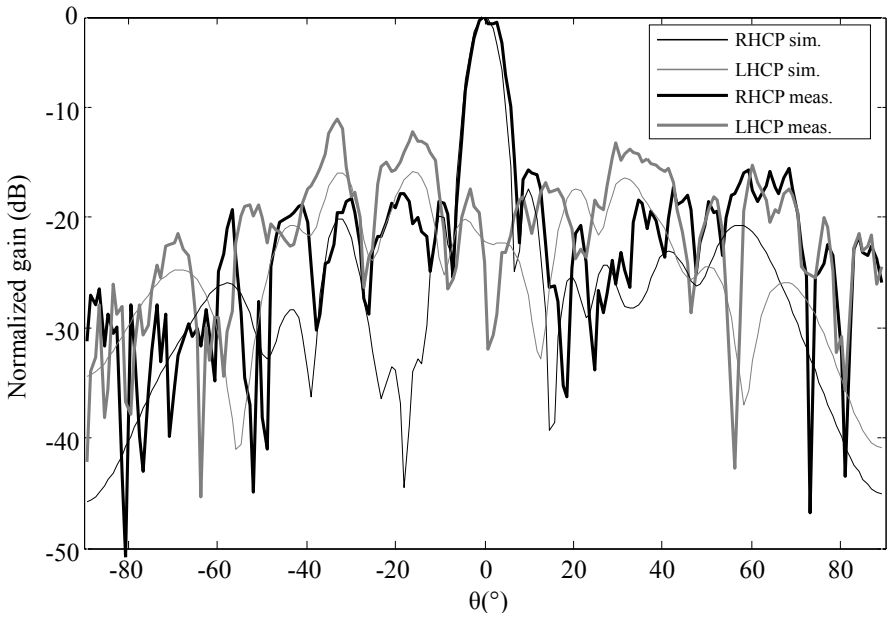

Figure C.10: Simulated and measured radiation patterns at 29 GHz of the co- and cross-polarized components (normalized gain) for the transmitarray with the 4×4 array of slot antennas designed in SIW technology: beam at broadside.

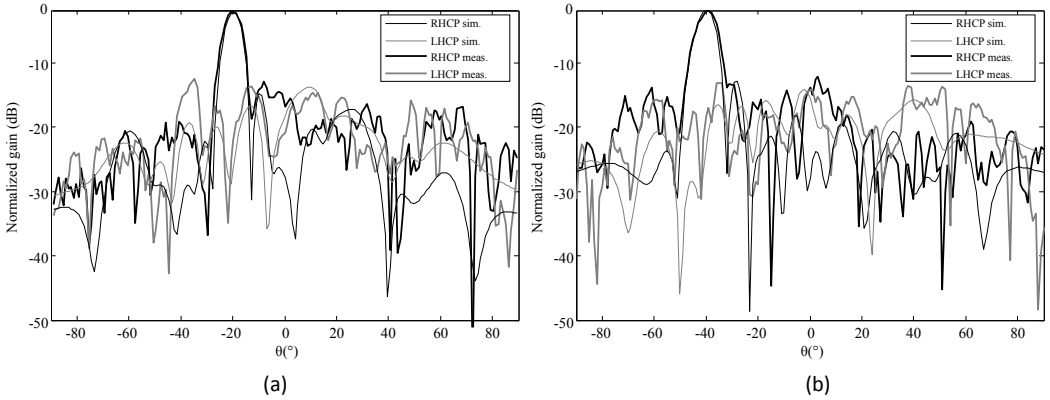

Figure C.11: Simulated and measured radiation patterns at 29 GHz of the co- and cross-polarized components (normalized gain) for the transmitarray with the 4×4 array of slot antennas designed in SIW technology: tilted beams at -20° (a) and -40° (b) in the horizontal plane.

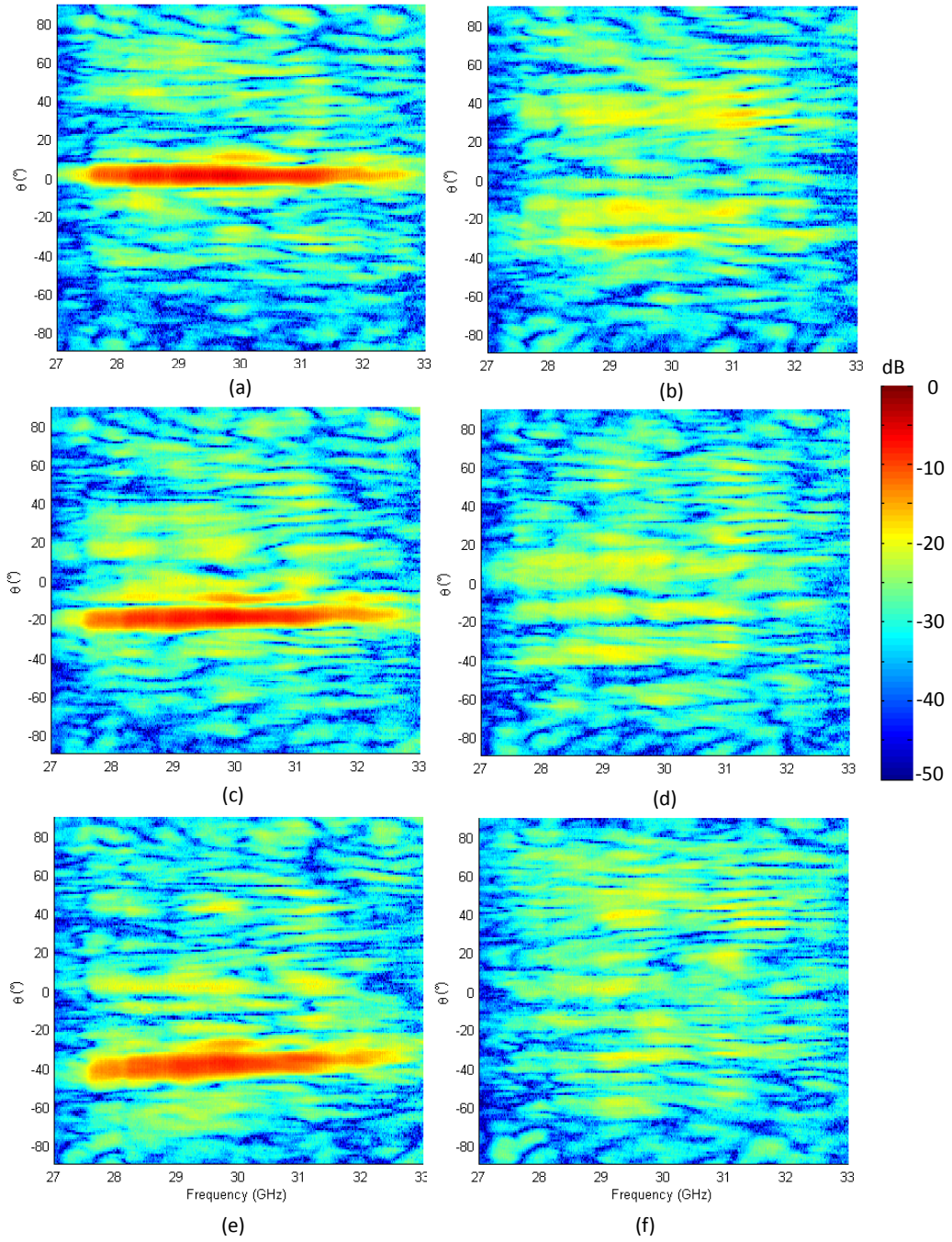

Figure C.12: Simulated and measured radiation patterns of the co- (a, c, e) and cross- (b, d, f) polarized components (normalized gain) for the transmitarray with the 4×4 array of slot antennas designed in SIW technology: broadside beam (a, b) and tilted beams at -20° (c, d) and -40° (e, f) in the horizontal plane.

Appendix D

Circularly-polarized unit-cell characterization setup

This appendix details the calibration technique used in the characterization of the circularly-polarized unit-cell presented in Chapter 5 and usind the setup shown in Fig. D.1. In order to correctly de-embed the junction J2 (Fig. D.1), an *ad hoc* procedure and specific calculations are needed. In particular, the use of the transfer (T) parameters instead of scattering (S) simplifies the calculations. The relation between S and T parameters for a two-port generic microwave network is defined as follows:

$$\underline{\underline{T}} = \left(\underline{\underline{A}} + \underline{\underline{B}} \cdot \underline{\underline{S}}\right) \cdot \left(\underline{\underline{C}} + \underline{\underline{D}} \cdot \underline{\underline{S}}\right)^{-1}, \tag{D.1}$$

where

$$\underline{\underline{A}} = \begin{pmatrix} 1 & 0 \\ 0 & 0 \end{pmatrix}, \underline{\underline{B}} = \begin{pmatrix} 0 & 0 \\ 0 & 1 \end{pmatrix}, \underline{\underline{C}} = \begin{pmatrix} 0 & 1 \\ 0 & 0 \end{pmatrix}, \underline{\underline{D}} = \begin{pmatrix} 0 & 0 \\ 0 & 1 \end{pmatrix}. \tag{D.2}$$

A similar expression can be found for the inverse transformation and it is omitted for the sake of brevity.

Since input and output signals at port 1 (Fig. D.1) cannot be directly measured, the junction J2 is characterized by measuring the scattering parameters with an ad-hoc rectangular-to-square adaptor of length $L_m = 9$ mm (Fig. D.3). This length has been optimized with full wave simulations. Its scattering parameters have been measured by connecting three short circuits of different length (L_1=7 mm, L_2=12 mm, L_3=19 mm) to the square port, as shown in Fig. D.2). For the two-port network, we have:

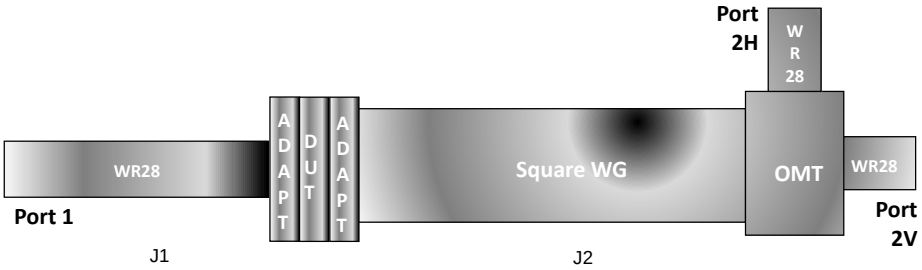

Figure D.1: Scheme of waveguide setup formed by two junctions J1 and J2, considered for the circularly-polarized unit-cell characterization. It includes two rectangular WR-28 straight waveguides, a square waveguide section, an OMT and two adaptors.

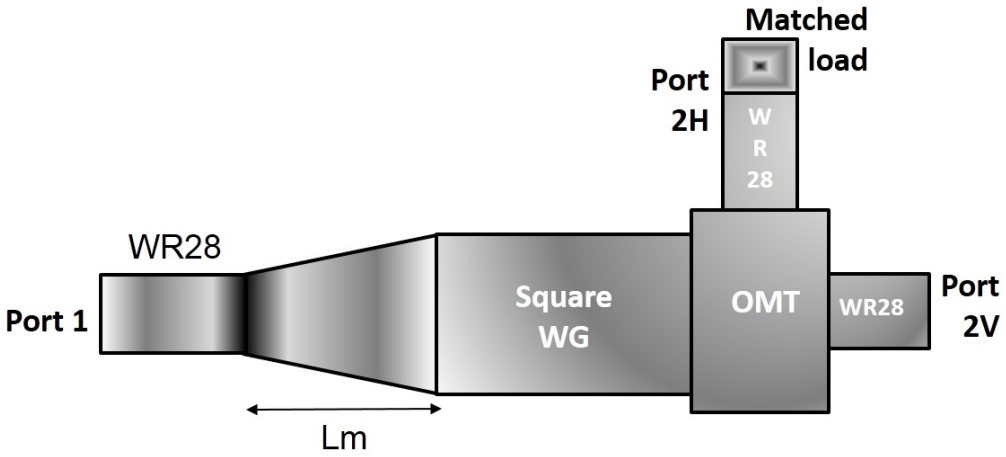

Figure D.2: Scheme of junction 2 connected to the adaptor in WR28 (L_m=9 mm).

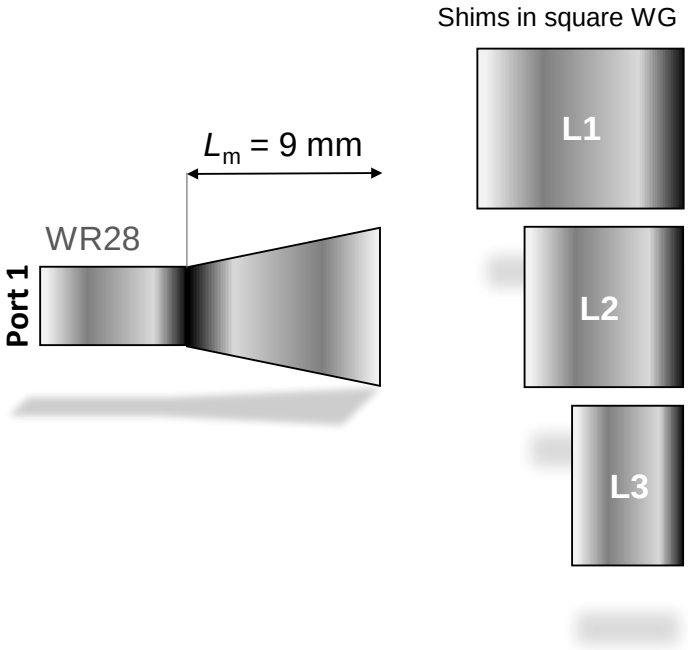

Figure D.3: Scheme of the short circuit method applied to the junction 2 for the vertical polarization.

$$\begin{pmatrix} b_1 \\ \\ b_2 \end{pmatrix} = \underline{\underline{S}}^{adapt} \begin{pmatrix} a_1 \\ \\ a_2 \end{pmatrix}, \tag{D.3}$$

where

$$\underline{\underline{S}}^{adapt} = \begin{pmatrix} S_{11}^{adapt} & S_{12}^{adapt} \\ \\ S_{21}^{adapt} & S_{22}^{adapt} \end{pmatrix}. \tag{D.4}$$

We can consider that $S_{21}^{adapt} = S_{12}^{adapt}$, because the component is reciprocal. It corresponds to the following system of equations:

$$\begin{aligned} b_1 &= S_{11}^{adapt} a_1 + S_{12}^{adapt} a_2. \\ b_2 &= S_{12}^{adapt} a_1 + S_{22}^{adapt} a_2. \end{aligned} \tag{D.5}$$

We define the three reflection coefficients $\Gamma_1, \Gamma_2, \Gamma_3$ (magnitude and phase) associated to the three lengths L_1, L_2, L_3. Connecting the first short circuit, we have

$$a_1 = \Gamma_1 b_1. \tag{D.6}$$

Considering the equation D.4, we obtain

$$\frac{a_1}{\Gamma_1} = S_{11}^{adapt} a_1 + S_{12}^{adapt} a_2, \tag{D.7}$$

$$a_1 = \frac{\Gamma_1 S_{12}^{adapt} a_2}{1 - \Gamma_1 S_{11}^{adapt}}, \tag{D.8}$$

and then

$$b_2 = a_2 \left(S_{22}^{adapt} + \frac{\Gamma_1 (S_{12}^{adapt})^2 a_2}{1 - \Gamma_1 S_{11}^{adapt}} \right) \tag{D.9}$$

The same equation is valid for the other two short circuits by replacing Γ_1 with Γ_2 and Γ_3. The following three equations associated to the three measurements can be found:

$$S_{22}^{meas1} = S_{22}^{adapt} + \frac{\Gamma_1 (S_{12}^{adapt})^2}{1 - \Gamma_1 S_{11}^{adapt}} \tag{D.10}$$

$$S_{22}^{meas2} = S_{22}^{adapt} + \frac{\Gamma_2 (S_{12}^{adapt})^2}{1 - \Gamma_2 S_{11}^{adapt}} \tag{D.11}$$

$$S_{22}^{meas3} = S_{22}^{adapt} + \frac{\Gamma_3 (S_{12}^{adapt})^2}{1 - \Gamma_3 S_{11}^{adapt}} \tag{D.12}$$

From the solution of the previous system of equation, the scattering parameters of the adaptor can be calculated as:

$$S_{11}^{adapt} = -\frac{\Gamma_1 S_{22}^{meas2} - \Gamma_1 S_{22}^{meas3} - \Gamma_2 S_{22}^{meas1} + \Gamma_2 S_{22}^{meas3} + \Gamma_3 S_{22}^{meas1} - \Gamma_3 S_{22}^{meas2}}{\Gamma_{11} S_{22}^{meas1} + \Gamma_{22} S_{22}^{meas2} + \Gamma_{33} S_{22}^{meas3}}, \tag{D.13}$$

$$S_{12}^{adapt} = \pm \sqrt{\frac{S_{22}^{meas1} S_{22}^{meas2} \Gamma_1 - S_{22}^{meas1} S_{22}^{meas3} \Gamma_1 - S_{22}^{meas1} S_{22}^{meas2} \Gamma_2 + S_{22}^{meas2} S_{22}^{meas3} \Gamma_2 + S_{22}^{meas1} S_{22}^{meas2} \Gamma_3 - S_{22}^{meas2} S_{22}^{meas3} \Gamma_3}{\Gamma_{11} S_{22}^{meas1} + \Gamma_{22} S_{22}^{meas2} + \Gamma_{33} S_{22}^{meas3}}}, \tag{D.14}$$

$$S_{22}^{adapt} = -\frac{\Gamma_{33} S_{22}^{meas1} S_{22}^{meas2} + \Gamma_{11} S_{22}^{meas2} S_{22}^{meas3} + \Gamma_{22} S_{22}^{meas1} S_{22}^{meas3}}{\Gamma_{11} S_{22}^{meas1} + \Gamma_{22} S_{22}^{meas2} + \Gamma_{33} S_{22}^{meas3}}, \tag{D.15}$$

where

$$\Gamma_{11} = \Gamma_1(\Gamma_2 - \Gamma_3), \Gamma_{22} = \Gamma_2(\Gamma_3 - \Gamma_1), \Gamma_{33} = \Gamma_3(\Gamma_1 - \Gamma_2). \tag{D.16}$$

The sign of the scattering parameter S_{12}^{adapt}, which gives an uncertainty of 180° for its phase, can be easily determined by considering the length L_m of the adaptor.

The junction J2 is represented by the scattering matrix:

$$\begin{pmatrix} S_{1H1H}^{J2} & S_{1H2H}^{J2} & 0 & 0 \\ S_{2H1H}^{J2} & S_{2H2H}^{J2} & 0 & 0 \\ 0 & 0 & S_{1V1V}^{J2} & S_{1V2V}^{J2} \\ 0 & 0 & S_{2V1V}^{J2} & S_{2V2V}^{J2} \end{pmatrix}. \tag{D.17}$$

It is worth to notice that inserting the null elements in the previous matrix corresponds to the approximation of considering ideal isolation between the orthogonal modes of the OMT. For a real device, this is not true and leads to an error that cannot be de-embedded. However, if in the working bandwidth the OMT has high isolation (> 30 dB), the impact of this approximation on the measurements accuracy is limited. With the procedure described above, the scattering parameters of the whole junction J2 $\underline{\underline{S}}_{meas,V}^{J2}$ and the relative transfer matrix $\underline{\underline{T}}_{meas,V}^{J2}$ are known. Then, the three two-ports measurements described in Chapter 5 can be carried out to calculate the scattering parameters of the unit-cell under test.

D.1 Numerical validation

The procedure presented in the previous section has been validated numerically by considering full-wave simulations of the whole measurement setup (Fig. D.4). For this purpose, a simple narrow-band OMT hase been designed and used in the setup. It is formed by a straight section of square waveguide ($6.5 \times 6.5\,\mathrm{mm}^2$) closed on a short circuit and two rectangular WR-28 waveguides placed on the side walls at optimized distances from the short circuit. The full-wave simulations show good performances (return loss higher than 10 dB at all the three ports and isolations between the V and H ports greater than 30 dB) in a bandwidth of 2.6 GHz around 29 GHz. This OMT has been characterized with the short circuit method presented in the previous section and the full setup of Fig. D.4 has been analyzed with full wave simulations. In this way, we obtained the scattering parameters associated to the three measurements described in Chapter 5 and we applied the calculation for the unit-cell characterization.

The results for the unit-cell proposed in Chapter 5 are shown in Fig. D.5 for the 0°-state. As we can observe, the simulated measurement results (markers) are very similar to the unit-cell scattering parameters considered alone in the waveguide setup (lines) in the frequency range between 27.5 GHz and 30 GHz both in magnitude and phase. Discrepancies are due to the approximation done in the procedure (perfect isolation between the two OMT

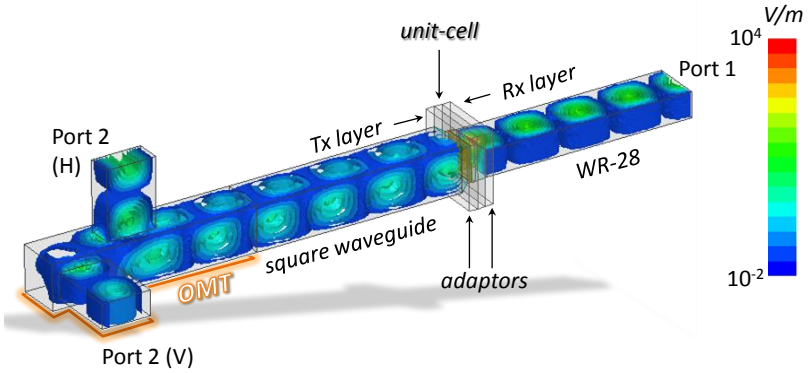

Figure D.4: Scheme of simulated waveguide setup. It includes: a simple narrow-band OMT formed by a square waveguide and two orthogonal rectangular WR-28 waveguides, a square waveguide ($6.5 \times 6.5\,\mathrm{mm}^2$), two waveguide adaptors, the unit-cell PCB and a rectangular WR-28 waveguide. Simulated electric-field at 29 GHz.

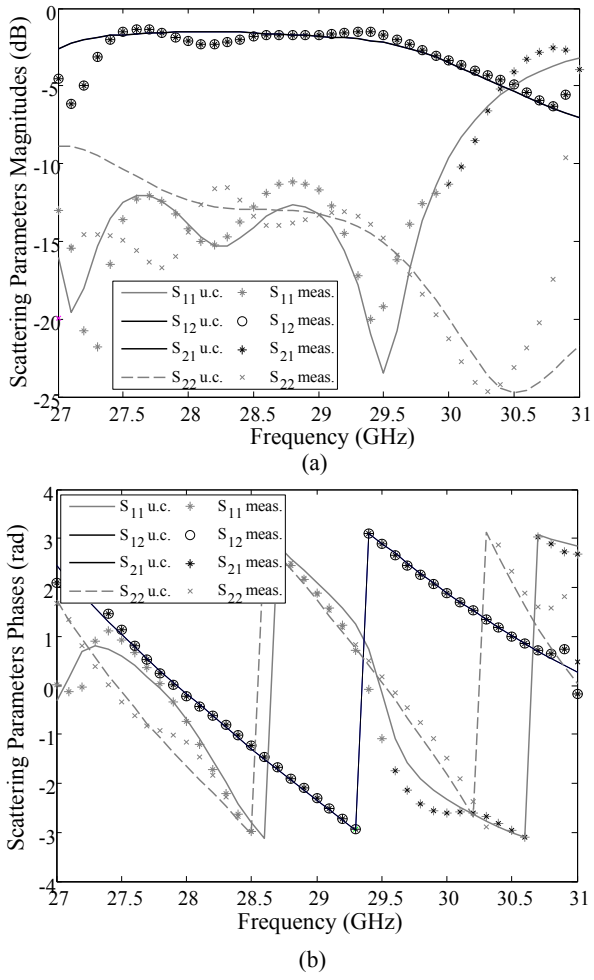

Figure D.5: Simulated scattering parameters of the measurements setup in magnitude (a) and phase (b) for the 0°-state.

ports). The degradation outside this frequency range is due to the narrow-band behavior of the considered OMT.

Bibliography

[1] J. Huang and J. Encinar, *Reflectarray antennas*. IEEE press, 2008.

[2] B. Mencagli, R. Gatti, L. Marcaccioli, and R. Sorrentino, "Design of large mm-wave beam-scanning reflectarrays," in *Wireless Technology, 2005. The European Conference on*, pp. 475–478, Oct 2005.

[3] R. Sorrentino, R. Gatti, and L. Marcaccioli, "Recent advances on millimetre wave reconfigurable reflectarrays," in *Antennas and Propagation, 2009. EuCAP 2009. 3rd European Conference on*, pp. 2527–2531, March 2009.

[4] S. Montori, L. Marcaccioli, R. Gatti, and R. Sorrentino, "Constant-phase dual polarization mems-based elementary cell for electronic steerable reflectarrays," in *Microwave Conference, 2009. EuMC 2009. European*, pp. 033–036, Sept 2009.

[5] C.-C. Cheng and A. Abbaspour-Tamijani, "Evaluation of a novel topology for mems programmable reflectarray antennas," *Microwave Theory and Techniques, IEEE Transactions on*, vol. 57, pp. 3333–3344, Dec 2009.

[6] H. Legay, B. Pinte, E. Girard, R. Gillard, M. Charrier, and A. Ziaci, "Low loss steerable reflectarray antenna for space application," in *25th ESA Antenna Workshop on Satellite Antenna Technology*, 2002.

[7] R. Pereira, R. Gillard, R. Sauleau, P. Potier, T. Dousset, and X. Delestre, "Four-state dual polarisation unit-cells for reflectarray applications," *Electronics Letters*, vol. 46, pp. 742–743, May 2010.

[8] E. Carrasco, M. Barba, and J. Encinar, "X-band reflectarray antenna with switching-beam using pin diodes and gathered elements," *Antennas and Propagation, IEEE Transactions on*, vol. 60, pp. 5700–5708, Dec 2012.

[9] P. Robustillo, J. Zapata, J. Encinar, and M. Arrebola, "Design of a contoured-beam reflectarray for a eutelsat european coverage using a stacked-patch element characterized by an artificial neural network," *Antennas and Wireless Propagation Letters, IEEE*, vol. 11, pp. 977–980, 2012.

[10] O. Bayraktar, O. Civi, and T. Akin, "Beam switching reflectarray monolithically integrated with rf mems switches," *Antennas and Propagation, IEEE Transactions on*, vol. 60, pp. 854–862, Feb 2012.

[11] E. Carrasco, M. Barba, J. Encinar, M. Arrebola, F. Rossi, and A. Freni, "Design, manufacture and test of a low-cost shaped-beam reflectarray using a single layer of varying-sized printed dipoles," *Antennas and Propagation, IEEE Transactions on*, vol. 61, pp. 3077–3085, June 2013.

[12] R. Florencio, J. Encinar, R. Boix, and G. Perez-Palomino, "Dual-polarisation reflectarray made of cells with two orthogonal sets of parallel dipoles for bandwidth and cross-polarisation improvement," *Microwaves, Antennas Propagation, IET*, vol. 8, no. 15, pp. 1389–1397, 2014.

[13] R. Florencio, J. Encinar, R. Boix, V. Losada, and G. Toso, "Reflectarray antennas for dual polarization and broadband telecom satellite applications," *Antennas and Propagation, IEEE Transactions on*, vol. 63, pp. 1234–1246, April 2015.

[14] G. Perez-Palomino, M. Barba, J. Encinar, R. Cahill, R. Dickie, P. Baine, and M. Bain, "Design and demonstration of an electronically scanned reflectarray antenna at 100 ghz using multiresonant cells based on liquid crystals," *Antennas and Propagation, IEEE Transactions on*, vol. 63, pp. 3722–3727, Aug 2015.

[15] K.-W. Lam, S.-W. Kwok, Y. Hwang, and T.-C. Lo, "Implementation of transmitarray antenna concept by using aperture-coupled microstrip patches," in *Microwave Conference Proceedings, 1997. APMC '97, 1997 Asia-Pacific*, vol. 1, pp. 433–436 vol.1, Dec 1997.

[16] P. de la Torre and M. Castaner, "Transmitarray for ku band," in *Antennas and Propagation, 2007. EuCAP 2007. The Second European Conference on*, pp. 1–5, Nov 2007.

[17] P. de la Torre and M. Castaner, "Design and prototype of a 12- GHz transmit-array," *Microwave and Optical Technology Letters*, 2007.

[18] H. Kaouach, L. Dussopt, R. Sauleau, and T. Koleck, "Design and demonstration of 1-bit and 2-bit transmit-arrays at x-band frequencies," in *European Microwave Conference, 2009. EuMC 2009.*, pp. 918–921, Sept 2009.

[19] A. Clemente, L. Dussopt, R. Sauleau, P. Potier, and P. Pouliguen, "Design and characterization of 2-bit passive unit-cells and transmit-arrays in x-band," in *Antennas and Propagation (EUCAP), Proceedings of the 5th European Conference on*, pp. 1484–1487, April 2011.

[20] C. G. Ryan, J. Bray, Y. Antar, M. Chaharmir, J. Shaker, and A. Ittipiboon, "A broadband transmitarray using double square ring elements," in *Antenna Technology and Applied Electromagnetics and the Canadian Radio Science Meeting, 2009. ANTEM/URSI 2009. 13th International Symposium on*, pp. 1–4, Feb 2009.

[21] C. G. Ryan, M. Chaharmir, J. Shaker, J. Bray, Y. Antar, and A. Ittipiboon, "A wideband transmitarray using dual-resonant double square rings," *Antennas and Propagation, IEEE Transactions on*, vol. 58, pp. 1486–1493, May 2010.

[22] S. Zainud-Deen, S. Gaber, H. Malhat, and K. Awadalla, "Multilayer dielectric resonator antenna transmitarray for near-field and far-field fixed RFID reader," in *Radio Science Conference (NRSC), 2012 29th National*, pp. 81–88, April 2012.

[23] A. Vorobyov, E. Fourn, R. Sauleau, Z. Baghchehsaraei, J. Oberhammer, D. Chicherin, and A. Raisanen, "Iris-based 2-bit waveguide phase shifters and transmit-array for automotive radar applications," in *Antennas and Propagation (EUCAP), 2012 6th European Conference on*, pp. 3711–3715, March 2012.

[24] J. Oh, G. Hutcheson, W. Hong, and Y. J. Lee, "Planar lens using mixed-order spatial elliptic filter," in *Antennas and Propagation Society International Symposium (APSURSI), 2014 IEEE*, pp. 735–736, July 2014.

[25] J. Oh, G. Hutcheson, F. Aryanfar, W. Hong, and Y. J. Lee, "Planar beam steerable lens antenna system using non-uniform feed method," in *Antennas and Propagation Society International Symposium (APSURSI), 2014 IEEE*, pp. 651–652, July 2014.

[26] J. Lau and S. Hum, "A low-cost reconfigurable transmitarray element," in *Antennas and Propagation Society International Symposium, 2009. APSURSI '09. IEEE*, pp. 1–4, June 2009.

[27] J. Lau and S. Hum, "Analysis and characterization of a multipole reconfigurable transmitarray element," *Antennas and Propagation, IEEE Transactions on*, vol. 59, pp. 70–79, Jan 2011.

[28] J. Lau and S. Hum, "Design and characterization of a 6 x 6 planar reconfigurable transmitarray," in *Antennas and Propagation (EuCAP), 2010 Proceedings of the Fourth European Conference on*, pp. 1–5, April 2010.

[29] A. Munoz-Acevedo, P. Padilla, and M. Sierra-Castaner, "Ku band active transmitarray based on microwave phase shifters," in *Antennas and Propagation, 2009. EuCAP 2009. 3rd European Conference on*, pp. 1201–1205, March 2009.

[30] L. Boccia, I. Russo, G. Amendola, and G. Di Massa, "Multilayer antenna-filter antenna for beam-steering transmit-array applications," *Microwave Theory and Techniques, IEEE Transactions on*, vol. 60, pp. 2287–2300, July 2012.

[31] J. Lau and S. Hum, "A wideband reconfigurable transmitarray element," *Antennas and Propagation, IEEE Transactions on*, vol. 60, pp. 1303–1311, March 2012.

[32] J. Lau and S. Hum, "Reconfigurable transmitarray design approaches for beamforming applications," *Antennas and Propagation, IEEE Transactions on*, vol. 60, pp. 5679–5689, Dec 2012.

[33] W. Pan, C. Huang, X. Ma, and X. Luo, "An amplifying tunable transmitarray element," *Antennas and Wireless Propagation Letters, IEEE*, vol. 13, pp. 702–705, 2014.

[34] M. Sazegar, Y. Zheng, C. Kohler, H. Maune, M. Nikfalazar, J. Binder, and R. Jakoby, "Beam steering transmitarray using tunable frequency selective surface with integrated ferroelectric varactors," *Antennas and Propagation, IEEE Transactions on*, vol. 60, pp. 5690–5699, Dec 2012.

[35] E. Erdil, K. Topalli, N. Esmaeilzad, O. Zorlu, H. Kulah, and O. Aydin Civi, "Reconfigurable nested ring-split ring transmitarray unit cell employing the element rotation method by microfluidics," *Antennas and Propagation, IEEE Transactions on*, vol. 63, pp. 1163–1167, March 2015.

[36] T. Chaloun, C. Hillebrand, C. Waldschmidt, and W. Menzel, "Active transmitarray submodule for k/ka band satcom applications," in *German Microwave Conference (GeMiC), 2015*, pp. 198–201, March 2015.

[37] C.-C. Cheng and A. Abbaspour-Tamijani, "Study of 2-bit antenna ndash;filter ndash;antenna elements for reconfigurable millimeter-wave lens arrays," *Microwave Theory and Techniques, IEEE Transactions on*, vol. 54, pp. 4498–4506, Dec 2006.

[38] C.-C. Cheng, B. Lakshminarayanan, and A. Abbaspour-Tamijani, "A programmable lens-array antenna with monolithically integrated mems switches," *Microwave Theory and Techniques, IEEE Transactions on*, vol. 57, pp. 1874–1884, Aug 2009.

[39] A. Clemente, L. Dussopt, B. Reig, R. Sauleau, P. Potier, and P. Pouliguen, "1-bit mems based reconfigurable unit-cell for transmit-array antennas at x-band frequencies," in *Proc. of 13th International Symposium on RF MEMS and RF Microsystems (MEMSWAVE 2012)*, 2012.

[40] A. Clemente, L. Dussopt, R. Sauleau, P. Potier, and P. Pouliguen, "1-bit reconfigurable unit cell based on pin diodes for transmit-array applications in x -band," *Antennas and Propagation, IEEE Transactions on*, vol. 60, pp. 2260–2269, May 2012.

[41] W. Pan, C. Huang, X. Ma, B. Jiang, and X. Luo, "A dual linearly polarized transmitarray element with 1-bit phase resolution in x-band," *Antennas and Wireless Propagation Letters, IEEE*, vol. 14, pp. 167–170, 2015.

[42] E. Feltrin and E. Weller, "New frontiers for the mobile satellite interactive services," in *Advanced satellite multimedia systems conference (asma) and the 11th signal processing for space communications workshop (spsc), 2010 5th*, pp. 155–161, Sept 2010.

[43] H. Fenech, A. Tomatis, S. Amos, V. Soumpholphakdy, and D. Serrano-Velarde, "Future high throughput satellite systems," in *Satellite Telecommunications (ESTEL), 2012 IEEE First AESS European Conference on*, pp. 1–7, Oct 2012.

[44] J. Christensen, "Itu regulations for ka-band satellite networks," in *International Communications Satellite Systems Conference (ICSSC)*.

[45] R. Williams and H. I. Paul, "Potential uses of the military ka-band for wideband milsatcom systems," in *Military Communications Conference, 1998. MILCOM 98. Proceedings., IEEE*, vol. 1, pp. 30–34 vol.1, Oct 1998.

[46] ITU Radio Regulations and Recommandations: www.itu.int.

[47] ETSI standards: www.etsi.org.

[48] FCC Regulations: www.fcc.gov.

[49] T. Rappaport, J. Murdock, and F. Gutierrez, "State of the art in 60-ghz integrated circuits and systems for wireless communications," *Proceedings of the IEEE*, vol. 99, pp. 1390–1436, Aug 2011.

[50] Z. Pi and F. Khan, "An introduction to millimeter-wave mobile broadband systems," *Communications Magazine, IEEE*, vol. 49, pp. 101–107, June 2011.

[51] T. Rappaport, E. Ben-Dor, J. Murdock, and Y. Qiao, "38 ghz and 60 ghz angle-dependent propagation for cellular amp; peer-to-peer wireless communications," in *Communications (ICC), 2012 IEEE International Conference on*, pp. 4568–4573, June 2012.

[52] F. Gutierrez, K. Parrish, and T. Rappaport, "On-chip integrated antenna structures in cmos for 60 ghz wpan systems," in *Global Telecommunications Conference, 2009. GLOBECOM 2009. IEEE*, pp. 1–7, Nov 2009.

[53] T. Rappaport, S. Sun, R. Mayzus, H. Zhao, Y. Azar, K. Wang, G. Wong, J. Schulz, M. Samimi, and F. Gutierrez, "Millimeter wave mobile communications for 5g cellular: It will work!," *Access, IEEE*, vol. 1, pp. 335–349, 2013.

[54] W. Roh, J.-Y. Seol, J. Park, B. Lee, J. Lee, Y. Kim, J. Cho, K. Cheun, and F. Aryanfar, "Millimeter-wave beamforming as an enabling technology for 5g cellular communications: theoretical feasibility and prototype results," *Communications Magazine, IEEE*, vol. 52, pp. 106–113, February 2014.

[55] ETSI-TR101982, "Electromagnetic compatibility and radio spectrum matters (erm); radio equipment to be used in the 24 ghz band; system reference document for automotive collision warning short range radar." ETSI standards: www.etsi.org, July 2002.

[56] ETSI-EN302288, "Electromagnetic compatibility and radio spectrum matters (erm); short range devices; road transport and traffic telematics (rttt); short range radar equipment operating in the 24 ghz range." ETSI standards: www.etsi.org, Jan. 2012.

[57] ETSI-EN301091, "Technical characteristics and test methods for radar equipment operating in the 76 ghz to 77 gh band." ETSI standards: www.etsi.org, 1998.

[58] S.-K. Lin and Y.-C. Lin, "A compact sequential-phase feed using uniform transmission lines for circularly polarized sequential-rotation arrays," *Antennas and Propagation, IEEE Transactions on*, vol. 59, pp. 2721–2724, July 2011.

[59] Y. Zhang, M. Abd-Elhady, W. Hong, and W. Li, "Research progress on millimeter wave transmitarray in sklmmw," in *High Speed Intelligent Communication Forum (HSIC), 2012 4th International*, pp. 1–2, May 2012.

[60] S. Zainud-Deen, S. Gaber, H. Malhat, and K. Awadalla, "Perforated transmitarray-enhanced circularly polarized antennas for high-gain multi-beam radiation," in *Antennas Propagation (ISAP), 2013 Proceedings of the International Symposium on*, vol. 01, pp. 484–487, Oct 2013.

[61] E. Plaza, G. Leon, S. Loredo, and F. Las-Heras, "Dual polarized transmitarray lens," in *Antennas and Propagation (EuCAP), 2014 8th European Conference on*, pp. 2305–2308, April 2014.

[62] R. Phillion and M. Okoniewski, "Lenses for circular polarization using planar arrays of rotated passive elements," *Antennas and Propagation, IEEE Transactions on*, vol. 59, pp. 1217–1227, April 2011.

[63] H. Kaouach, L. Dussopt, J. Lanteri, T. Koleck, and R. Sauleau, "Wideband low-loss linear and circular polarization transmit-arrays in v-band," *Antennas and Propagation, IEEE Transactions on*, vol. 59, pp. 2513–2523, July 2011.

[64] C. Pfeiffer and A. Grbic, "Millimeter-wave transmitarrays for wavefront and polarization control," *Microwave Theory and Techniques, IEEE Transactions on*, vol. 61, pp. 4407–4417, Dec 2013.

[65] P. Hall and M. Smith, "Sequentially rotated arrays with reduced sidelobe levels," *Microwaves, Antennas and Propagation, IEE Proceedings*, vol. 141, pp. 321–325, Aug 1994.

[66] P. Hall, "Feed radiation effects in sequentially rotated microstrip patch arrays," *Electronics Letters*, vol. 23, pp. 877–878, August 1987.

[67] A. Smolders and H. Visser, "Low side-lobe circularly-polarized phased arrays using a random sequential rotation technique," *Antennas and Propagation, IEEE Transactions on*, vol. 62, pp. 6476–6481, Dec 2014.

[68] A. Smolders, "Random sequential rotation: A new technique for sidelobe control of circularly-polarized phased arrays," in *Antennas and Propagation Society International Symposium (APSURSI), 2014 IEEE*, pp. 1359–1360, July 2014.

[69] P. Hall, "Application of sequential feeding to wide bandwidth, circularly polarised microstrip patch arrays," *Microwaves, Antennas and Propagation, IEE Proceedings H*, vol. 136, pp. 390–398, Oct 1989.

[70] P. Hall, "Design principles of sequentially fed, wide bandwidth, circularly polarised microstrip antennas," *Microwaves, Antennas and Propagation, IEE Proceedings*, vol. 136, pp. 381–389, Oct 1989.

[71] P. Hall and M. Smith, "Sequentially rotated arrays with reduced sidelobe levels," *Electronics Letters*, vol. 28, pp. 1761–1763, Aug 1992.

[72] P. Hall, "Dual polarisation antenna arrays with sequentially rotated feeding," *Microwaves, Antennas and Propagation, IEE Proceedings H*, vol. 139, pp. 465–471, Oct 1992.

[73] A. Clemente, L. Dussopt, R. Sauleau, P. Potier, and P. Pouliguen, "Wideband 400-element electronically reconfigurable transmitarray in x band," *Antennas and Propagation, IEEE Transactions on*, vol. 61, pp. 5017–5027, Oct 2013.

[74] A. Clemente, *Design of ransmitarrays with beamforming/beamtilting capability.* PhD thesis, University of Rennes 1, 2012.

[75] H. Kaouach, *Quasi-optical reconfigurable antennas at mm-wave frequencies.* PhD thesis, University of Rennes 1, 2009.

[76] Flann Microwave: www.flann.com.

[77] Advanced Technical Materials Inc. (ATM): www.atmmicrowave.com.

[78] Rogers Corp., available online: www.rogers.com.

[79] Arlon, available online: www.arlonmed.com.

[80] Ansys HFSS v.15, available online: www.ansys.com.

[81] D. Pozar, "The active element pattern," *Antennas and Propagation, IEEE Transactions on*, vol. 42, pp. 1176–1178, Aug 1994.

[82] L. Baggen, S. Holzwarth, W. Simon, and O. Litschke, "Phased array using the sequential rotation principle: analysis of coupling effects," in *Phased Array Systems and Technology, 2003. IEEE International Symposium on*, pp. 571–576, Oct 2003.

[83] MACOM technologies: www.macom.com.

[84] Picoprobe GGB Industries Inc.: www.ggb.com.

[85] P. Hannan and M. Balfour, "Simulation of a phased-array antenna in waveguide," *Antennas and Propagation, IEEE Transactions on*, vol. 13, pp. 342–353, May 1965.

[86] J. Huang, "A technique for an array to generate circular polarization with linearly polarized elements," *Antennas and Propagation, IEEE Transactions on*, vol. 34, pp. 1113–1124, Sep 1986.

[87] K. Kerby and J. Bernhard, "Sidelobe level and wideband behavior of arrays of random subarrays," *Antennas and Propagation, IEEE Transactions on*, vol. 54, pp. 2253–2262, Aug 2006.

[88] I. Minin and O. Minin, *Basic principles of Fresnel Array Antennas*. Springer, 2008.

[89] SAMTEC Inc.: www.samtec.com.

[90] MM-Microwave: www.mm-microwave.com.

[91] S. M. Sherman and D. K. Barton, *Monopulse Principles and Techniques*. Artech House, 1984.

[92] R. M. Page, "Monopulse radar," *IRE Convention Record*, pp. 132–134, 1955.

[93] A. Lopez, "Monopulse networks for series feeding an array antenna," *Antennas and Propagation, IEEE Transactions on*, vol. 16, pp. 436–440, Jul 1968.

[94] Z.-W. Yu, G.-M. Wang, and C. xin Zhang, "A broadband planar monopulse antenna array of c-band," *Antennas and Wireless Propagation Letters, IEEE*, vol. 8, pp. 1325–1328, 2009.

[95] H. Wang, D.-G. Fang, and X. Chen, "A compact single layer monopulse microstrip antenna array," *Antennas and Propagation, IEEE Transactions on*, vol. 54, pp. 503–509, Feb 2006.

[96] H. Wang, D. Fang, and M. Li, "A single-channel microstrip electronic tracking antenna array with time sequence phase weighting on sub-array," *Microwave Theory and Techniques, IEEE Transactions on*, vol. 58, pp. 253–258, Feb 2010.

[97] R. Kinsey, "An edge-slotted waveguide array with dual-plane monopulse," *Antennas and Propagation, IEEE Transactions on*, vol. 47, pp. 474–481, Mar 1999.

[98] B. Liu, W. Hong, Z. Kuai, X. Yin, G. Luo, J. Chen, H. Tang, and K. Wu, "Substrate integrated waveguide (siw) monopulse slot antenna array," *Antennas and Propagation, IEEE Transactions on*, vol. 57, pp. 275–279, Jan 2009.

[99] Y. J. Cheng, W. Hong, and K. Wu, "94 ghz substrate integrated monopulse antenna array," *Antennas and Propagation, IEEE Transactions on*, vol. 60, pp. 121–129, Jan 2012.

[100] W. Hu, M. Ismail, R. Cahill, J. Encinar, V. Fusco, H. Gamble, D. Linton, R. Dickie, N. Grant, and S. Rea, "Liquid-crystal-based reflectarray antenna with electronically switchable monopulse patterns," *Electronics Letters*, vol. 43, pp. –, July 2007.

[101] L. Schulwitz and A. Mortazawi, "A monopulse rotman lens phased array for enhanced angular resolution," in *Microwave Symposium, 2007. IEEE/MTT-S International*, pp. 1871–1874, June 2007.

[102] S. Raman, N. Barker, and G. Rebeiz, "A w-band dielectric-lens-based integrated monopulse radar receiver," *Microwave Theory and Techniques, IEEE Transactions on*, vol. 46, pp. 2308–2316, Dec 1998.

[103] J. Branigan and R. Miller, "A low-profile full aperture monopulse antenna assembly," tech. rep., Patent n. US 5223850, 1988.

[104] R. Kinsey, "Dual-plane monopulse antenna," tech. rep., Patent n. US 5612702, 1997.

[105] K. Lee and R.-S. Chu, "Design and analysis of a multimode feed horn for a monopulse feed," *Antennas and Propagation, IEEE Transactions on*, vol. 36, pp. 171–181, Feb 1988.

[106] L. Di Palma, A. Clemente, L. Dussopt, R. Sauleau, P. Potier, and P. Pouliguen, "Reconfigurable transmit-array antenna with multiple focal sources," in *Antennas and Propagation (EuCAP), 2014 8th European Conference on*, pp. 1418–1422, April 2014.

[107] M. Bozzi, A. Georgiadis, and K. Wu, "Review of substrate-integrated waveguide circuits and antennas," *Microwaves, Antennas Propagation, IET*, vol. 5, pp. 909–920, June 2011.

[108] L. Yan, W. Hong, G. Hua, J. Chen, K. Wu, and T. J. Cui, "Simulation and experiment on siw slot array antennas," *Microwave and Wireless Components Letters, IEEE*, vol. 14, pp. 446–448, Sept 2004.

[109] M. Comisso, "Theoretical and numerical analysis of the resonant behaviour of the minkowski fractal dipole antenna," *Microwaves, Antennas Propagation, IET*, vol. 3, pp. 456–464, April 2009.

[110] H. Farahani, A. Kabir-Salmani, M. Tayarani, R. Sadeghzadeh, and S. Chamaani, "A novel approach for bandwidth enhancement of siw-based slot array antenna," in *Antennas and Propagation (EUCAP), 2012 6th European Conference on*, pp. 1–3, March 2012.

[111] Southwest Microwave: mpd.southwestmicrowave.com.

List of Publications

International Journals

- L. Di Palma, A. Clemente, L. Dussopt, R. Sauleau, P. Potier, P. Pouliguen, *1-bit reconfigurable unit-cell for transmit-array applications*, IEEE Antennas and Wireless Propagation Letters, 2015 (in press). doi:10.1109/LAWP.2015.2458179

- L. Di Palma, A. Clemente, L. Dussopt, R. Sauleau, P. Potier, P. Pouliguen, *Circularly-polarized transmitarray in Ka-band*, IEEE Trans. Antennas and Propagation, 2015 (in press). doi:10.1109/TAP.2015.2474149

- L. Di Palma, A. Clemente, L. Dussopt, R. Sauleau, P. Potier, P. Pouliguen, *Reconfigurable transmitarray antenna with reduced focal distance*, International Journal of Microwave and Wireless Components, Cambridge University Press (under review).

- L. Di Palma, A. Clemente, L. Dussopt, R. Sauleau, P. Potier, P. Pouliguen, *Reconfigurable transmitarray antenna for monopulse radar applications*, IEEE Trans. Antennas and Propagation (under preparation).

- L. Di Palma, A. Clemente, L. Dussopt, R. Sauleau, P. Potier, P. Pouliguen, *Circularly-polarized reconfigurable transmitarray in Ka-band*, IEEE Trans. Antennas and Propagation (under preparation).

International Conferences

- L. Di Palma, A. Clemente, L. Dussopt, R. Sauleau, P. Potier, P. Pouliguen, *LHCP/RHCP Reconfigurable Transmitarray in Ka-Band*, IEEE AP-S International Symposium on Antennas and Propagation, Vancouver, Canada, July 2015.

- L. Di Palma, A. Clemente, L. Dussopt, R. Sauleau, P. Potier, P. Pouliguen, *Experimental Characterization of Reconfigurable Transmitarray with Reduced Focal Distance in X-Band*, IEEE AP-S International Symposium on Antennas and Propagation, Vancouver, Canada, July 2015.

- L. Di Palma, A. Clemente, L. Dussopt, R. Sauleau, P. Potier, P. Pouliguen, *1-bit Unit-Cell for Transmitarray Applications in Ka-Band*, 9th European Conference on Antennas and Propagation (EuCAP), Lisbon, Portugal, 12-17 April 2015 (oral presentation).

- L. Di Palma, A. Clemente, L. Dussopt, R. Sauleau, P. Potier, P. Pouliguen, *Radiation Pattern Synthesis for Monopulse Radar Applications with a Reconfigurable Transmitarray in X-Band*, 9th European Conference on Antennas and Propagation (EuCAP), Lisbon, Portugal, 12-17 April 2015 (oral presentation).

- L. Di Palma, A. Clemente, L. Dussopt, R. Sauleau, P. Potier, P. Pouliguen, *Reconfigurable Transmit-array Antenna with Multiple Focal Sources*, 8th European Conference on Antennas and Propagation (EuCAP), The Hague, The Netherlands, 6-12 April 2014 (oral presentation). doi:10.1109/EuCAP.2014.6902277

- L. Di Palma, A. Clemente, L. Dussopt, R. Sauleau, P. Potier, P. Pouliguen, *Circularly Polarized Transmit-array Antenna with Sequentially Rotated Elements in Ka-Band*, 8th European Conference on Antennas and Propagation (EuCAP), The Hague, The Netherlands, 6-12 April 2014 (oral presentation). doi:10.1109/EuCAP.2014.6902046

National Conferences

- L. Di Palma, A. Clemente, L. Dussopt, R. Sauleau, P. Potier, P. Pouliguen, *Antennes à Réseaux transmetteurs Reconfigurables*, Forum Innovation DGA, Paris, Nov. 2015.

- L. Di Palma, A. Clemente, L. Dussopt, R. Sauleau, P. Potier, P. Pouliguen, *Réseau transmetteur Reconfigurable en Polarization Circulaire*, Journées Nationales Microondes (JNM), Bordeaux, June 2015.

- L. Di Palma, A. Clemente, L. Dussopt, R. Sauleau, P. Potier, P. Pouliguen, *Concéption et Charactérisation Expérimental des Réseaux Transmetteurs avec Distance Focale Réduite*, Journées Nationales Microondes (JNM), Bordeaux, June 2015. (Prix du Meilleur Papier)

Patents

- L. Di Palma, A. Clemente, L. Dussopt, *Four-quadrant monopulse radar with electronic beam-steering* (pending).

- L. Di Palma, A. Clemente, L. Dussopt, *2-bits reconfigurable unit-cell for transmitarray applications* (under preparation).

VU :

Le Directeur de Thèse

Prof. Ronan SAULEAU

VU :

Le Responsable de l'École Doctorale

VU pour autorisation de soutenance

Rennes, le

Le Président de l'Université de Rennes 1

Guy CATHELINEAU

VU après soutenance pour autorisation de publication :

Le Président de Jury

Antennes Réseaux Transmetteurs Reconfigurables aux Fréquences Millimétriques

De nombreuses applications civiles et militaires (faisceaux hertziens, futurs réseaux mobiles, communications par satellite, radars automobiles, systèmes d'imagerie haute résolution) nécessitent des antennes à faisceau reconfigurable (dépointage de faisceau, faisceaux multiples, faisceaux formés). Les antennes à réseaux transmetteurs apparaissent comme une alternative aux réseaux phasés classiques ou aux réseaux réflecteurs pour ces applications. L'objectif principal de cette thèse est de démontrer la faisabilité de réseaux reconfigurables fabriqués avec des technologies standards en bande Ka (20-30 GHz).

Divers cellules élémentaires utilisant des diodes p-i-n et fonctionnant en polarisation linéaire ou circulaire ont été conçues, optimisées et caractérisées. Les mesures en guide d'onde montrent des pertes minimales de 1,09 dB à 29,0 GHz et une bande passante à 3 dB de 14,7%. Une méthode de simulation hybride a été développée afin d'analyser efficacement des réseaux de grandes dimensions utilisant des rotations séquentielles d'éléments pour optimiser la qualité de polarisation et les diagrammes de rayonnement. Un réseau de 400 cellules élémentaires fonctionnant en polarisation circulaire a été réalisé et testé en chambre anéchoïque. Un dépointage électronique de ±60° et la possibilité de commuter entre les deux polarisations circulaires (droite/gauche) ont été démontrés.

Reconfigurable Transmitarray Antennas at Millimeter-Wave Frequencies

Several civil and military applications (hertzian beams, satellite communications, automotive radars, high resolution imaging systems) require antennas with reconfigurable beam capabilities (beam-scanning, beam-shaping, multiple beam generation). Transmitarray antennas are good candidates and represent an alternative to classical phased arrays or reflect-arrays for these applications. The main objective of this thesis is to demonstrate the feasibility of reconfigurable transmitarrays fabricated with standard technologies in Ka-band (20-30 GHz).

Different unit-cell designs based on p-i-n diodes have been developed to work in linear and circular polarization. Their optimization and experimental characterization have been performed. Waveguide measurements show insertion losses of 1.09 dB at 29.0 GHz with a 3-dB bandwidth of 14.7%. A hybrid simulation technique has been developed in order to analyze efficiently large transmitarrays in which the sequential rotation technique has been applied to optimize the polarization quality and the radiation patterns. A 400-elements transmitarray operating in circular polarization has been realized and tested in anechoic chamber. A beam-scanning angular coverage of ±60° and circular polarization selection (left/right) have been demonstrated.